STRUCTURAL AND ELECTRONIC CHARACTERISATION OF SUB-NANOMETRE METAL PARTICLES

by

CHRISTOPHER JAMES HEARD

A thesis submitted to the

University of Birmingham

for the degree of

DOCTOR OF PHILOSOPHY

School of Chemistry

College of Engineering and Physical Sciences

University of Birmingham

May 2014

UNIVERSITY OF
BIRMINGHAM

University of Birmingham Research Archive

e-theses repository

This unpublished thesis/dissertation is copyright of the author and/or third parties. The intellectual property rights of the author or third parties in respect of this work are as defined by The Copyright Designs and Patents Act 1988 or as modified by any successor legislation.

Any use made of information contained in this thesis/dissertation must be in accordance with that legislation and must be properly acknowledged. Further distribution or reproduction in any format is prohibited without the permission of the copyright holder.

Abstract

This thesis contains a collection of computational studies of the structural, electronic and energetic properties of ultrasmall metal clusters over a range of conditions, including free, substrate supported and organic molecule-ligated environments. The first two chapters outline a general introduction to the experimental and theoretical understanding of small group 10 and 11 metal clusters, along with the computational methodologies applied in this work. The following work is separated into two parts, the first devoted to studies of coinage metal clusters, and the second to palladium-based clusters. The first part begins with a chapter regarding the electronic structure global optimisation of octameric neutral mixed coinage metal clusters, and is concerned with the dopant-induced 2D to 3D transition of global stability. The second chapter of the section considers the structure prediction of tetrameric gold-silver cations from a combined experimental-theoretical perspective, combining global optimisation and simulation of optical spectra with longitudinal beam depletion spectroscopy to unambiguously determine the preferred isomers in experiment. The third chapter is concerned with the simulation of the optical properties of exotic helical clusters at the subnanometre size, finding a dopant position and dopant level dependent shift of the significant molecular excitations. The section is completed with a computational energy landscape exploration of a mixed, neutral copper-silver octamer which combines structure prediction with a statistical analysis of the transitions between isomers and the topology of minima. The next part contains chapters concerned with the structures of bare and oxidised palladium subnanometre clusters, from a joint theoretical-experimental study of water splitting electrocatalysis, and from a computational study of cluster size, support identity and oxidation level effects on cluster structure. The next chapter extends the interest in surface binding for subnanometre clusters to include a direct surface Genetic Algorithm investigation of Pd-Ag and Pd-Pt tetramers upon MgO (100). The section concludes with a chapter on palladium clusters bound by dibenzylideneacetone, which considers the effect of ligand and cluster size on the energetics, charge states and energy landscapes of a popular catalyst system.

Acknowledgments

Academically, my thanks must go to the various members and iterations of the Johnston group at Birmingham, and in particular Andy Logsdail, Sven Heiles, Paul Jennings and Mark Oakley, the scientific, technical and advisory efforts of whom have been invaluable for each of my projects and problems. Beyond the group, I owe a debt to a great number of collaborators, particularly Stefan Vajda and Glen Ferguson at Argonne National Laboratory, Christian Schön, Sridhar Neelamraju and Manish Sultania at the Max Planck Institute for Solid State Research in Stuttgart, and Armin Shayeghi and Rolf Schäfer in Darmstadt. Most of all, and without question, my supervisor Roy Johnston deserves thanks beyond that which I can commit to a small paragraph. His attention to detail, willingness to go (and send me) that extra 1000 miles, and scientific insight have made my time at Birmingham immeasurably more productive and interesting than they could otherwise have been. I wish him considerably better than his ill-fated football team gives him.

I also acknowledge those organisations and bodies which have supported my time here, including both the funding of the EPSRC and the School of Chemistry at the University of Birmingham, and the facilities (and people associated) of Bluebear, HECToR, MidPlus and the Center for Nanoscale Materials (Argonne), for computational access, cpu time and technical help.

On a personal note, I thank Simon Neville, Rory Steven and Christopher Robertson for continuing to enhance my chemistry education, as well as Nick Silverman and Ray Steller, (who would never dream of leaving a man behind). My long-suffering housemates Tom Embury, Kirsty Reynolds and Christopher Barnes deserve a thank you, for providing an endless supply of mugs and support. Last among mentions but first among people, I thank Simon Jenkins, who has made my time here not only a chemical enlightenment, but a philosophical, political and moral one too.

Abbreviations

- **NP** Nanoparticle
- **GO** Global Optimisation
- **GA** Genetic Algorithm
- **BCGA** Birmingham Cluster Genetic Algorithm
- **DFT** Density Functional Theory
- **GGA** Generalised Gradient Approximation
- **TDDFT** Time Dependent Density Functional Theory
- **CIS** Configuration Interaction Singles
- **PF** Probability Flow
- **BO** Born-Oppenheimer
- **DOS** Density of States

Contents

I **1**

1 Introduction **2**

1.1 Clusters and nanoparticles 2

1.1.1 Subnanometre clusters 3

1.1.2 Synthesis of clusters 4

1.1.3 Growth 5

1.1.4 Applications 6

1.1.5 Group 10 and 11 metals 8

2 Methodology **11**

2.1 Energy Landscapes 11

2.2 Energetic models 13

2.2.1 Semi-empirical potentials 13

2.2.2 Molecular Quantum Mechanics 15

2.2.3 Density Functional Theory 17

2.2.3.1 Exchange correlation functionals 19

2.2.3.2 Generation of KS density 21

2.2.3.3 Basis functions 22

2.2.4 Time Dependent Density Functional Theory 25

2.3 Global optimisation and landscape exploration techniques 27

2.3.1 Genetic Algorithm 28
2.3.1.1 Birmingham Cluster Genetic Algorithm 29
2.3.1.2 GA-DFT 33
2.3.1.3 Surface BCGA 33
2.3.2 Threshold Algorithm 34
2.3.3 Basin hopping 36
2.3.4 Transition state searching 37
2.3.4.1 Sampling configuration space 38

II **42**

3 A density functional global optimisation study of neutral 8-atom CuAg and CuAu clusters **43**
3.1 Introduction 43
3.2 Publication 46

4 Optical and electronic properties of mixed Au-Ag tetramer cations **46**
4.1 Introduction 46
4.1.1 Author contribution 48
4.2 Publication 49

5 A theoretical study of the structures and optical spectra of helical copper-silver clusters **50**
5.1 Introduction 50
5.2 Publication 52

6 Energy landscape exploration of the Cu_4Ag_4 cluster with the threshold algorithm **53**
6.1 Introduction 53
6.2 Publication draft 55

III **56**

7 Size-Dependent Sub-Nanometer Pd Cluster (Pd_4, Pd_6 and Pd_{17}) Water Oxidation Electrocatalysis **57**

7.1 Introduction 57
7.2 Author Contribution 59
7.3 Publication 60

8 Support and Oxidation Effects on Subnanometer Palladium Nanoparticles **61**

8.1 Introduction 61
8.2 Publication 64

9 $Pd_nAg_{(4-n)}$ and $Pd_nPt_{(4-n)}$ clusters on MgO(100): A density functional surface genetic algorithm investigation **65**

9.1 Introduction 65
9.2 Publication draft 68

10 Dibenzylideneacetone-ligated subnanometre palladium clusters **69**

10.1 Introduction 69
10.2 Publication draft 72

11 Discussion **73**

11.1 Group 10 and 11 elements 73
11.2 Global optimisation 75
11.3 Energetic properties 76
11.4 Electronic properties 78
11.5 Tunability of cluster properties 80
11.6 Composition control 81
11.7 Chemical ordering 83
11.8 Conclusions 86
11.9 Current and future work 86

Part I

Chapter 1

Introduction

1.1 Clusters and nanoparticles

Clusters are defined broadly as discrete aggregates of molecular or atomic units, which extend anywhere from between three units and hundreds of nanometres across (millions of units) [1]. Often, the term “cluster” is applied to the ultrasmall end of this size spectrum, particularly to the subnanometre range, while “nanoparticle” refers to the larger regime. This is a convention which will be employed in the present work. Clusters, then, may be small collections of molecules, fragments of ionic solids, or aggregates of metal atoms, either bare or passivated, with some individual identity distinct from their environment. In this work, the focus is upon metallic clusters, restricted to the size range of less than twenty atoms. Metal clusters can be formed variously as the accumulation of atoms either through collions in a gas phase mixture [2, 3, 4], the result of growth and sintering upon a substrate [5, 6, 7], or the agglomeration of single atoms bound to ligands in the solvent phase [8, 9, 5]. They represent both a phase in their own right, intermediate in size between atoms and nanoparticles (and ultimately the bulk), and a metastable range during growth, dependent on the physical and chemical environment. Their properties are known to be distinct both from the nanoparticular (NP) and atomic, displaying structures, binding energies, cohesive energies, electronic structure and chemical reactivity which are not necessarily predictable from knowledge of the atomic or nanoscale properties

[10, 11, 12]. Furthermore, the properties of clusters are uniquely variable, as compared to other size ranges. Nanoparticles are sufficiently large that their properties may be well represented by consideration of surface energies and cohesive energies of the metal atoms. Thus, control of growth, reactivity and overall particle stability may be understood in terms of relatively few factors. For clusters, in which there is no well defined core or surface, the concepts of geometric facets or surfaces cease to be useful descriptors. Furthermore, the large-scale geometric control present in nanoparticles is predominantly, but not entirely, replaced by electronic control in clusters.

1.1.1 Subnanometre clusters

Finite size quantum mechanical effects, such as orbital shell closing [10, 12, 13], magnetism [14, 15], and hybridiation between orbitals [16, 17, 18, 19] becomes much more prevalent in clusters than NPs, and leads to dramatic variation of properties at the single atom level. This is the well-known “every atoms counts” [20] regime. Early experiments which determined ionization potentials and the abundance of clusters by size in molecular beams, displayed complex variations which correspond to electronic shell closings [21, 13, 22, 23]. The valence charge distribution which results from the underlying electronic structure of the cluster affects the reactive properties through binding, promoting attachment to binding sites at the atomic level, which necessitates the understanding of the specific location of each atom, unlike in the case of larger systems. The charge upon individual atoms is controlled by geometric frustration, in which through-bond transfer is limited by the asymmetric binding common to ultrasmall clusters, particularly in undercoordinated, planar forms [24, 25]. Additionally, the charge transfer mediated by electronegativity is a powerful means to manipulate the charge distribution for multicomponent or substrate-bound clusters, and an important factor in predicting the final mechanisms and reactivities of the cluster [26, 27, 28].

Geometry plays some role in the properties and stabilities of clusters, determining the binding arrangements of ligands or reactive adsorbates, the number of intracluster bonds which determine the total cohesive energy, and the strength of cluster-substrate interactions [3, 29, 30, 31, 32, 33, 34]. Uniquely for clusters, the competition between two and three dimensional geometric motifs is close, and may be influenced by many subtle factors. For four or more atoms, the energetic balance of planar and compact forms is controlled by quantum effects, such as s/d orbital hybridization, or the preferential distribution of valence electronic density in mixed clusters [35], which is therefore affected by the element, the size and the composition. External factors introduce a further influence, by distorting the electronic and geometric makeup of the cluster. Binding upon substrates has a great effect [36, 4, 26, 27, 37, 38, 39, 40], as the rotational and translational symmetry of the free cluster is broken, providing a subset of preferred orientations and binding sites, controlled by the substrate symmetry, elemental composition or defects. For metallic particles bound to oxide supports, the metal-oxygen bond often dominates the structural space available to the cluster [41, 42, 39, 43, 44, 45, 46], while highly symmetric surfaces, such as MgO(100) may drive epitaxial arrangements of cluster atoms either through growth upon the surface, or kinetically excited rearrangements of deposited particles [47, 48]. Some surfaces, including metallic and graphitic substrates are known to cause flattening of clusters, with the growth of “islands” of metal clusters which wet the substrate [49], forming almost complete monolayers before growing upon the first cluster layer (normal to the surface). This layer growth is electronically and geometrically controlled with the lattice spacing of the substrate and charge transfer [50], and is employed in many catalytic and industrial applications.

1.1.2 Synthesis of clusters

In synthesis with atomic precision, the philosophy is atom-centric, and fine control of growth is required to generate specific, preferred geometries, sizes or compositions. For metallic clusters, a common preparation method is that of laser ablation, followed by a supersonic expansion into a cluster beam [51, 24, 52, 53]. This method has proved effective for many transition metals and metalloids [54, 55, 56]. In laser ablation, the laser beam is directed onto a source rod of bulk metal, causing evaporation of atoms from the surface, which are introduced to a stream of inert carrier gas, frequently argon or xenon and expanded into a chamber, controlled by a pressure gradient, which generates a collimated beam of atoms and small clusters. The cluster size may be finely tuned by the density of the carrier and metal gas, the expansion rate and dimensions of the nozzle. Growth occurs through low energy collisions between atoms and cluster fragments, while heat transfer is mediated by the carrier gas. In this manner, mono and bimetallic clusters are generated, and further analysed by various spectroscopic tools. Time-of-flight mass spectrometry allows for size distributions to be both determined and selected for, while photoexcitation methods, such as longitudinal beam photodepletion [51] provides a means for optical absorption spectra to be generated. Beam deflection measurements [56] can determine dipole moments, and deposition at the end of the beam chamber allows for these generation methods to be applied as schemes to produce size selected, deposited subnanometre particles for catalysis [57, 58].

Another "bottom-up" cluster generation scheme involves wet-chemical aggregation through metal salt reduction. Ionic metal complexes are reduced *in situ* to release the neutral metal atom, which may aggregate with other atoms either through diffusive collisions with atom metal atoms or clusters, or by an autocatalytic process involving further metal ions [59, 60]. An example of this is the generation of gold clusters, from the reduction of $Au^{+}Cl_4^{-}$ with sodium citrate [61]. The size of the resulting particles is then defined by concentrations, the strength of the reducing agent, which controls the size of the particle nucleus, and the choice of stabilising ligand. Thermolytic decomposition of metal complexes have also been applied to the generation of mono- and bimetallic nanoparticles of Pd, Pt and Cu [62], with a range of heating mechanisms, including irradiation of the solution with microwave radiation [63]. Again, passivating ligands may be employed to control the final size of the cluster.

1.1.3 Growth

It is usually the case that the enthalpy gain of maximising metal coordination drives the growth of clusters towards the bulk. This growth may however be limited by entropic contributions, such as trapping in metastable configurations or slowing the cluster motion with temperature control. As previously suggested, this driving force towards growth has a significant role in the structural, electronic and reactive properties of the cluster. Therefore, control of growth is an important feature of cluster design for experimental applications. For surface-deposited clusters, the deposition rate and density of clusters incident upon the surface may be controlled, reducing both the likelihood of cluster-on-cluster deposition, and sintering. The growth of cluster size by sintering processes is well studied, and the phenomena are established for systems over the size range from atoms to nanoparticles, for pure and mixed clusters [7, 5], with mixing of elements and encapsulation proposed as a means to reduce migration of noble metal particles [64]. These processes serve to alter the size of the particles from those which are deposited, which reverses the control applied in the cluster production step. Furthermore, it is possible that the monodispersivity of the sample and homogeneity of the reactive properties is enhanced, by reducing the number of smaller clusters, which vary slightly in size, but whose properties may differ significantly, creating few, larger particles, which are less sensitive to small size differences, through Ostwald ripening. The density of particles is thus necessarily reduced, which is an adverse result for clusters intended for reactive uses. These processes are usually uncontrolled, and rarely are of benefit to specific applications. Choice of substrate allows for the minimisation of cluster migration, either by increasing the cluster-surface interaction strength through judicious choice of surface elements, or through the application of intrinsic defects which pin the cluster in place [39, 42, 65, 66, 67]. The tuning of the support to the application is therefore an important factor in the design of systems in which the cluster plays an active role.

1.1.4 Applications

The tunability of properties by size, shape and composition, the ease by which particles may be produced and the wide variety of methods that exist to do so, and the unique set of properties themselves, which are not present in the bulk are the most significant factors in the broad range of applications of metallic nanoparticles. Optical properties include high reflectivity and optical absorption at around the visible range which were exploited in surface coatings and dyes, even before the advent of the scientific field involving nanoparticles [68]. The tunable absorption, and in particular the existence of a remarkably strong surface plasmon response in coinage metals, have led to a great deal of research into sensing applications in technology and medicine [69, 70]. That this resonance may be finely controlled by particle size, aspect ratio [71, 72, 73, 74], choice of element [75, 76, 77] and alloying [16, 74] has been established, and it is of interest that a notable absorption response is observed down to the subnanometre range in silver [75, 78]. The minimum cluster size for which large optical responses are observed is a current area of research for metallic systems.

The utilisation of nanoparticles for catalytic purposes is a wide ranging field, incorporating cluster and surface science and traditional chemistry, and is applied for highly selective and active reactions in a number of ways. In the form of heterogeneous catalysis in which clusters are deposited upon substrates and subjected to gas phase reactant molecules [79, 80], the particle may be employed as a direct binding site, which provides the appropriate electronic and steric conditions to facilitate a reaction between gas molecules [26, 81, 82, 83]. In this case, the cluster may be tuned to bind gas phase adsorbates with well-defined binding energies, so as to maximise deposition, and thus reactant concentrations, while minimising poisoning, in which tightly bound species block catalytic sites on the cluster [84]. Another means by which heterogeneous catalysis is improved with NPs is by electronic means, through photocatalysis, in which the cluster may be bound to a semiconductor surface, such as Au on TiO_2 [85], and through the modulation of the band structure of the overall system, the electronics are tuned to support particular reactions. In solvent phase reactions, metals are commonly applied for catalysis, either as nanoparticles, which show promise for noble metal-catalysed cross coupling reactions [86], or as single atoms attached to molecular precursors [87]. The growth of clusters may be encouraged, and have some synergistic catalytic properties, as found for example in CFC hydrogenation with subnanometre palladium particles [8], or may be a byproduct of the thermodynamic driving forces towards metal-metal bonding. In the former, there is research devoted to the design and application of clusters to colloidal and solvent phase reactions [86, 88, 89, 90, 91]. In the latter, the mechanisms of growth, structures of intermediates and the means by which growth may be controlled, are required to maximise the activity of the catalysts.

For subnanometre clusters, all of these applications are potentially available, and they have in recent years been found not only to show similar promise to nanoparticles, but often, enhanced activity and selectivity towards reactions [92, 57]. Direct heterogeneous catalysis with subnanometre metal clusters shows turnover numbers hundreds of times higher than the analogous NPs for silver [93], gold [92, 94] and platinum [58, 57] particles in a range of reactions. Electronically, clusters are dissimilar to NPs, lacking the band structure which characterises metals, instead showing molecular excitations, which in turn affects optical response spectra, charge localisation and reactivity/nobility. While selectivity and activity may be increased for subnanometre cluster catalysts, stability is a concern which is more severe than for larger systems. Harsh experimental conditions, such as highly oxidising atmospheres, strongly binding adsorbates or defective substrates will acutely affect the structure, and thus potential of a catalytic cluster, owing to the small total cohesive energy and undercoordination present at such small sizes. There is evidence that the stability of these clusters may be higher than expected, however, with studies finding particles of less than twenty atoms to be sustained over several catalytic cycles without loss of activity or sintering [92]. Where the clusters are not unusually resistant to sintering, the common stabilising procedure used for nanoparticles, such as passivating with long chain molecules are not available. This is due to the lack of reactive sites on ultrasmall clusters, which become rapidly blocked by such ligands. However, substrate control remains an applicable option, with appropriately chosen metal or oxide surfaces or defect binding of the cluster, in order to minimise migration and structural rearrangement.

1.1.5 Group 10 and 11 metals

The metals of groups 10 and 11 contain many of the noble metals, so-named for their lack of reactivity, specifically to corrosion or oxidation in the bulk. These metals have since been found to show considerable reactivity at the nanoscale and subnanoscale, which is selective and tunable [95, 96, 97].

The group 10 elements, platinum and palladium are exceptional catalysts for both the oxygen reduction reaction (ORR) [98, 99] and the oxygen evolution reaction (OER) [100, 101] in oxygen and water splitting reactions, respectively, both of which are extremely important to the application of fuel cells for energy generation. In an atomic form, palladium is utilised for a wide range of chemical synthesis reactions involving carbon, such as cross coupling and bond activation processes, including the Hiyama [102, 103], Suzuki [87] and Negishi [104, 105, 106] reactions. Surface supported, subnanometre platinum clusters were recently found to catalyse the oxidative dehydrogenation of propane [58], with activity up to 100 times higher than traditional platinum catalysts, while maintaining the required product selectivity.

The coinage metals, copper, silver and gold display highly chemoselective catalytic activity towards many oxidation, hydrogenation and dehydrogenation reactions, while silver and gold are remarkably inert in the bulk phase. The oxidation of carbon monoxide by gold nanoparticles was the first major example of nanoscale metal catalysis with metals which are inert at larger sizes [107], and has recently been found to extend to the subnanometre scale [92]. The epoxidation of propylene with silver has been observed for the bulk phase, 3.5 nm particles and the subnanometre particle Ag_3 [93]. The authors report that the NP and trimer show a reduction in unwanted side reactions, suggesting that the smaller clusters provide a less expensive and more selective route to a traditional heterogeneous catalysis reaction. For copper, the electroreduction of oxygen has recently been observed for size selected subnanometre particles [108].

These elements are electronically characterised by a full valence d shell. For the coinage metals, this leads to applications dependent on s electron binding. An example is the deposition of coinage metal clusters upon oxide supports, in which the bond length to the surface is greater than for other transition metals [109, 27]. The overlap of the valence s electron is weaker to the surface oxygen than the diffuse d electrons of the transition metals, resulting in a weaker and thus, longer bond. This promotes cluster mobility and affects the charge distribution of the cluster/surface system, which in turn will alter the reactivity of the cluster. For group 10 metals, the promotion energy from the d^{10} to the d^9s^1 electronic configuration varies with size and chemical environment [27, 28]. Thus, the chemistry may be a complex interplay between d and s orbital filling. As a result, magnetism is present in many group ten metal systems, while the bulk metal Pd or Pt is spin unpolarised. For coinage metals, the separation of s and d orbitals is smaller than in most elements, and thus, s/d hybridisation occurs to an extent which affects both the structural and the chemical properties. For gold, in which the d electrons are found closest to the Fermi energy, the s/d hybridisation is most significant. This mixing is the cause of the later transition from 2D to 3D structures, as inclusion of the d band into the metal-metal binding promotes planarity [110, 25, 36], and the more diffuse orbitals are able to sustain charge better over a less compact geometry. This planarity then affects the role of gold as a substrate for adsorbates in reactions, and its opto-electronic properties.

The mixing of metals for subnanometre cluster catalytic applications is an area in its infancy, due to experimental limitations on size and composition selectivity. Theoretically, potential mixed metal systems may be predicted and tuned, and this is an area of current interest for late transition metals, with the result that new catalytic pathways may be promoted on doping single atoms into small clusters, as found recently for Au/Ag clusters upon MgO(100) [83].

In the following work, we attempt to probe the nature of free, deposited and ligated subnanometre metal clusters, through prediction of structure, and subsequent calculation of energetic and electronic properties.

Chapter 2

Methodology

2.1 Energy Landscapes

Energy landscapes are a conceptual framework for the description of the energetic response to structural rearrangements in many-body systems. The requirement of a mapping between position and energy in an appropriate coordinate basis is sufficient to define an energy landscape. This mapping usually takes the form of an energy function with the general expression $E = E(\mathbf{R}_N)$, where the energy E is a continuous function of the coordinate vector **R**, which is an N-dimensional vector for a system of N components, although continuity is not necessarily required. In the case of atomistic studies of chemical and physical systems, it is often convenient to consider a Cartesian coordinate basis, which converts **R** into a $3N$-dimensional vector, with values for the x, y, and z components for each of the N atoms, such that $E = E(\mathbf{R}_{3N})$. This high dimensional hypersurface contains special points which correspond to physically interesting features. Local minima correspond to stable structures, which represent the possible isomers available to the system. Saddle points represent transition states between pairs of minima, where the Hessian rank of the saddle indicates the number of directions in which the stationary point is a local maximum. Saddle points of order greater than one are rarely considered from a chemical point of view. Minimum energy pathways (MEP) are the paths across the landscape which interconvert two minima, traversing the lowest possible saddle point. Figure 2.1 displays

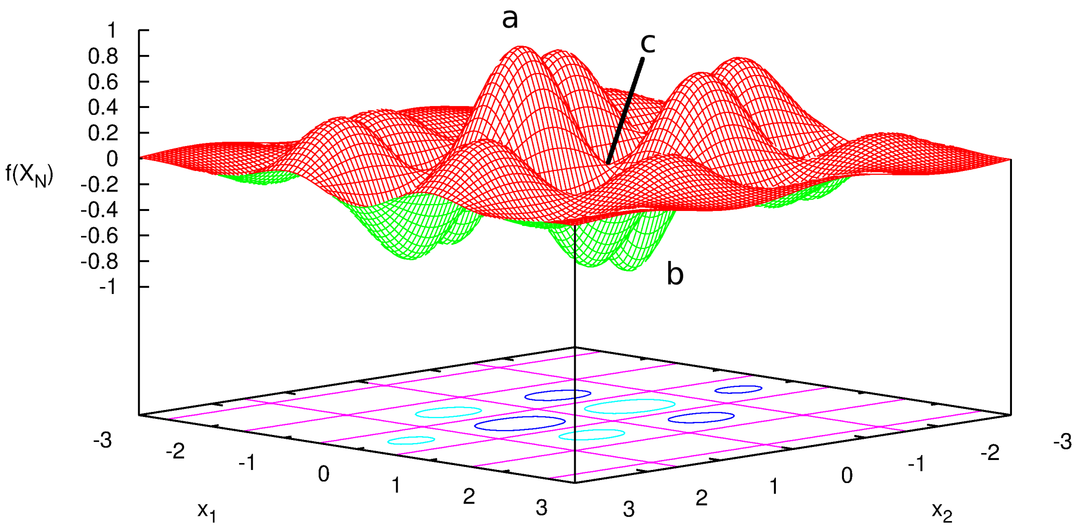

Figure 2.1: Two dimensional energy landscape with general form $f(\mathbf{X}_N) = f(\mathbf{x}_1, \mathbf{x}_2, ..\mathbf{x}_N)$, described by the function $\cos(3\mathbf{x}_1)\sin(2\mathbf{x}_2)\exp(-0.3\mathbf{x}_1^2 - 0.1\mathbf{x}_2^2)$. Special features of the landscape are labelled. The global maximum is denoted **a**, the global minimum is denoted **b**, and a rank 1 saddle point is denoted **c**.

a schematic two dimensional energy landscape with important features highlighted. The dynamic and thermodynamic properties of chemical systems are therefore closely aligned with such analyses, and sophisticated search methods have been developed to exploit these features, described in section 2.3.

For clusters, the energy landscape allows one to consider physical processes, such as the migration of surface atoms, inversion of core and shell atoms for mixed particles, interconversion between locally stable isomers and also chemical processes, including chemisorption and reactions. Furthermore, numerical values for the thermodynamic and kinetic properties of a system such as enthalpies, activation energies, ergodicity and rate constants may be elucidated by analogy to well depths, barriers, phase volumes and pathways on the energy landscape, respectively. [111, 112, 113, 114, 115]

The simplest form of landscape for a chemical system is the potential energy surface, which may be defined with a large variety of functions, and provides a first-order approximation to the energetics of the system. These functions either consider temperature as a scaling factor in the energy, rather than an intrinsic feature of the energy response, or neglect the effect of temperature altogether. It is thus commonly stated that the potential energy surface represents the system at absolute zero temperature, or more accurately, in the athermal regime.

2.2 Energetic models

2.2.1 Semi-empirical potentials

For metallic clusters, a range of potentials have been developed to model the bonding, and thus predict favourable structures, including the Murrell-Mottram [116] or Gupta potential [117] classes. These potentials contain free parameters which are informed by bulk properties such as the cohesive energy, lattice spacing, or for mixed clusters, the enthalpy of mixing, and may therefore be parameterised for particular metals and pairs of metals, with reasonable transferability.

For the noble metals with closed d electron shells, the Gupta potential has been used extensively to predict structures and model energetics [118, 119, 120, 11]. This class of potentials is based on the second moment approximation to tight binding theory, and attempts to represent the delocalised nature of bonding in metals with a many-body term reflecting the embedding of ionic cores into an electron density field across the entire system. This term represents the hopping of electrons between ionic sites, with the ζ prefactor representative of the total hopping probability. The second moment is thus given by the set of transitions between sites, whose total path contains two steps, and returns to the original ionic site. This moment is the variance in the electronic band, and thus provides information on the total band energy of the electronic states at an atomic site, from the relation $\mu \propto W^2$, where W is the width of the band. The total energy of the band at the ionic centre is naturally obtained from the square root of the second moment term, which is approximated by an analytic function, as show in equation 2.3. The repulsive pair term of equation 2.2 is included in the final potential in order to guarantee stability of the underlying lattice. The functional form of the potential is given in equations 2.1 to 2.5, with free parameters A, p, q, ζ and r_0, which are fitted to the cohesive energy, lattice spacing, solution energy, elastic constants and bulk modulus.

$$V_{Gup} = \sum_{i} \left(V^{i}_{pair} + V^{i}_{many} \right) \tag{2.1}$$

where V^{i}_{pair} is given by

$$\sum_{j} \phi(\mathbf{r}_{ij}) \tag{2.2}$$

and V^{i}_{many} is given by

$$-[\zeta^2 \sum_{j} \rho(\mathbf{r}_{ij})]^{\frac{1}{2}} \tag{2.3}$$

and the individual functions ϕ and ρ are radially decaying exponential functions which depict the decreasing strength of interaction with distance, given by

$$\phi(\mathbf{r}_{ij}) = Ae^{-p(\mathbf{r}/r_0-1)} \tag{2.4}$$

and

$$\rho(\mathbf{r}_{ij}) = e^{-2q(\mathbf{r}/r_0-1)} \tag{2.5}$$

The surface of the particle, which makes up a larger contribution to the overall structure as cluster size decreases, causes a departure from the bulk regime from which most potential functions derive their values. Table 2.1 displays the ratio of surface to core atoms as a function of size for some commonly encountered geometric motifs. The number of core atoms only begin to outnumber the surface atoms when $n > 309$ and $n > 201$ for the Ico/Ino and TO respectively. The limitations of potentials for smaller clusters also come about due to quantum electronic effects, such as electronic shell closing, spin and orbital hybridisation, which play a less significant role in determining the geometry for large particles and bulk systems.

S	Ico	Ino	TO
1	12	12	∞
2	3.23	3.23	5.33
3	1.67	1.67	1.54
4	1.10	1.10	0.87
5	0.82	0.82	0.60

Table 2.1: The ratios of surface to core atoms as a function of the number of complete magic number shells (S), for the icosahedron (Ico), square-faced Ino decahedron (Ino) and truncated octahedron (TO). The Ino and Ico clusters have the same growth function, and equivalent magic number sizes (13, 55, 147, 309, 561 ..), whereas the TO has magic numbers of 38, 116, 201, 225 and 314 atoms.

2.2.2 Molecular Quantum Mechanics

Electronic structure calculations which aim to explicitly treat the quantum nature of the electrons of multielectronic systems are based on the application of the Born Oppenheimer (BO) approximation to an appropriate Schrödinger equation for a particular electronic state of the system. This equation relates the wavefunction, which contains all information on the spatial and spin distribution of electrons to the energy, according to the operator relationship

$$\hat{H}\psi = E\psi \tag{2.6}$$

where the wavefunction ψ is a multivariate function over all nuclei and electrons,

$$\psi = \psi(\mathbf{r}_1, \mathbf{r}_2, ..\, \mathbf{r}_N, \mathbf{R}_1, \mathbf{R}_2, ..\, \mathbf{R}_M) \tag{2.7}$$

with $\mathbf{r}_j$ equal to the position of the j'th electron and $\mathbf{R}_k$ equal to the k'th ionic core (nucleus).

$$\hat{H} = \hat{H}_{Te} + \hat{H}_{Tn} + \hat{H}_{Eee} + \hat{H}_{Enn} + \hat{H}_{Ene} \tag{2.8}$$

Equation 2.8 is the expanded Hamiltonian operator, in terms of the individual contributions from the kinetic energy of the electrons and the nuclei

$$\hat{H}_{Te} = -\frac{1}{2}\sum_{j}^{N}\nabla_j^2 \tag{2.9}$$

$$\hat{H}_{Tn} = -\frac{1}{2m_N}\sum_{k}^{M}\nabla_k^2 \tag{2.10}$$

the electron-electron and nucleus-nucleus Coulomb repulsion

$$\hat{H}_{Eee} = +\sum_{j=1}^{N}\sum_{j'>j}^{N}\frac{1}{r_{jj'}} \tag{2.11}$$

$$\hat{H}_{Enn} = +\sum_{k=1}^{M}\sum_{k'>k}^{M}\frac{Z_k Z_{k'}}{r_{kk'}} \tag{2.12}$$

and the Coulomb attraction between electrons and nuclei

$$\hat{H}_{Ene} = -\sum_{k=1}^{M}\sum_{j=1}^{N}\frac{Z_k}{r_{jk}} \tag{2.13}$$

where the index j runs over all electrons from 1 to N, and k runs over all nuclei from 1 to M. These operators make up the time-independent Schrödinger equation and are given in a system of reduced units, such that the electronic charge e and rest mass of the electron m_e become unity, and the permittivity of free space becomes $1/4\pi$.

The BO approximation states that the wavefunction may separated into a product of independent electronic and nuclear components, which greatly reduces the complexity of equation 2.6. This approximation is justified by the vastly differing masses of nuclei and electrons, and states that it is reasonable to consider the motion of the electrons to be governed by a potential generated by the interaction with static nuclei. The electronic wavefunction (ψ_e) then varies only parametrically with the nuclear coordinates, and so, under this approximation

$$\psi = \psi_e(\mathbf{r};\mathbf{R})\psi_n(\mathbf{R}) \tag{2.14}$$

with ψ_n the nuclear wavefunction. The Schrödinger equation becomes

$$\hat{H}\psi = \hat{H}_e\psi_e + \hat{H}_n\psi_n = E_e\psi_e + E_{Tn}\psi_n + E_{Enn}\psi_n \tag{2.15}$$

Therefore, for a particular electronic configuration, the solution of the electronic equation

$$\hat{H}_e\psi_e = E_e\psi_e \tag{2.16}$$

gives the electronic energy, which is sufficient for the majority of chemical and physical analyses. The total energy for the nuclear configuration may, if required, be calculated separately.

This approximation allows for the recovery of an energy landscape, which is defined as the hypersurface generated by the interaction of electrons and nuclei in a static nuclear configuration. In general, the BO approximation is valid for ground state electronic structure calculations such as the structure prediction conducted in the presented work. The approximation breaks down when electronic excitations occur, as these are often coincident with a change in nuclear configuration, which may be represented as the crossing of several BO surfaces.

2.2.3 Density Functional Theory

A drastic simplification of the Schrödinger equation is made by replacing the full wavefunction ψ_e as the central concept, with the electron density $\rho(\mathbf{r})$, reducing the dimensionality from 3N for an N-electron system (or 4N for an N-electron spin polarized system) to 3 (4). The electron density is a probability distribution function for the location of electrons, and is defined to be the probability of locating an electron within a volume element $d\mathbf{r}$. The integral $\int \rho(\mathbf{r})d\mathbf{r}$ is then the total number of electrons N. This modification was first applied in the Thomas-Fermi model [121, 122], which describes the kinetic energy of an electron gas as a functional of the electron density

$$T[\rho(\mathbf{r})] = A\int f(\rho(\mathbf{r}))d\mathbf{r} \tag{2.17}$$

where A is a numerical constant, and goes on to show that the total energy is a functional of the density, assuming the variational principle applies to the density, i.e. the ground state is given by the density which minimises the total energy. With this assumption, they found that the total energy is determined fully from knowledge of the three dimensional density function.

This principle is applied to modern density functional theory as developed by Hohenberg, Kohn and Sham [123, 124]. Hohenberg and Kohn formulated the electronic Hamiltonian for polyelectronic systems as

$$\hat{H} = \hat{H}_T + \hat{H}_{Eee} + \hat{H}_{ext} = \hat{H}_F + \hat{H}_{ext} \tag{2.18}$$

in which the electron index e is suppressed. The solution is then

$$E[\rho(\mathbf{r})] = E_F[\rho(\mathbf{r})] + \int d^3\mathbf{r}\rho(\mathbf{r})V_{ext} \tag{2.19}$$

This rearrangement separates the Hamiltonian into a term which may be considered the response of the electrons to an external field due to the nuclei $V_{ext}[\rho]$, and a system independent energy term $E_F[\rho]$, made up of the electron kinetic energy and the electron-electron interaction. Each of these energetic terms are functionals of the electron density, and the first Hohenberg-Kohn theorem states (and may be simply proven), that the density uniquely defines the external potential $V_{ext}[\rho]$. With this uniqueness theorem, the electronic energy of the multielectron system is exactly determined as a functional of the density from equation 2.19.

The second Hohenberg-Kohn theorem states that where the energy is uniquely defined by the density, the ground state energy is equal to the energy of the system with the ground state density. This provides a variational route to determining in a self consistent manner, the optimal density ρ_0, and thus the ground state energy E_0.

$$E_0 = E[\rho_0(\mathbf{r})] \tag{2.20}$$

The means to solve the Schrödinger equation exactly are provided, by guessing and iterating over attempts for $\rho_0(\mathbf{r})$ and applying these solutions to equation 2.19. Density functional theory is in practice not exact, due to the inability to find exact functional forms for the electronic kinetic energy operator $\hat{H}_T$ or the non-classical component of the electron-electron interaction $\hat{H}_{ee-nc}$, whose eigenvalues are defined by:

$$E_F[\rho] = E_T[\rho] + E_{Ee}[\rho] = E_T[\rho] + E_J[\rho] + E_{ee-nc}[\rho] \tag{2.21}$$

where the **r**-dependence is suppressed for clarity. By expanding E_F in this way, the total electronic energy may be written as:

$$E[\rho] = E_T[\rho] + E_{ee-nc}[\rho] + E_J[\rho] + E_{Ene}[\rho] \tag{2.22}$$

which contains the exactly soluble E_J and the approximate E_T and E_{ee-nc}. Kohn-Sham theory states that by converting the system into a set of auxillary, non-interacting, one electron basis functions which have the same density as the exact system, the kinetic energy is perturbed from E_T to an auxillary energy E_{Ts}. This modification allows for the exact calculation of E_{Ts}, with the perturbation $E_T - E_{Ts}$ combined with the other unknown energetic contributions into an exchange correlation functional E_{xc}, so that the total energy finally becomes

$$E[\rho] = E_{Ts}[\rho] + E_J[\rho] + E_{Ene}[\rho] + E_{xc}[\rho] \tag{2.23}$$

with

$$E_{xc}[\rho] = (E_T[\rho] - E_{Ts}[\rho]) + E_{ee-nc}[\rho] \tag{2.24}$$

This Kohn-Sham method allows for the definition of parameterized, semi empirical exchange correlation functionals, which are system independent, to in principle, calculate the total electronic energy to arbitrary accuracy.

2.2.3.1 Exchange correlation functionals

The accuracy of an exchange-correlation functional is dependent on its parameterisation, and thus a wide range of solutions have been developed for different classes of similar chemical and physical systems. These include the local density approximation (LDA) [125], which has been successful for bulk solid systems, with impressive accuracy in calculating lattice spacings and cohesive energies. Systems with strong electron correlation effects, such as conjugated molecules, heavy metals and many metal oxides are less well represented. LDA assumes that E_{xc} is that of a gas of electrons embedded into a uniform positive charge distribution, and that the exchange and correlation energies per atom are defined individually as $\epsilon_x(\rho(\mathbf{r}))$ and $\epsilon_c(\rho(\mathbf{r}))$ respectively, such that the total energy E_{xc} is equal to the integral of the per-atom energies calculate at a point, weighted by the density of the point. This implicitly assumes that the density is fixed at each point.

$$E_{xc} = \int \rho(\mathbf{r})(\epsilon_x(\rho(\mathbf{r})) + \epsilon_c(\rho(\mathbf{r})))d\mathbf{r} \tag{2.25}$$

The generalised gradient approximation (GGA) improves on the treatment of LDA, by allowing E_{xc} to depend both on the density and its gradient. The assumption of a smoothly varying density is a more realistic representation of the electron distribution than the fixed value from LDA. The Perdew-Berke-Ernzerhof (PBE) functional [126] is a commonly used example of this type, and is a standard functional for the treatment of bulk and cluster phase metallic systems. Hybrid GGA's are a further advancement, which allow for the mixing of direct Hartree-Fock exchange from the Kohn-Sham wavefunction expansion and GGA xc terms, with proportions which may be optimised for a particular system. Meta-GGAs are a natural extension which refers to the inclusion of the kinetic energy density. This class includes the Minnesota functionals [127], a local version of which (MO6-L) is used in the following work, having shown promise for transition metal and organometalllic systems [128].

A recent improvement to GGA functionals is the range-corrected functional, which allows for a better treatment of the charge separation in systems which exhibit long range charge transfer, such as bimetallics with elements of significantly differing electronegativities [129, 51], or molecules with spatial charge separation, as found in organic photovoltaics [130, 131, 132]. Additionally, the modelling of excitations to high energy orbitals are significantly improved with these methods, which is useful for calculating the optical response with time dependent DFT (TDDFT). These functionals aim to more accurately describe the asymptotic long range behaviour of the electron-electron interaction, which does not tend towards $1/\mathbf{R}_{ij}$ as it should, between the components i and j of a charge transfer process. This description is improved by the separation of the Coulomb term into short and long range components, in which the short range part is DFT exchange, and the long range part is exact Hartree Fock exchange. The parameter which controls the switching-on of the Hartree Fock exchange is a tunable value which may be optimised. One example of this type of functional, used in the following work, is the LC-ωPBE functional [133, 129], which has the form

$$E_{xc} = E_x^{PBE}(\omega) + E_c^{PBE} + E_x^{HF}(\omega) \tag{2.26}$$

where ω determines the distance at which the long range HF exchange is switched on, to gradually replace the short range PBE exchange.

2.2.3.2 Generation of KS density

In order to find the ground state energy of a system, an orthogonal set of one electron KS orbitals $\{\psi_j\}$ must be generated. These orbitals enter into the calculation in terms of the density according to the equation

$$\rho(\mathbf{r}) = \sum_j^N |\psi_j(\mathbf{r})|^2 \tag{2.27}$$

such that a choice of KS orbitals generates a density, which when applied to equation 2.19 gives an electronic energy. In order to find the approximate KS orbitals, the KS equation is generated:

$$f_{KS}\psi_j = \epsilon_j \psi_j \tag{2.28}$$

where

$$f_{KS}(\mathbf{r}) = -\frac{1}{2}\nabla^2 + V_{KS} = -\frac{1}{2}\nabla^2 + \int \frac{\rho(\mathbf{r})}{\mathbf{r} - \mathbf{r'}} d\mathbf{r'} + V_{ext}(\mathbf{r}) + V_{xc}(\mathbf{r}) \tag{2.29}$$

Equation 2.28 is a set of eigenvector equations, the solutions of which gives the set $\{\psi_j\}$ of KS orbitals, and thus a self consistent method to generate $\{\psi_j\}$ is found.

In equation 2.29, all components are known once a guess at $\rho(\mathbf{r})$ is made, except V_{xc}. This exchange correlation potential is defined as the functional derivative of the exchange correlation energy with respect to the density, and thus, with an approximation for E_{xc}, V_{xc}, and hence V_{KS} can be determined for the choice of $\rho(\mathbf{r})$. Application of V_{KS} to the KS equation gives the orbitals which define $\rho(\mathbf{r})$, and thus the energy is calculated finally from:

$$\begin{aligned} E[\rho] = -\frac{1}{2}\sum_{j}^{N}\int \psi_j \nabla^2 \psi_j d\mathbf{r}_1 + \frac{1}{2}\sum_{j}^{N}\sum_{j'}^{N}\int\int |\psi_j(1)|^2 \frac{1}{r_{12}} |\psi'_j(2)|^2 d\mathbf{r}_1 d\mathbf{r}_{2'} \\ -\sum_{j}^{N}\int\sum_{k}^{M}\frac{Z_k}{r_{1k}}|\psi_j|^2 d\mathbf{r}_1 + E_{xc} \end{aligned} \tag{2.30}$$

which is the expanded final form of equation 2.19 and includes both one and two electron integrals.

2.2.3.3 Basis functions

An appropriate choice of basis functions with which to represent the one electron KS orbitals must be made. Two methods are commonly applied, the linear combination of atomic orbitals (LCAO) approach, and the plane wave (PW) approach.

LCAO involves expanding the KS orbitals as a sum of basis functions, chosen to generate appropriate distributions for electrons in atoms. An example of a valid basis is the set of spherical harmonics, which are the exact solutions to the monoelectronic hydrogen atom Schrödinger equation. The generation of KS orbitals is given by the equation:

$$\psi_j = \sum_{\mu=1}^{D} c_{\mu j}\chi_{\mu} \tag{2.31}$$

such that the KS orbital ψ_j is a linear combination of the D basis functions χ_μ weighted by their contribution $c_{\mu j}$. This sum produces D KS orbitals, and is necessarily incomplete. There is no guarantee of a monotonic improvement in quality on increasing the number of basis functions, and there is a dependence on the quality of the chosen basis function class. Two basis set types are commonly applied in DFT calculations: Slater type orbitals (STO) and Gaussian type orbitals (GTO).

STO are hydrogen-like in form, and correctly reproduce the long and short range geometric electron distribution, with a cusp at zero distance from the nucleus, with $\nabla\chi(\mathbf{r}_0) = \infty$. The unnormalised functional form is given in equation 2.32, containing the spherical harmonic function $Y_{lm}(\Omega, \phi)$, and a dependence on quantum numbers l, m and n. GTO are Gaussian forms, and therefore give incorrect short range distributions, with zero gradient at the nucleus, given by equation 2.33. Additionally, the long range decay is too rapid, which underestimates the spatial extent of the orbital. One benefit of the Gaussian basis is that the product of Gaussian functions gives a Gaussian function, so contracted basis sets containing several functions may be employed to increase the accuracy of the basis.

$$\chi_{STO} = \exp{(-\zeta\mathbf{r})}Y_{lm}(\Theta, \phi)\mathbf{r}^{n-1} \tag{2.32}$$

$$\chi_{GTO} = \exp(-\alpha\mathbf{r}^2)x^l y^m z^n \tag{2.33}$$

The performance and efficiency of the basis functions may be enchanced by splitting the basis into core and valence regions, under the assumption that chemical properties are dominated by outer shell electrons. By considering a cutoff, below which the orbitals are treated with a lower quality basis, computational cost may be reduced. Conversely, increasing the quality of the valence electrons is possible, by using multiple functions for each orbital. For example, triple zeta bases, used extensively in the following work, employ three basis functions to represent each orbital. One further advancement may be made by including additional functions of high angular momentum. These “polarization” functions are commonly employed to increase the freedom of the electron distribution to vary in a chemical environment. def2-TZVPP [134] is one such basis set employed in the present work, and is of triple zeta quality, with two additional polarization functions included.

Plane wave methods are designed to treat periodic systems, such as the infinitely repeating unit of an extended surface or bulk material. The KS equations are generated from an expansion of PW functions, which are naturally periodic and have several advantages over the LCAO functions. Each basis function is orthogonal to all others by construction, and by extending the expansion to wavefunctions of higher wave vector (**G**), and thus energy, the basis may be increased to arbitrary quality. A monotonic increase of basis set quality allows for control of the accuracy of the calculation through the basis set cutoff energy, although a disadvantage is that much larger basis sets are required than for LCAO methods.

The PW approach utilises the requirement of Bloch's theorem and periodic boundary conditions to generate wavefunctions. All wavefunctions of a periodic system belong the general Bloch function class:

$$\psi^{(\mathbf{k})}(\mathbf{r}) = u^{(\mathbf{k})}(\mathbf{r})e^{i\mathbf{k}.\mathbf{r}} \tag{2.34}$$

in which there is a complex phase factor $e^{i\mathbf{k}.\mathbf{r}}$ and a function which obeys periodicity $u^{(\mathbf{k})}(\mathbf{r})$, both of which depend on the k-vector. This allows for the reduction of the wavefunction of the entire system to that of the unit cell. Two further rules allows us to define the plane wave basis set. First is the ability to generate any function from a Fourier transform of it's reciprocal space analogue. The second rule is that the requirement of periodicity means that for any Fourier transform, the reciprocal vector over which we integrate (**G**) is constrained, such that $e^{i\mathbf{G}.\mathbf{a}_j} = 1$ where $\mathbf{a}_j$ is a unit vector in direction j. These rules mean that the Bloch function $u^{(\mathbf{k})}(\mathbf{r})$ is a exponential function of the wavevector **G**, defined as $\mathbf{G} = \sum_{\alpha=1}^{3} n_\alpha \mathbf{b}_\alpha$ where $\mathbf{b}_\alpha$ is the lattice vector in direction α. If the expansion is complete, the Bloch function is given by the following unnormalised fourier series:

$$u^{(\mathbf{k})}(\mathbf{r}) = \sum_{\mathbf{G}=0}^{\infty} C^{\mathbf{k}}(\mathbf{G})e^{i\mathbf{G}.\mathbf{r}} \tag{2.35}$$

so that the overall wavefunction becomes:

$$\psi^{(\mathbf{k})}(\mathbf{r}) = e^{i\mathbf{k}.\mathbf{r}} \sum_{\mathbf{G}}^{\infty} C^{\mathbf{k}}(\mathbf{G})e^{i\mathbf{G}.\mathbf{r}} \tag{2.36}$$

which by comparison to equation 2.31 defines the final basis function χ as $e^{i(\mathbf{G}+\mathbf{k}).\mathbf{r}}$, and the coefficient c as the fourier series coefficient $C^{\mathbf{k}}(\mathbf{G})$.

With PW methods, the core electrons, which vary rapidly with $\mathbf{r}$ and become extremely computationally expensive to treat, are usually treated with a pseudopotential. This is analogous to the effective core potential approximation for LCAO orbitals, and is a means to replace the true potential generated by the ionic cores with a smoothly varying, nodeless potential function, which converges to the correct form as the distance approaches a cutoff distance $\mathbf{r}_c$. The valence electrons are treated explicitly, and thus the wavefunction beyond the cutoff, if well chosen, may be correct to chemical accuracy.

2.2.4 Time Dependent Density Functional Theory

Time dependent DFT (TDDFT) is an analogue of Kohn Sham DFT in which the aim is the solution of an approximation to the time-dependent Schrödinger equation:

$$-i\hbar\frac{\partial}{\partial t}\psi = \hat{H}\psi \tag{2.37}$$

It was determined by Runge and Gross[135] that the time-dependent Schrödinger equation may be solved with a time-dependent functional of the electron density, analogous to the first Hohenberg Kohn theorem for DFT, and thus the development of RG theory is very similar. The uniquely defined density $\rho(\mathbf{r},t)$ maps to the time-varying external potential $V_{ext}(\mathbf{r},t)$, and thus a set of one electron KS orbitals may be defined with the same density of the true system, allowing for a self consistent means to solve for $E[\rho(\mathbf{r},t)]$. The KS equation becomes:

$$f_{KS}\psi_j = i\frac{\partial}{\partial t}\psi_j \tag{2.38}$$

where the KS operator is:

$$f_{KS} = -\frac{1}{2}\nabla^2 + V_{KS} = -\frac{1}{2}\nabla^2 + V_J(\mathbf{r},t) + V_{ext}(\mathbf{r},t) + V_{xc}(\mathbf{r},t) \tag{2.39}$$

The time dependent KS potential is more complex to construct than in DFT, and the KS orbitals which generate the density are more difficult to generate, owing to the fact that the analogue to the second HK theorem is not available. There is no variation principle for the density in TDDFT, as energy is no longer conserved, and so there is no clear route to determining the best density to calculate the energy. A reformulation was presented by Runge and Gross, to use the stationary points of the quantum action to create KS orbitals:

$$A[\psi] = \int_{t_0}^{t_1} \int d^3\mathbf{r}\, \psi(\mathbf{r}, t)^* \left(i\frac{\partial}{\partial t} - \hat{H}(\mathbf{r}, t) \right) \psi(\mathbf{r}, t) \tag{2.40}$$

The gradient of the action vanishes for a choice of orbitals which solves the time dependent Schrödinger equation. Furthermore, according to the formulation of Keldish, the action may be defined in such as way that the exchange correlation potential V_{xc} becomes the functional derivative of the xc term in the action with respect to the density, which provides a route to generating the full KS potential (equation 2.39.)

With a method similar to DFT, which formally scales equivalently, and uses the same approximations (the requirement of a good xc functional), TDDFT has become popular for the determination of dynamical features of systems, such as the response to external electric fields [51, 74, 78, 136, 137]. The optical absorption spectra may be simulated with an appropriate method to determine vertical excitation energies from a ground state DFT electronic configuration. This is commonly acheived using linear response theory, which makes the assumptions that the perturbation to the potential on exposure to an external field is small, and so the new Kohn Sham potential may be written:

$$\hat{V}'_{KS} = V_{KS} + dV_{eff} = V_{KS} + dV_{ext} + dV_J + dV_{xc} \tag{2.41}$$

where $\hat{V}'_{KS}$ is the new KS potential, and dV_{eff} is the perturbation to the potential due to the external field. The density then is affected by this new potential, and if sufficiently small, the perturbative expansion of the density may be truncated at the term which is linear in dV_{eff}. The dependence of the density upon the perturbative potential is then:

$$d\rho(\mathbf{r}, t) = \chi_{KS}(\mathbf{r}, t, \mathbf{r}', t')dV_{eff}(\mathbf{r}', t') \tag{2.42}$$

recovering the linear response function $\chi_{KS}(\mathbf{r}, t, \mathbf{r'}, t')$.

This method is powerful because the excitation energies are calculated from the response function, and for the range of excitations well modelled by the xc functional, the spectrum of vertical excitation energies are available. The approximation breaks down for very high lying Rydberg electronic states, due to the poor asymptotic decay of the electron-electron interaction, and may be improved by the use of range corrected functionals. This correction is applied in the following work, and have been shown to increase the accuracy of TDDFT spectral simulations.

2.3 Global optimisation and landscape exploration techniques

In the computational structure prediction and characterisation of clusters, the primary goal is to locate the low-lying minima on the energy landscape, and in particular the global minimum, which corresponds to the energetically most favourable structure. Once a library of stable minima is generated, static properties may be calculated, such as charge distributions or the density of states (DOS). Alternatively, dynamic properties may be considered, including the calculation of MEP, activation energy barriers, and transition rates between isomers. For statics, many global optimisation techniques have been developed, including the genetic algorithm, Monte Carlo [138] and basin hopping [139]. For dynamics, procedures include the threshold method [140], discrete path sampling [141], and elastic band type methods, along with time domain simulations such as molecular dynamics. Complex energy landscapes of multidimensional energy functions of the type frequently encountered in optimisation problems, and ubiquitous in cluster structure prediction are usually considered to be NP hard. This means there is no exact algorithmic approach which will guarantee complete and efficient exploration of a landscape, and consequently, no guarantee that any given minimum is a true global minimum without an exhaustive search, which is impossible for all but trivial cases. Sampling efficiency is hence the central factor for a good GO method.

2.3.1 Genetic Algorithm

The genetic algorithm (GA) is a nature-inspired global optimisation scheme, which mimics the techniques employed in natural selection to optimise a cost function with respect to its cost. Information which encodes the cost function is mapped onto the "genes" (individual variables) in the form of "chromosomes" (the vector set containing all genes). If, for example, we consider the chromosome to make up the structural information (in a cartesian basis) of individual 1 of a population, the chromosome Θ_1 is defined as the set $\{\phi_i, \phi_j, \phi_k, \phi_l, ..\phi_{3N}\}$, where ϕ_i is the gene responsible for coordinate i. Variation of a gene incurs a change to the fitness of the chromosome, and thus the individual. Several evolutionary procedures are then applied in order to produce this variation, inducing mixing between elements of the population and mutation to the genes. Subsequent improvement of overall fitness over several generations is then made, until the cost function is deemed to be globally optimised.

Crossover, or mating is applied to combine the genetic code of two parent elements of the population. The way in which this process is performed is determined by the manner in which the genetic information is encoded. For example, in a GA, the exchange of genes from one parent with the corresponding genes on the other reproduces crossover in nature, and introduces the required variation to the genetic makeup of the population. For example, if the crossover operator $\hat{C_{12}}$ acting upon Θ_1 and Θ_2 crosses the chromosomes after the 3rd gene, the two parents $\Theta_1 = \{\phi_{i1}, \phi_{j1}, \phi_{k1}, \phi_{l1}, ..\phi_{3N1}\}$ and $\Theta_2 = \{\phi_{i2}, \phi_{j2}, \phi_{k2}, \phi_{l2}, ..\phi_{3N2}\}$ generate the offspring $\hat{C_{12}}\Theta_1 = \{\phi_{i1}, \phi_{j1}, \phi_{k1}, \phi_{l2}, ..\phi_{3N2}\}$ and $\hat{C}_{12}\Theta_2 = \{\phi_{i2}, \phi_{j2}, \phi_{k2}, \phi_{l1}, ..\phi_{3N1}\}$. In an evolutionary algorithm (EA) of the kind commonly applied for clusters, the concept of a chromosome is defined by a geometric representation of the individual itself. This subtle change of focus relies on the idea that the genetic diversity determines the phenotypic expression, and so changes made directly at the phenotypic level are sufficient to control the fitness of the individual. For clusters, fitness is usually correlated with energy, and so the fitness function (the potential energy function) is a function of the geometric coordinates. The crossover is found to be more appropriate and physically meaningful when cluster structures themselves are cut along predefined planes and recombined as offspring. This method, introduced by Deaven and Ho [142], named the cut and splice method, may then be simply generalised to mutiple crossover points, weighted crossover and other advancements.

Mutation is another method by which genetic diversity is introduced into the population. Unlike crossover, which may only mix together features already present in the members of a population, mutation can provide new pathways to improved fitness. The operator may take many forms, the effectiveness of which is system-dependent. For an EA applied to clusters, these include a simple replacement of a cluster in the population with a new, randomly generated one ($\hat{M}_1$), replacement of one atom with a new, randomly placed one ($\hat{M}_2$), or in the case of a system of several elements, the exchange of the positions of atoms of different atom type ($\hat{M}_3$). In the notation previously employed, with the additional label of element type (A and B), an example of each mutation type if $\Theta = \{\phi_i^A, \phi_j^A, \phi_k^B, \phi_l^A, ..\phi_{3N}^B\}$, is $\hat{M}_1\Theta = \{\phi_{i'}^A, \phi_{j'}^A, \phi_{k'}^B, \phi_{l'}^A, ..\phi_{3N'}^B\}$, $\hat{M}_2\Theta = \{\phi_i^A, \phi_j^A, \phi_{k'}^B, \phi_l^A, ..\phi_{3N}^B\}$ and $\hat{M}_3\Theta = \{\phi_i^A, \phi_j^B, \phi_k^A, \phi_l^A, ..\phi_{3N}^B\}$.

The extent to which the mutation and crossover affect the population may be modulated by the choice of operator type, and also the rates at which they are applied. Stagnation of the population will occur when the global minimum is found, but also can arise from a lack of genetic diversity, which will lead to convergence to sub-optimal minima. Therefore, the desire to maximise variation in the population is derived from the requirement to effectively sample the energy landscape, and avoid early convergence. The balance between this and the practical need to minimise computational cost for a given global optimisation represents a Pareto front, which is system-dependent.

2.3.1.1 Birmingham Cluster Genetic Algorithm

The Birmingham Cluster Genetic Algorithm (BCGA) [143] is an EA, developed specifically to locate global minimum structures of mono and bimetallic nanoparticles. The procedure of the BCGA is given by the flowchart in figure 2.2 and contains several points at which the method may be optimised for a given system.

The initial generation of a population of clusters, is performed at random inside a spheri-

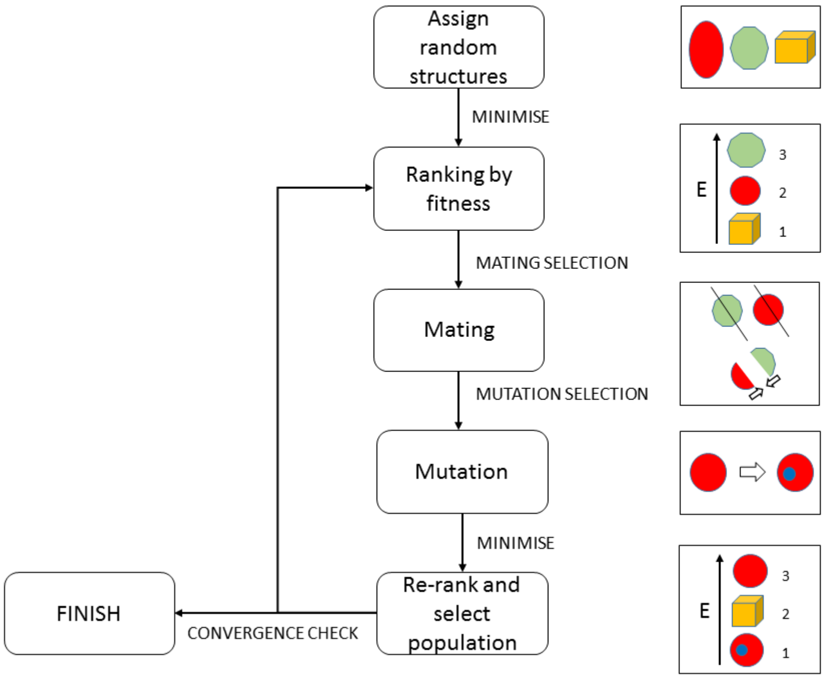
Assign random structures
MINIMISE
Ranking by fitness
MATING SELECTION
Mating
MUTATION SELECTION
Mutation
MINIMISE
Re-rank and select population
CONVERGENCE CHECK
FINISH
E
3
2
1
E
3
2
1

Figure 2.2: A schematic of the procedures undertaken by the BCGA, with generalised cluster structures (cubic, octahedral and spherical).

cal box of predefined size, which is dependent on an estimated metal-metal bond length. The number of clusters in the population is chosen to balance energy landscape searching with computational cost, and so depends on the potential function. Mating consists of two stages: the selection of parents, followed by the crossover step. There are two commonly used parent selection methods employed within the BCGA, the roulette and tournament processes. Roulette-type selection involves calculating a fitness value for each of the clusters in the population, then assigning a label to each cluster, within a range whose size is proportional to the fitness. A random number generator is employed to produce a value, which corresponds to a label, and thus a parent. In this way, pairs of parents are selected with likelihoods according to their fitness, but with some stochastic nature inherent to the process. Tournament selection involves taking a subset of the population, assigning fitness to each element of the subset, and choosing the fittest element as a parent for the mating step. Several subsets are generated, which may be as small as pairs, and the parents are thus mated in a pairwise manner, to produce a set of progeny. In this method the randomness is ingrained in the random selection of the population subset, and the incompleteness of this step. Mating is performed either with one or two-point crossover, with the Deaven-Ho cut and splice procedure, in which the parent clusters are cut by a randomly oriented plane, with the condition that the total number of atoms in the offspring cluster remains the same as the parents. A weighted crossover may also be applied, in which the plane through which the cluster is cut is displaced so that the fitter of the two parents provides the larger fraction of the overall progeny structure.

Mutation in the BCGA is undertaken by the three operators defined in the preceeding section. This variation makes a large difference to the quality of the population, and so is commonly employed with a low rate (approximately 10%).

After each mating or mutation step, the cluster structure is locally minimised. This local minimisation ensures that each cluster in a generation corresponds to a locally stable structure, and in effect means the energy landscape searched is reduced from the full function space to a series of connected plateaux at the energies of local minima, as depicted in figure 2.3. From the evolutionary point of view, the local optimisation is an adaptation which improves fitness before the next evaluation and effectively allows the cluster to improve itself with respect to it's immediate environment, and further, to pass on this improvement to further generations. This corresponds to Lamarckian evolution and provides a more efficient route to optimisation of a cost function than a Darwinian scheme.

After a cycle of genetic operators and local optimisation, the population, which consists of parents, progeny and unused elements is finally assigned fitness and ranked, with the fittest elements passed on to constitute the next generation. In general, global optimisation of multidimensional functions provides no means to unambiguously decide whether the true global minimum has been found. Furthermore, stagnation of a population may occur without a good candidate for the global minimum. As a result, all means by which the cycle is stopped are artifical. The BCGA uses either a preset number of generations, which is usually significantly higher than the number required for convergence for a successful calculation, or a stagnation limitation, for which the calculation stops once the lowest energy cluster in the generation changes by less than a small tolerance for a set number of cycles. The latter is usually employed in practice.

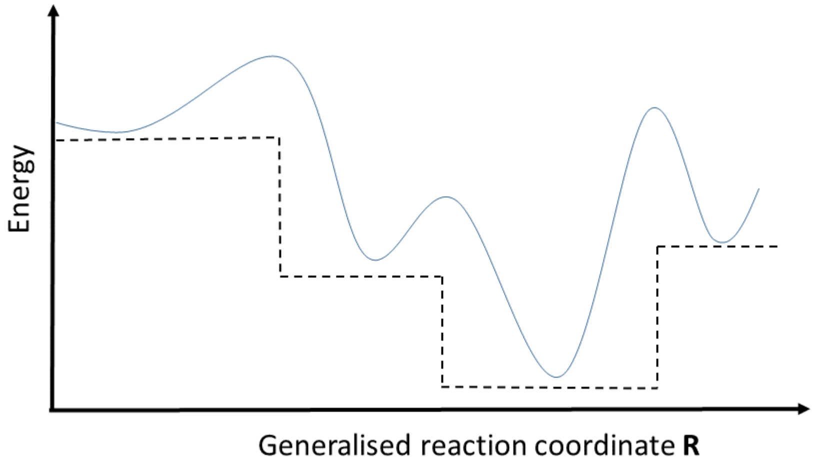
Energy
Generalised reaction coordinate **R**

Figure 2.3: A schematic one dimenional slice through an energy landscape. The blue curve represents the true potential function, while the dashed black line represents the converted landscape which is searched by the Lamarckian GA or BH algorithm. Basins are the regions which share a common minimum, denoted by plateaux.

2.3.1.2 GA-DFT

In order to extend the utility of the BCGA to ultrasmall clusters for which electronic structure methods are required, a DFT modification was generated (GA-DFT) [35]. This advancement involves applying the genetic operators to a population of clusters, and passing the calculation of energies and local geometry optimisation with appropriate minimiser routines to external DFT codes. This procedure has been applied both to plane wave codes (VASP and Quantum Espresso [144]) and an orbital based code (NWCHEM [145]). In order to balance computational cost with search efficiency, smaller populations are employed than in the case of empirical potentials, and looser electronic convergence criteria are used in the DFT calculations than would be employed in a standalone minimisation of a single cluster. This procedure benefits from the proven effectiveness of the BCGA to efficiently search an energy landscape and locate low-energy minima, whilst retaining enough accuracy in the initial search to guide the final energetic ranking of structures. The GA-DFT is usually therefore employed in a two-stage manner, in which a library of low-lying minima are determined with loosened electronic criteria, followed by a higher accuracy reminimisation of structure in the second step. This second step may then introduce additional factors which are prohibitively expensive for a global search, such as spin-orbit coupling or systematic parameter sweeps of various exchange-correlation functionals. This process has been successfully used for systems such as coinage metal clusters [35], tin-bismuth cages [55], lead clusters [54] and transition metal bimetallic clusters Pt-Ti and Pt-V [146].

2.3.1.3 Surface BCGA

The surface BCGA is a new modification of the BCGA which allows for direct surface binding of clusters during the global optimisation. For active supports in particular, which react chemically with bound clusters, the structure of the free cluster is unlikely to give a good indication of the stable structures on deposition, and therefore global optimisation of gas phase clusters may only represent a first order approximation to the final geometry. Ultrasoft landing of clusters may constrain the particle to small-scale rearrangements through kinetic trapping, but high deposition or reaction temperatures will both contribute to overcome energetic barriers to new, low-lying structural motifs. In these cases, global optimisation must take into account the role of the support in distorting the energy landscape.

In the surface BCGA, a slab of substrate material is included into the unit cell inside which the cluster is locally optimised during DFT calculations. In the case of plane wave codes, the unit cell is extended to create a supercell in which the surface extends infinitely in one plane, with sufficient vacuum layers in the direction of the surface normal to avoid vertical image-image interactions. For non-periodic codes, the unit cell is simply predefined to contain the unit cell of the slab, which must be large enough to avoid spurious edge effects and in-plane image self-interactions. The cluster is then deposited inside a sphere truncated at a fixed height above the surface, to avoid cluster atoms from entering the surface. Within this truncated sphere the cluster is subjected to the same series of BCGA operators, but with any energetic influence of the surface implicitly included, due to its presence in single point energy and local geometry optimisation calculations. In addition, the surface atoms may be allowed to locally relax in response to the presence of the cluster if required.

2.3.2 Threshold Algorithm

The threshold algorithm is a method which combines an unbiased energy landscape searching with global optimisation and statistical analysis of the underlying microstates of continuous systems. The procedure involves performing a stochastic exploration of the landscape at energies restricted below pre-defined “threshold” or “lid” values. This constrained random walk, in principle, allows for ergodic sampling of the available landscape, and the determination of equilibrium statistics in the restricted range. By sequentially raising the lid and repeating the sampling, new regions of the landscape become available, and thus information regarding transitions between basins may be obtained. Furthermore, upper-bound estimates to the energetic barriers for interconversion between structural motifs are made.

The threshold algorithm is embedded into a modular code which contains a number of search techniques and local minimisation routines, which are chosen to suit the system of study

[147]. For exploration of the surface, MC, Metropolis MC or simulated annealing type programs may be employed, whereas for local optimisation, steepest descent, or quenched MC moves are available.

In a typical threshold simulation for a cluster with no restricted degrees of translational freedom, a random walk is performed in order to explore configurational space, with regular quenches to low-lying regions of the landscape during the run. This combined search allows for exploration of the high-lying regions which contain the greatest density of configurational states, with a simultaneous sampling of the basins to which the high-lying states belong. In this way, low temperature thermodynamics are considered alongside the kinetics which dominate the higher energy regions. After a fixed number of MC steps, the simulation restarts from the same initial geometry, with a higher energy threshold, allowing for exploration of new regions of the hypersurface. As the threshold energy crosses energy barriers (transition state energies) between minima, new structural classes become available, and the nodal structure of the landscape may be built up. Additionally, sampling of the frequency at which states of particular energy are located allows for the growth of configurational densities of states with energy to be developed. This statistical tool provides a means to map the growth of the phase volume of individual basins, and to compare the topology of various basins, which correspond to different structural classes.

A useful quantity available from the local minimisations performed on the fly during a simulation is the probability flow (PF) [148]. By recording the frequency at which minimisations find particular minima, the concept of the catchment area of a basin is defined. As a function of lid energy, the distribution of probability of locally minimising to a given structure is determined for all available minima. This provides an analogue to a transition rate, which in effect states the probability of a transition from one minimum to another. The temperature dependence of this PF is obtained implicitly from repeating the calculation for each lid energy. In addition, the comparison of PF for forward and backward rearrangements between a pair of minima provide further information on the nature of the transition, from which a dynamic view of the landscape may emerge.

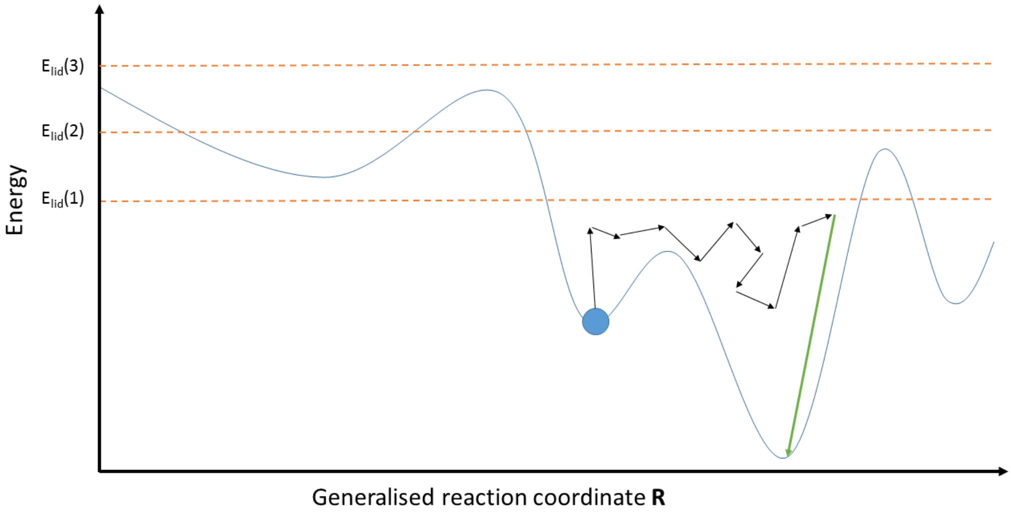

Figure 2.4: A schematic of the threshold algorithm. Black arrows correspond to the MC random walk below predetermined lid energy $E_{lid}(1)$ (red dashed line.) As the lid energy increases, new basins become available. The green arrow is a steepest descent quench to the local minimum.

A further concept, that of entropic barriers may be investigated using this tool [149]. It is commonly found that at energies significantly above the barrier height for the transition between two minima, there is negligible flow between them. This discrepancy between the version of the landscape depicted by the purely thermodynamic tree graph and more dynamic version obtained with the PF is due to entropic barriers. Commonly, while it is energetically possible to reach a new basin, and thus find the new minimum, there are few routes, with few configurational states which allow the transition, and so the rearrangement is statistically under-represented.

After a complete threshold run from a starting point is performed, the list of minima is updated, and the search repeated from additional starting points, which are usually chosen to be at the minimum of a basin. This repetition allows for a more exhaustive search of the landscape, and the discovery of new minima.

2.3.3 Basin hopping

Basin hopping (BH) [139, 150] is a global optimisation method which combines MC steps with local structure optimisation between steps. The strength of the method is that the local optimisation converts MC moves between locations on the energy hypersurface to steps between local minima. This minimisation removes uphill barriers between minima, which represent a major challenge for dynamic simulation methods (such as molecular dynamics) and allows the search to more efficiently explore the landscape. The flattening of the landscape is akin to the approach of the BCGA, and is represented by figure 2.3. Choice of the moveclass is determined by the type of system under study. For clusters, the MC steps are often cartesian moves of individual atoms. Exchange moves may also be included as a fraction of the total steps, which aids sampling of configurational space for mixed systems. For molecular mechanics potentials in which atomic connectivity is fixed, cartesian steps are no longer efficient, and so rotational moves may be considered, in which a subset of bonds are deemed available for rotation. This type of BH simulation is effective for organic or biological systems and is employed in the current work (Chapter 10).

2.3.4 Transition state searching

The number of minima n_{min} on the landscape is suggested to grow exponentially with system size (N), according to the empirically determined formula:

$$n_{min} = 2\prod_{\gamma} N_{\gamma}! e^{\alpha N^{\beta}} \tag{2.43}$$

where α and β are system dependent numerical constants usually on the order of 1 and γ is the index of an element in a heterometallic system [151]. The permutational inversion isomers, which are equivalent, but occupy separate regions of configuration space introduce the prefactor.

The number of first order stationary points, which are the transition states between minima, and have Hessian rank 1, have been shown empirically to vary approximately according to a linear function of the number of minima [152]. That the growth of transition states is not significantly more rapid than that of minima is convenient for their characterisation, however complexity arises from the difficulty in locating such points. Transition states are minima in all coordinates of the landscape except one, in which they are local maxima. The single negative Hessian eigenvector corresponding to this downhill pathway therefore provides a means to

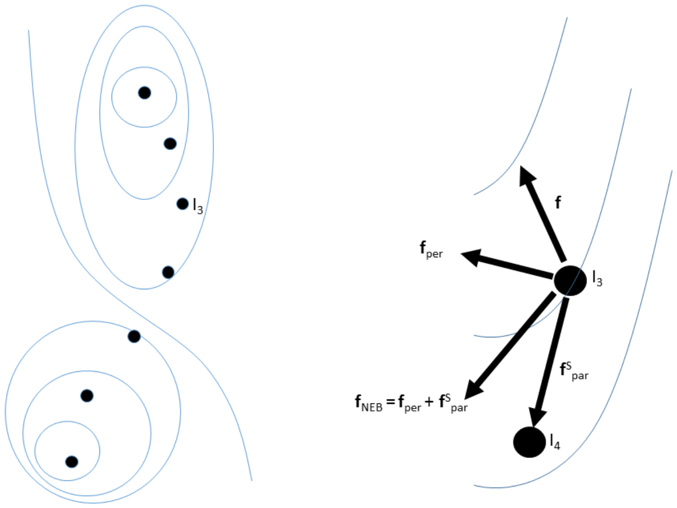

Figure 2.5: Schematic of NEB. Left: projection down the energy axis of the landscape showing the string laid between two endpoints. Right: A view of the force upon image 3, where **f** is the force due to the potential, $\mathbf{f}_{per}$ is the potential force perpendicular to the string, $\mathbf{f}_{par}^{S}$ is the parallel string force, and $\mathbf{f}_{NEB}$ is the NEB force.

connect pairs of minima through their transition state, according to the forward and backward direction of the eigenvector. Convergence to the transition state, and further the elucidation of the set of Hessian eigenvectors from which the path is found is non-trivial, and has led to a number of search and convergence methods.

2.3.4.1 Sampling configuration space

Both single- and double-ended searches are possible for locating transition states, and depend on whether one or two minima are involved in the process, respectively. In the global energy landscape search for an entire system, in which many minima and transition states are required, double-ended searches allow for the development of a library of connected pathways. This double-ended approach is applied in the following work.

Nudged elastic band (NEB) methods attempt to find a pathway between a pair of minima by creating a set of images $\{I_0, I_1, I_2, ..\ I_N\}$, each of which a geometric configuration, which are connected by an attractive spring force, defined by the potential V_s

$$V_s = -\frac{1}{2}\sum_{i=1}^{N} |I_i - I_{i-1}|^2 \tag{2.44}$$

In this way, the spring ensures the images (configurations) stay bound, in order to avoid all configurations from moving to the bottom of the potential well. This string interacts with the true potential, moving the images in order to converge to a low energy pathway between minima [153]. Climbing image methods attempt to find transition states by selecting and image and moving along a high gradient pathway, to reach the local maximum (transition state).

In order to avoid corner cutting, which is an unwanted feature of the interaction between string and potential gradients, and will give erroneous pathways, particular gradient components are projected out of the overall forces, "nudging" the string. The final NEB force $\mathbf{f}_{NEB}$ is equal to the sum of the string force parallel to the string direction of the image, $\mathbf{f}^S_{par}$ and the force due to the potential which is perpendicular to $\mathbf{f}^S_{par}$, denoted $\mathbf{f}_{per}$. In the following work, doubly nudged elastic band (DNEB) [154] methods are employed. This advancement is a compromise which reintroduces a small portion of the perpendicular string gradient $\mathbf{f}^S_{per}$, in order to enhance stability in the local minimisation steps. The DNEB path gives good starting points (images) which are close to the final transition state to which eigenvector-following (EF) methods may more tightly converge [111].

EF or hybrid-EF methods find accurate transition state configurations by isolating the eigenvectors of the Hessian and moving along the path with the lowest positive eigenvalue. This move will take the configuration to a low energy transition state and can be tightly converged. Hybrid-EF techniques are used where the Hessian is unknown or too expensive to calculate accurately, such as a Rayleigh-Ritz method which variationally finds low energy pathways [155]. In these cases, the EF steps may be coupled to a local minimisation in the subspace of orthogonal directions to the EF path.

In the case of clusters or molecules, we are interested in both the minima and the transition states which interconvert them, and so it is useful to build up a connected network of min-ts-min paths. From the connectivity of the network, the likely classes of structures to be found are determined, along with the energetic likelihood of interconversion between minima. Kinetic trapping and entropic considerations may additionally be examined from the number of minima in a class and the barrier heights required to escape them. Visualisation of these networks is commonly undertaken with disconnectivity graphs, or tree graphs [111, 156, 140], which reduce the landscape to a one-dimensional representation, embedded in a two dimensional plot, with energy the additional coordinate. Nodes on the tree represent minima, whilst branch points between pairs of minima are the lowest energy transition states found to interconvert them. An example is shown in figure 2.6, for the $Cu_{12}Au_1$ cluster produced with the Gupta semi empirical potential, showing the global minimum at -35.04 eV, the first suboptimal minimum at -32.52 eV and various transition state barriers between minima. This is a funnelled landscape, in which the GM is separated from other minima by large energies, yet the barriers to reach the GM from high lying minima are low, suggesting a structure-seeking system. This is often the case for thirteen atom coinage metal clusters, as this size is a magic number for the icosahedron. The GM in fig 2.6 corresponds to an icosahedron with the gold dopant in the central site, while the second minimum is an icosahedron with the gold atom at the surface. Higher minima correspond to less stable, more exotic structures.

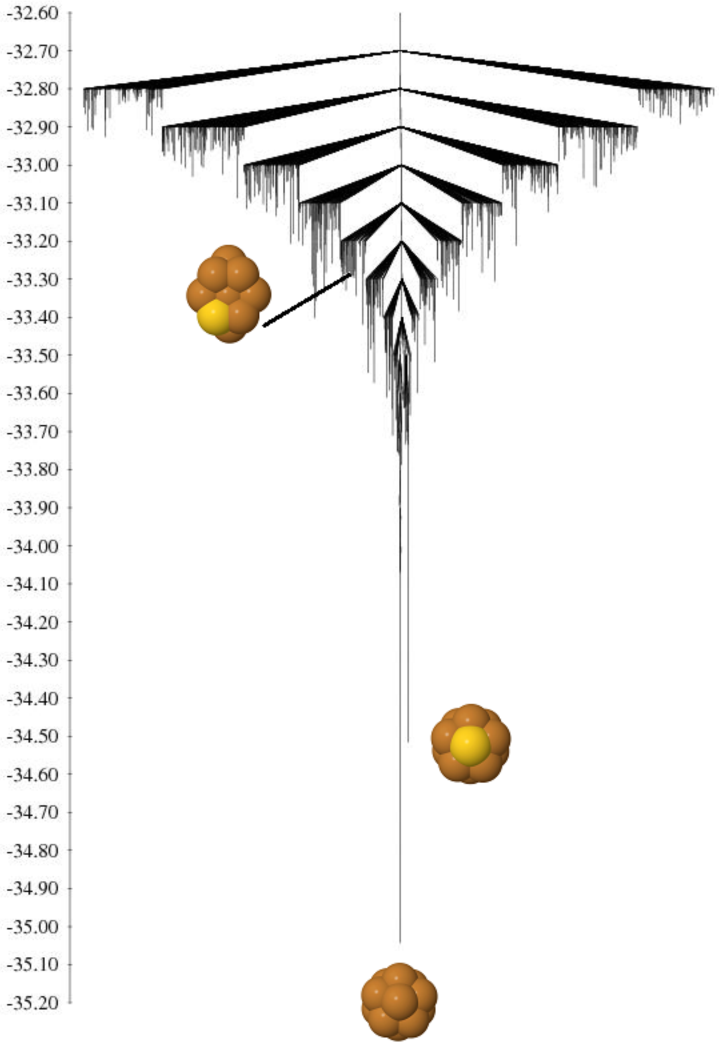

Figure 2.6: Disconnectivity graph of the thirteen atom $Cu_{12}Au_1$ Gupta cluster in units of eV, displaying a "Palm Tree" structure.

Part II

Chapter 3

A density functional global optimisation study of neutral 8-atom CuAg and CuAu clusters

3.1 Introduction

In this study, the newly developed GA-DFT mode of the BCGA is applied to ultrasmall coinage metals in order to illuminate the transition in dimensionality of globally stable cluster structures. The coinage metals are commonly considered to be noble in character, due to their full d electron shells, and singly occupied s orbital valence shell. In addition, the eight atom clusters are predicted and found to exhibit a complete Jellium shell, forming especially stable magic numbers. There is a known size dependent transition from 2D to 3D structures on increasing size, the position of which is known to vary with metal identity and charge state, and in most cases is still an unresolved question. For gold clusters Au_n, the position of this transition for the cationic cluster is around $7 \leq N \leq 8$ [157, 158, 159] and for the anion, at $N = 12$ [4, 160, 161]. The position for the neutral system lies in between these values. The charge dependence is rationalised in terms of the extra (reduced) stability afforded on occupation (depletion) of diffuse orbitals with low electronic repulsion. For silver clusters, the transition is predicted from experiments and theoretical studies to lie between $N = 6$ and $N = 7$ [25, 162] for the neutral charge state and at $N = 5$ [163] for the cation. The explanation for the significant difference between gold and silver transition points is given in terms of s/d hybridisation in the near Fermi energy region. The onset of the highest lying d band in gold is considerably closer in energy to the Fermi level than in silver, due to the relativistic contraction of the s orbitals in gold. This increased s/d hybridisation promotes additional stability of planar configurations and is an example of the non-nobility of the coinage metals at small sizes. Copper clusters, with a further reduced relativistic electronic contribution exhibit this d band onset at considerably lower energies relative to the Fermi level than silver or gold, and so have an earlier transition from 2D to 3D than both silver and gold (between $N = 5$ and $N = 6$ for the neutral and the anion [164, 165], and $N = 4$ for the cation [163]). Octameric clusters therefore represent a size at which particular stability is observed experimentally, and the transition in dimensionality is complete in silver and copper, but not in gold.

The importance of the dimensionality and in general, the structure of the clusters is great in the subnanometre range, due to the role clusters of this size are found to play in reactions [166, 167, 168]. Noble metal clusters of the subnanometre size range are known to be active for a number of catalytic reactions, both when surface supported [92, 58, 169] and free in the gas phase [166, 170, 96]. The effect of structure is critical, as binding strengths and modes to reactive species are controlled by the structure of the host particle, and in particular the electronic structure and charge distribution. The accurate determination of preferred geometries is therefore especially important for ultrasmall metal clusters, and the rational prediction and design of geometries through controllable factors, such as size, charge state or doping is a valuable pursuit.

By modulating the electronic structure of the overall cluster, it is expected that dopants will insert or deplete d band electronic states close to the Fermi energy, and thus affect the stability of planar clusters. This has been observed recently for neutral gold-silver octameric clusters, which show a transition from 2D to 3D global minima at between Ag_2Au_6 and Ag_3Au_5 [35]. By observing the extent to which the doping affects the transition point both through electronic and energetic means, accurate predictions of the role of dopants may be made in the size range at which every atom counts.

Dopant studies of small metal clusters are few, owing in part to the complexity in controlling composition dependence of particles produced through molecular beam type methods. Using the BCGA, the structural motifs of the global and low-lying suboptimal isomers may be found directly at the DFT level, and the electronic factors which control the preference to be observed, with projected densities of states and charge analysis.

3.2 Publication

Authors Christopher J. Heard and Roy L. Johnston

Title A density functional global optimisation study of neutral 8-atom Cu-Ag and Cu-Au clusters

Submitted 28 September 2012

Accepted 05 December 2012

Information *Eur. Phys. J. D.* **67**, 34, (2013)

Eur. Phys. J. D (2013) 67: 34
DOI: 10.1140/epjd/e2012-30601-7

THE EUROPEAN
PHYSICAL JOURNAL D

Regular Article

A density functional global optimisation study of neutral 8-atom Cu-Ag and Cu-Au clusters[⋆]

Christopher J. Heard[a] and Roy L. Johnston

School of Chemistry, University of Birmingham, Edgbaston, Birmingham, UK

Received 28 September 2012 / Received in final form 4 December 2012
Published online 6 March 2013 – © EDP Sciences, Società Italiana di Fisica, Springer-Verlag 2013

Abstract. The effect of doping on the energetics and dimensionality of eight atom coinage metal subnanometre particles is fully resolved using a genetic algorithm in tandem with on the fly density functional theory calculations to determine the global minima (GM) for $\mathrm{Cu}_n\mathrm{Ag}_{(8-n)}$ and $\mathrm{Cu}_n\mathrm{Au}_{(8-n)}$ clusters. Comparisons are made to previous ab initio work on mono- and bimetallic clusters, with excellent agreement found. Charge transfer and geometric arguments are considered to rationalise the stability of the particular permutational isomers found. An interesting transition between three dimensional and two dimensional GM structures is observed for copper-gold clusters, which is sharper and appears earlier in the doping series than is known for gold-silver particles.

Chapter 4

Optical and electronic properties of mixed Au-Ag tetramer cations

4.1 Introduction

For molecular beam type experiments, size selectivity may be controlled finely [58, 51, 171], but there is often ambiguity in the preferred isomer for a given cluster size. Unlike strongly covalent systems, for metal clusters there is usually little separation in energy between similar isomers, as the factors which separate possible configurations, such as hybridisation or bond directionality are not present. Unrestrained bond orders, multidirectional bonding and atomic fluxionality due to delocalised electronic states all contribute additionally to the complexity of the energy landscape for metallic clusters. As a result, there are generally many competitive isomers, often separated by less than the thermal equipartition energy [51], between structures of vastly different classes. For nanoalloys, there will be several permutational isomers or homotops for a given geometric motif and composition. This factor will usually drastically increase the number of possible isomers in a small energy range, as the dopant location often has a minute effect on the total energy of the cluster. This complex situation makes unambiguous determination of the product or products of cluster generation experiments difficult in practice.

Experimentally, controls may be put into place to reduce the available configuration space, such as the thermalisation procedure, which may be tuned to limit the possibility of thermal collisions between clusters [171, 1], and thus the means by which isomeric rearrangements become possible. This method will reduce the freedom to attain high energy geometric motifs, and is in fact a form of kinetic trapping, but does not account for the possibility that the clusters may initially be produced in a sub-optimal geometry which may occur for entropic reasons.

Theoretical studies of cluster structure, particularly those performed with potential energy functions or with DFT, represent to a first order approximation the behaviour at absolute zero temperature and are usually concerned with finding low energy structures. This approach is unlikely to be sufficient in describing the result of a finite temperature experiment, and thus studies are required to combine the predictions of a theoretical model with the results of experiment. There have been several combined investigations, which usually take the form in the case of small metallic clusters of calculating a small number of low-lying structures with DFT, followed by the simulation of some property which may be measured by the beam experiment, such as the vibrational spectrum [3, 29, 172], optical response spectrum [16, 75, 78], photoelectron spectrum [2, 173] or ion mobilities [174, 24]. For these combined approaches to successfully distinguish between isomers potentially present in the beam, the calculated observable must be sensitive enough to the often small changes in structure between isomers. Further, many of the observables which distinguish between isomers are insensitive to changes in permutational isomer, which complicates the choice of method.

In the following work, a multiple-approach combined theoretical-experimental study is made, in which the structure of the mixed gold-silver tetramer cations are elucidated. By combining an unbiased global optimisation using GA-DFT with TDDFT optical response simulations, the isomer(s) present in a longitudinal beam photodepletion experiment are rationalised. Ion mobility simulations of the low lying isomers are performed, with several methods compared, including the novel introduction of accurate charges into the mobility calculation. The three computational analyses are complementary, each providing new information to discriminate between isomers, with two means to directly compare to experiment. The method is presented as a proof of principle, that multiple combined approaches are necessary for small coinage metal clusters, and are sufficiently accurate and computationally cost effective.

4.1.1 Author contribution

The following publication is a collaborative effort between groups at the Technical University of Darmstadt and the University of Birmingham. The author's contribution involved making amendments to the BCGA code required for the systems of study along with an advisory role in the calculations of the optical response. The post-calculation analysis of charge distributions for each of the low lying structures for each composition was performed by the author. Additionally, the ion mobility simulations, including the Projector Approximation, Charge Transfer Trajectory method, and the refinement of the CT-TR method to include Bader charge were performed by the author, along with the post simulation analysis. The computational part of section II, section IIIA and all ion mobility results of section IIIB were all written by the author.

4.2 Publication

Authors Armin Shayeghi, Christopher J. Heard, Roy L. Johnston and Rolf Schäfer

Title Optical and electronic properties of mixed Au-Ag tetramer cations

Submitted 06 December 2013

Accepted 12 January 2014

Information *J. Chem. Phys.* **140**, 054312, (2014)

THE JOURNAL OF CHEMICAL PHYSICS **140**, 054312 (2014)

Optical and electronic properties of mixed Ag-Au tetramer cations

A. Shayeghi,[1,a)] C. J. Heard,[2] R. L. Johnston,[2] and R. Schäfer[1]
[1]*Eduard-Zintl-Institut, Technische Universität Darmstadt, Alarich-Weiss-Straße 8, 64287 Darmstadt, Germany*
[2]*School of Chemistry, University of Birmingham, Edgbaston, Birmingham B15 2TT, United Kingdom*

(Received 6 December 2013; accepted 13 January 2014; published online 7 February 2014)

We present experimental and theoretical studies of the optical response of mixed $Ag_nAu_{4-n}^+$ (n=1–3) clusters in the photon energy range $\hbar\omega = 1.9$–3.5 eV. Absorption spectra are recorded by a newly built longitudinal molecular beam depletion spectroscopy apparatus providing lower limits to absolute photodissociation cross sections. The experimental data are compared to optical response calculations in the framework of long-range corrected time-dependent density functional theory with initial cluster geometries obtained by the unbiased Birmingham Cluster Genetic Algorithm coupled with density functional theory. Experiments and excited state calculations shed light on the structural and electronic properties of the mixed Ag-Au tetramer cations. © *2014 AIP Publishing LLC.* [http://dx.doi.org/10.1063/1.4863443]

I. INTRODUCTION

A major goal of modern nanoscience is the study of size and composition-dependent physical and chemical properties of nanoscale materials with respect to their specific design and adaptation in advanced applications.[1,2] In particular, optical properties of nanoscale systems and building blocks are commonly investigated due to their importance in plasmonic sensoring[3] and nanophotonics,[4] but also as a new class of nanoscale materials in general.[5]

The long term realization of such a goal, however, requires a fundamental investigation of the considered systems at the challenging atomic scale with model systems such as clusters containing only a few atoms. The noble metal elements gold and silver play a central role in current research particularly due to their very interesting optical properties.

While the optical properties of bare and rare gas tagged gold and silver clusters have been intensively investigated from both experimental[6–22] and theoretical points of view,[23–27] studies of their alloys at small sizes are rare at present, apart from photoelectron (PE) spectroscopy measurements of $Au_nAg_m^-$ ($2 \leq n+m \leq 4$) clusters.[28]

In general, less experimental information is available about small cationic Ag-Au clusters, except the ion mobility experiments of Weis *et al.*, who compared collision cross sections of $Ag_mAu_n^+$ ($m+n<6$) clusters to structural predictions from density functional theory (DFT).[29] They showed that most of the tetrameric clusters are rhombus shaped, while Ag_3Au^+ has a Y-structure with the gold atom in the center. They explained their results in terms of a significant charge transfer leaving most of the ions positive charge on the silver atoms. Bonačić-Koutecký *et al.* also discussed the dominant role of charge transfer from Ag to Au for structural properties in their investigation of neutral and charged bimetallic Ag_mAu_n ($3 \leq m+n \leq 5$) clusters.[30]

Gold, as a dopant, has a dominant influence on the optical properties of Ag clusters due to a strong relativistic effect,[31,32] leading to great interest in how the electronic behaviour of silver clusters for instance can be manipulated by doping them with gold.[33–36] From a theoretical point of view, optical properties of Ag-doped Au_{20} clusters have been studied by a first principles analysis showing the HOMO-LUMO transitions being shifted to lower photon energies with increasing Ag concentration.[37] Octameric Au_mAg_n ($m+n$=8) clusters have also been investigated using time-dependent density functional theory (TDDFT) showing odd–even oscillations of the optical gaps with the variation of the number of gold atoms.[38]

In this article, we present photodissociation spectra of $Ag_nAu_{4-n}^+$ (n=1–3) clusters in the photon energy range $\hbar\omega = 1.9$–3.5 eV combined with calculations of the optical response in the framework of TDDFT. Our initial cluster structures are obtained using the Birmingham Cluster Genetic Algorithm (BCGA),[39] coupled with DFT (GADFT).[40–44] The long-range corrected (LC) exchange correlation (xc) functional LC-ωPBEh, a version of LC-ωPBE,[45,46] with parameters recommended by Rohrdanz *et al.*,[47] is used in our analysis. It has been shown to perform well for the calculation of ground and excited state properties of gold,[27,48] and silver clusters,[48] where it leads to a reliable prediction of optical absorption spectra.

II. EXPERIMENTAL AND COMPUTATIONAL DETAILS

The experimental setup is described in detail in Ref. 48. Briefly, the tetramer cluster cations are produced by pulsed laser vaporization and separated by a time-of-flight mass spectrometer (TOF-MS). Before entering the acceleration zone of the TOF-MS and subsequent detection, the clusters are irradiated by a tunable ns-laser pulse in order to record photodissociation spectra by monitoring the ion signal depletion upon photon absorption. The Lambert–Beer law is used assuming a perfect overlap between dissociation laser and

---

[a)] Author to whom correspondence should be addressed. Electronic mail: shayeghi@cluster.pc.chemie.tu-darmstadt.de

0021-9606/2014/140(5)/054312/9/$30.00

© 2014 AIP Publishing LLC

molecular beam. Relative errors of our cross sections are estimated to be ±10% within the visible region and ±30% in the UV range as described in detail in our previous work. The experiment does not provide additional information about possible dissociation channels and therefore we cannot make any conclusions about the dynamics after photon absorption.

We employ an optical parametric oscillator (OPO) pumped by the third harmonic generation (355 nm) of an Nd:YAG laser extended with a harmonic generation unit as a tunable laser source to cover the photon energy range $\hbar\omega = 1.9$–3.5 eV. The available photon fluence is on average at least about 0.2/Å^2 (356 nm) and at most about 0.5/Å^2 (366 nm) in the UV range, while in the visible range it is at least 2.0/Å^2 (410 nm) and at most 8.5/Å^2 (562 nm).

Fluence dependencies of the main optical transitions of Ag_3Au^+ and $AgAu_3{}^+$ show an exponential decay and can be well-fitted with a single Lambert–Beer absorption law. Thus, the transitions can be attributed to one-photon processes. In the case of $Ag_2Au_2{}^+$ the situation is more complicated as the fluence dependencies cannot be fitted well with a single Lambert–Beer law and also not be described by a two-photon process, which argues for the simultaneous presence of several discrete isomers. However, a single Lambert–Beer absorption law does not rule out multiple species in the beam, if these species have similar absorption cross sections. But we would like to point out that, even in the case of a single isomer in the molecular beam, simultaneously occurring one- and two-photon processes could neither be interpreted with a multiple Lambert-Beer fit nor with a fit according to a two-photon process.

The configuration space for all tetramers is searched using the GADFT global optimization approach, in which the plane-wave self-consistent field (PWscf) code within the Quantum Espresso (QE) package,[49] has been coupled with the Lamarckian BCGA.[39] For the DFT calculations, 11 electrons for each atom are treated explicitly and the remaining 36 and 68 core electrons for Ag and Au, respectively, are described by ultrasoft Rabe-Rappe-Kaxiras-Joannopoulos pseudopotentials.[50] An additional nonlinear correction is applied for gold and the Perdew–Burke–Ernzerhof (PBE)[51] xc functional is employed within the generalized gradient approximation (GGA) framework of spin-unrestricted DFT. Within the code, local optimization of cluster structures is performed for each cluster in a generation, with an electronic self-consistency criterion of 10^{-5} eV, and total energy and force convergence considered to be reached when below the threshold values of 10^{-3} eV and 10^{-2} eV/Å, respectively.

The lowest lying potential global minimum (GM) candidates are subsequently locally optimized using NWChem v6.1,[52] employing an extensive 19-electron def2-TZVPP basis set and the corresponding effective core potential (def2-ECP) of Weigend and Ahlrichs.[53] The long-range corrected xc functional LC-ωPBEh[45,47] is used in order to accurately recover the asymptotic $1/r$ behaviour at large distances of the electrons from the nucleus. This has been shown to more reliably reproduce vertical electronic excitation spectra.[25,27,47,48,54] The PBE and the M06-L functional are also studied for comparison purposes. The energy is calculated using a grid of high density (*xfine* integration grid, *tight* optimization criterion). Additionally, a harmonic frequency analysis is performed for all isomers in order to verify whether the structures are actually minima on the potential energy surface (PES).

Partial atomic valence charges are calculated for all DFT local minima at the LC-ωPBEh/def2-TZVPP level within the Bader approach using the program of Tang *et al.*[55] A cubic grid of 101 × 101 × 101 points over a 5.0 × 5.0 × 5.0 Å cube is used to calculate the Bader charges centred upon atomic sites.

For minimum-energy structures resulting from the DFT optimizations, electronic excitation spectra are calculated using spin-unrestricted TDDFT considering 60 excited states. All excited state calculations are performed with NWChem v6.1,[52] using the same xc functional and basis set as used in the geometry optimization step. The output from optical response calculations is analysed using Chemissian, an analytical tool for electronic structure and spectra calculations.[56]

An additional method for the structure elucidation of clusters is to perform ion mobility measurements. The experimental mobilities may be compared with calculated values for the set of candidate structures, as was utilized by Weis *et al.* to determine the structures of $Ag_mAu_n{}^+$ ($m+n<6$) considering the projection approximation (PA) and a modified trajectory method (TR).[29] For their trajectory calculations, Weis *et al.*[29] consider two situations, one in which the charge on the cluster is equally distributed (EQ-TR), and one in which the silver atoms equally transfer charge to the gold, for a total transfer of 0.5 *e* from Ag to Au.

PA corresponds to a simplification of the average collision cross section $\Omega^{(1,1)}_{avg}$, in which the projection of the possible contact area by He buffer gas travelling in the x direction upon the cluster is given as its shadow in the yz plane. Equation (1) shows the average collision cross section as an integral over the impact parameter b (which is a function of the scattering angle χ) and the relative velocities of gas and cluster v, then orientationally averaged over the three angles θ, ϕ, and γ, while μ is the reduced mass[57]

$$\begin{aligned}\Omega^{(1,1)}_{avg} = \frac{1}{8\pi^2}\int_0^{2\pi} d\theta \int_0^{\pi} d\phi \sin\phi \int_0^{2\pi} d\gamma \frac{\pi}{8}\left(\frac{\mu}{k_B T}\right)^3 \\ \times \int_0^{\infty} db\ 2b(1-\cos\chi(\theta,\phi,\gamma,v,b)) \\ \times \int_0^{\infty} dv \exp(-\mu v^2/(2k_B T))v^5. \qquad (1)\end{aligned}$$

By counting the collision probability *M*/*N* upon this yz plane, for a set of *N* He atoms, the simplified cross section Ω is computed as Eq. (2). This model assumes hard spheres for both interaction species, and does not consider the effects of the anisotropy of the cluster, any local coordination effects or the interaction between the He gas and the charges on the cluster

$$\begin{aligned}\Omega = \frac{1}{4\pi}\int_0^{\pi} d\phi \sin\phi \\ \times \int_0^{2\pi} d\gamma \int_{-\infty}^{+\infty}\int_{-\infty}^{+\infty} M(\phi,\gamma,y,z)dydz. \qquad (2)\end{aligned}$$

TR calculates the cross sections from a set of classical trajectories of the He gas over a set of collision events with the cluster. This requires an empirical potential V for He-cluster interactions of the Lennard Jones (LJ) + dipolar form of Eq. (3), where ε and σ are standard LJ parameters, α_{He} is the polarizability of helium, q_i is the charge on atom i of the cluster ion, and r_{ij} is the relative position of atom i in the j direction,

$$V = \mathrm{U}_{LJ} + \mathrm{U}_{Dipole}, \tag{3}$$

where

$$\mathrm{U}_{LJ} = 4\varepsilon \sum_{i}^{n} \left[\left(\frac{\sigma_i}{r_i} \right)^{12} - \left(\frac{\sigma_i}{r_i} \right)^{6} \right] \tag{4}$$

and

$$\mathrm{U}_{Dipole} = -\frac{\alpha_{He}}{8\pi\varepsilon_0} \sum_{j}^{3} \left(\sum_{i}^{n} \frac{q_i r_{ij}}{r_i^3} \right)^2 . \tag{5}$$

In this work, we define a modified charge transfer trajectory calculation (CT-TR) method which uses the accurate Bader charges in order to further elucidate the structures and compare with previous results. For the low-lying minima of Ag-Au tetramer cations, calculated with the LC-ωPBEh functional, collision cross sections are calculated by the PA and the CT-TR method within the MOBCAL code of Mesleh *et al.*,[58] using the same potential parameters as Weis *et al.*:[29] $\varepsilon = 1.35$ meV, $\sigma_{AuHe} = 3.1$ Å, $\sigma_{AgHe} = 3.0$ Å, $r_{HardSphere} = 2.70$ Å and 2.63 Å for Au-He and Ag-He, respectively, and $\alpha_{He} = 0.205$ Å^3. For each TR simulation 2×10^6 classical trajectories are run.

III. RESULTS AND DISCUSSION

A. Calculated structures

Low energy isomers are obtained by the BCGA with the PBE functional, and subsequently locally optimized using a range of xc functionals frequently used for Au clusters: PBE, M06-L, and LC-ωPBEh at the LCAO-TZVPP level. M06-L is a local meta-GGA functional recommended for transition metal systems and those which exhibit non-covalent interactions.[59] LC-ωPBEh is a modified version of the range separated LC-ωPBE xc functional, which reproduces the long range asymptotic decay of the coulomb interaction by separating Hartree-Fock energies into long range and short range contributions. In our experience, the resulting structures and energies are very similar to those produced with LC-ωPBE, nevertheless we will restrict our analysis of theoretical absorption spectra to results obtained by LC-ωPBEh as will be shown in Sec. III B.

Figures 1–3 depict the energies of the four most stable structures produced with the BCGA locally optimized with all three functionals. The overlaid structures are those calculated with LC-ωPBEh, but all functionals give the same local minima, with minute distortions of bond lengths. The small size of the clusters ensures the BCGA is able to find every possible structure and permutational isomer (homotop) for each composition. We have checked that no other isomers are introduced on local relaxations with different functionals.

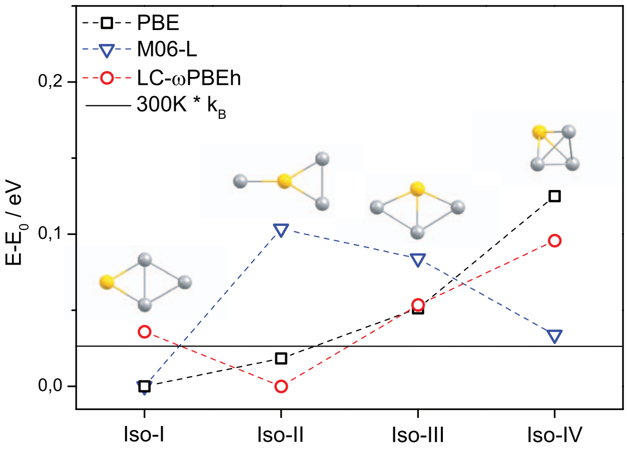

FIG. 1. Lowest lying Ag_3Au^+ isomers relaxed at the LC-ωPBEh/def2-TZVPP level of theory and their relative energies in eV (circles) compared to relative energies by the PBE (squares) and the M06-L (triangles) xc functional. Dashed lines connecting the data points are a guide to the eye. The horizontal line represents the thermal energy at 300 K. The LC-ωPBEh functional clearly determines the Y-shape isomer as the GM, contrary to the ordering predicted by the PBE and the M06-L functional.

Overall, we observe that there are three competing motifs, the rhombus, the distorted tetrahedron, and the Y-shaped structure, the last of which may exist in a symmetric or bent arrangement, depending on the composition and homotop.

The results of the PBE calculations are in almost perfect agreement with the findings of Weis *et al.*[29] (who used the BP86 functional) for all compositions, the only deviation is a reordering of the almost degenerate tetrahedron and bent Y-shape isomers of $Ag_2Au_2^+$ at 0.1 eV.

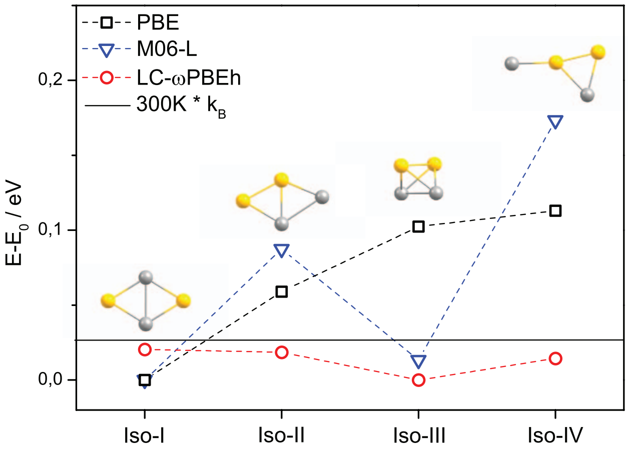

FIG. 2. Lowest lying $Ag_2Au_2^+$ isomers relaxed at the LC-ωPBEh/def2-TZVPP level of theory. For a description of symbols refer to Fig. 1. For the LC-ωPBEh functional, all isomers lie below 300 K in disagreement with qualitatively similar results obtained by the PBE and the M06-L functional, which only disagree in the description of the compact structure Iso-III.

For Ag_3Au^+, there are four isomers from three structural motifs within 0.15 eV of the GM, for all functionals, suggesting a close competition for favourability in experiment. PBE and M06-L agree upon the rhombus-shaped Iso-I as the GM, whereas LC-ωPBEh suggests an additional stabilization of the Y-shaped cluster. Weis *et al.* claim that despite the slight

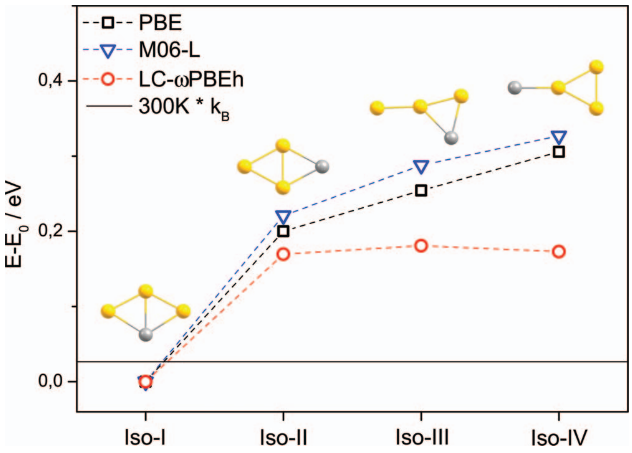

FIG. 3. Lowest lying $AgAu_3{}^+$ isomers relaxed at the LC-ωPBEh/def2-TZVPP level of theory. For a description of symbols refer to Fig. 1. In a qualitatively good agreement, all employed functionals find Iso-I being the most favored structural motif. For the LC-ωPBEh functional again the Y-shaped isomers seem to be generally more favored compared to the PBE and the M06-L functional which show similar results.

energetic preference for the rhombus (at the PBE level), the Y-shape is found in experiment, for which they cite the evidence of ion mobility collision cross section calculations for the Y-shape which fit the experimental data better than the rhombus.[29] Our LC-ωPBEh result supports this conclusion.

Overall, the range separated and PBE functionals agree well, whereas M06-L drastically favours the tetrahedron, and disfavours the Y-shaped structures, giving clear preference to maximal coordination.

For $Ag_2Au_2^+$, the two PBE-based functionals agree less well than for Ag_3Au^+ showing the strong influence of the LC in this case. While again, the lowest four isomers are identical, LC-ωPBEh suggests a narrowing of the energy spacings between minima, even to below the thermal energy at 300 K (shown as a horizontal solid line on each plot). This suggests that the rhombus, tetrahedron, and Y-shape can all potentially exist in the molecular beam, and while no thermal barriers are calculated, rearrangements between isomers may occur. Again, M06-L follows the trend of preference for higher coordination, with the Y-shape least favourable.

$AgAu_3^+$ displays excellent quantitative agreement between all three functionals, for which the rhombus is clearly preferred over the Y-shape, by a margin of around 0.2 eV, and thus experimentally we may expect the dominance of one isomer in the molecular beam. However, as in the case of $Ag_2Au_2^+$, LC-ωPBEh predicts a smaller energy difference between isomers than the other functionals. It is well established that gold clusters prefer planar structures up to a larger size than silver, with gold clusters reported to be planar for up to 7 atoms for the monocation.[60–62] But still it is surprising that even with the M06-L functional, the tetrahedral geometry has not been found at this level of theory in the lowest few isomers although it has been found for Au_4^+.[29,48]

The preference for a given structure is complicated to understand in the case of mixed clusters due to the presence of permutational isomers, the number of which depend on the symmetry of the cluster. For the Y-shape motif there are up to four homotops for $Ag_2Au_2^+$, and the preference for a particular homotop depends sensitively on a number of factors, including homo- and heterophilicity, electronegativity, and atomic radius. It may be said that there is a first order preference, based on the result of these factors, in which atoms occupy sites on the rigid cluster, followed by a second order effect, which is the extra stabilization (or destabilization) of that isomer due to the structure itself, such as frustration for spin or charge distributions. In this way we may rationalize the preferred permutational isomers of the clusters investigated here.

For the tetrahedron, no conclusions may be drawn, as for a monodoped and 50:50 composition clusters, all sites and combinations are essentially degenerate. For the rhombus, we observe that silver atoms preferentially occupy the high coordination sites – most strikingly in the case of $AgAu_3^+$, which exhibits a large energy gap between the lowest isomers. This behaviour is commonly observed in mixed metal clusters containing gold,[35,63] and agrees exactly with the results of Bonačić-Koutecký, in which they claim heterometallic bonding is generally preferred,[30] and from which the only deviation is observed for Ag_3Au^+, which has nearly degenerate rhombic homotops. For $AgAu_3^+$, the rhombus containing three heterometallic bonds is preferred to the isomers with two, and in $Ag_2Au_2^+$, the homotop with four mixed bonds is preferable to that with three. This result is attributed to the maximization of charge-transfer from silver to gold, which is displayed in Table I.

For the Y-shaped clusters the trend of maximal Ag-Au mixed bonding no longer applies. We attribute this to the fact that the cluster has a frustrated geometry, with energetics dominated by charge transfer effects. Gold has a Pauling electronegativity of 2.5, as compared to 1.9 for silver, and draws significant charge from silver atoms. This may be seen most clearly for $AgAu_3^+$, in which the two-coordinate silver homotop is preferred to the three-coordinate, which in turn is higher

TABLE I. Site by site charge transfer of the four lowest lying isomers at the LC-ωPBEh level relative to +0.25 *e*/atom. Silver atoms are displayed in bold.

	Charge transfer *e*/atom		
	Ag_3Au^+	$Ag_2Au_2^+$	$AgAu_3^+$
Iso-I	**0.05**	−0.19	−0.11
	0.10	**0.19**	−0.03
	0.10	**0.19**	**0.25**
	−0.25	−0.19	−0.11
Iso-II	**0.13**	−0.17	**0.18**
	0.13	**0.21**	−0.04
	−0.42	−0.18	−0.10
	0.16	**0.14**	−0.04
Iso-III	**0.06**	−0.26	−0.12
	−0.28	−0.26	**0.26**
	0.06	**0.26**	−0.19
	0.16	**0.26**	0.05
Iso-IV	−0.39	−0.15	−0.01
	0.13	**0.25**	−0.21
	0.13	−0.30	**0.23**
	0.13	**0.20**	−0.01

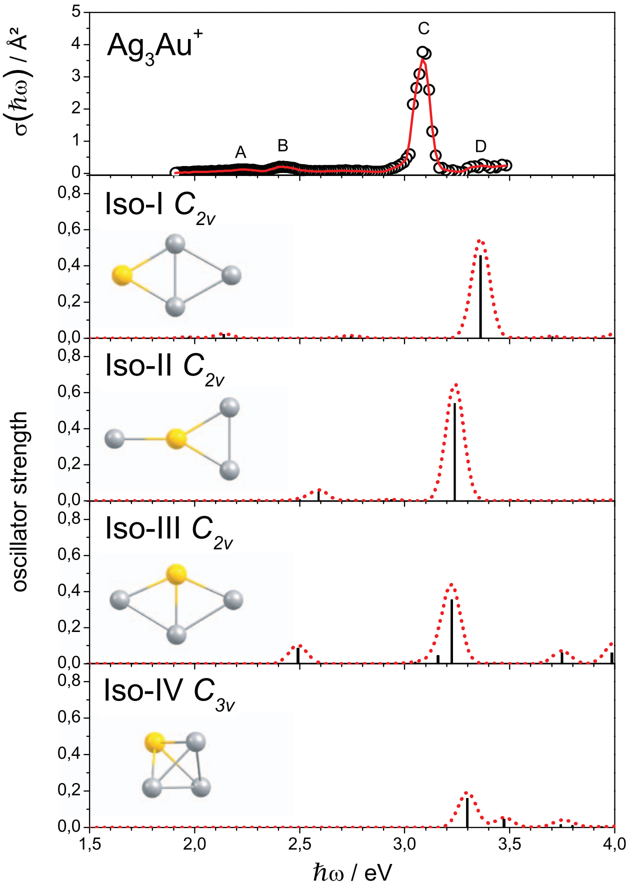

FIG. 4. Experimental Ag_3Au^+ absorption spectrum data points (open circles) and a 3-pt adjacent average of these to guide the eye (solid line) compared to TDDFT calculations for the lowest lying isomers relaxed at the LC-ωPBEh/def2-TZVPP level of theory.The calculated linespectra (vertical lines) are convoluted with Gaussian functions with a full width at half maximum of 0.1 eV (dotted lines).

in energy even than the one-coordinated site. This result is explained by the frustrated nature of the Y-shape and is an example of a second order charge transfer effect. By comparison with the monometallic Ag_4^+ and Au_4^+ structures, we may decouple the effect due to the choice of homotop, and that from the structure itself. For rhombic Ag_4^+ and Au_4^+, there is negligible charge redistribution, beyond the +0.25 *e*/atom due to the single positive charge on the cluster. However, for the Y-shape, there is an additional accumulation of approximately 0.1 *e*/atom upon the central, three-coordinate site. This causes the gold atom to occupy this site. We therefore note that it is important to consider both causes of charge transfer when discussing the factors which determine homotop ordering in mixed metal clusters.

This charge transfer is maximized by gold occupation of the central site, and is a strong enough effect to outweigh the usual preference for low coordination.

B. Experimental and theoretical optical absorption spectra

1. Ag_3Au^+

Figure 4 shows the experimental absorption spectrum of Ag_3Au^+ in the photon energy range $\hbar\omega$ = 1.9–3.5 eV

TABLE II. Oscillator strengths *f* of experimentally observed transitions (A–D) of the tetramers. Peak positions in eV as maxima of Gaussian fits to experimentally observed transitions are given in brackets.

	Oscillator strength f^a of transition			
Tetramers	A	B	C	D
Ag_3Au^+	0.015 (2.21)	0.018 (2.43)	0.334 (3.09)	…
$Ag_2Au_2^+$	0.078 (3.12)	…	…	…
$AgAu_3^+$	0.003(2.16)	0.012 (2.84)	0.195 (3.10)	0.037(3.28)

[a] Determined by Gaussian deconvolution according to $f = 0.91103\int_{Band}\sigma(\hbar\omega)d(\hbar\omega)$.[64]

and theoretical optical absorption spectra for the four lowest energy GADFT candidates from LC-TDDFT calculations. The experimental spectrum exhibits two smaller features at 2.21 eV (A) and 2.43 eV (B), and is dominated by an intense absorption at 3.09 eV (C) followed by a broad structure in the range 3.2–3.4 eV (D).

The comparison to TDDFT at the LC-ωPBEh/def2-TZVPP level of theory for the lowest lying isomers is shown below. The simulated spectra for Iso-I and Iso-IV can be ruled out, whereas Iso-II and Iso-III show a close competition in describing the experimental spectrum, capturing peaks B and C (also feature A for Iso-II with a very small oscillator strength of 0.008) with reasonable agreement on both position and relative oscillator strength.

Experimental oscillator strengths are calculated by Gaussian deconvolution of the respective peaks in an experimental spectrum. The values are given in Table II for all major peaks of each isomer. We find that for the intense transition C, values calculated with LC-ωPBEh for Iso-II (0.540) and Iso-III (0.399 as sum of oscillator strengths of two transitions in the range 3.1–3.3 eV), Iso-III gives a better agreement with the experimental value of 0.334. In addition, the slight tailing of signal C towards lower photon energies in the experimental spectrum seems to be better captured by Iso-III. However, it should be noted that the disagreement between theoretical

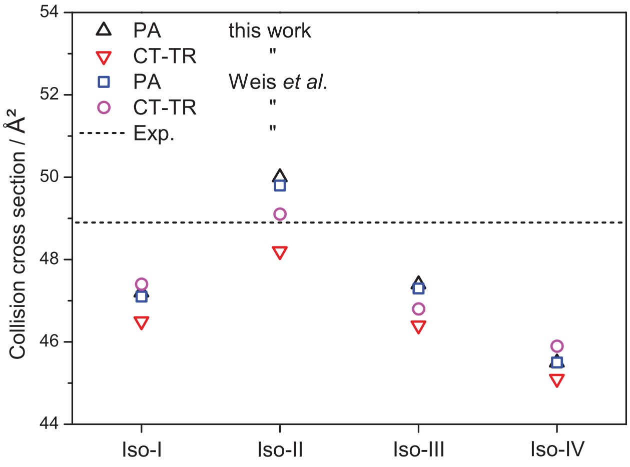

FIG. 5. Experimental collision cross section of Ag_3Au^+ (dashed line) compared to calculated collision cross sections for the lowest lying isomers obtained by the PA (squares) and the CT-TR (circles) approach (experiments and calculations taken from Ref. 29) and calculations for cluster geometries from this work also using the PA (triangles) and CT-TR (inverse triangles) approach including Bader charges in the CT-TR calculations.

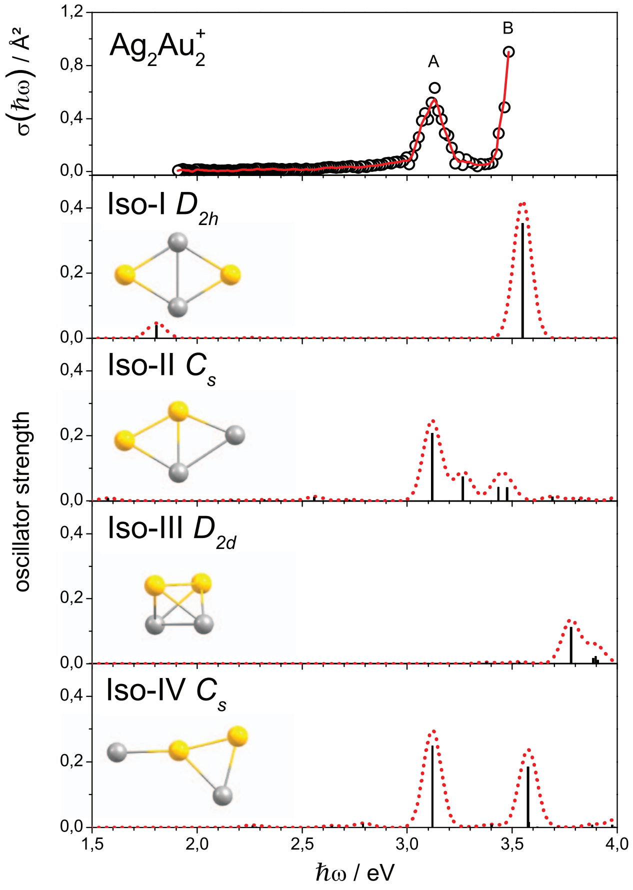

FIG. 6. Experimental $Ag_2Au_2{}^+$ absorption spectrum data points (open circles) and a 3-pt adjacent average of these to guide the eye (solid line) compared to TDDFT calculations for the lowest lying isomers relaxed at the LC-ωPBEh/def2-TZVPP level of theory. The calculated linespectra (vertical lines) are convoluted with Gaussian functions with a full width at half maximum of 0.1 eV (dotted lines).

and experimental oscillator strengths in general may either be attributed to inaccuracies of TDDFT or to experimental errors in measuring photodissociation cross sections. Hence, the comparison of oscillator strengths is not a sufficient criterion to rule out isomers especially in this case. Therefore, it is reasonable to compare the optical absorption spectra to ion mobility data in order to explicitly rule out one isomer.

In agreement with previous ion mobility experiments,[29] our calculated collision cross sections show the Y-shape with C_{2v} symmetry (Iso-II) to fit most closely with experimental data for both the PA and modified CT-TR methods (see Figure 5). This result is consistent with both the energetic analysis of the GADFT at the LC-ωPBEh level (see Figure 1) and the conclusions of the optical spectra simulations. It is clear that when Bader charges are included in the CT-TR approach, we may conclude unambiguously that Iso-II is the predominant species in the molecular beam.

2. $Ag_2Au_2{}^+$

Figure 6 shows the experimental absorption spectrum of $Ag_2Au_2{}^+$ and theoretical optical absorption spectra for the four lowest energy GADFT candidates from LC-TDDFT calculations. The experimental spectrum shows a feature at 3.12 eV (A) and one transition with a maximum beyond the experimental range (B).

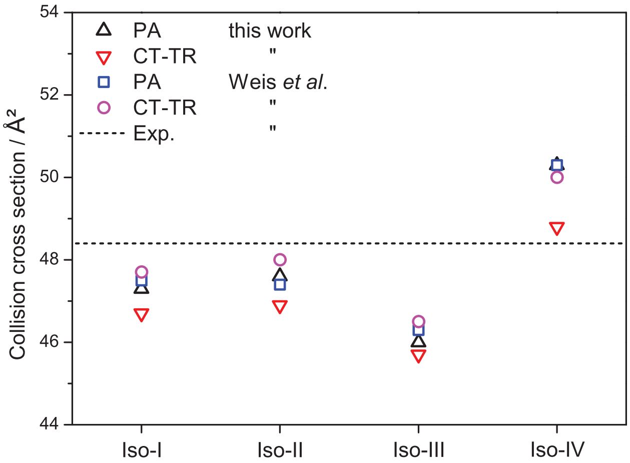

FIG. 7. Experimental collision cross section of $Ag_2Au_2{}^+$ (dashed line) compared to calculated collision cross sections for the lowest lying isomers obtained by the PA (squares) and the CT-TR (circles) approach (experiments and calculations taken from Ref. 29) and calculations for cluster geometries from this work also using the PA (triangles) and CT-TR (inverse triangles) approach including Bader charges in the CT-TR calculations.

The comparison to the simulated optical response using LC-ωPBEh for the lowest lying isomers is presented below and shows a strong competition between isomers. In agreement with relative energies from LC-ωPBEh relaxations (see Fig. 2), the four lowest lying isomers are very close in energy and possibly all together present in the molecular beam. Even though the Y-shaped Iso-IV with C_s symmetry would be sufficient to qualitatively describe the experimental features A and B, the experimental oscillator strength of transition A (0.078) and the features of the spectrum could be explained by the sum of contributions from Iso-I and Iso-II. However, also Iso-IV or even a mixture of all three isomers could be present in the molecular beam (for experimental oscillator strengths see Table II).

The cluster with 1:1 composition presents a difficult situation for unambiguous structure elucidation, as there is a near energetic degeneracy of isomers in the GADFT predictions. Weis *et al.*[29] also note that the energetic separation between isomers is small, and the collision cross sections of each are very similar, and so do not claim to determine which structure is in existence. With the addition of our spectral predictions, we take the further step of claiming that several isomers are likely coexistent in the beam. As shown in Figure 7, the collision cross section of Iso-III is significantly lower than the experimental value, and this, coupled with its optical spectrum means we may tentatively exclude it. The systematic reduction of the CT-TR values we observe with our structures and charge method bring Iso-IV most in line with the experimental result, our mobility calculations indicate Iso-I and Iso-II move further from the experimental value, while iso-IV gets closer. But due to the close competition between isomer energies, it is unlikely that Iso-IV will be present in isolation in the molecular beam although it cannot be definitely ruled out.

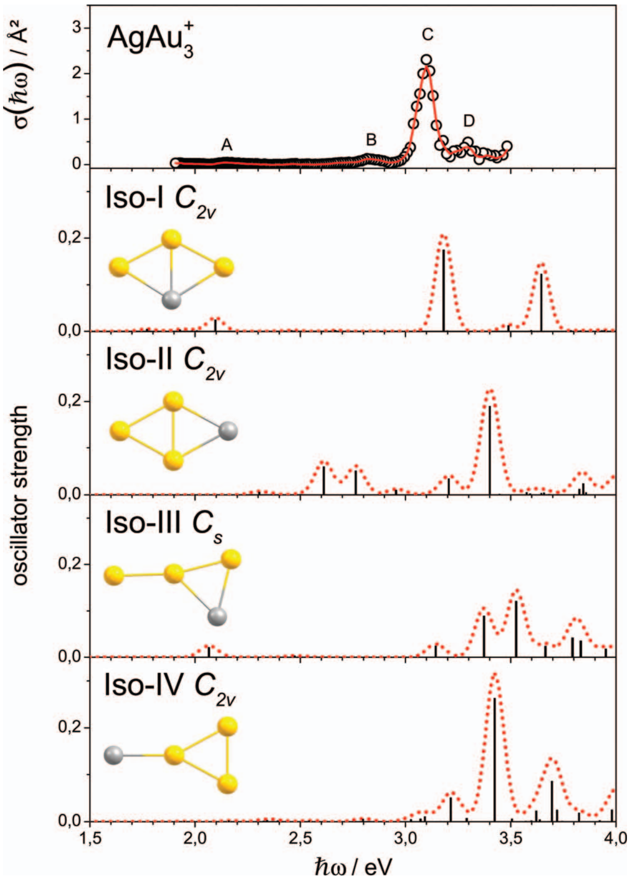

FIG. 8. Experimental AgAu$_3^+$ absorption spectrum data points (open circles) and a 3-pt adjacent average of these to guide the eye (solid line) compared to TDDFT calculations for the lowest lying isomers relaxed at the LC-ωPBEh/def2-TZVPP level of theory. The calculated linespectra (vertical lines) are convoluted with Gaussian functions with a full width at half maximum of 0.1 eV (dotted lines).

3. AgAu$_3^+$

Figure 8 shows the experimental absorption spectrum of AgAu$_3^+$ and theoretical optical absorption spectra for the four lowest energy GADFT candidates. The experimental spectrum shows two smaller features at 2.16 eV (A) and 2.84 eV (B), but is dominated by an intense absorption at 3.10 eV (C). The spectrum shows a broad weak feature at 3.28 eV (D) and a transition out of the experimental range at higher photon energies.

It is clear that the LC-TDDFT for Iso-I shows the best agreement with the experimental spectrum and agrees with the energy ordering of the GADFT results, for which Iso-I is the GM. Nevertheless, the experimental feature B is not covered by the calculated optical response for Iso-I and may potentially only be associated with a very weak transition at 2.67 eV with an oscillator strength of 0.002, which is hardly visible in Figure 8. However, its origin could also be attributed to a contribution of Iso-II to the experimental spectrum. But then one would expect more features to appear in the range 2.5–3.0 eV.

The oscillator strength for the intense experimental transition C (0.195) is in a very good agreement with the theoretical value (0.174) for the corresponding feature in the optical response of Iso-I at the LC-ωPBEh/def2-TZVPP level of theory (for experimental oscillator strengths see Table II).

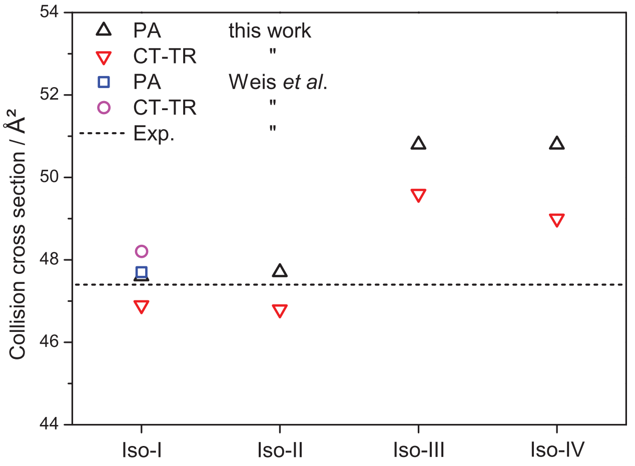

FIG. 9. Experimental collision cross section of AgAu$_3^+$ (dashed line) compared to calculated collision cross sections for the lowest lying isomers obtained by the PA (squares) and the CT-TR (circles) approach (experiments and calculations taken from Ref. 29) and calculations for cluster geometries from this work also using the PA (triangles) and CT-TR (inverse triangles) approach including Bader charges in the CT-TR calculations.

It is clear from both spectral and GADFT analysis that there is likely only the one isomer, Iso-I in the molecular beam. Since the next isomer (Iso-II) is much higher in energy (0.17 eV at the LC-ωPBEh/def2-TZVPP level, see Figure 3), collision cross sections for AgAu$_3^+$ are only given for Iso-I in Ref. 29. For completeness we have calculated collision cross sections for the four lowest lying isomers (see Figure 9). It is unsurprising that Iso-III and Iso-IV exhibit cross sections vastly different from the experimental value, but interesting that Iso-II shows excellent agreement, essentially identical to Iso-I, because both Iso-I and Iso-II are rhombic structures, with very similar shapes. This underlies the importance of a multi-component analysis for structure elucidation. However, due to the large energetic discrepancy and the optical absorption spectra compared to TDDFT predictions, we conclude that only Iso-I is present in the experimental beam.

IV. CONCLUSIONS

The measured photodissociation spectra presented here have been shown to be useful for determining the structures of the Ag-Au tetramer cations in the molecular beam, when combined with systematic structural minima search and subsequent LC-TDDFT calculations. Our investigations from both experimental and theoretical points of view are in good agreement with previous ion mobility measurements, not only supporting their validity, but also allowing a different perspective on the electronic properties of the systems considered here. In general, the methods used allow an extensive correlation to be made between experimental data and electronic structure analysis.

While in the case of Ag$_3$Au$^+$ and AgAu$_3^+$ the Y-shaped Iso-II (C_{2v}) and the rhombus Iso-I (C_{2v}), respectively, can be clearly assigned, the situation is complicated in the case of $Ag_2Au_2^+$. The nearly degenerate isomers (at the LC-ωPBEh/def2-TZVPP level of theory) Iso-I (D_{2h}), Iso-II (C_s), and Iso-IV (C_s) can all potentially contribute to the observed experimental spectrum, while the lowest lying Iso-III (D_{2d}) can be ruled out due to its significantly lower collision cross section compared to the experimental value. We would like to clarify this issue in future experiments by performing measurements at reduced nozzle temperatures. Recently, we have extended our experimental spectral tuning range to 4.4 eV which will provide additional information to rationalize our current results in more detail, especially when combined with experiments at lower nozzle temperatures.

The three competing structural motifs and all permutational isomers within these motifs have been rationalized in terms of first order preferences for a particular homotop based on homo- and heterophilicity, electronegativity and atomic radii followed by second order effects such as frustration for charge distributions.

The comparison of the experimental data to optical response calculations shows that the LC-ωPBEh functional describes oscillator strengths for the tetramer cation spectra which are in qualitative agreement with our experimental data. Hence, it is confirmed to be a good xc functional for the description of ground and excited state properties of the cationic tetramer alloys of silver and gold. Therefore, this combined experimental and theoretical approach shows promise as a convenient and efficient procedure for the description of larger mixed Ag-Au cluster cations, which are currently being investigated.

ACKNOWLEDGMENTS

A.S. and R.S. acknowledge financial support by the DFG (Grant No. SCHA 885/10-1) and the Merck'sche Gesellschaft für Kunst und Wissenschaft. We are thankful to Urban Rohrmann and Daniel A. Götz for technical support and helpful discussions.

The calculations reported here are performed on the following HPC facilities: The University of Birmingham BlueBEAR facility (Ref. 65); the MidPlus Regional Centre of Excellence for Computational Science, Engineering and Mathematics, funded under EPSRC Grant No. EP/K000128/1 (R.L.J.); and via our membership of the UK's HPC Materials Chemistry Consortium funded under EPSRC Grant No. EP/F067496 (R.L.J.), this work made use of the facilities of HECToR, the UK's national high-performance computing service, which is provided by UoE HPCx Ltd at the University of Edinburgh, Cray Inc and NAG Ltd, and funded by the Office of Science and Technology through EPSRC's High End Computing Programme.

[1] W. A. de Heer, Rev. Mod. Phys. **65**, 611 (1993).
[2] R. Ferrando, J. Jellinek, and R. L. Johnston, Chem. Rev. **108**, 845 (2008).
[3] M. Käll, Nat. Mater. **11**, 570 (2012).
[4] J. K. Gansel, M. Thiel, M. S. Rill, M. Decker, K. Bade, V. Saile, G. von Freymann, S. Linden, and M. Wegener, Science **325**, 1513 (2009).
[5] A. W. Castleman Jr., and S. N. Khanna, J. Phys. Chem. C **113**, 2664 (2009).
[6] G. A. Bishea and M. D. Morse, J. Chem. Phys. **95**, 8779 (1991).
[7] S. Fedrigo, W. Harbich, and J. Buttet, J. Chem. Phys. **99**, 5712 (1993).
[8] W. Harbich, S. Fedrigo, and J. Buttet, Z. Phys. D: At., Mol. Clusters **26**, 138 (1993).
[9] B. A. Collings, K. Athanassenas, D. Lacombe, D. M. Rayner, and P. A. Hackett, J. Chem. Phys. **101**, 3506 (1994).
[10] A. Terasaki, S. Minemoto, M. Iseda, and T. Kondow, Eur. Phys. J. D **9**, 163 (1999).
[11] D. Schooss, S. Gilb, J. Kaller, M. M. Kappes, F. Furche, A. Köhn, K. May, and R. Ahlrichs, J. Chem. Phys. **113**, 5361 (2000).
[12] A. Schweizer, J. M. Weber, S. Gilb, H. Schneider, D. Schooss, and M. M. Kappes, J. Chem. Phys. **119**, 3699 (2003).
[13] J. Li, X. Li, H.-J. Zhai, and L.-S. Wang, Science **299**, 864 (2003).
[14] S. Gilb, K. Jacobsen, D. Schooss, F. Furche, R. Ahlrichs, and M. M. Kappes, J. Chem. Phys. **121**, 4619 (2004).
[15] M. Harb, F. Rabilloud, D. Simon, A. Rydlo, S. Lecoultre, F. Conus, V. Rodrigues, and C. Félix, J. Chem. Phys. **129**, 194108 (2008).
[16] P. Gruene, D. M. Rayner, B. Redlich, A. F. G. van der Meer, J. T. Lyon, G. Meijer, and A. Fielicke, Science **321**, 674 (2008).
[17] A. N. Gloess, H. Schneider, J. M. Weber, and M. M. Kappes, J. Chem. Phys. **128**, 114312 (2008).
[18] A. Terasaki, T. Majima, C. Kasai, and T. Kondow, Eur. Phys. J. D **52**, 43 (2009).
[19] K. Egashira, C. Bartels, T. Kondow, and A. Terasaki, Eur. Phys. J. D **63**, 183 (2011).
[20] S. Lecoultre, A. Rydlo, C. Félix, J. Buttet, S. Gilb, and W. Harbich, J. Chem. Phys. **134**, 074302 (2011).
[21] Z. Yang, I. Leon, and L.-S. Wang, J. Chem. Phys. **139**, 021106 (2013).
[22] I. León, Z. Yang, and L.-S. Wang, J. Chem. Phys. **138**, 184304 (2013).
[23] V. Bonačić-Koutecký, V. Veyret, and R. Mitrić, J. Chem. Phys. **115**, 10450 (2001).
[24] J. C. Idrobo, W. Walkosz, S. F. Yip, S. Ögüt, J. Wang, and J. Jellinek, Phys. Rev. B **76**, 205422 (2007).
[25] D. W. Silverstein and L. Jensen, J. Chem. Phys. **132**, 194302 (2010).
[26] S. Goel, K. A. Velizhanin, A. Piryatinski, S. A. Ivanov, and S. Tretiak, J. Chem. Phys. C **116**, 3242 (2012).
[27] J. V. Koppen, M. Hapka, M. M. Szcześniak, and G. Chalasinski, J. Chem. Phys. **137**, 114302 (2012).
[28] Y. Negishi, Y. Nakamura, A. Nakajima, and K. Kaya, J. Chem. Phys. **115**, 3657 (2001).
[29] P. Weis, O. Welz, E. Vollmer, and M. M. Kappes, J. Chem. Phys. **120**, 677 (2004).
[30] V. Bonačić-Koutecký, J. Burda, R. Mitrić, M. Ge, G. Zampella, and P. Fantucci, J. Chem. Phys. **117**, 3120 (2002).
[31] P. Schwerdtfeger, Heteroat. Chem. **13**, 578 (2002).
[32] P. Pyykkö, Annu. Rev. Phys. Chem. **63**, 45 (2012).
[33] G. Jian-Jun, Y. Ji-Xian, and D. Dong, Commun. Theor. Phys. **48**, 348 (2007).
[34] G. F. Zhao and Z. Zeng, J. Chem. Phys. **125**, 014303 (2006).
[35] P. Lu, X.-Y. Kuang, A.-J. Mao, Z.-H. Wang, and Y.-R. Zhao, Mol. Phys. **109**, 2057 (2011).
[36] L. Hong, H. Wang, J. Cheng, X. Huang, L. Sai, and J. Zhao, Comput. Theor. Chem. **993**, 36 (2012).
[37] X.-D. Zhang, M.-L. Guo, D. Wu, P.-X. Liu, Y.-M. Sun, L.-A. Zhang, Y. She, Q.-F. Liu, and F.-Y. Fan, Int. J. Mol. Sci. **12**, 2972 (2011).
[38] G.-F. Zhao, J.-M. Sun, and Z. Zeng, Chem. Phys. **342**, 267 (2007).
[39] R. L. Johnston, Dalton Trans. **2003**, 4193.
[40] S. Heiles, A. J. Logsdail, R. Schäfer, and R. L. Johnston, Nanoscale **4**, 1109 (2012).
[41] S. Heiles, K. Hofmann, R. L. Johnston, and R. Schäfer, ChemPlusChem **77**, 532 (2012).
[42] D. A. Götz, S. Heiles, R. L. Johnston, and R. Schäfer, J. Chem. Phys. **136**, 186101 (2012).
[43] S. Heiles, R. L. Johnston, and R. Schäfer, J. Phys. Chem. A **116**, 7756 (2012).
[44] S. Heiles and R. L. Johnston, Int. J. Quantum Chem. **113**, 2091 (2013).
[45] O. A. Vydrov and G. E. Scuseria, J. Chem. Phys. **125**, 234109 (2006).
[46] O. A. Vydrov, J. Heyd, A. V. Krukau, and G. E. Scuseria, J. Chem. Phys. **125**, 074106 (2006).
[47] M. A. Rohrdanz, K. M. Martins, and J. M. Herbert, J. Chem. Phys. **130**, 054112 (2009).
[48] A. Shayeghi, R. L. Johnston, and R. Schäfer, Phys. Chem. Chem. Phys. **15**, 19715 (2013).
[49] P. Giannozzi, S. Baroni, N. Bonini, M. Calandra, R. Car, C. Cavazzoni, D. Ceresoli, G. L. Chiarotti, M. Cococcioni, I. Dabo, A. Dal Corso, S. de

Gironcoli, S. Fabris, G. Fratesi, R. Gebauer, U. Gerstmann, C. Gougoussis, A. Kokalj, M. Lazzeri, L. Martin-Samos, N. Marzari, F. Mauri, R. Mazzarello, S. Paolini, A. Pasquarello, L. Paulatto, C. Sbraccia, S. Scandolo, G. Sclauzero, A. P. Seitsonen, A. Smogunov, P. Umari, and R. M. Wentzcovitch, J. Phys. Condens. Matter **21**, 395502 (2009).

[50] A. M. Rappe, K. M. Rabe, E. Kaxiras, and J. D. Joannopoulos, Phys. Rev. B **41**, 1227 (1990).

[51] J. Perdew, K. Burke, and M. Ernzerhof, Phys. Rev. Lett. **77**, 3865 (1996).

[52] M. Valiev, E. J. Bylaska, N. Govind, K. Kowalski, T. P. Straatsma, H. J. J. Van Dam, D. Wang, J. Nieplocha, E. Apra, T. L. Windus, and W. A. de Jong, Comput. Phys. Commun. **181**, 1477 (2010).

[53] F. Weigend and R. Ahlrichs, Phys. Chem. Chem. Phys. **7**, 3297 (2005).

[54] F. Rabilloud, J. Phys. Chem. A **117**, 4267 (2013).

[55] W. Tang, E. Sanville, and G. Henkelman, J. Phys. Condens. Matter **21**, 084204 (2009).

[56] Chemissian, *A Computer Program to Analyse and Visualise Quantum-Chemical Calculations* (L. Skripnikov, 2012).

[57] C.-K. Siu, Y. Guo, I. S. Saminathan, A. C. Hopkinson, and K. W. M. Siu, J. Phys. Chem. B **114**, 1204 (2010).

[58] M. F. Mesleh, J. M. Hunter, A. A. Shvartsburg, G. C. Schatz, and M. F. Jarrold, J. Phys. Chem. **100**, 16082 (1996).

[59] Y. Zhao and D. G. Truhlar, J. Chem. Phys. **125**, 194101 (2006).

[60] D. Schooss, P. Weis, O. Hampe, and M. M. Kappes, Philos. Trans. R. Soc. A **368**, 1211 (2010).

[61] A. V. Walker, J. Chem. Phys. **122**, 094310 (2005).

[62] P. Weis, Int. J. Mass Spectrom. **245**, 1 (2005).

[63] C. J. Heard and R. L. Johnston, Eur. Phys. J. D **67**, 34 (2013).

[64] J. Friedrich, S. Gilb, O. T. Ehrler, A. Behrendt, and M. M. Kappes, J. Chem. Phys. **117**, 2635 (2002).

[65] See http://www.bear.bham.ac.uk/bluebear for a description of the BlueBEAR HPC facility.

Chapter 5

A theoretical study of the structures and optical spectra of helical copper-silver clusters

5.1 Introduction

The application of optical spectral simulations to condensed matter systems such as clusters and bulk materials is a growing area of research, which has proved successful for a range of optically interesting metals, including aluminum [76], copper [77, 175], silver [176, 177] and gold [178, 179]. The widespread use of these simulations is possible due to developments in TDDFT methods, including appropriate functionals [180, 129], and the availability of sufficient computing resources.

Coinage metals are known to exhibit pronounced plasmon spectra, the position, width and intensity of which depends not only on metal identity, but also on particle size and geometry [75]. There is a growing literature regarding the simulation of optical response spectra, and in the case of silver, there is some evidence that for specific geometries, the subnanoscale may support plasmons [75]. Putative global minimum structures corresponding to compact pseudo-spherical structures have been considered [181, 71], along with more exotic structures, such as nanorods [74, 72, 73, 182] and tetrahedra [75]. The structure dependence is noted to be at least as strong as the size effect in controlling the position and height of the plasmonic peak [70].

Recently, focus has been directed towards the alloying of metals in coinage metal nanoparticles, in order to design tunable plasmon resonances. This alloying has usually been simulated with silver-gold particles, which have the stronger response, and has been applied to spherical [16] structures and nanorods [183]. The observation of a systematic shift in peak position and intensity has been found to depend sensitively on size and the type of alloying present. Studies comparing core-shell, inverse core-shell and alloyed particles give significantly differing results, implying that the choice of dopant site is vital to accurately predict the optical properties.

Helical clusters are an exotic form found on the subnano- and nanoscale in a variety of conditions [184, 185, 186]. Their inherent chirality, both from geometric and dopant sources, in addition to their likely optical properties suggests these systems may have promise in optical, catalytic or reactive fields. By combining a range corrected TDDFT simulation procedure with a systematic study of doping, we probe the electronic behaviour of a new class of clusters and predict their response in the molecular excitation size range. In order to extend the understanding of dopant location and doping level effects, we investigate a number of regimes, and apply charge analysis to probe the energetic preferences that result. For the spectral response of gold-silver particles, the choice of exchange-correlation functional plays a crucial role in accurately predicting excitations.

5.2 Publication

Authors Christopher J. Heard and Roy L. Johnston

Title A theoretical study of the structures and optical spectra of helical copper-silver clusters

Submitted 30 December 2013

Accepted 12 February 2014

Information *Phys. Chem. Chem. Phys.* (2014)

PCCP

PAPER

View Article Online
View Journal

Published on 03 March 2014. Downloaded by University of Birmingham on 28/03/2014 23:44:12.

A theoretical study of the structures and optical spectra of helical copper–silver clusters†

Cite this: DOI: 10.1039/c3cp55507k

Christopher J. Heard* and Roy L. Johnston*

The structures and optical response of helical clusters ("Bernal spirals") with compositions $Ag_{12}Cu_1^+$ and $Ag_1Cu_{12}^+$ are calculated within Kohn–Sham density functional theory and the configuration interaction singles variant of time dependent density functional theory. The effects of dopant position within the cluster on the vertical excitation spectrum are investigated according to the underlying electronic structure of the major transitions. The roles of symmetry and geometry are investigated by calculating the optical response of helical, icosahedral and nanorod-like clusters of Ag_{13}^+, finding local structure to be significant in driving the resultant optical response at the subnanometre scale. Further, it is noted that helical clusters have optical properties which are quite distinct from those of nanorods of similar dimensions. The effect of multiple doping is studied by introducing copper atoms into the centre of the silver helix, over the composition range Ag_{13}^+ to $Ag_6Cu_7^+$. There is a complex variation of the major plasmon-like peak over this range, attributed to subtle variations in the influence of the copper 3d band on the excitations and charge transfer for different sites within the cluster. This work suggests that coinage metal nanohelices have unusual, tunable electronic properties, which in addition to their inherent chirality makes them interesting systems to study for chiral catalysis and optoelectronics.

Received 30th December 2013,
Accepted 28th February 2014

DOI: 10.1039/c3cp55507k

www.rsc.org/pccp

Published on 03 March 2014. Downloaded by University of Birmingham on 28/03/2014 23:44:12.

Published on 03 March 2014. Downloaded by University of Birmingham on 28/03/2014 23:44:12.

Published on 03 March 2014. Downloaded by University of Birmingham on 28/03/2014 23:44:12.

Published on 03 March 2014. Downloaded by University of Birmingham on 28/03/2014 23:44:12.

Published on 03 March 2014. Downloaded by University of Birmingham on 28/03/2014 23:44:12.

Published on 03 March 2014. Downloaded by University of Birmingham on 28/03/2014 23:44:12.

Published on 03 March 2014. Downloaded by University of Birmingham on 28/03/2014 23:44:12.

Published on 03 March 2014. Downloaded by University of Birmingham on 28/03/2014 23:44:12.

Published on 03 March 2014. Downloaded by University of Birmingham on 28/03/2014 23:44:12.

Supplementary information for "A theoretical study of the structures and optical spectra of helical copper-silver clusters"

C. J. Heard*[a] and Roy L. Johnston†[a]

February 13, 2014

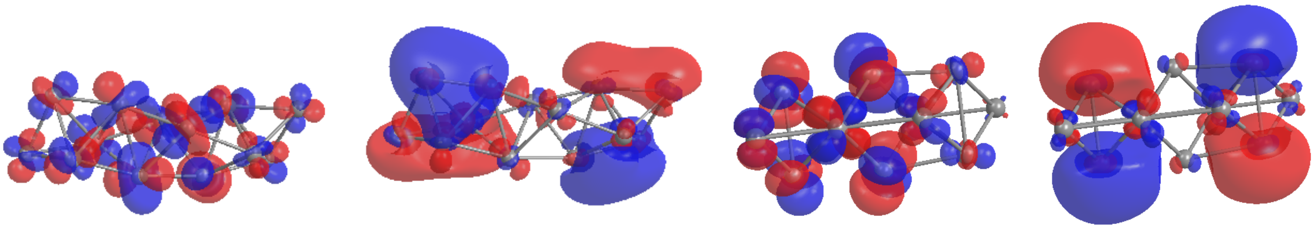

Figure S1: The interband transition-dominated excitations from the high energy regions of Ag_{13}^{+} optical response spectra. From left to right: the hole and particles states of the Bernal spiral, and the hole and particle states of the nanorod. The hole states in both cases are considerably less collective than for the lower energy excitations, and display predominantly d-like atomic orbitals, localised upon atoms.

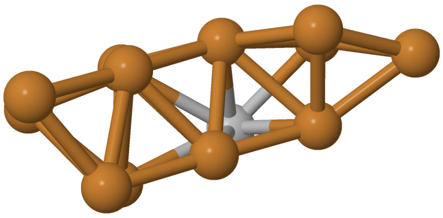

Figure S2: Resultant local minimum after reminimisation of $Cu_{12}Ag_{1}^{+}$, with the silver atom doped into site 6 of the spiral, at the NWCHEM-TZVPP level of theory. The cluster rearranges from the Bernal spiral to an unsymmetrical structure with some fcc-character, which is distorted by the presence of the silver atom.

---

[a] School of Chemistry, University of Birmingham, Edgbaston, Birmingham, UK, B15 2TT.
∗ Email: cjh085@bham.ac.uk
† Email: r.l.johnston@bham.ac.uk

Peak Position	Oscillator Strength
2.99	0.087
3.00	0.093
3.28	0.086
3.29	0.083
3.63	0.231
3.79	0.080
3.79	0.080
3.98	0.178
3.96	0.182
4.23	**0.929**
4.41	**1.400**
4.42	**1.399**
4.63	**0.594**

Table S1: Positions of all transitions in the spectrum of Ag_{13}^{+} (icosahedron) with oscillator strengths above 0.05. Transitions with oscillator strengths above 0.5 are indicated by bold font.

Peak Position	Oscillator Strength
2.88	0.099
3.37	**0.535**
3.50	0.105
3.71	0.111
3.78	**2.764**
3.90	0.123
4.09	0.051
4.11	0.137
4.26	0.250
4.35	**1.420**
4.42	0.057
4.46	0.144
4.64	0.083
4.65	0.056
4.79	**0.503**
4.80	0.156
4.82	0.152
4.87	**0.890**
4.88	0.131
4.90	0.146
4.92	0.253
4.96	0.074
4.97	0.241
5.05	0.062
5.10	0.061
5.19	0.072

Table S2: Positions of all transitions in the spectrum of Ag_{13}^{+} (rod) with oscillator strengths above 0.05. Transitions with oscillator strengths above 0.5 are indicated by bold font.

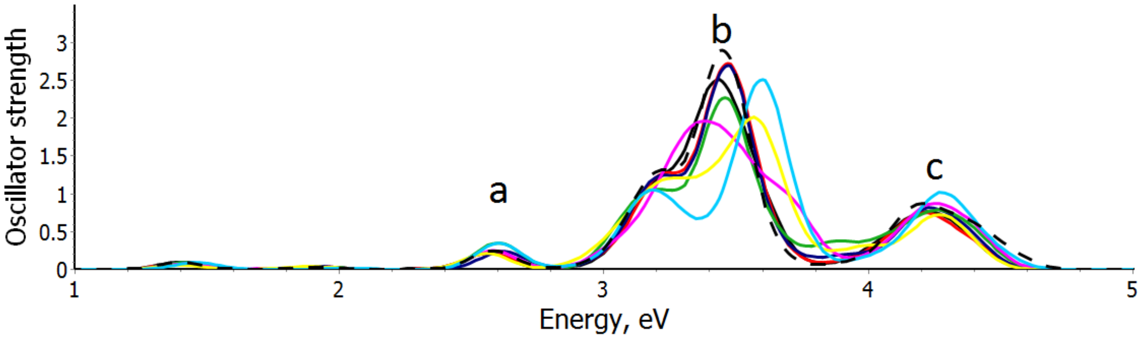

Figure S3: Overlaid view of the $Ag_{12}Cu_1^+$ def2-TZVPP spectra, showing a significant deviation only for the centrally doped sites, and little significant variation of oscillator strengths. Site 1 is black, site 2 is red, site 3 is dark blue, site 4 is green, site 5 is pink, site 6 is yellow and site 7 is cyan. Major peak regions are labelled a, b and c.

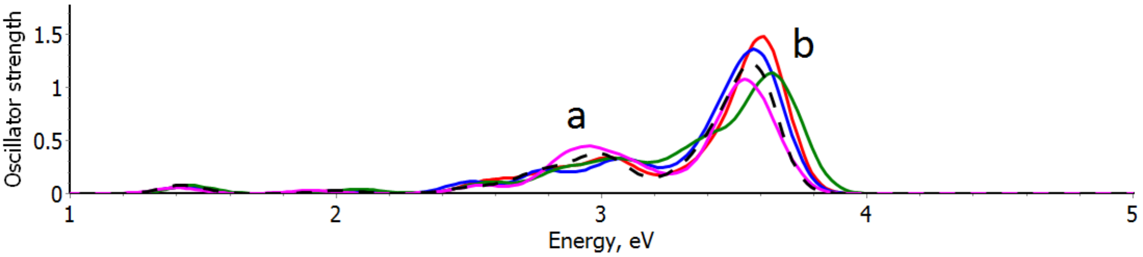

Figure S4: Overlaid view of the $Cu_{12}Ag_1^+$ def2-TZVPP spectra of dopant sites 1 (red), 3 (blue), 5 (green) and 7 (pink). The dashed line corresponds the pure Cu_{13}^+ helix for comparison.

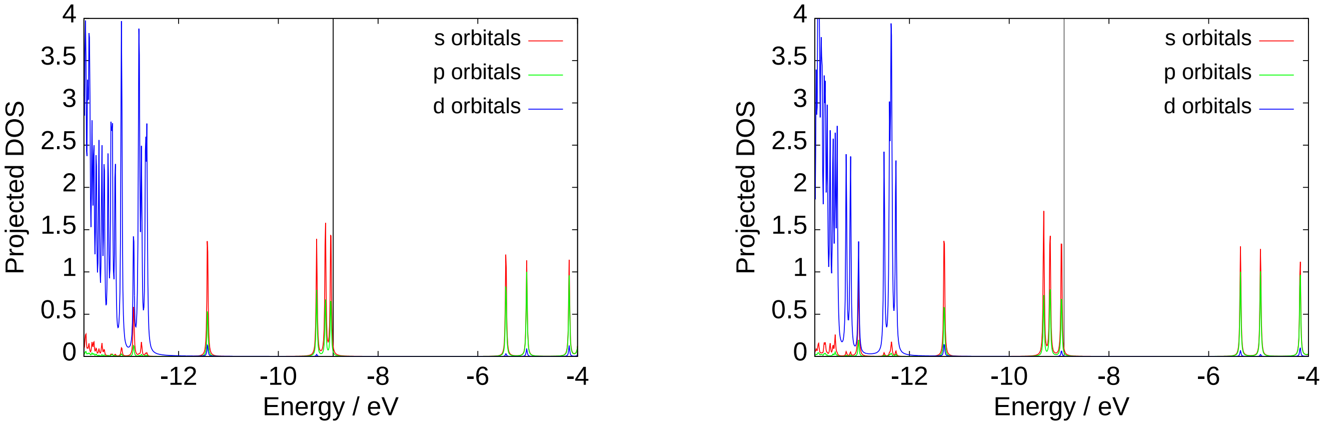

(a) Ag$_{12}$Cu$_1^+$ Site 1

(b) Ag$_{12}$Cu$_1^+$ Site 1

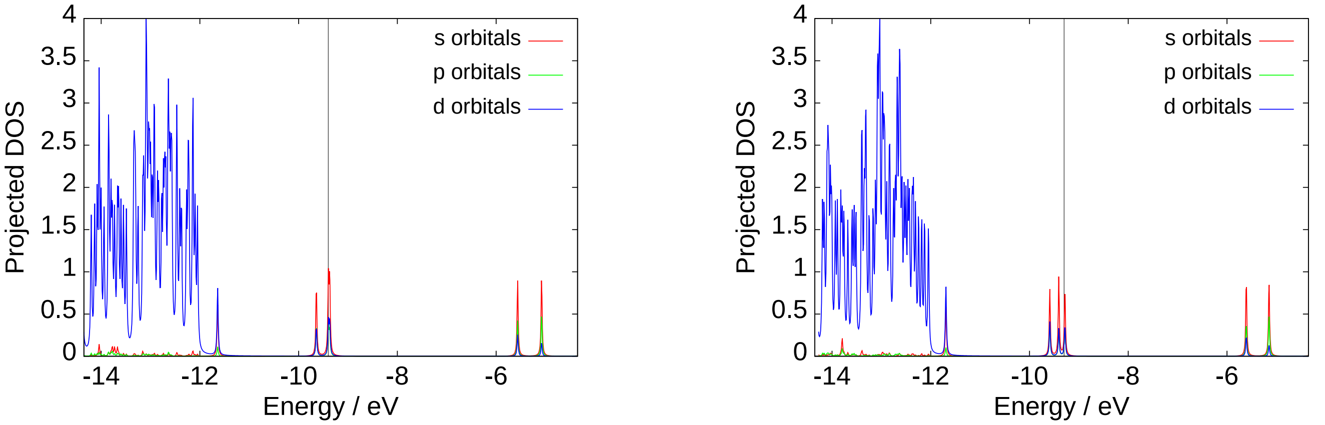

(c) Cu$_{12}$Ag$_1^+$ Site 1

(d) Cu$_{12}$Ag$_1^+$ Site 7

Figure S5: Projected DOS plots for Ag$_{12}$Cu$_1^+$ and Cu$_{12}$Ag$_1^+$, with dopants in positions 1 and 7. It is notable that there is significantly greater d-band density in the calculated range for the copper-rich clusters, and that the d band extends to higher energies than in the silver-rich clusters. In addition, the Fermi energies for Ag$_{12}$Cu$_1^+$ are -8.9 and -8.9 eV, whereas for Cu$_{12}$Ag$_1^+$, they are -9.4 and -9.4 eV, giving a reduced gap between HOMO and d-band for copper-rich helices. Finally it should be noted that the DOS profiles are not significantly changed with varying dopant position for either cluster.

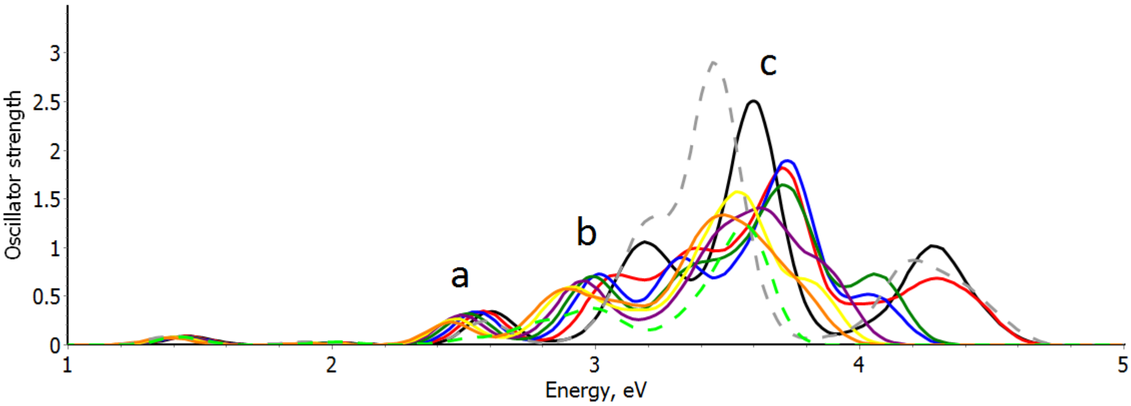

Figure S6: Overlaid view of the TDDFT spectra of $Ag_{(13-x)}Cu_x^+$ (x = 0-7 and 13), calculated with the def2-TZVPP basis and the LC-ωPBE xc-functional. Colours correspond to x = 1 (black), x = 2 (red), x = 3 (dark blue), x = 4 (green), x = 5 (purple), x = 6 (yellow), x = 7 (orange), Both pure spirals Ag_{13}^+ (grey dashed) and Cu_{13}^+ (green dashed) are included for comparison.

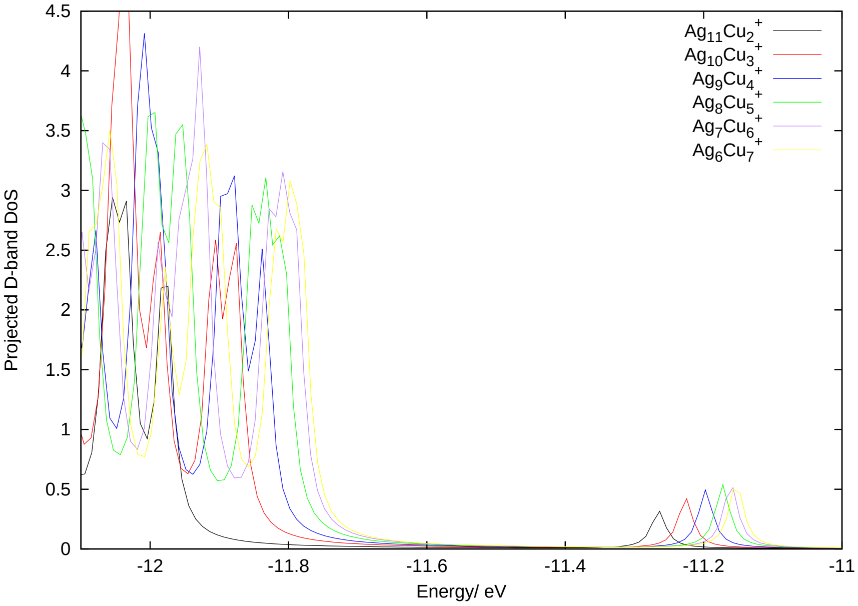

Figure S7: Projected d band densities of states for each dopant level of $Ag_{(13-x)}Cu_x^+$ x = 2-7, showing a systematic increase in d band edge energy on increased copper doping level. This trend is consistent both for the major d-band region below -11.7 eV, and for the much smaller region around -11.2 eV which also corresponds to d electrons.

Chapter 6

Energy landscape exploration of the Cu_4Ag_4 cluster with the threshold algorithm

6.1 Introduction

The statistical basis for structural and energetic preferences, derived from an energy landscape perspective, is a useful means to determine the underlying physics and thermodynamics of a continuous system [147, 111]. This approach has been applied to molecular systems [148], ionic solids [114, 149, 187] and clusters both with empirical potentials and DFT [188]. Very little has however been directed towards making comparisons between the results of both levels of theory, and in particular, for small metallic clusters.

Copper, silver and mixed copper-silver subnanoscale particles have been considered both as prototypical models for larger systems which have uses in optical and catalytic applications, and as systems in the quantum regime, with properties unique to the ultrasmall size range. The structures of the clusters are determined with combined theory-experimental methods, and their optical properties have been explored with TDDFT [74, 16, 183]. The structures may be determined and ranked by energy, however, the role of barriers to rearrangement, and therefore the thermodynamics of the basins to which minima belong, are significant in describing the nature of the clusters. Additionally, entropic barriers, basin volume and the growth of the basins with temperature allow for a kinetic interpretation which extends the energetic view found by GO methods.

The application of these statistical methods to small clusters of interest will isolate the role of the individual structural basins in controlling the favourability of particular minima. These are systems where small changes in size are known to have a large effect on their physics, and therefore the chemistry.

In this paper, we apply the threshold algorithm, recently interfaced with the Quantum Espresso plane-wave DFT package, to search the energy landscape with both the Gupta semi-empirical potential and DFT for the Cu_4Ag_4 free metal cluster. The barrier heights to rearrangement between homotops and geometric classes, growth profiles of structural basins and comparison between the energetic favourability across levels of theory are calculated.

6.2 Publication draft

Authors Christopher J. Heard, Roy L. Johnston and J. Christian Schön

Title Energy landscape exploration of the Cu_4Ag_4 cluster with the threshold algorithm

Energy landscape exploration of the Cu_4Ag_4 cluster with the threshold algorithm

Christopher J. Heard,*[a] Roy L. Johnston[a] and J. Christian Schön[b]

Received Xth XXXXXXXXXX 20XX, Accepted Xth XXXXXXXXX 20XX
First published on the web Xth XXXXXXXXXX 200X
DOI: 10.1039/b000000x

The energy landscapes of subnanometre bimetallic coinage metal clusters are explored with the threshold algorithm coupled with the Birmingham Cluster Genetic Algorithm for unbiased global structure prediction. Low lying minima and their permutational isomers are located for the Cu_4Ag_4 composition at the Gupta semi empirical potential and density functional theory (DFT) levels, in order to compare the energetic rankings and activation energy barriers to rearrangement. Statistical tools are employed to map the connectivity of the energy landscape and the growth of the basins with energy for stable structures, while the thermodynamics of interconversion are probed, based on probability flows between minima. The DFT landscape is found to be significantly more frustrated than the Gupta potential, with several classes of open, pseudo-planar geometries which are energetically competitive with the known tetrahedral global minimum, with high barriers to interconversion. The empirical potential is found to be at variance with the DFT calculation for these clusters, and fails to reproduce many of the low-lying geometric motifs, which suggests it has limited utility as a guiding potential for subnanoscale CuAg clusters.

1 Introduction

The detailed structural investigation of ultrasmall, gas phase coinage metal clusters has received a significant amount of experimental[1–6] and theoretical[1,6–15] attention since the advent of size specific methods to generate small clusters[16,17]. The realisation of their potential as catalysts[10,18,19] and their optielectronic properties[20–22] have driven the interest in their atomistic, geometric properties. Gas phase clusters represent the fundamental cluster system, in the absence of external perturbations, such as solvents, substrates or reactants, and therefore, accurate structure prediction is crucial in understanding the reactive properties, stability and electronic structure. For coinage metals, there is an additional complexity afforded by the close s/d orbital hybridisation in the valence region, which promotes planar structures, and in turn modifies their catalytic and optical properties. This effect has been found to be adequately described by density functional methods[15]. Empirical and semi-empirical potentials cannot reproduce such electronic behaviour, but are still commonly applied to larger clusters, where the geometric role is greater, and finite size, quantum mechanical considerations may fairly be neglected. Furthermore, these potentials are often used as a primary screen for energetically low-lying structures to be reoptimised at the DFT level[9,23–25]. This practical method assumes a reasonable mapping of structures between the two levels of theory, such that there are few isomers in the set which are high in energy at the empirical level, and low in energy with DFT.

The extension of the analysis beyond static structures is available through the exploration of the underlying potential energy surface, or energy landscape[26,27]. By modelling through simulation, the rearrangement between minima, important thermodynamic characteristics, such as barriers[27–29], transition dynamics[30–32] and the topology of the basins[30,33,34] may be determined. At the level of the potential function, much research has been done, both in developing efficient methods to explore and map the landscape[26,35], and to use these tools to elucidate patterns in cluster growth, doping and element type. It is known that the dynamic properties of clusters are important in predicting behaviour, and that the additional information provided by considering the landscape allows for a description which improves on static structures.

In this article, we test the ability for a semi-empirical potential to reproduce the low energy structures of the DFT analogue of a copper-silver subnanometre cluster in the gas phase, and map the energy landscape with a range of statistical tools. This work utilises the threshold algorithm[30], which has previously been successfully applied to ionic solids[36–38], molecular clusters[39] and noble metal clusters[40] and has been recently extended to work in tandem with a plane wave DFT code for direct electronic structure energy landscape exploration. The tree graph of connectivity and activation energy barrier heights[29] is calculated for the low-energy region of the Gupta potential energy surface in section 3.1.1. Dynamic fea-

---

[a] *School of Chemistry, University of Birmingham, Edgbaston, Birmingham, UK.; E-mail:cjh085@bham.ac.uk*
[b] *Max Planck Institute for Solid State Research, Heisenbergstrasse 1, 70569 Stuttgart, DE*

ture are estimated, and the evolution of entropic traps between basins are simulated in section 3.1.2 with probability flow[39]. In section 3.1.3, the growth of the densities of configurational states are estimated, in order to map the volume of individual structural basins. Comparison with the structures and tree graph from DFT calculations are given in section 3.2.

2 Methodology

We take a hierarchical approach to exploring the energy landscape of small clusters, based on an unbiased global optimisation of structure, followed by searching the potential energy surface with the threshold method. Sampling of configuration space is performed on-the-fly, in order to collect statistical information regarding the configurational densities of states.

2.1 Models

This investigation is undertaken using a semi-empirical potential function to represent the interactions between metal atoms. The ability of these potentials to reproduce the bonding and preferred structures of clusters is well tested, particularly for large clusters. For sub-nanoscale particles, in which every atom counts, and quantum effects play a role, the accuracy of potentials is however, not guaranteed. In the current work, we consider copper-silver clusters, which are known to exhibit limited s/d mixing, and a small degree of charge transfer compared to gold-containing clusters, and thus should be fairly well treated by the Gupta potential[8,41]. This potential is derived from the second moment approximation to tight binding theory, which aims to model the hopping of electrons between atomic sites. The form of the potential, given by equations 1-4, show an attractive many-body term related to the shared electronic density across multiple metal atoms V_i^{att}, and a repulsive pair term V_i^{rep}, which are summed over all sites to give the total energy V_{tot}. The potential contains five parameters $A, q, p, \zeta,$ and r_0, which are parameterised to empirical values for the cohesive energy, elastic constants, bulk modulus and lattice spacing. The parameters q, p and r_0 for mixed bonds are derived from the arithmetic means of the homometallic values. All parameters are as used in recent work[42], which are originally generated in ref[43].

$$V_{tot} = \sum_i \left[V_i^{\text{rep}} + V_i^{\text{att}}\right] \tag{1}$$

which is equivalent to

$$V_{tot} = \sum_{i \neq j} \left[\sum_j \theta(r_{ij}) - [\zeta^2 \sum_j \phi(r_{ij})]^{\frac{1}{2}} \right] \tag{2}$$

where

$$\theta(r_{ij}) = A e^{-p(\frac{r_{ij}-r_0}{r_0})} \tag{3}$$

Element	A	q	p	ζ	r_0
Cu-Cu	0.0894	2.430	10.55	1.2799	2.5560
Cu-Ag	0.0980	2.805	10.70	1.2274	2.72405
Ag-Ag	0.1031	3.180	10.85	1.1895	2.89210

Table 1 Free parameters for Gupta potential.

and

$$\phi(r_{ij}) = e^{-2q(\frac{r_{ij}-r_0}{r_0})} \tag{4}$$

The values used in this study are given in table 1.

For electronic structure calculations, plane wave GGA-DFT is employed within the Quantum Espresso package[44], with ultrasoft RRKJ pseudopotentials[45], which contain eleven valence electrons per atom, and the Perdew-Berke-Ernzerhof (PBE)[46] exchange correlation functional, which is well established for the study of metals and metallic clusters. During threshold algorithm simulations, the convergence criteria are relatively tight, in order to ensure accurate local minimum structures, and well-converged electronic states (to within 10^{-6} Ry). During local minimisation, the total energy and forces are considered converged when they vary between cycles by less than 10^{-3} Ry and 10^{-4} Ry/a_0, respectively. The Methfessel-Paxton[47] smearing scheme is employed to improve the treatment of metallic states, with a smearing width of 0.005 Ry.

2.2 Structure prediction

An unbiased global optimisation of clusters in the gas phase is performed at both Gupta and DFT levels of theory, using the Birmingham Cluster Genetic Algorithm (BCGA)[48,49]. At the Gupta level of theory, standard GA parameters are employed, as described in ref.[48]. 100 random seeds are used to create initial geometries, with each generation containing 40 individual clusters. Mating is achieved through a weighted Deaven-Ho crossover method, and mutation is performed by replacement of the selected cluster with a randomly generated new cluster structure, at a probability of 0.1 (four mutation events per GA-Gupta generation and one event per GA-DFT generation).

2.3 Threshold Algorithm

The lowest lying isomers produced in the BCGA optimisation step are used as starting points for threshold analysis. The threshold algorithm combines a Monte Carlo random walk in configuration space below a predefined maximum energy value (threshold or lid) with systematic quenches to low-lying states. In this way, the energy landscape local to the starting minimum may be mapped fairly exhaustively, whilst searching further afield for new minima is also possible. The distance in configuration space which may be adequately sampled is determined by the moveclass, the step size and the lid value. By varying the moveclass, many types of walk may be allowed, including simple Cartesian steps in configuration space, basin-hopping type steps in which Monte Carlo moves are coupled with local quenches, or large-scale mutation-like moves which allow the walker to make “jumps” across the landscape. In the current work, we use Cartesian displacements in one direction for a single atom as the moveclass. The step size is important from the point of view of efficiency. Large steps may cross barriers, effectively coarse-graining the search, but losing fine detail regarding the landscape topology. Smaller steps however, increase the number of moves required to effectively explore configuration space. This value is system specific, and is taken to be 0.1 Å for the current work. The lid value is crucial to analysis of barrier structure. Lids confine the walker to pockets of configuration space, or basins, allowing the cluster to move between minima, crossing barriers of energies no higher than the threshold. In this way, small lid values allow us to exhaustively explore well-defined subsets of the landscape, producing locally ergodic regions. Larger values may be chosen to build up an arbitrarily accurate picture of the barrier structure between minima.

The benefit of the threshold algorithm in the “long-time” limit, which is available to simple energy functions such as the Gupta potential, is that statistical information on the growth of the density of states may be gathered on the fly. In this way, estimations of the size of locally ergodic regions, in addition to their growth rates and barrier heights may be obtained.

3 Results

3.1 Gupta landscape of Cu_4Ag_4

The 50:50 composition guarantees the maximal number of possible permutational isomers, N_H, which for a binary AB system of N atoms is defined by

$$N_H = \frac{N!}{N_A!(N_B!)} \tag{5}$$

N_H is maximsed in the case that $N_A = N_B$, giving a maximum of 70 non-degenerate homotops for each isomer of Cu_4Ag_4, and so we may expect a rich energy landscape with two energy scales, one relating to the barriers between structural isomers, and one relating to homotop exchange.

The genetic algorithm is able to find all low-lying isomers, a selection of which are given in figure 1. The global minimum is found to be the dodecahedral structure, with copper atoms occupying the innermost sites. The capped pentagonal bipyramid is almost degenerate at +0.056 eV, followed by two forms of bicapped octahedra, at +0.272 and +0.280 eV, denoted BcOh and FCC, respectively. It is notbale that the decahedron structure is interconverted to a further bicapped octahedron by a small rearrangement in the bond angles and bond lengths of the capping atoms. The next lowest structure is a tetrahedral-based structure at +0.384 eV, which is tri-capped, with the fourth ”shell” atom occupying a μ-2 bridging site. This differs slightly from the well-known tetracapped tetrahedron, which is interestingly found to lie much higher in energy at the Gupta level of theory, more than 1 eV above the global minimum. The sixth isomer is a polytetrahedral chain at + 0.425 eV, which may be considered as three interwined chains, forming the basis of a Bernal spiral, which is a motif previously observed for coinage metal clusters in this size range. For clusters from 12 atoms and above, the icosahedral motif begins to dominate the low-lying range of structures, but at this size, the structures, whilst similarly compact, are predominantly constructed from smaller building blocks - the tetrahedron, octahedron and pentagonal bipyramid. There exist several low-lying homotops of each structure, with energies intermediate between those of the structural motifs, complicating the landscape as expected. For example, there are three homotops of the global minimum at energies lower than that of the first capped pentagonal bipyramid.

The preference of homotops which place silver on low coordination sites is strong, and is caused both by the lower surface energy of silver, and also the higher cohesive energy of copper, as represented by the greater value of A for Cu-Cu bonds over Cu-Ag and Ag-Ag. This reproduces the experimental cohesive energies, which are 336 kJ mol^{-1} and 284 kJ mol^{-1} for copper and silver, respectively.

The threshold algorithm is employed with the lowest six isomers as starting points. Each isomer is put through the following threshold programme: Ten lids, equally spaced, from -18.56 eV to -18.00 eV (0.01 eV/atom lid spacings or 0.08 eV/lid) are set up, chosen to sample the range from the global minimum to a reasonable energy for stable, suboptimal structures, and for each lid, a simulation is performed in which one walker makes 2.5×10^5 Monte Carlo steps. Every 10000 steps, the walker makes five downhill quench walks, in order to locate low-lying minima. By allowing the walker to make stochatic downhill steps, we allow the same holding point to access multiple minima. In total, we generate 250 potential minima, per lid, and explore the landscape bounded by an energy approximately 0.65 eV above that of the global minimum structure. This is found to be sufficient to interconvert all of the major structural motifs and to find several homotops for each.

Figure 2 shows the trajectory of a typical threshold run. We note that the majority of steps are taken within a small energy range below the maximum value. This is expected, due to the shape of the energy landscape. The number of states grows exponentially with increasing energy, so higher energy states dominate configuration space. Quenches are shown to con-

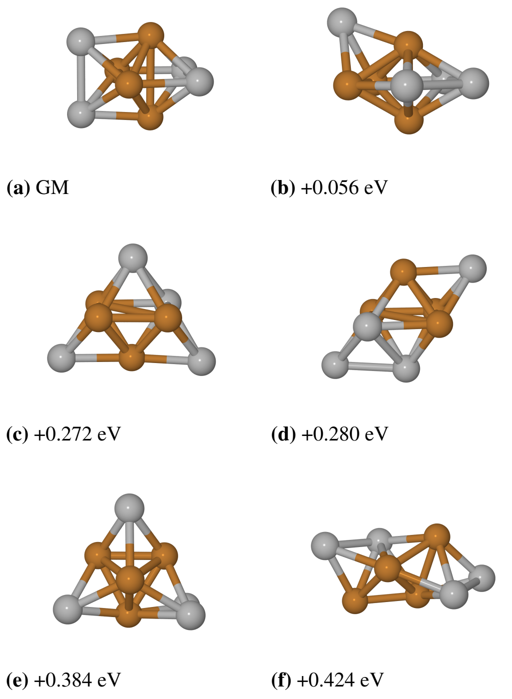

(a) GM (b) +0.056 eV

(c) +0.272 eV (d) +0.280 eV

(e) +0.384 eV (f) +0.424 eV

Fig. 1 The six lowest energy geometric isomers as found from Gupta potential global optimisation, showing compact structures. From a to e, the dodecahedral (dodec), mono-capped pentagonal bipyramidal (McPB), bicapped octahedral (BcOh), another isomer of the bicapped octahedral (FCC), distorted tetracapped tetrahedron (TcTd), and polytetrahedral tetrahelix (helix) geometries.

verge tightly to minima, of which there are many in a small range, which is typical for bimetallic clusters. In some regions of the simulation, we observe that the holding point from which quenches begin is a transition region, as it finds more than one minimum on local optimisation.

3.1.1 Tree graph Tree graphs, which are also often termed disconnectivity graphs, allow for the visual representation of the energy landscape, by projecting the connectivity of minima along a 1D energy axis. The reduction of dimensionality allows for the direct comparison of the energies of local minima and the lowest energy transition states which interconvert them. For the Cu_4Ag_4 cluster at the Gupta level of theory, this graph is given in figure 3, and is produced by considering the results of the threshold run. As the lid energy increases beyond the energetic barrier between a pair of minima, the walker may access the basin region corresponding to the new minimum. An upper-bound estimate of the transition state energy for the particular interconversion is determined for each pair of minima thus connected. In fig 3, a tree graph representative of the conversion between each low-lying minimum and the global minimum is shown for a set of lid energies ranging between -2.33 and -2.25 eV/atom (which corresponds to a total energy range of 0.64 eV). Minima are grouped into structural classes, including the dodec, TcTd, McPB, FCC, BcOh and helix motifs found by global optimisation. It can be observed that in the energy range considered, no new structural motifs become available. This implies that while it is not guaranteed that there are no lower-lying minima which have higher barriers to the putative global minimum, they will not be available without a great energy input to perturb the system from the global minimum (or other competitive minima). That other motifs are not found with the GA either suggests that there are no such additional structures in the low energy range.

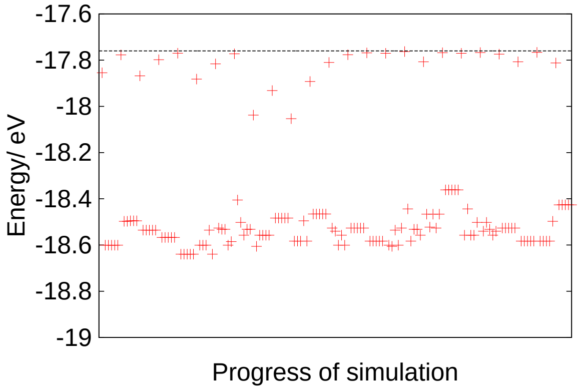

Fig. 2 A schematic threshold trajectory profile for a simulation with GM at -18.63 eV, and a lid at -17.76 eV. The walker makes moves below the lid (dashed line), and is periodically quenched (lower points).

It is notable that the tree graph is dominated by two geometries, the dodec and the McPB clusters, which make up a large proportion of the total minima found, and additionally are the lowest energy pair of structures. This result suggests that the two motifs make up a significant fraction of configuration space in the low energy range, and that many of the homotops of the two structures are lower in energy than any homotop of any other geometries. Therefore, the landscape is hierarchical, with a separation of energy scales between the permutational isomers of each structure, and the different structural motifs. It is not generally true however, that the landscape which results is without frustration. In the case of the McPB motifs, the barriers to convert to the GM (dodec) are remarkably high, even for minima which are low in energy. This thermodynamic frutration reduces the probability of interconverting motifs, despite similarity in final energy, and leads to a dominance of the dodecahedral motif. Frustration due to high transition state energies therefore serves to oppose the result that there are 18 minima within 0.16 eV of the global minimum.

The higher lying structural motifs are severely under-represented in the tree graph, with only one example of the BcOh, TcTd and helix, and two homotops of the FCC geometry in the energy range considered. There are two causes for this under-represenation. Firstly, the basins which contain these minima occupy smaller regions of configurational space, and are less frequently sampled by the MC walker during the simulation, which may be explored by analysis of the density of states (DOS). Secondly, the barriers to interconversion between these motifs and the global minimum are high. Both explanations lead to the result that these structures are unlikely to be observed experimentally, according to the Gupta potential.

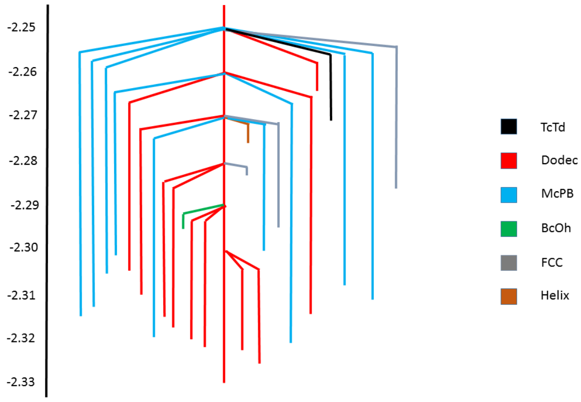

Fig. 3 Tree graph for the low-lying region of the Cu_4Ag_4 energy landscape.

3.1.2 Probability Flow Sampling the distribution of minima found on quenching during threshold runs provides statistical information on the rearrangements of the cluster. If the sampling of the region available to the walker is ergodic, it may be stated that the occupation probabilities of the available minima are analogous to their equilibrium mole fraction at the temperature represented by the lid energy. Additionally, by comparing the probability flow between minima at various lid values, the effect of temperature on the distribution of available structures can be obtained. The temperature not only restricts the access to new basins, and thus minima, but alters the probabilities of particular available transitions. This is a thermodynamic effect which may be captured with a probability flow analysis.

Figure 4 shows the flow for the lowest energy homotops of the two more favourable structural motifs, the dodec and the McPB clusters. The analysis is performed for two lid values, -2.27 eV/atom, which is the lowest lid which allows the interconversion of these minima, and a higher energy, -2.25 eV/atom, which allows the rearrangement between the GM and all of the isomers shown in the tree graph in figure 3. The percentage of quenches which lead to a particular minimum is given as the number on the line connecting the pair of minima. Minima are labelled by their total energy per atom, and coloured according to the key in figure 3. For clarity, all minima which are located for either of the starting structures, which are found with less than 3% of the quenches are omitted, except those which are reached from both starting structures. Also omitted are the frequencies of quenches which lead back to the starting minimum and thus were trapped configurations. Therefore, the sum of the percentages does not equal 100.

From the lower energy lid, it is notable that the dodec minimum predominantly finds other dodec minima, and that there is one dominant minimum, which is found in 52% of quenches. This homotop is the first suboptimal minimum, and is also the structure located with the lowest barrier of all minima. At a lid of -2.27 eV/atom it may be said that there is a local ergodicity between the two minima. In fact, the GM quenches to this minimum more frequently than returning to the starting structure, which is found in 18.8% of quenches. The McPB minimum, at -2.322 eV/atom escapes its basin much less frequently, suggesting barriers to other structures are higher for this minimum than the global minimum. Interestingly, the two minima do not directly interconvert. From either starting point, none of the quenches reached the other end point. This result is at variance with that of the tree graph, which shows it is thermodynamically possible to interconvert this pair at -2.27 eV/atom. The dynamical view of the probability flow shows that while there exists a transition state which allows the rearrangement, the pathway is difficult to traverse. This is likely to be due to a narrow pathway through configurational space with few states, and is an example of a configurational entropic barrier, whereby the free energy required to interconvert minima, in practice, is higher than the minimum energy defined by the transition state. There are minima which are reached by both starting structures, which in the case of the low energy lid, are both McPB structures. From both endpoints, the flow is very small, and so these intermediate McPB structures do not provide good alternative routes to interconvert the endpoint structures.

For the higher energy lid, it is possible to reach a large number of additional minima from either endpoint, and so the flow diagram contains many more minima. It may qualitatively be stated that the sampling of the low lying regions of the landscape are considerably more ergodically sampled for a lid of -2.25 eV/atom than -2.27 eV/atom. Further, it is notable that almost all minima which may be reached are found by both starting structures. This means that indirect conversion, whilst low in frequency for most paths, combines to produce many routes between the endpoints, with a high overall statistical weight. Furthermore, there is a route to direct rearrangement, as observed for the pathway with frequency 5.6% from -2.329 eV/atom (dodec GM) to -2.322 eV/atom (lowest McPB). Remarkably, there is no direct reverse route, which implies that there is a large entropic barrier for the backward rearrangement. This is especially striking, as thermodynamically, given the barrier between the two minima is relatively large, the difference between the forward and backward barriers should also be large, thereby favouring the backward reaction (to the GM) strongly. That this is reversed suggests the dynamics of the McPB basin is dominated by other structures, and few routes lead to the GM. The ergodicity of most paths is further evident from the reduced bias of either starting structure to motifs of its own kind, and from the reduction in self-quenching. The GM is trapped in its own basin only 8.0%, as compared with 18.8% for the lower lid.

3.1.3 Density of States

Density of configurational states are defined by

$$n(E) = \sum_{E} g(E)dE \tag{6}$$

where dE is a small energy interval, $g(E)$ is the local density of states and $n(E)$ is the total number of configurational states over the range of E. By sampling every step during the simulation and discretising the states into small energy bands, we gather density of states profiles for 250000 steps per lid by the frequency at which each band is reached by the walker. The growth of the density of states with lid energy is then calculated by stitching together the local DOS for each lid using equation 7.

$$g(E) = e^{\alpha(E-E_{\min})} \tag{7}$$

where α is a growth rate, which accounts for the increase in the number of discrete states as a function of energy. The energy is given in terms of the difference E-E_{min}, so that the result from separate lids can be connected together. Once the growth rate for each lid is determined, the DOS profile is generated for the minimum from which the simulation was begun, and the basin of which the DOS calculation samples. The individual profiles merge when they share a common gradient, which represents the energy at which they access the same superbasin and may be considered connected.

In figure 5, we observe that for the low-lying structural motifs of the Gupta landscape, there is a separation of basin volumes between the dodec and McPB structures, and the other, higher-lying motifs. The total basin volume in configurational space, as approximated by the DOS, is considerably larger for McPB than for other structures. It is unremarkable that the basins for FCC and BcOh minima are very similar, both in growth rate with energy and total number of states, as they are very similar structures, interconverted by single migrations of atoms. However, it is of note than the helical cluster, which is structurally distinct from all other low energy minima, has a similar DOS growth profile to BcOh and FCC. This cluster has considerably lower symmetry, and is based on face sharing tetrahedral subunits, rather than the octahedron, and so it is not necessary that the classes should share statistical similarities. The helix, FCC and BcOh motifs all join the superbasin of the dodec/McPB at approximately equal energies, below -2.27 eV/atom, which is in agreement with the results from the connectivity analysis. This implies not only that the growth of their basins is marginal, with small growth rates, as given by the gradient of their profiles, but that these minima belong to

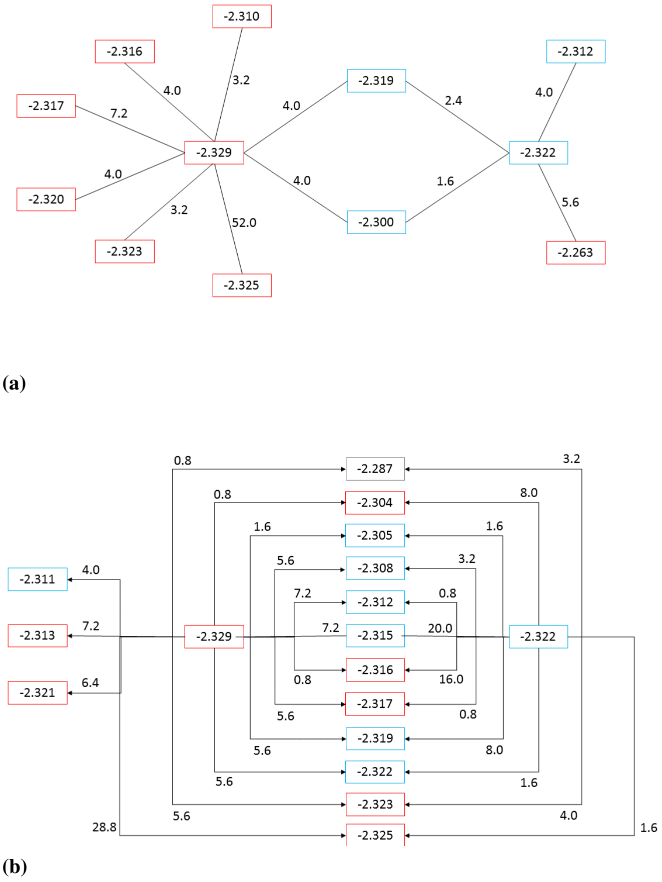

Fig. 4 Probability flow between the lowest energy homotops of dodec (-2.329) and McPB (-2.322), at lids of a) -2.27 eV/atom and b) -2.25 eV/atom. The minima are coloured consistently with the key in figure 3, and the percentages for the transition are shown along the lines which interconnect minima.

This journal is © The Royal Society of Chemistry [year]

basins of small total volume. By constrast, the growth rates are much higher for McPB and dodec structures and, owing to their lower energies, have basins which grow to large total volumes before merging with the higher-lying minima. It is interesting that the McPB motif has a higher rate of DOS growth than the dodec, such that the total volume of the basin will be larger, and the total DOS exhibits a crossing at 0.007 eV/atom (56 meV) above the GM energy. This results in an interesting additional frustration effect whereby the lowest energy structure is not statistically the most likely to be found through a quench from a random starting geometry and the high barrier to interconversion between McPB and Dodec motifs further reinforces this trapping.

The structure of the landscape may be considered to be of two large basins corresponding to McPB, and several small basins which connect to the large dodec/McPB superbasin at similar energies.

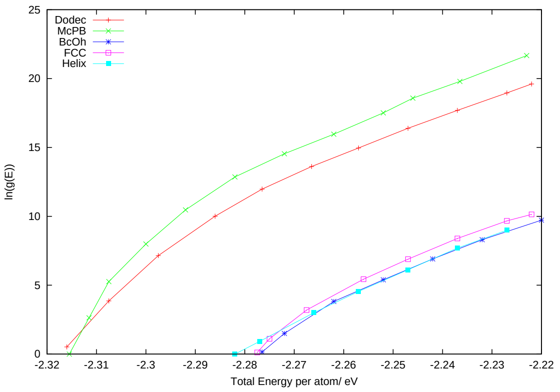

Fig. 5 The DOS profiles of low-lying Gupta minima showing the growth with energy.

3.2 DFT landscape of Cu_4Ag_4

Global optimisation at the DFT level produces a different set of low-lying structures from the Gupta potential, as shown in figure 6. Most strikingly, the tetracapped tetrahedron is found to be the global minimum at the DFT level, whereas the equivalent member of that class is more than 1 eV higher than the GM at the Gupta level, and a defective form with lower symmetry iliess at +0.384 eV. This geometry is optimal at the DFT level due to the stronger effect of surface energy and size differences between copper and silver from the DFT calculations, whilst charge transfer from copper to silver, an effect which is absent from the semi-empirical potential also plays some role in favouring the capping of copper by silver, as explained in ref . The dodec, McPB and BcOh motifs are again found to be relatively low lying, at +0.200 eV and +0.400 eV and +0.432 eV respectively. The preferred homotop is identical between levels of theory for all three of these structures, although the bond lengths are noticeably changed.

There are additional structures which are not present in the Gupta simulation, including a buckled pentagonal-based structure, the lowest energy variant of which lies at +0.160 eV, and a capped trigonal prismatic structure at +0.328 eV. These forms are more open than the previously found geometries, and represent a class which become dramatically stabilised at DFT level relative to the empirical potential. The Gupta potential is known to overestimate the strength of metal-metal bonding, such that compact structures are too greatly preferred. DFT calculations should provide a more accurate representation of the system, as electron delocalisation, formal charge transfer and orbital hybridisation, all known to play a role in coinage metal bimetallic clusters, are explicitly considered. The result is that structures with more severe undercoordination and pseudo-planar geometries become stabilised. It is notable that even for a system where the global minimum is a compact, three dimensional structure, there are several energetically low-lying open isomers, which the empirical potential cannot reproduce. As a result, the tree graph appears very different. Figure 7 displays the graph of minima which are connected by a single transition state to the TcTd global minimum, with a maximum transition state barrier of -1095.3 eV/atom, which is 2.48 eV above the GM. Within this range, there is a more even distribution of minima than found for Gupta, with several homotops found for all six of the structural classes. Furthermore, it is striking that while the differences in total energy between minima is very similar between the two levels of theory, the barriers for the DFT rearrangements are significantly higher. Very few minima are interconverted until the barrier height reaches -1095.35 eV/atom (GM + 2.08 eV), at which point many new basins become available. Higher barriers to rearrangement between similar structural motifs were observed in a previous threshold algorithm study for MgF_3 clusters , with DFT and a Coulomb plus Buckingham type potential. The necessity to attain high energies in order to increase the variety of potential minima suggests that frustration is even greater in the case of the DFT energy landscape. It is interesting to note that there are a large number of distinct minima, belonging to several structural classes which are essentially degenerate, between + 0.4 and 0.48 eV, despite the varying barrier heights which allow access to them.

4 Discussion

The various statistical analyses applied to the Gupta cluster allow for a semi-quantitative view of the energy landscape to emerge, in which the hierarchy of energy scales, the frustration inherent in the topology of the surface and particular in-

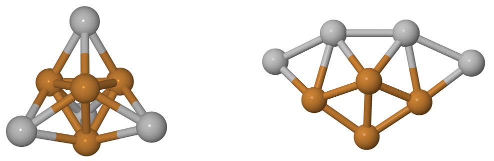

(**a**) GM (**b**) +0.160 eV

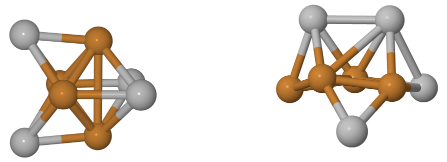

(**c**) +0.200 eV (**d**) + 0.328 eV

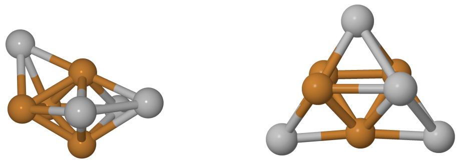

(**e**) + 0.400 eV (**f**) + 0.432 eV

Fig. 6 The lowest energy geometric isomers as found from DFT global optimisation, showing compact structures. From a to e, the tetracapped tetrahedron (TcTd), the buckled pseudo-planar bicapped (doubly bridged) pentagon, the dodecahedral-based (dodec) which has now rearranged suficiently to be better described as an additional bicapped octahedron isomer, the monocapped trigonal prism or capped non-helical polytetrahedron (McTP), the capped pentagonal bipyramid (McPB) and the bicapped octahedron (BcOh) geometries.

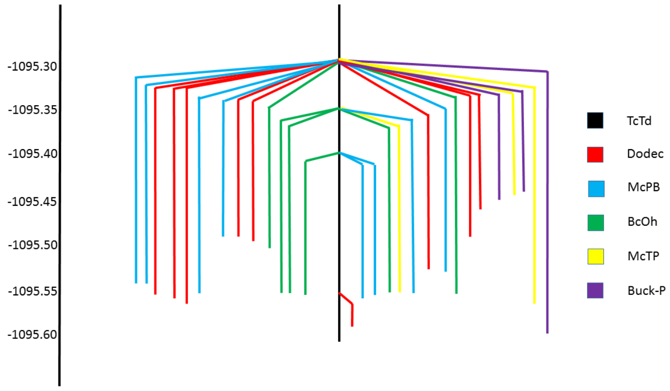

Fig. 7 The tree graph for minima directly connected to the global minimum at the GGA-DFT level.

formation, separated by basin, about the growth and shape of the basin are available. From the tree graph, the probability flows and the DOS profiles, this information is combined, and it is observed that the results are complementary. The energies at which the various basins merge with that of the global minimum is consistent from the tree graph and the DOS curves, while the latter additionally provide information on the size of the basins. It is interesting to note that there is not a strong correlation between the growth rate of the basin with energy and the energy of the minimum. While the lowest two minima correspond to the largest basins with highest growth rates, the GM has a lower growth rate than the first suboptimal structure, and the BcOh, FCC and helical clusters, which differ in minimum energy by 0.15 eV, have essentially equivalent growth rates and densities of states. The total volume of the basins which contain the high energy minima are however smaller than the lower energy basins, as to a reasonable approximation, the height of the barrier corresponds to the depth of the minimum. This observation has been made in several studies of energy landscapes, and, with some exceptions for McPB structures, it is found for the Gupta Cu_4Ag_4 cluster. This empirical rule means that high lying minima are interconverted with low lying minima for relatively low activation energy costs, if the transition begins at the high-lying structure. As a result, the basin which contains the less stable structure does not reach a large volume before connecting with that of the more favourable structure.

Application of the threshold method to clusters at the DFT level allows both for an advancement of the method to higher accuracy, in order to capture finite size quantum behaviour of ultrasmall metallic clusters, and for testing of the accuracy of the empirical potential by comparison. The Cu_4Ag_4 cluster was selected due to its known preference for compact, pseudo-spherical structures, as noted in DFT studies, and from experimental work on both Ag_8 and Cu_8, for which both clusters are three dimensional. By maximising the number of homotops, the study is complicated, and allows for comparison of chemical ordering preference between the two levels of theory. It is expeced that of the coinage metals, the CuAg cluster should be best represented by the Gupta potential, as there is a limited electronegativity difference between the metals, and the relativistic effect which favours planarity in gold clusters is reduced. While there is overlap between the structures found to be energetically competitive with the GM for both calculations, it is interesting to note that the Gupta potential gives a different GM, and that the GM at the DFT level is uncompetitive at the Gupta level. The homotop preference is in exact agreement for those structures which are present in both simulations, and so the potential may have utility in predicting chemical order, but there are large classes of structures which do not appear in the Gupta analysis. Polytetrahedral (non-helical), buckled planar and intersecting planar motifs are found on the DFT landscape, some of which are directly competitive with the global minimum. It is observed that the cost of undercoordination is less severe for the DFT structures than Gupta clusters, as several motifs exhibit silver atoms in sites which bridge two atoms. Such structures were not found, even after much higher barriers were allowed in Gupta simulations, implying an inability for the potential to stabilise such forms, rather than incomplete exploration. These varied, low symmetry motifs are not often reported in DFT studies of CuAg clusters, and underline the importance of a truly unbiased global exploration of the energy landscape. Furthermore, the need to extend the analysis to high activation barriers is great for the DFT clusters, as the landscape exhibits a large degree of frustration. This frustration is significantly more severe than for the Gupta case, and implies a rougher surface which is more difficult to explore. The result is that while there are many low-lying motifs, several of which are competitive with the GM, and many of which are essentially energetically degenerate with each other, when the cluster finds the TcTd motif, it cannot escape the high transition barriers to find other minima and becomes synergistically thermodynamically and kinetically trapped.

5 Conclusions

The energy landscape of a prototypical coinage metal bimetallic cluster has been investigated at Gupta and DFT levels of theory. Several statistical tools have been utilised to map the landscape, providing independent and cooperative information which suggests a frustrated system, with distinct energetic hierarchy between homotops and structural motifs at the empirical potential level. Comparison between energetics of minima and transition states between the potential and with GGA-DFT suggest that even for the case where the cluster is chosen to have a compact 3D global minimum and little charge transfer, the potential performs poorly, failing to reproduce several classes of open, undercoordinated minima. The competition between these open minima is close at the DFT level, suggesting that the dominance of 3D structures in previous studies of this cluster is due primarily to the frustration of the landscape, rather than the energetics of the local minima. We propose that global studies of the underlying landscape at the electronic structure level are vital for a complete understanding of even such simple metallic systems.

6 Acknowledgments

The work has been performed under the HPC-EUROPA2 project (project number: 228398) with the support of the European Commission - Capacities Area - Research Infrastructures. CJH wishes to thank the School of Chemistry, University of Birmingham, and the EPSRC for Ph.D. funding. This research was supported by the University of Birmingham through the BlueBEAR cluster, *http://www.bear.bham.ac.uk/bluebear*.

References

1 de Heer W., *Rev. Mod. Phys.*, 1993, **65**, 611–676.
2 Brack M., *Rev. Mod. Phys.*, 1993, **65**, 677–732.
3 Fielicke A., Rabin I. and Meijer G., *J. Phys. Chem. A.*, 2006, **110**, 8060.
4 Furche F., Ahlrichs R., Weis P., Jacob C., Gilb S., Bierweiler T. and Kappes M.M., *J. Chem. Phys.*, 2002, **117**, 6982.
5 Häkkinen H., Moseler M., Kostko O., Morgner N., Hoffmann M.A. and v. Issendorff B., *Phys. Rev. Lett.*, 2004.
6
7 Häkkinen H., Moseler M. and Landman U., *Phys. Rev. Lett.*, 2002, **89**, 033401.
8 Heard C.J. and Johnston R.L., *Eur. Phys. J. D.*, 2013, **65**, 1–6.
9 Paz-Borbón L.O., Johnston R.L., Barcaro G. and Fortunelli A., *Eur. Phys. J. D.*, 2009, **52**, 131–134.
10 Guvelioglu G.H., Ma P., He X., Forrey R.C. and Cheng H., *Phys. Rev. Lett.*, 2005, **94**, 026103.
11 Fournier R., *J. Chem. Phys.*, 2001, **115**, 2165.
12 Yang M., Jackson K.A., Koehler C., Frauenheim T. and Jellinek J., *J. Chem. Phys.*, 2004, **126**, 024308.
13 Bonacić-Koutecký V., Veyret V. and Mitric R., *J. Chem. Phys.*, 2001, **115**, 10450.
14 Darby S., Mortimer-Jones T.V, Johnston R.L. and Roberts C., *J. Chem. Phys.*, 2002, **116**, 1536.
15 Bonacić-Koutecký V., Burda J., Mitrić R., Ge M. Zampella G. and Fantucci P., *J. Chem. Phys.*, 2002, **117**, 3120.
16 deHeer W., *Rev. Mod. Phys.*, 1993, **65**, 611–.
17 Johnston R.L., *Atomic and molecular clusters*, Taylor and Franicis, 1st edn, 2002.
18 Zhang H., Watanabe T., Okumura M., Haruta M. and Toshima N., *Nature Mater.*, 2012, **11**, 49.
19 Sanchez A., Abbet S., Heiz U., Scheider W.D., Häkkinen H., Barnett R.N. and Landman U., *J. Phys. Chem. A.*, 1999, **103**, 9573–9578.
20 Idroboo J.C., Walkosz W., Yip S.F., Ögüt S., Wang J. and Jellinek J., *Phys. Rev. B.*, 2007, **76**,.
21 Bonacic-Koutecký V., Boiron M., Pittne J., Fantucci P. and Koutecký J., *Eur. Phys. J. D.*, 1998, **9**, 183.
22 Chen F.Y. and Johnston R.L., *Appl. Phys. Lett.*, 2007, **90**, 153123.
23 Paz-Borbon L.O. and Johnston R.L., *Compuational Studies of Transition Metal Nanoalloys*, Springer-Verlag, 1st edn, 2011.
24 Rossi G., Ferrando R., Rappallo A., Fortunelli A., Curley B.C, Lloyd L.D. and Johnston R.L., 2005, **122**, 194309.
25 Rapallo A., Rossi G., Ferrando R., Curley B.C, Lloyd L.D., Tarbuck G.M. and Johnston R.L., *J. Chem. Phys.*, 2005, **122**, 194308.
26 Wales D.J., *Energy Landscapes With Applications To Clusters, Glasses and Biomolecules*, Cambridge University Press, 2003.
27 Jansen M., Doll K. and Schön J.C., *Acta. Crystallograhica.*, 2010.
28 Doye J.P.K., Miller M.A. and Wales D.J., *J. Chem. Phys.*, 1999, **111**, 8417.
29 Becker O.M. and Karplus M., *J. Chem. Phys.*, 1997, **106**, 1495.
30 Schön J.C., Putz H. and Jansen M., *J. Phys.: Condens. Mater.*, 1996, **8**, 143.
31 Doye J.P.K. and Wales D.J., *Z. Phys. D.*, 1997, **40**, 194.

32 Mousseau N. and Barkema G.T., *Phys. Rev. E.*, 1998, **57**, 2419.

33 Rylance G.J. Johnston R.L., Matsunaga Y., Li C.-B., Baba A. and Komatsuzaki T., *Proc. Natl. Acad. Sci. USA*, 2006, **103**, 18551.

34 Smeeton L.C., Oakley M.T. and Johnston R.L., *J. Comput. Chem.*, 2014, **accepted**,.

35 H. S. and J. R.L., *Int. J. Quant. Chem.*, 2013, **113**, 2091.

36 Wevers M.A.C., Schön J.C. and Jansen M., *J. Phys.: Condens. Mater.*, 1999, **11**, 6487.

37 Schön J.C, Wevers M.A.C. and Jansen M., *J. Phys.: Condens. Mater.*, 2003, **15**, 5479.

38 Schön J.C., Cancarevic Z.P., Hannemann A. and Jansen M., *J. Chem. Phys.*, 2008, **128**, 194712.

39 Neelamraju S., Schön J.C., Doll K. and Jansen M., *Phys. Chem. Chem. Phys.*, 2012, **14**, 1223.

40 Pacheco-Contreras R., Dessens-Felix M., Borbon-Gonzalez D.J., Paz-Borbon L.O., Johnston R.L., Schön J.C. and Posada-Amarillas A., *J. Phys. Chem. A.*, 2012, **116**, 5235.

41 Cleri F. and Rosato V., *Phys. Rev. B.*, 1993, **48**, 22.

42 Nunez S. and Johnston R.L., *J. Phys. Chem. C.*, 2010, **114**, 13255.

43 Baletto F. and Mottet C. Ferrando R., *Phys. Rev. B.*, 2002, **66**, 155420.

44 Giannozzi P., Baroni S., Bonini N., Calandra M., Car R., Cavazzoni C., Ceresoli D., Chiarotti G. L., Concoccioni M. and Dabo I. *et al.*, *J. Phys.: Condens. Matter*, 2009, **21**, 395502.

45 Rappe A. M., Rabe K. M., Kaxiras E. and Joannopoulos J. D., *Phys. Rev. B.*, 1990, **41**, 1227–1230.

46 Perdew J. P., Burke K. and Ernerhof M., *Phys. Rev. Lett.*, 1996, **77**, 3865–3868.

47 Methfessel M. and Paxton A. T., *Phys. Rev. B.*, 1989, **40**, 3616–3621.

48 Johnston R. L., *Dalton Trans.*, 2003, **22**, 4193–4207.

49 Heiles S., Logsdail A.J., Schäfer R. and Johnston R.L., *Nanoscale*, 2012, **4**, 1109–1115.

This journal is © The Royal Society of Chemistry [year]

Part III

Chapter 7

Size-Dependent Sub-Nanometer Pd Cluster (Pd_4, Pd_6 and Pd_{17}) Water Oxidation Electrocatalysis

7.1 Introduction

The application of subnanometre metal particles to catalytic reactions is a developing field, in which experiment and theory may be combined to predict and describe the activity of the cluster in practice. Metal nanoparticles are employed as they combine the reactive properties of the element with increased densities of active sites, due to a larger surface area to mass ratio than surfaces [189, 79, 80, 95]. The extension for metal clusters down to the subnanometre regime is a novel branch of investigation [59], which if feasible, would provide an inexpensive route to catalytic mechanisms and activities unavailable at larger sizes. There is evidence of particularly high activity for coinage metal clusters in the reactions of CO oxidation upon gold [92], and for mixed metal cluster trimers of gold and [79], and for group 10 metals in the oxidative dehydrogenation of alkanes with platinum [58]. It has been frequently reported that the activities are higher for the subnanometre cluster systems than their nanoparticle counterparts, suggesting a route to less expensive, more efficient metal heterogeneous catalysts. It is likely that other metals which are active at the nanoscale may continue to be active in the subnanometre regime, and additionally, that some metals which are inert at larger sizes may become active, due to the changes in their structural and electronic properties.

Within the field of metal-based heterogeneous catalysis, water splitting reactions are an area of intense research [190, 191, 192, 193, 194, 195, 196, 197, 198, 199], owing to the great importance of hydrogen production with efficient chemical means, for the hydrogen economy of the future. Splitting of water molecules requires a great energy input, and may be separated into two main reactions, the hydrogen evolution reaction (HER) and the oxygen evolution reaction (OER), given by equations 7.1, 7.2 and 7.3 respectively.

$$2H^+ + 2e^- \rightarrow H_2 \tag{7.1}$$

$$2H_2O \rightarrow 2O_2 + 4H^+ + 4e^- \ (acid) \tag{7.2}$$

$$4OH^- \rightarrow 2H_2O + O_2 + 4e^- \ (base) \tag{7.3}$$

Maximising the efficiency of these reactions, particularly the OER, is the major goal of this research. Iridium is the most active transition metal water splitting electrocatalyst known at present, whereas fractional monolayers of cobalt oxide deposited on gold have been found to give very high turnover rates [200]. It is difficult to produce ultrasmall, monodisperse, composition-controlled metal particles for deposition upon a substrate for investigation of catalyst activity, and further, to achieve the accurate characterisation of structure and size effects on the efficiency of the catalyst. As a result, few studies have been undertaken for the water splitting reaction at the subnanometre level, and fewer still have atomic resolution information on the active species in the reaction.

For industrial applications, the stability and the activity of the catalyst must be balanced and this requirement presents a problem for small, supported nanoparticles. While the activity and selectivity towards particular reactions may be well established for a range of metal particles, the stability is difficult to elucidate in theory, and is likely to present difficulty in practice.

A systematic study of catalytic utility for subnanometre metal particles must include the atomistic determination of cluster structure, size and oxidation state, measurement of the activity of the catalyst, and an analysis of it's stability over repeated reaction cycles. The structure prediction of clusters under realistic reaction conditions is therefore a vital component of the analysis, and is approached with combined theoretical-experimental methods. The information gathered through high resolution synchrotron methods, such as EXAFS, XANES and GIXAS provides information which when combined with computational predictions based on energetic grounds may elucidate the role of the cluster in the reaction, and allow for better informed catalyst design. This proposal is applied in the following publication to ultrasmall, size selected palladium clusters.

7.2 Author Contribution

The work in this paper is predominantly experimental in nature, and was performed at Argonne National Laboratory, including the preparation of the supported catalyst system, the reaction cycles and the post experiment synchrotron spectroscopic analysis. The author's contribution to this work was a theoretical global optimisation study of free palladium subnanoparticles of several sizes, and for the smallest cluster, several oxidation states. The elucidation of the optimal structure and oxidation state on the basis of total DFT energies provided the initial structures for thermochemical analysis performed on the reaction intermediates which support the experiment. The role of oxidation was determined, both in order to predict the likely oxidation state found in the oxidised regime present during the active phase of the reaction, and to determine the effect of oxidation on the cluster structure, which in turn is found to affect the activity of the cluster.

7.3 Publication

Authors Gihan Kwon, Glen A. Ferguson, Christopher J. Heard, Eric C. Tyo, Chunrong Yin, Janae DeBartolo, Sönke Seifert, Randall E. Winans, A. Jeremy Kropf, Jeffrey Greeley, Roy L. Johnston, Larry A. Curtiss, Michael J. Pellin and Stefan Vajda

Title Size-Dependent Subnanometer Pd cluster (Pd_4, Pd_6, and Pd_{17}) Water Oxidation Electrocatalysis

Submitted 14 February 2013

Accepted 25 June 2013

Information *ACS Nano*, **7**, 5808, (2013)

Size-Dependent Subnanometer Pd Cluster (Pd_4, Pd_6, and Pd_{17}) Water Oxidation Electrocatalysis

Gihan Kwon,[†,#] Glen A. Ferguson,[†,#] Christopher J. Heard,[∥,#] Eric C. Tyo,[⊥] Chunrong Yin,[†] Janae DeBartolo,[‡] Sönke Seifert,[‡] Randall E. Winans,[‡] A. Jeremy Kropf,[§] Jeffrey Greeley,[∞] Roy L. Johnston,[∥] Larry A. Curtiss,[†,∞,*] Michael J. Pellin,[†,*] and Stefan Vajda[†,∞,⊥,*]

[†]Materials Science Division, [‡]X-ray Science Division, [§]Chemical Sciences and Engineering Division, and [∞]Nanoscience and Engineering Division, Argonne National Laboratory, 9700 South Cass Avenue, Argonne, Illinois 60439, United States, [∥]School of Chemistry, University of Birmingham, Edgbaston, Birmingham B15 2TT, United Kingdom, and [⊥]Department of Chemical and Environmental Engineering, School of Engineering & Applied Science, Yale University, 9 Hillhouse Avenue, New Haven, Connecticut 06520, United States. [#]These authors contributed equally to this work.

ABSTRACT Water oxidation is a key catalytic step for electrical fuel generation. Recently, significant progress has been made in synthesizing electrocatalytic materials with reduced overpotentials and increased turnover rates, both key parameters enabling commercial use in electrolysis or solar to fuels applications. The complexity of both the catalytic materials and the water oxidation reaction makes understanding the catalytic site critical to improving the process. Here we study water oxidation in alkaline conditions using size-selected clusters of Pd to probe the relationship between cluster size and the water oxidation reaction. We find that Pd_4 shows no reaction, while Pd_6 and Pd_{17} deposited clusters are among the most active (in terms of turnover rate per Pd atom) catalysts known. Theoretical calculations suggest that this striking difference may be a demonstration that bridging Pd–Pd sites (which are only present in three-dimensional clusters) are active for the oxygen evolution reaction in Pd_6O_6. The ability to experimentally synthesize size-specific clusters allows direct comparison to this theory. The support electrode for these investigations is ultrananocrystalline diamond (UNCD). This material is thin enough to be electrically conducting and is chemically/electrochemically very stable. Even under the harsh experimental conditions (basic, high potential) typically employed for water oxidation catalysts, UNCD demonstrates a very wide potential electrochemical working window and shows only minor evidence of reaction. The system (soft-landed Pd_4, Pd_6, or Pd_{17} clusters on a UNCD Si-coated electrode) shows stable electrochemical potentials over several cycles, and synchrotron studies of the electrodes show no evidence for evolution or dissolution of either the electrode material or the clusters.

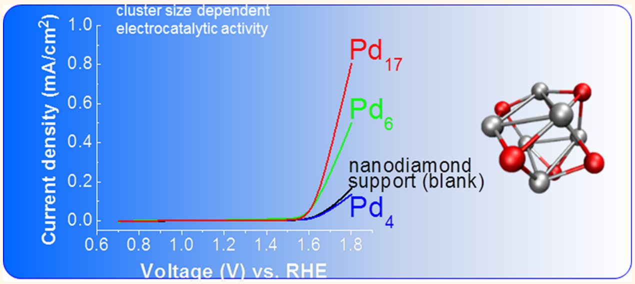

KEYWORDS: palladium · subnanometer clusters · nanocrystalline diamond · hybrid nanostructures · nanoparticles · catalysis · electrocatalysis · water oxidation · water splitting · X-ray absorption · GIXAS · GIXAFS · X-ray scattering · GISAXS

* Address correspondence to
vajda@anl.gov,
pellin@anl.gov,
curtiss@anl.gov.

Received for review February 14, 2013
and accepted June 25, 2013.

Published online June 25, 2013
10.1021/nn400772s

© 2013 American Chemical Society

Supplemental Material

Size-Dependent Subnanometer Pd Cluster (Pd_4, Pd_6 and Pd_{17}) Water Oxidation Electrocatalysis

Gihan Kwon,[1€] Glen A. Ferguson,[1€] Christopher J. Heard,[5€] Eric C. Tyo,[6] Chunrong Yin,[1] Janae DeBartolo,[2] Sönke Seifert,[2] Randall E. Winans,[2] A. Jeremy Kropf,[3] Jeffrey Greeley,[4] Roy L. Johnston,[5] Larry A. Curtiss,[1,4*] Michael J. Pellin,[1*] and Stefan Vajda[1,4,6*]

1. Materials Science Division, Argonne National Laboratory, 9700 South Cass Avenue, Argonne, IL 60439, USA;

2. X-ray Science Division, Argonne National Laboratory, 9700 South Cass Avenue, Argonne, IL 60439, USA;

3. Chemical Sciences and Engineering Division, Argonne National Laboratory, 9700 South Cass Avenue, Argonne, IL 60439, USA;

4. Nanoscience and Engineering Division, Argonne National Laboratory, 9700 South Cass Avenue, Argonne, IL 60439, USA;

5. School of Chemical Sciences, The University of Birmingham, Edgbaston, Birmingham B15 2TT, United Kingdom,

6. Department of Chemical and Environmental Engineering, School of Engineering & Applied Science, Yale University, 9 Hillhouse Avenue, New Haven, CT 06520, USA

[€] Equally contributing authors (GK, GAF and CJH)

[*] Corresponding authors: vajda@anl.gov (SV), pellin@anl.gov (MJP) and curtiss@anl.gov (LAC)

Experimental

Cyclic Voltammetry Data:

Current Density Normalized to Pd atoms and per Cluster Turn-Over Rates.

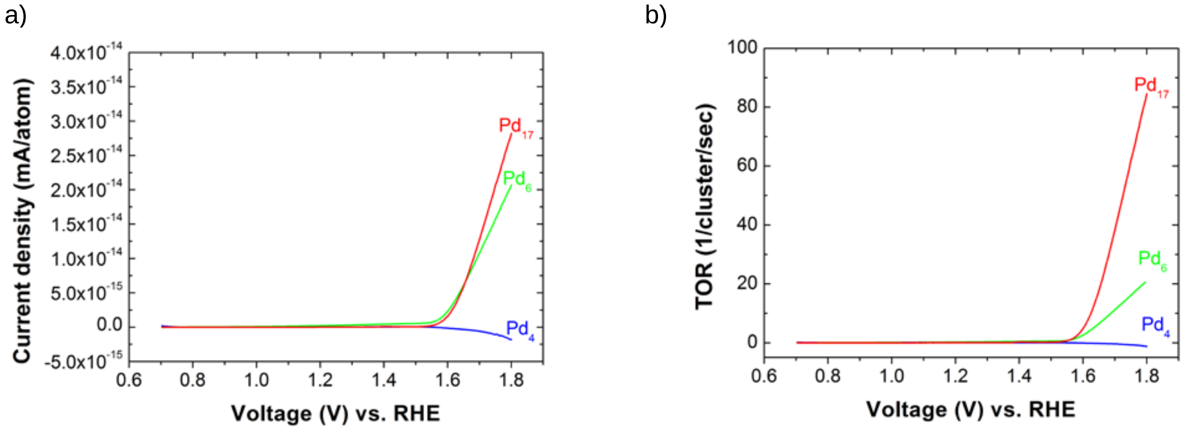

Figure S1. Background corrected (*i.e.* after subtraction of the current of the blank UNCD support) currents normalized for Pd atom (a) and per cluster turn-over rates (b).

GIXAS Data

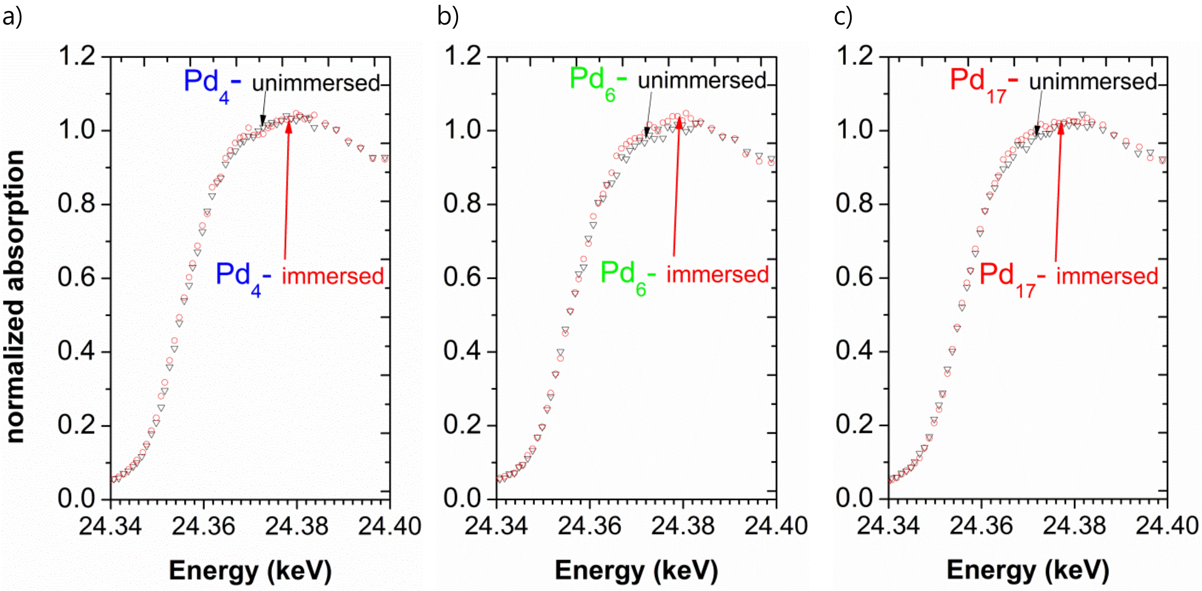

Figure S2. Unsmoothed X-ray absorption spectra, merged from three scans, showing the enlarged edge region for unimmersed (as deposited, black triangles) and immersed and cycled (red circles) areas of electrodes with Pd_4 (a) , Pd_6 (c) and Pd_{17} (e) clusters investigated (c.f. smoothed spectra shown in Figure 2 of the paper).

Chronoamperommetry of the blank UNCD support and of UNCD-supported Pd_4, Pd_6 and Pd_{17} cluster samples.

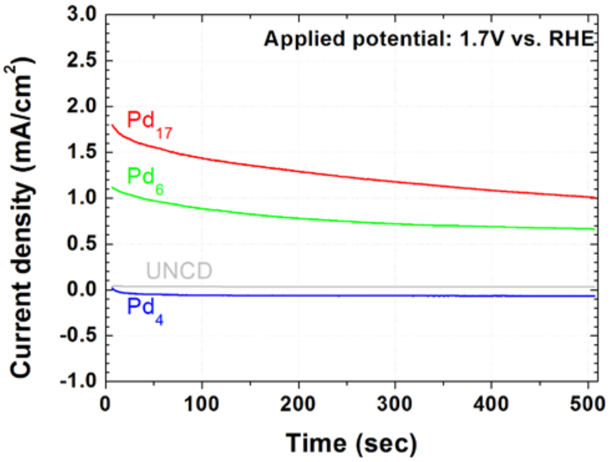

Figure S3. Chronoamperometry at 700mV *vs.* Ag/AgCl (1.7V *vs.* RHE). Current data were calibrated by cluster spot area. Chronoamperometry was performed before collecting cyclic voltammetry data.

Cyclic Voltammetry of the blank UNCD support and of UNCD-supported Pd_4, Pd_6 and Pd_{17} cluster samples.

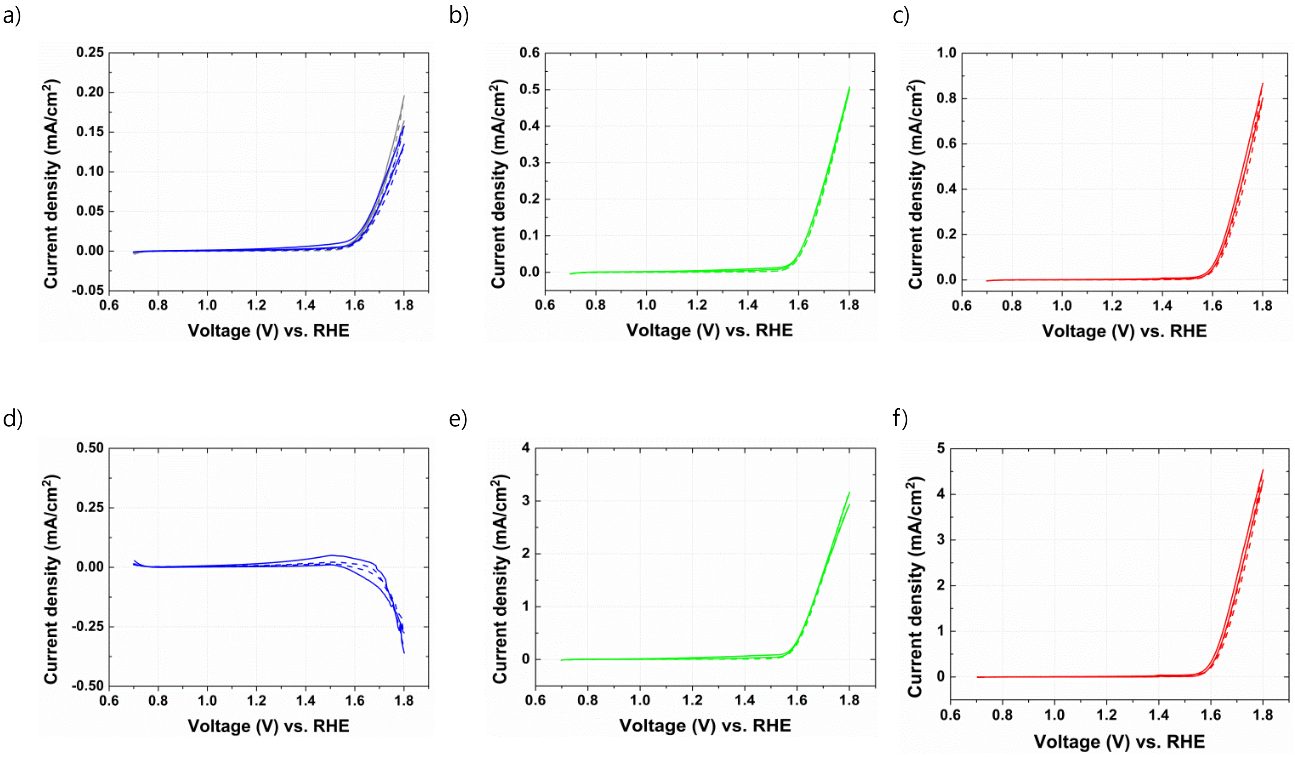

Figure S4. Cyclic voltammetry data (3 cycles) for UNCD-supported Pd_4 (a), Pd_6 (b) and Pd_{17} (c)clusters under pH 13.6 (1M NaOH) with current densities normalized to the dipped chip area, s in Figure 1 of the main text, S_{chip}, for the blank UNCD support (gray, dashed line), Pd_4 (blue), Pd_6 (green) and Pd_{17} (red) clusters. Solid line: scanning towards higher voltage; dashed line: scanning towards lower voltage. The fraction of surface area, $S_{cluster}$, covered by clusters was 9.4%, 7.9% and 11.0% for the Pd_4, Pd_6, and Pd_{17} clusters respectively calculated as $S_{cluster}/S_{chip} \times 100$. (d), (e) and (f) show background corrected current (i.e. after subtraction of the current of the blank UNCD support) currents normalized for the cluster covered area, for (a), (b) and (c), respectively.

Computational Results

Pd_4 cluster structure

Global optimisation of the Pd_4 clusters with the BCGA shows a preference for the tetrahedral geometry over the perfectly planar square, which has relative total energy of +0.74 eV. Capped triangular (or y- shape) and linear structures were found to be considerably less favourable, at +1.67 eV and +2.78 eV respectively. This may be explained by considering the maximisation of coordination of metal atoms, and is in line with previous theoretical work on clusters of the same size [SR1, SR2].

It might be expected that the bond lengths for the global minima in clusters may be shorter than corresponding bulk phase bonds, due to their diminished coordination. This is observed by Krüger et al [SR3] with all-electron DFT calculations, who also report a well correlated relationship between bond length and coordination number. The authors note that the GGA functionals overestimate the bulk bond length with respect to experiment, and find a Pd4 tetrahedral bond length of 2.66 Å and 2.59 Å for GGA and LDA functionals respectively. Reference [SR4] gives a palladium dimer bond length of 2.49 Å and a bulk bond length of 2.79 Å with the PBE functional. Therefore our value of 2.61 Å for the tetrahedron occupies an intermediate position between dimer and bulk values as expected, and is shorter than the all-electron GGA bond lengths of Krüger. For the square cluster, our bond length is 2.51 Å, reflecting its nature as a dimer-of-dimers.

Pd4Oy, y = 3, 4 structures

The effect of oxidation upon the structures and energetics of Pd4O3 and Pd4O4 clusters is investigated by DFT global optimisation. This method is designed to find the best few isomers of a cluster, rather than produce an exhaustive library,of minima, so in ordershould be noted to extend the range of considered structures, the optimisation procedure is supplemented by local relaxation of some interesting constructed geometries. It should be noted however, that in no cases were those structures constructed found to be more stable than the best of the BCGA, so we may claim that the putative global minima are indeed global minima. The structures of global minima (GM) for both oxidised species (along with Pd4) are shown in Table S1 and Table S2.

Pd_4O_3 structures.

The six isomers found to be within 1.0 eV of the global minimum are displayed in Table S1, from which we may note that dimeric oxygen is beginning to be found at intermediate energies, but is uncompetitive with broken, palladium-bound oxygen atoms.

Table S1: Geometries and energies of clusters within 1.0 eV of the global minimum for Pd_4O_3. Oxygen atoms are in red, palladium is light green. The global minimum for Pd_3O_3 is included for comparison with that of Pd_4O_3.

Total energy / eV	Relative Energy (to GM) / eV	Structure
-5431.055	000	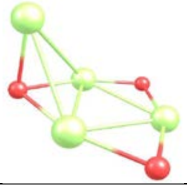
-5430.814	+240	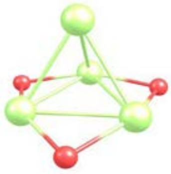
-5430.578	+480	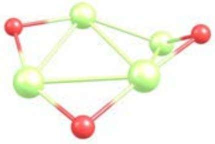
-5430.552	+500	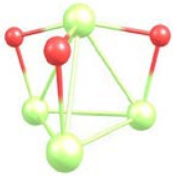
-5430.508	+550	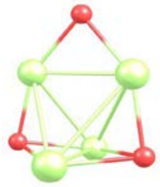
-5430.222	+830	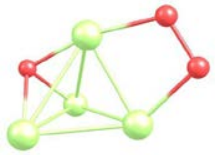
Pd_3O_3 global minimum		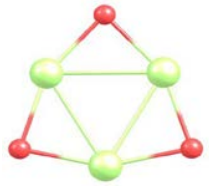

The global minimum geometry is significantly distorted with respect to the tetrahedron of Pd_4, with an opening out of the cluster towards a two-dimensional shape, such that the angle γ is increased from 60° to 134.3° and one of the Pd-Pd bonds is lost. This butterfly structure is an intermediate between the tetrahedron and the planar geometry found to be the two isomers lowest in energy for the bare clusters and it may be noted that the oxygens form a perfectly planar hexameric ring of three -Pd-O-Pd- units, (which is found by global optimisation to be the global minimum for Pd_3O_3: see end of table S1). The same motif is observed for the first suboptimal minimum, which displays the tetrahedral structure, whilst maintaining the hexameric $(PdO)_3$ ring. The GM exhibits an extension of the five remaining Pd-Pd bonds by an average of 0.10 Å relative to Pd_4 (tetrahedron).

Oxygen atoms bind preferably to the μ-2 palladium bridging sites over μ-3 face-capping sites. This may be seen from the fact that the four best isomers contain almost exclusively two-coordinate oxygens bridging palladium atoms. In comparison, the structure with all face-capping oxygens is found the be the considerably higher in energy, at +1.74 eV.

Pd_4O_4 structures.

The structures of minima up to +1.0 eV above the global minimum, and their reaction energies are displayed in Table S2.

Table S2: Geometries and energies of clusters within 1.0 eV of the global minimum for Pd_4O_4. Oxygen atoms are in red, palladium is light green.

Total energy / eV	Relative Energy (to GM) / eV	Structure
-5864.028	+000	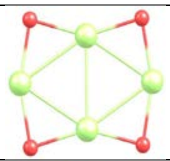
-5863.894	+130	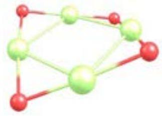
-5863.767	+260	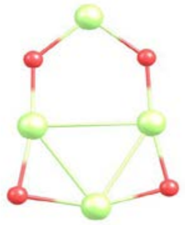
-5863.587	+440	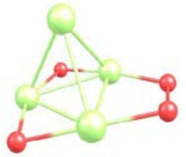
-5863.422	+610	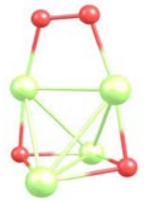
-5863.204	+820	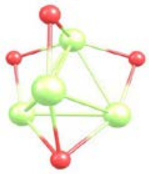
-5863.148	+880	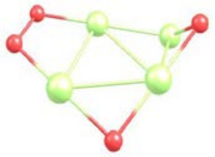

The transformation from the tetrahedron to the perfectly planar rhombic geometry is complete for the GM of y = 4, containing Pd-Pd bonds of 2.62 Å (extended to 2.80 Å for the medial bond). This represents an analogue of the planar structure found as the first suboptimal isomer for the bare cluster., but with a significant average extension of 0.15 Å for Pd-Pd bonds. The apparent weakening of the Pd- Pd framework is counteracted both by the preference of a rhombus to the square, which allows for an extra metallic bond, and the maximisation of Pd-O bonds, of which there are eight for this geometry, as compared to six for the best tetrahedral Pd_4O_4 structure.

The suboptimal Pd_4O_4 clusters again show a strong preference for oxygen μ-2 binding over μ-3 binding, due to the crowding of Pd-O binding sites. Oxygen dimers bound to palladium are found to be prevalent, making up the non-planar local minima up to +824 meV. Furthermore, tetrahedra without dimers are not found until energies of +1.13 eV and above. This may be ascribed to the steric hindrance for oxygen atoms decorating the palladium frame.

It is interesting to note that the tetracapped tetrahedron, which allows each oxygen atom to occupy a Pd_3 face, and which is the global minimum for some mixed metallic clusters of eight atoms[SR5] is found at +3.00 eV. This further displays the unwillingness of oxygen to cap Pd_3 faces when at high oxidation states.

Table S3: Reaction energy for the Pd_4 / O system

Reaction	Pd-Pd bonds	Pd-O bonds	Total bonds	Rel. Energy /eV
Pd_4	6	0	6	0
Pd_4+ 3O	5	7	12	-17.04
Pd_4 + 4O	5	8	13	-22.00

The reaction energy shows the increased energetic stability of the global minimum for oxygenated clusters relative to the bare metal cluster plus isolated oxygen atoms. Negative numbers indicate higher stability. In both cases, Pd4Oy is more stable than Pd4 + yO; consequently, one might expect these clusters to become easily oxidised in conditions of excess oxygen, without the need to invoke le Chatelier's principle to explain the high oxidation state in experiment. The total coordination increases on addition of oxygen atoms, alongside a shift in abundance from Pd-Pd bonds towards Pd-O bonds.

The energetic favourability of producing Pd-O bonds where possible is seen in the fact that separate oxygen molecules, free of the cluster, are never found. While oxygen dissociation barriers have not been calculated in this work, we may be confident that the globally stable arrangement is to increase Pd-O bonds to the detriment of the strength and overall number of Pd-Pd bonds. This result is supported by experimental heat of formation values of 1.036 ± 0.16 eV and 3.95 ± 0.87 eV for dimeric gas phase Pd- Pd and Pd-O bonds respectively[SR6].

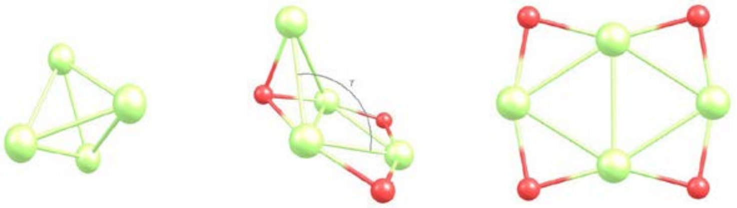

Figure S5. Geometries of the Pd4, Pd4O3 and Pd4O4 clusters found using the Birmingham Cluster Genetic Algorithm.

We note that the difference in total energy between the most stable few isomers is small for both oxidised clusters, on the order of <500 meV. This is characteristic of small binary clusters, and suggests that there may well be significant coexistence of a number of structures in the gas phase. This will be further exascerbated by the presence of a substrate. We expect these issues to be of diminishing concern for the larger particles, and so may contribute somewhat to the lack of activity found for Pd_4 on UNCD.

Pd_4O_3 Free Energy Diagram

The Pd4O3 cluster is not expected to exist in the in the harsh oxidizing conditions of the electrochemical cell. Therefore, the results presents are meant to be illustrative of effects that are conducive to OER on supported clusters. The inclusion of these clusters is not, in any way meant to imply that the cluster exists in under the conditions present in the cell nor that the cluster is presented as a realistic catalyst.

The oxygen binding to the Pd4O3 cluster-bridging site has a similar type of bonding to the Pd4O4 global minimum. While oxygen binding to the top site of the Pd4O3 cluster is significantly different in bonding allowing the cluster to be optimized to a local minimum. This is not the case for the oxygen binding to the Pd4O3 cluster-bridging site, upon optimization this cluster converts to the Pd4O4 global minima. To approximate the binding energy for the cluster the oxygen binding was approximated in the following manner. Using the oxygen position and cluster geometry from the optimized Pd4O3 cluster with the hydroxyl bound as the starting point the cluster was frozen during the optimization by projecting out the forces on the Pd4O4 atoms. This geometry was further relaxed by removing the constraints from the Pd atoms bound to the oxygen. The energy difference between these structures is 0.01 eV. This energy of the partially relaxed structure was then used as the energy to calculate the binding of O to the Pd4O3 bridging site.

Supplemental References

[SR1] Mehmood, F.; Greeley, J.; Curtiss, L. A. Density Functional Studies of Methanol Decomposition on Subnanometer Pd Clusters. *J. Phys. Chem. C* **2009**, *113*, 21789-21796.

[SR2] Sebetci, A. Does Spin-Orbit Coupling Effect Favor Planar Structures for Small Platinum Clusters*? Phys. Chem. Chem. Phys*. **2009**, *11*, 921-925.

[SR3] Krueger, S.; Vent, S.; Nortemann, F.; Staufer, M.; Roasch, N. The Average Bond Length in Pd Clusters Pd_n, n = 4-309: A Density-Functional Case Study on the Scaling of Cluster Properties. *J. Chem. Phys.* **2001**, *115*, 2082-2087.

[SR4] Zarechnaya, E. Y.; Skorodumova, N. V.; Simak, S. I.; Johansson, B,; Isaev, E. I. Theoretical Study of Linear Monoatomic Nanowires, Dimer, and Bulk of Cu, Ag, Au, Ni, Pd and Pt. *Comput. Mater. Sci.* **2008,** *43*, 522-530.

[SR5] Heiles, S.; Logsdail, A. J.; Schaefer, R.; Johnston, R. L. Dopant-Inducted 2D-3D Transition in Small Au-Containing Clusters: DFT-Gloval Optimisation of 8-atom Au-Ag Nanoalloys. Nanoscale **2012**, *4*, 1109-1115.

[SR6] Lide, D. R. In *CRC Handbook of Chemistry and Physics*, 81st ed.; CRC Press/Taylor and Francis: Boca Raton, FL, 2001.

Chapter 8

Support and Oxidation Effects on Subnanometer Palladium Nanoparticles

8.1 Introduction

The growing interest in subnanometre metallic particles for the catalysis of a wide range of reactions has led to the discovery of a number of impressively active and stable systems [169, 92, 57, 93, 201, 202], with great promise as future chemical and industrial materials. Atomistic understanding of the structure of these particles is a vital component of the prediction and design of materials with high activity and selectivity. The coordination, and particularly the undercoordination of nanoparticle atoms is significant in modulating the electronic structure, and thus the binding of reactants [79, 83, 203, 27, 28]. Additionally, the role of the support is known to be of great importance [204, 205, 206, 207]. The interplay between charge accumulation/depletion and the cluster structure has been studied in detail [27, 28, 36, 81, 208, 26], and requires an atomic resolution of cluster structure to fully explain. Non conductive supports may also alter the reactive properties of deposited particles by driving structural modifications, both through direct bonding to cluster atoms, and by inducing changes in further layers as a result [209, 210]. In some cases, the surface drives the cluster to epitaxy according to the same process as is found in atomic layer deposition experiments, and may even drive complete crystallisation of the nanoparticle. From an energy landscape perspective, the binding to a large, continuous system, which breaks the translational symmetry of the free cluster and introduces directional bonding of varying strengths, drastically alters the relative depths of minima, and affects the barrier heights to intra-cluster rearrangements.

The growth and deposition methods are experimental considerations which have a significant effect on cluster structure, with cluster growth strongly affected by the environment. If the cluster is generated in the gas phase and subsequently deposited, the structures of the gas phase low energy minima will dominate the resulting library of minima. If the cluster is grown upon the surface, or is formed by the agglomeration of smaller clusters by ripening processes, the role of the surface will be greater, and the region of configuration space belonging to the structures which are stable in the gas phase are unlikely to be sampled.

This study requires the isolation and investigation of a large number of variables, including the chemical and electronic role of the support, the size of the cluster, the deposition method and the metal identity. The unbiased structure prediction of these systems is therefore a complex issue, and one which is difficult to solve experimentally, due to the often harsh experimental conditions, and the small size of the reaction species. Theoretical examination provides a route to control the various factors and make predictions regarding the structure of the clusters.

In the following paper, several of the major factors which may affect the structures of ultrasmall, deposited palladium clusters are considered with a DFT structure prediction study. Cluster size, oxidation level and support identity, along with binding mode and site are all considered. In isolating these factors, we investigate the extent of their contribution, and the synergistic and competitive roles they play in controlling cluster geometries. It is known from recent experimental data that there is a significant size dependence of the catalytic activity of palladium clusters at the size range we consider, and thus a fuller understanding of this effect is of value in making predictions for future subnanoscale materials. The experimental procedure modelled in this investigation is that of the ultrasoft landing of clusters produced and equilibrated in a molecular beam, followed by post-deposition oxidation. This scheme aims to reproduce the major features of recent experiments which have established the catalytic utility of subnanometre palladium clusters. Furthermore, this work attempts to elucidate general trends which impact on catalyst efficiency for the understanding and design of a novel class of cluster materials.

8.2 Publication

Authors Christopher J. Heard, Stefan Vajda and Roy L. Johnston

Title Support and Oxidation Effects on Supported Subnanometer Palladium Nanoparticles

Submitted 08 November 2013

Accepted 30 January 2013

Information *J. Phys. Chem. C.*, **118**, 3581, (2014)

THE JOURNAL OF
PHYSICAL CHEMISTRY C
Article
pubs.acs.org/JPCC

Support and Oxidation Effects on Subnanometer Palladium Nanoparticles

Christopher J. Heard,[†] Stefan Vajda,[‡,§] and Roy L. Johnston*[,†]

[†]School of Chemistry, University of Birmingham, Edgbaston, Birmingham, U.K. B15 2TT

[‡]Materials Science Division and Nanoscience and Engineering Division, Argonne National Laboratory, 9700 South Cass Avenue, Argonne, Illinois 60439, United States

[§]Department of Chemical and Environmental Engineering, School of Engineering & Applied Science, Yale University, 9 Hillhouse Avenue, New Haven, Connecticut 06520, United States

S *Supporting Information*

ABSTRACT: The effect of cluster size, oxidation state, and the support upon the structures and energetics of subnanometer palladium nanoparticles is investigated within a density functional framework. Gas phase global minima of Pd_4 and Pd_{10} along with their suboxide counterparts are determined using a genetic algorithm and deposited upon MgO (001) and a high-index alumina surface. It is observed that there is an oxidation-dependent transition in the smaller clusters from three-dimensional to two-dimensional structures both in the gas phase and when supported by a surface. MgO strongly promotes a change from tetrahedral- and icosahedral-based structures toward cubic forms, while alumina induces significant distortion of the cluster and the breaking of Pd−Pd bonds. Increased oxygenation contributes cooperatively to these effects, causing disruption of the Pd−Pd bond network, favoring the incorporation of oxygen into the cluster structure, further complicating unambiguous structure prediction.

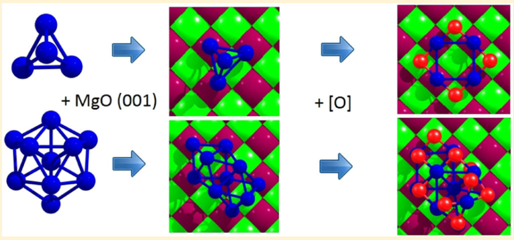

© 2014 American Chemical Society

dx.doi.org/10.1021/jp411019t | *J. Phys. Chem. C* 2014, 118, 3581−3589

[redacted]

Supplementary Information for "Support and Oxidation Effects on Subnanometer Palladium Nanoparticles"

Christopher J. Heard,[†] Stefan Vajda,[†,¶] and Roy L. Johnston[*,‡]

Materials Science Division and Nanoscience and Engineering Division, Argonne National Laboratory, 9700 South Cass Avenue, Argonne, Illinois 60439, United States, and School of Chemistry, University of Birmingham, Edgbaston, Birmingham, UK, B15 2TT

E-mail: r.l.johnston@bham.ac.uk

---

[*] To whom correspondence should be addressed

[†] Materials Science Division and Nanoscience and Engineering Division, Argonne National Laboratory, 9700 South Cass Avenue, Argonne, Illinois 60439, United States

[‡] School of Chemistry, University of Birmingham, Edgbaston, Birmingham, UK, B15 2TT

[¶] Department of Chemical and Environmental Engineering, School of Engineering & Applied Science, Yale University, 9 Hillhouse Avenue, New Haven, Connecticut 06520, United States

Table S1: E_d and E_d/atom for MgO (001) bound Pd_4O_x clusters

Cluster composition	Ed/ eV	Ed per Pd atom /eV atom^{-1}
Pd_4	-5.36	-1.34
Pd_4O_1	-5.35	-1.34
Pd_4O_2	-5.37	-1.34
Pd_4O_3	-5.31	-1.33
Pd_4O_4	-5.35	-1.34

Table S2: E_d and E_d/atom for Alumina bound Pd_4O_x clusters

Cluster composition	Ed/ eV	Ed per Pd atom /eV atom^{-1}
Pd_4	-0.20	-0.05
Pd_4O_1	-0.21	-0.05
Pd_4O_2	-0.20	-0.05
Pd_4O_3	-0.15	-0.04
Pd_4O_4	-0.14	-0.04

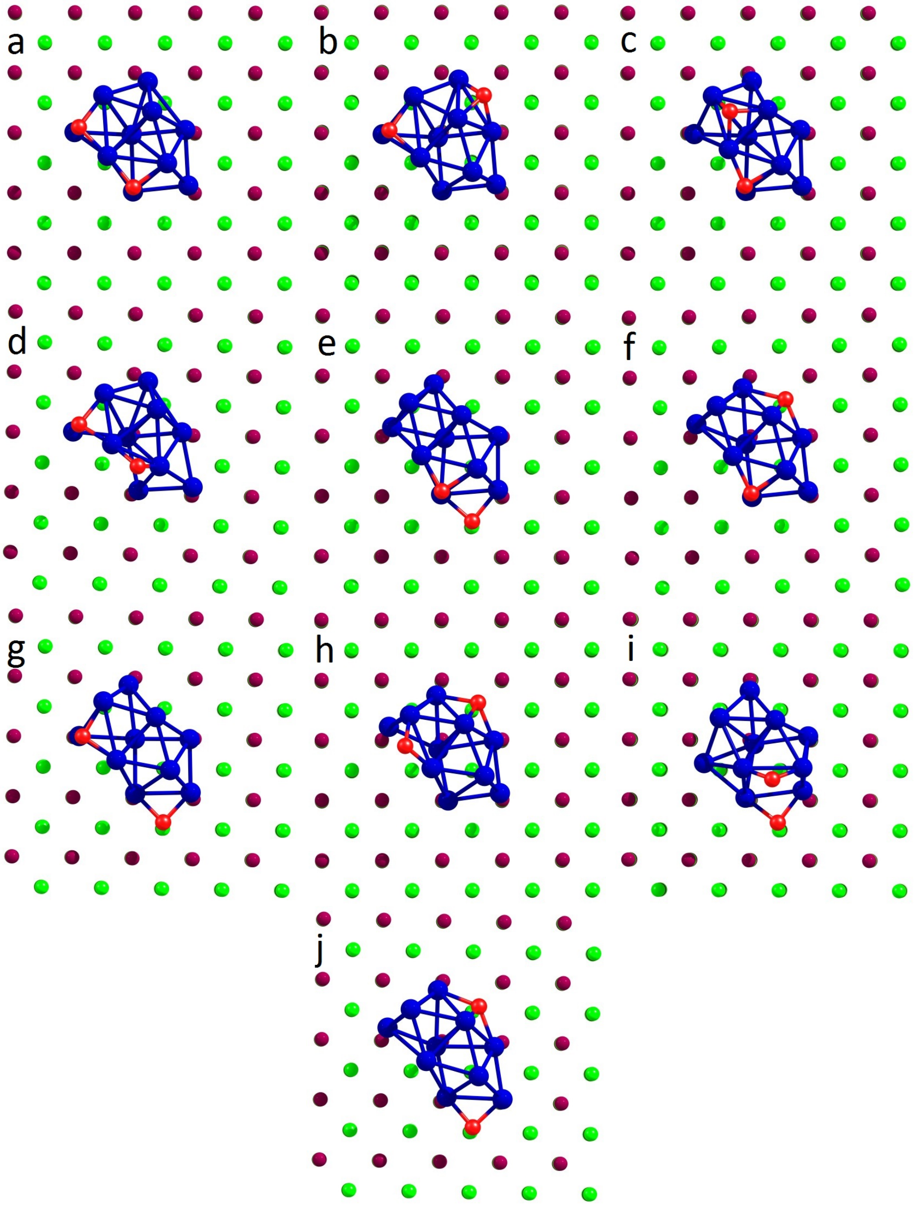

Figure S3: Candidate structures for $Pd_{10}O_2$ on MgO in order of increasing energy, as given in table 2 in the main text. a) Between layers I, b) Between layers II, c) Between layers + μ-3 top, d) Between layers + μ-2 top, e) Between layers + surf/cluster, f) Between layers II + surf/cluster, g) Between layers III + surf/cluster, h) Surf/cluster + μ-2 top, i) Surf/cluster + μ-2 top, j) Surf/cluster.

Table S4: Bader valence charge transfer to palladium clusters and deposited oxygen atoms for each composition of Pd_4O_x upon MgO. There is a close correspondence between the MgO and Alumina-bound charge transfer, with transfer from the surface to the cluster, and further to the deposited oxygen. The extend of charge abstraction from the surface is larger for MgO than in the Alumina case.

Cluster composition	Pd e^- gain/ e	Oxygen e^- gain /e
Pd_4	0.56	-
Pd_4O_1	-0.20	0.73
Pd_4O_2	-1.05	1.67
Pd_4O_3 (planar)	-2.50	1.76
Pd_4O_3 (3D)	-1.75	2.56
Pd_4O_4	-2.88	3.97

Chapter 9

$\mathbf{Pd}_n\mathbf{Ag}_{(4-n)}$ and $\mathbf{Pd}_n\mathbf{Pt}_{(4-n)}$ clusters on MgO(100): A density functional surface genetic algorithm investigation

9.1 Introduction

Sophisticated GO methods have been developed and applied successfully to the prediction of cluster structures for nano and subnanoscale clusters [11, 211]. The majority of this development has been in the field of free clusters, with the aim of finding the lowest lying structures when unperturbed by external factors such as gases, surfaces or solvents. This approximation is a great simplification of the energy landscape, and thus significantly reduces the computational cost of GO. There are many cases in which this approximation is valid, such as in molecular beam experiments [51, 171], or when a cluster is embedded in an inert matrix or helium droplet [212, 213]. In situations where this approximation breaks down, there may be utility in beginning with a free cluster GO, in order to provide initial structures before modification. Soft landing experiments, where the gas phase structure represents the initial form before binding to a surface is a case where the gas phase global minimum is likely to be related to the final structure [210]. One method to recreate experimentally relevant results, where the cluster is not in isolation, is to produce the low lying gas phase minima, and subsequently include the additional system and locally reminimise structures. This method remains less computationally expensive than a full GO simulation of the combined system, but will not allow for exploration of regions of the energy landscape which do not contain the subset of structures initially found in the gas phase. It is often the case that these regions become low-lying when the full system is considered, and so the final structures do not contain the global minimum.

In order to ensure the true global minimum is found, an unbiased GO strategy, which includes the full cluster/substrate system must be employed. There are few approaches which attempt to achieve this efficiently, although DFT-BH methods with explicit substrates [83] and GA upon surfaces for gold clusters [214] have recently been used. For such methods, the number of atoms included in the simulation is substantially increased, due to the inclusion of the substrate, and thus the computational cost becomes the most important consideration. Efficient means to sample configuration space are required, along with appropriate modifications to the model to reduce the cost of the search. For DFT calculations, this is commonly manifested as a reduction in the size of the basis set for the Kohn Sham wavefunctions.

The BCGA has been extended to include explicit surfaces, allowing for direct substrate-bound cluster GO at the DFT level of theory. Low lying minima which may be missed in the two phase approach are therefore identified. This improvement allows for unbiased structure prediction for systems which are important in heterogeneous catalysis, in particular for subnanometre metal cluster catalysis. This is a field in which the small size of the active species is beneficial to theoretical analysis, as higher level calculation methods are available for a given total cost. Despite this synergy between size and activity, the model applied to the surface BCGA must necessarily be modified to allow for the large number of surface atoms required to avoid image-image interactions in the simulation cell, and to correctly reproduce the charge distributions. This modification takes the form of loosened electronic, energy and force convergence criteria.

The BCGA is applied to subnanometre clusters of potential heterogeneous catalytic interest. Palladium and palladium-containing bimetallic clusters are selected, so as to systematically identify the structural, energetic and electronic trends across the doping series and by metal identity. Previous experimental and theoretical studies have investigated palladium clusters for electrocatalysis, in addition to the various factors which affect their structures. The increase of complexity to bimetallic clusters represents a further tunable feature which may be exploited for catalyst design.

9.2 Publication draft

Authors Christopher J. Heard, Sven Heiles, Stefan Vajda and Roy L. Johnston

Title $Pd_nAg_{(4-n)}$ and $Pd_nPt_{(4-n)}$ clusters on MgO(100): A density functional surface genetic algorithm investigation

$Pd_nAg_{(4-n)}$ and $Pd_nPt_{(4-n)}$ clusters on MgO (100): A density functional surface genetic algorithm investigation

Christopher J Heard,[a*] **Sven Heiles,**[b] **Stefan Vajda**[c,d,e,f] **and Roy L. Johnston**[a]

Received Xth XXXXXXXXXX 20XX, Accepted Xth XXXXXXXXX 20XX
First published on the web Xth XXXXXXXXXX 200X
DOI: 10.1039/b000000x

The novel surface mode of the Birmingham Cluster Genetic Algorithm (S-BCGA) is employed for the global optimisation of noble metal tetramers upon an MgO(100) substrate at the GGA-DFT level of theory. The effect of element identity and alloying in surface-bound neutral subnanometre clusters is determined by energetic comparison between all compositions of $Pd_nAg_{(4-n)}$ and $Pd_nPt_{(4-n)}$. While the binding strengths to the surface increase in the order $Pt > Pd > Ag$, the excess energy profiles suggest a preference for mixed clusters for both cases. The binding of CO is also modelled, showing that the adsorption site can be predicted solely by electrophilicity. Comparison to CO binding on a single metal atom shows a reversal of the 5σ-d activation process for clusters, weakening the cluster surface interaction on CO adsorption. Charge localisation determines homotop, CO binding and surface site preferences. The electronic behaviour, which is intermediate between molecular and metallic particles allows for tunable features in the subnanometre size range.

1 Introduction

Subnanometre noble metal clusters are currently attracting a great deal of attention from both experimental and theoretical communities, due to their interesting structural and electronic properties, which lie intermediate between atomic and nanoparticular systems. With structures often dominated in the gas phase by low dimensional motifs, such as rhombuses[1,2], squares[3] and y-shaped geometries[4,5], many systems display a complex size and composition dependence on structure[5–7]. Upon surfaces, geometry is additionally affected by the metal-on-top effect[8,9], in which polarisation of the electron distribution by additional metal layers strengthens the surface binding, such that unusual binding modes and charge distributions are common. These properties are of interest both to fundamental studies and reactive and catalytic applications. Heterogeneous catalysis upon subnanometre particles is an area of recent success, with several investigators finding not only impressive turnover frequencies, but surprising stability to repeated cycles and selectivity of reactions catalysed by clusters which have less utility at larger sizes, in particular, the metals Au[10–12], Ag[13], Pd[14–19] and Pt[20–23].

The binding of small molecule adsorbates is the mode by which subnanometre clusters perform their heterogeneous catalytic function and the preferred binding site of these molecules is controlled through particle geometry and electronic structure[24]. For example, the electrocatalytic activity of subnanometre palladium particles upon an oxide support is found to be controlled at the single Pd-Pd bond level, in which the role of the substrate and the geometry of the particle are both factors[15,25]. The binding of carbon monoxide (CO) has been well studied for small surface-bound clusters, both as a potentially disruptive influence[26,27], and in the catalysis of CO oxidation[18,21,28–31]. For CO chemisorption upon M_1 and M_2 (M = Pd, Pt, Ag, Au), Grönbeck and Broqvist found that reorganisation of the atom-CO electronic states allows for enhanced surface binding on CO adsorption[32,33], and thus that molecule adsorption and cluster mobility are closely linked.

MgO(100) is a well studied support for theoretical investigations of noble metal clusters, as it represents a stable, geometrically simple substrate which is largely chemically inert. Studies of defect binding[34–39], cluster growth[40,41] and cluster mobility[42–46] have been considered for noble metals M_N ($N \leq 4$) upon MgO(100), while the role of subnanometre cluster catalysis on MgO(100) has been extended to Au[29,30,47–50], Pd[25] and Pt[18].

Control of reactivity for such systems has been explored as a function of cluster size and surface defects, but less well studied are the mixed metal particles, in which both compo-

---

[a] *School of Chemistry, University of Birmingham, Edgbaston, Birmingham, UK. E-mail: cjh085@bham.ac.uk*
[b] *Department of Chemistry, University of California Berkeley, Berkeley, United States*
[c] *Materials Science Division, Argonne National Laboratory, 9700 South Cass Avenue, Argonne, Illinois 60439, United States*
[d] *Nanoscience and Technology Division, Argonne National Laboratory, 9700 South Cass Avenue, Argonne, IL 60439, USA*
[e] *Institute for Molecular Engineering, The University of Chicago, 5747 South Ellis Avenue, Chicago, IL, 60637, USA*
[f] *Department of Chemical and Environmental Engineering, School of Engineering & Applied Science, Yale University, 9 Hillhouse Avenue, New Haven, CT 06520, USA*

sition and chemical order provide additional tunable parameters for the design of particles with specific properties[51,52]. These mixed metal systems are difficult to produce experimentally, and work is currently ongoing to reliably generate them[53,54], which would represent a great advancement in the design of cluster-based catalysts. Theoretical studies of ultrasmall mixed noble metal clusters upon MgO[55–59] have found that control of composition may have a drastic effect on structure, and thus reactivity. Barcaro and colleagues showed that alloying Cu, Au and Pd with Ag on a double vacancy MgO substrate allowed for the selective recovery of electronic and geometric magic numbers, and control of the stability of the particle upon the surface.

Global optimisation (GO) is a computational means to determine low energy structural motifs, compositions and homotops of small catalytic clusters. Subsequent calculation of properties of interest, such as charge transfer, binding energies, mobility and adsorption energies may then be made, in order to support experimental studies. High accuracy calculations may also provide information on an atomic basis which may not be available to experimental analyses. For heterogeneous cluster systems, several studies have invoked a two-phase process, involving the subsequent deposition of low energy gas phase isomers upon substrates. This approach is adopted because of the computational expense of performing trend studies on systems which require large unit cells and numbers of atoms. This approximation breaks down when structures which are not stable in the gas phase are particularly low in energy upon the surface; i.e. the surface plays a large role in templating the cluster structure. Similarly, density functional reoptimisation of structures produced with empirical potentials is commonly applied to substrate-bound clusters, and remains the only practical method for large clusters[60]. Subnanometre clusters upon surfaces however, present a synergistic combination of quantum size effects which require electronic structure methods to reproduce, and sufficiently small particle sizes to allow for direct global optimisation. A few recent studies have considered direct DFT GO upon surfaces, such as the work of Fortunelli and coworkers, who used a surface basin hopping algorithm to determine the catalytic potential of Ag_xAu_{3-x} clusters upon MgO. Additionally, Vilhelmsen and Hammer have applied a genetic algorithm to the problem of Au_n (n = 6-12), upon F centers of MgO(100)[49].

In this paper, we introduce the newly developed surface Birmingham Cluster Genetic Algorithm (S-BCGA) to globally optimise neutral mixed tetrameric metal clusters upon an MgO (100) substrate. This work is presented as a case study of the role of metal identity, composition and permutational isomer on the energetic stability of supported ultrasmall noble metal clusters. Global optimisation and subsequent higher accuracy reminimisation is performed for the range of compositions of $Pd_nPt_{(4-n)}$ and $Pd_nAg_{(4-n)}$ over all potential spin states, as reported in sections 3.1 - 3.2. Comparison with the binding of a single atom upon MgO(100) allows for size dependent trends to be considered (section 3.3). The binding of catalytically relevant CO ligands is simulated in section 3.4, by attachment to all possible binding sites, with their subsequent energetic stabilities, geometries and underlying electronic structure analysed.

2 Computational details

Low energy cluster structures are generated by the BCGA within the framework of density functional theory, utilising the plane-wave PWscf code of Quantum Espresso (QE)[61]. Ultrasoft RRKJ-type pseudopotentials[62] are applied for all metallic species, carbon and oxygen, whereas a norm-conserving Vanderbilt pseudopotential[63] is used to treat magnesium atoms. The PBE exchange correlation functional, which has been used extensively in the treatment of small, mixed metal clusters, is employed. Within the primary screening of structures with the S-BCGA, necessarily relaxed convergence criteria are applied, with the plane wave basis expanded to an energy cutoff of 20.0 Ry, an electronic convergence criterion of 10^{-5} Ry, with a Methfessel-Paxton[64] smearing scheme applied to aid convergence for metallic states, and a smearing width of 0.03 Ry.

2.1 S-BCGA

For local geometry optimisation, the BFGS algorithm within QE is used, with clusters deemed to be locally converged when the difference between energies and total forces between successive structures drop below 10^{-4} Ry and 10^{-3} Ry a_0^{-1}, respectively. Standard selection methods and genetic operators are used within the S-BCGA, including mutate-exchange at a rate of 10% (one in ten clusters is selected randomly for replacement), single point Deaven-Ho cut and splice type crossover[65] for mating steps, and a roulette selection scheme for mating. These procedures are described in more detail in ref[66], and have been successfully employed for recent DFT-BCGA calculations[67,68]. The genetic algorithm is modified to allow for direct structure prediction upon a rigid surface by the inclusion of a multilayer substrate slab into the unit cell, repeated infinitely in a 3D supercell. Cluster structures are generated within a sphere truncated by the substrate, offset vertically by a minimum distance defined by an approximate metal-surface bond length to avoid repulsive overlap. Inclusion into the simulation cell of the surface allows for DFT bonding interactions during local optimisation, and may be relaxed for substrates which exhibit variation on deposition. In this study, a rigid, bilayer MgO (100) surface is used, with 64 atoms in total, ensuring a minimum distance of 6 $\AA$ between individual clusters over repeat unit cells of 11.7 × 11.7 × 29.25 $\AA$. Surface atoms are remained fixed during simulations, as it has been found in previous work that noble metal clusters of subnanometre size have an insignificant effect on the surface geometry of MgO(100), owing to the strong, highly symmetric bonding within the surface[25,32]. Two layers of MgO have been found to suffice for the recovery of accurate bond lengths, energies and electronics in several investigations at the GGA-DFT level[32,33,42,60]. Moments of inertia descriptors are employed to filter out repeated geometries from the population after the application of genetic operators. The small population size (ten individuals) currently limits the utility of additional operators, such as predation or increased mutation rates.

2.2 Reoptimisation of structure

The stagnation condition applies after five consecutive generations which contain an unchanged putative global minimum energy structure, and the entire population is subjected to GGA-DFT reminimisation with tighter convergence criteria. The plane wave basis is expanded to 50.0 Ry for all atoms, with a charge density cutoff of 500.0 Ry. The smearing parameter is reduced to 0.002 Ry, in order to more accurately reproduce metallic states. The self consistency convergence cutoff is reduced to 10^{-8} Ry. Spin restricted calculations are performed on all local minima after spin-free reminimisation, including all possible spin states for the cluster. This restriction allows for each platinum or palladium atom to contribute zero or two unpaired electrons (d^{10} or d^9s^1 electronic configurations) as both states are energetically competitive, and for silver to contribute one unpaired electron (with a $d^{10}s^1$ configuration). The binding of CO is modelled by the attachment of the adsorbate to each available binding site upon the global minimum cluster for each composition, and subsequent local minimisation with the same convergence criteria as the cluster. Spin states of the combined surface/cluster/molecule system are allowed to vary between the maximal value of the cluster without deposited CO, and the minimal value available to the surface/cluster complex. CO-induced quenching of the cluster's spin is therefore allowed.

2.3 Analysis

For single metal atom binding, an identical cell and computational procedure is applied to the DFT optimisation of bond lengths as for the cluster. Atoms are deposited over the two inequivalent atop sites, upon Mg and O, and locally relaxed. Spin restricted local minimisations are undertaken with the spin-free regime for all atom types, and additionally, the constrained doublet for silver and singlet and triplet for palladium and platinum. For CO binding upon single metal atoms, the molecule is bound atop the atom and in a mode parallel to the surface, and relaxed in the same manner as for the cluster. Calculation of the charge distribution of the system is undertaken by separating atomic sites into volumes of with the Bader method[69], using a regular mesh of 100×100×100 points, ensuring the recovery of all electron density to within a tolerance of 0.001 electrons. Electronic densities of states are calculated according to a projection scheme within a post processing module of QE. This projection is employed to calculate the enhancement and depletion of individual metal d orbitals on binding.

3 Results

3.1 Structure prediction

The structure of each composition of $Pd_nAg_{(4-n)}$ and $Pd_nPt_{(4-n)}$ upon a fixed bilayer substrate of MgO (100) is determined with the S-BCGA. Due to the small size of the clusters, and the reduced configuration space available on the fixed substrate, the algorithm only required between six and fifteen generations in total to reach convergence for each composition. This value is comparable to the gas phase DFT-BCGA investigations of coinage metals recently performed, which find global minima after 10-20 generations[68]. Pt and Pd clusters find the tetrahedral global minimum after eight and six generations, respectively, whereas the Ag tetramer required fifteen generations. This implies that the silver cluster exhibits a more complex energy landscape than the group 10 metals, which may be due either to a larger number of bound geometric states, or a narrower basin of attraction for the global minimum geometry, which is a metal-on-top (MOT) planar rhombic motif. The bimetallic clusters required more generations than the monometallics in the case of PdPt, due to the additional landscape complexity introduced by the existence of homotops (inequivalent permutational isomers). In the gas phase, the tetrahedral clusters have no homotops, but the addition of the surface breaks the threefold rotational symmetry and introduces the extra complexity. In the case of PdAg, the bimetallic optimisation is intermediate between that of Pd and Ag. This result implies that palladium atoms simplify the landscape, reducing the number of isomers available to the search.

The entire final generation of clusters after GA convergence are reminimised with tighter energetic, force and orbital smearing width parameters, in order to obtain tightly converged global minima structures. The resulting putative global minima for each composition are displayed in figure 1. There was significant reordering between minima on reoptimisation, suggesting that an accurate reminimisation is required to obtain energetic trends, and underlies the importance of a sufficiently large population size during the global structure search, to maximise coverage of the search space.

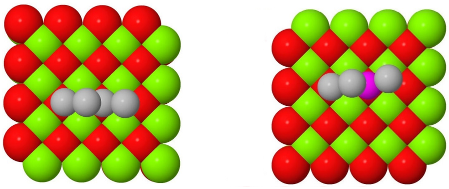
(a) Ag_4 **(b)** Ag_3Pd

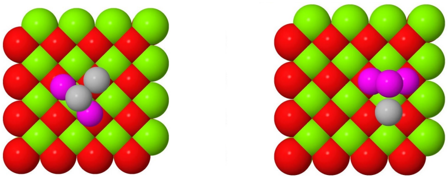
(c) Ag_2Pd_2 **(d)** $AgPd_3$

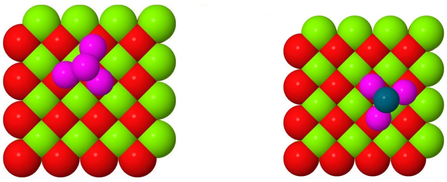
(e) Pd_4 **(f)** Pd_3Pt

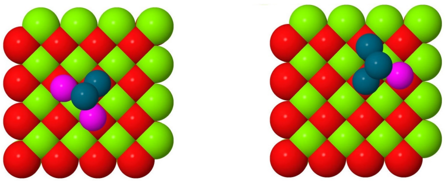
(g) Pd_2Pt_2 **(h)** $PdPt_3$

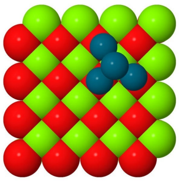
(i) Pt_4

Fig. 1 The structure of the lowest energy configuration for each composition of $Pd_nAg_{(4-n)}$ and $Pd_nPt_{(4-n)}$ clusters upon MgO (100) after local reoptimisation of the S-BCGA final generation.

The Ag_4 GM remains a MOT rhombic structure as suggested in previous work[42]. On replacement of silver with palladium atoms, there is a conversion from the rhombus to a tetrahedral geometry, which is known to be the GM for Pd_4 on MgO (100)[42,43]. This switch in preferred geometry occurs between Ag_3Pd_1 and Ag_2Pd_2, suggesting that palladium has a stronger effect on the energetics than silver, and is a result of the change of bonding from valence s orbitals to valence d orbitals as group 11 atoms are replaced with those from group 10. In addition, within the final generation of the BCGA calculation for Ag_2Pd_2, there were no MOT rhombic structures found. This result implies that palladium plays a great role in the control of available minima. There is a trend of preference for palladium rather than silver to bind to the surface oxygen atoms, as the binding of Pd to surface oxygen is stronger than that of Ag to the surface. There is an exception at Ag_1Pd_3. This cluster adopts a second tetrahedral motif, which differs from the first by a rotation upon the substrate, as noted by Fortunelli and Ferrando[42]. This rotated structure matches the lattice spacing of the surface less well, and forms weaker bonds to surface oxygen. For monometallic species, it is found to be higher in energy than the epitaxially strained tetrahedron for many cluster species. However, in the case of Ag_1Pd_3, the epitaxial form is found to be very slightly higher in energy, by 11 meV, so there is a near degeneracy between the rotational isomers. The isomer with all three palladium atoms bound to the surface is significantly higher in energy, the lowest energy rotamer of which is at +118 meV. This result displays the delicate balance between homo and hetero- metallic binding and binding to the surface.

The $Pd_nPt_{(4-n)}$ clusters all prefer tetrahedral geometries, with a clear trend for palladium to occupy surface-bound sites for all compositions, while adopting the epitaxial, pseudo-tetrahedral motif. This strained binding mode has been found in previous studies for Pd_4 and other tetrameric metal clusters upon MgO(100) and is due to the rigidity of the surface[25,42]. It is manifested as a stretching of one of the metal-metal bonds along the plane of the surface. This strain is more favourably taken by the palladium atom, as may be observed in the 1:1 composition clusters. For both Ag_2Pd_2 and Pd_2Pt_2, the GM is the permutational isomer which has palladium atoms in the strained sites, giving a Pd-Pd bond extension of 0.32 $\AA$ and 0.53 $\AA$ relative to the gas phase GGA tetrahedral bond length of 2.57 $\AA$. By analogy to the Ag_3Pd_1 cluster, the Pt_3Pd_1 isomer with the palladium atom in the apical position is 178 meV higher in energy than the GM, suggesting little competition between isomers for this cluster.

3.2 Spin states

For small transition metal clusters, there is strong evidence for magnetism, even for metals which exhibit no permanent magnetic dipole in the bulk[70,71]. In order to investigate the role of spin in the energetics and structures of the tetrameric clusters, we consider all possible spin states of each inequivalent local minimum resulting from the reminimisation of structures in the previous section.

The resulting spin-polarized minima are almost universally unchanged from the structures of the unpolarized clusters. In the majority of cases, the minima converge to the same geometry, although there are several cases in which the landscape of a particular spin state did not have a nearby local minimum, and thus did not converge at all. Of the 99 total reoptimizations, 69 retained their original geometry, while 16 failed to converge. The remaining 14 clusters predominantly converted to other structures found to be low-lying in the spin-unpolarized regime. New isomers were found for a small number of high energy, high spin clusters, including some planar and "butterfly" geometries. Those structures which were not present in the BCGA populations are shown in figure 2.

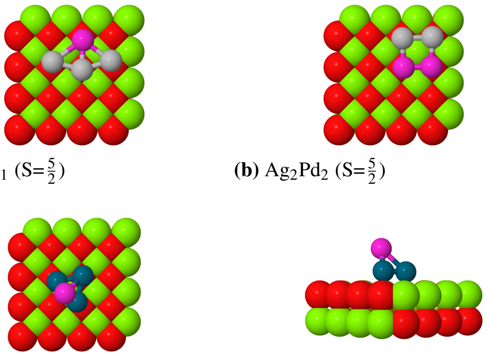
(a) Ag_3Pd_1 (S=$\frac{5}{2}$) **(b)** Ag_2Pd_2 (S=$\frac{5}{2}$)

(c) Ag_1Pd_3 (S=$\frac{5}{2}$) **(d)** Ag_1Pd_3 (S=$\frac{5}{2}$) side view

Fig. 2 The structures of minima found at high spin on reminimisation of S-BCGA clusters.

Those compositions which provided new structures are entirely within the $Ag_nPd_{(4-n)}$ class, suggesting that the PdPt clusters are more resilient to structural deviation for a wide range of spin states and over all compositions. For Ag_4, the tetrahedron, which is energetically unfavourable for the low-spin state, becomes the global minimum at high spin. All other structural deviations of $Ag_nPd_{(4-n)}$ correspond to a flattening of the cluster, in which all available palladium atoms bind directly to the surface.

For every composition, the structure of the spin unpolarized global minimum remains the lowest energy structure, whilst the overall trend of spin preference is that for all clusters containing silver, the lowest possible spin is most favourable. Therefore, for Ag_4 and Ag_2Pd_2, the lowest energy spin state is the singlet configuration, whereas for Ag_3Pd_1 and Ag_1Pd_3, a doublet is most stable. For all clusters which do not contain silver, the possible spin states are 0, 2, 4, 6 or 8 unpaired electrons. In every case, the optimal electronic configuration is the triplet state. For each of the $Pd_4Pt_{(4-n)}$ clusters, the diamagnetic configuration is approximately 250 meV higher in energy. The stability of the global minimum structures, as for the suboptimal minima decreases rapidly as a function of number of unpaired electrons. This is shown in figure 3, in which the energetic variation of the GM structure with number of unpaired electrons is displayed.

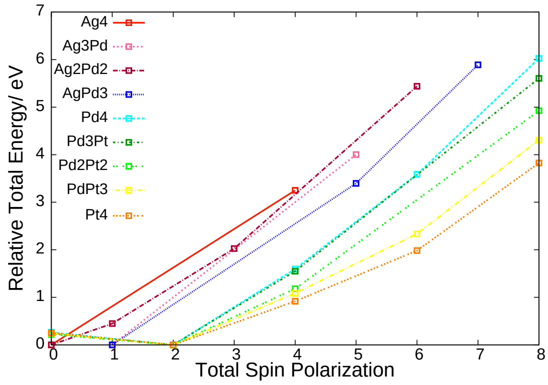

Fig. 3 Variation of energy for reminimised global minimum structures as a function of the number of unpaired electrons, for each composition of $Ag_nPd_{(4-n)}$ and $Pd_4Pt_{(4-n)}$.

The relative stabilities of GMs across the dopant series may be probed by considering the mixing energy $E^{\mathrm{surf}}_{\mathrm{mix}}$, which is defined as the total energy gain in combining two metallic species (A and B) into a bimetallic cluster, over the GM of the monometallic clusters of the same size when bound to the substrate. For a binary cluster of four atoms, this energy is given by equation 1

$$E^{\mathrm{surf}}_{\mathrm{mix}} = E\left(A_nB_{(4-n)}\right) - \frac{1}{4}\left(nE\left(A_4\right) - (4-n)E\left(B_4\right)\right) \qquad (1)$$

Figure 4 displays the mixing energy profiles for both series. For both clusters, all mixed compositions are more stable than the monometallic counterparts, suggesting a thermodynamic driving force towards disproportionation of the pure clusters and formation of mixed particles. For Ag_3Pd_1 and Ag_1Pd_3, the gain is approximately equal to the corresponding Pd_1Pt_3 and Pd_3Pt_1 results. For the 1:1 compositions, the AgPd cluster exhibits a significant energy gain of 0.46 eV over the pure clusters, and is a notably stronger effect than found in the corresponding 1:1 PdPt system. For PdPt, the mixing energy profile is more asymmetric, with a preference towards Pd_3Pt_1.

The energetics of binding the cluster to the surface are investigated by the binding energy $E^{\mathrm{surf}}_{\mathrm{b}}$, which is defined in equation 2 as the difference between the total energy of the optimised surface bound cluster E_{tot}, and the sum of the total energies of the surface E_{surf} and the cluster E_{clust} fixed at that geometry. This measure accounts for the effect solely of

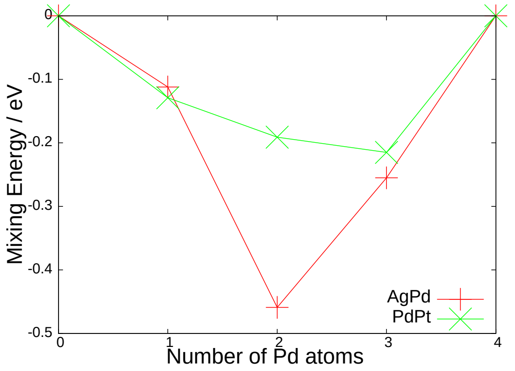

Fig. 4 Mixing energies ($E^{\mathrm{surf}}_{\mathrm{mix}}$) for each composition of $Ag_nPd_{(4-n)}$ and $Pt_nPd_{(4-n)}$ clusters upon MgO (100) after reminimisation.

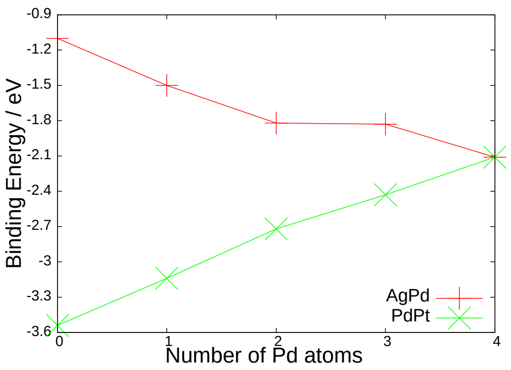

Fig. 5 Surface binding energies E^{surf}_{b} for each composition of $Ag_nPd_{(4-n)}$ and $Pd_nPt_{(4-n)}$.

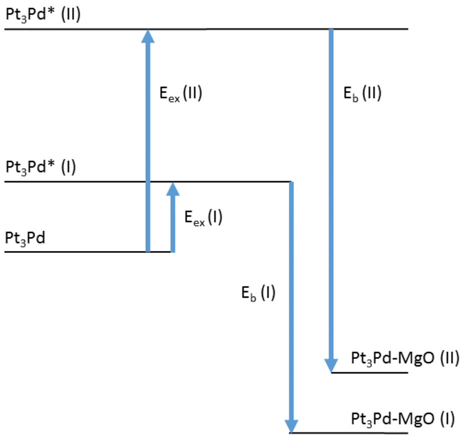

Fig. 6 The gas phase cluster is excited to one of two inequivalent isomers, with corresponding excitation energies. On deposition at the fixed geometry, the isomers relax (E_b) to their surface-bound minima. Isomer I has the smaller binding energy, but a lower overall energy when bound to the substrate.

binding the cluster, rather than the structural rearrangements which may occur on deposition.

$$E^{\mathrm{surf}}_{\mathrm{b}} = E_{\mathrm{tot}} - E_{\mathrm{surf}} - E_{\mathrm{clust}} \tag{2}$$

Figure 5 displays the variation of E_{b} with palladium content. It is notable that, despite the fact that palladium preferentially occupies surface-bound sites over platinum, the overall binding is weaker for more palladium-rich clusters of PdPt. An explanation for this is that the polarisability of palladium is greater than platinum. As displayed for an example of Pd_1Pt_3 in figure 6, the excitation energy (E_{ex}) to the distorted structure is lower for the isomer (I) which will have the palladium atom bound to the surface than isomer II. Therefore, though the binding energy E_b is larger for the platinum-bound case (II), the final energy of the bound state is lower for isomer I than isomer II. This trend is reversed for the AgPd clusters, due to the significantly weaker Ag-O binding. The variation for both cluster types is monotonic. For PdPt, the binding weakens by an average of 0.36 eV per palladium atom. An exception is found between Ag_2Pd_2 and Ag_1Pd_3, because the single silver atom in Ag_1Pd_3 occupies a surface bound position. Therefore, the surface-cluster interaction is between a Pd_2Ag_1 triangle and the substrate for both compositions.

3.3 Single atom binding

To identity the effects of three dimensional clustering on the binding and electronic properties of M_4 on MgO, we compare the results to the analogous single atom binding. Pt, Pd and Ag are bound and locally optimised upon the surface, giving binding energies (which are equivalent to adsorption energies) of 1.32, 1.08 and 0.49 eV, respectively, in agreement with previous GGA-DFT studies[32,33]. Platinum and palladium atoms bind in a similar manner and with similar strength, whilst silver, with an additional electron in the s orbital has a stronger repulsive overlap between the d orbitals and the filled 2p orbital in the oxygen to which it is bound. This repulsion drives the silver further from the surface, and weakens the covalent bond formed. Furthermore, the poorer ability for oxygen to rehybridise the d electrons to minimise Ag dz^2-O 2p repulsion (due to the full d band) contributes to the weaker binding. All metal atoms prefer the atop oxygen binding site. Comparing the bond lengths of M_1-O with the average M-O bond length of M_4 in table 1, it is noted that platinum bonds are shortened, palladium bonds are lengthened and silver bonds are virtually unchanged. This result implies that the strongest driving force for binding to the surface is found for platinum, and that silver, which has fewer bonds to the surface, and binds more weakly, does not exhibit any strong size dependent cooperative effects on clustering. Palladium-surface binding is weakened relative to the single atom, suggesting that increasing the size of the cluster may increase the mobility of the cluster, which has been predicted previously for Pd_n ($n < 5$)[42,43].

Cluster	M_1-O bond / $\AA$	M_4-O ave / $\AA$	Difference / $\AA$
Pt_n	2.28	2.21	-0.07
Pd_n	2.26	2.34	+0.08
Ag_n	2.43	2.43	+0.00

Table 1 Table of metal-surface oxygen bond lengths for M_1 and M_4

The charge distribution in clusters plays a major role in their catalytic activity and reactivity. Sites which may be engineered to attain large charge excesses are promising as individual binding sites of absorbates. By comparing the charge upon the atom and the cluster, we find that in both cases, the trend for all metals is for electron density to be transferred from the surface to the metal. Additionally, this charge transfer is found to be remarkably localised, with significant differences in total valence charge between adjacent surface atoms, and between adjacent cluster atoms. Furthermore, the trend is for more charge to be drawn by platinum than palladium, which is expected due to the slightly higher electronegativity of platinum. Silver induces very little charge redistribution, and so is unlikely to fulfill any reactive role involving electrophilic addition to the particle. Table 2 displays the valence charge accumulation for M_1 and the maximal and average per-atom charges on M_4. While the total charge upon the cluster is much greater than for the single atom, the per-atom charge gain is significantly lower. For adsorbates which bind in a highly localised manner, this suggests that on an electronic basis, the tetramers are poorer binding sites than single atoms. For larger adsorbates, or those which bind in a chelating mode, this electron deficiency will be overcome, due to the larger total excess charge.

	Charge /e		
Cluster	M_1 total	M_4 maximum	M_4 average
Pt_n	-0.35	-0.27	-0.21
Pd_n	-0.21	-0.17	-0.13
Ag_n	-0.11	-0.09	-0.07

Table 2 Charge accumulation on surface binding for the single deposited atom (M_1) and the tetrameric cluster (M_4)

Due to the asymmetry of the surface binding site, there is an asymmetric charge distribution across atomic sites on the cluster. For Pd_4 and Pt_4, the atop site accumulates charge which is intermediate between the two inequivalent surface atom locations (0.20 and 0.14 e^- for Pt and Pd respectively). Of the surface-bound sites, the pair of equivalent atoms along the strained epitaxial bond accrue the maximum charge (0.27 and 0.16 e^-), whilst the second location attains very little charge (0.09 and 0.06 e^-). This distribution implies that for small electrophilic adsorbates, there will be a preference for a surface-bound atom as the binding site.

Varying the composition and chemical order of a mixed metal particle will further break the symmetry of the charge distributions. The per-atom charges are calculated for each composition of $Ag_nPd_{(4-n)}$ and $Pd_nPt_{(4-n)}$. It is found that platinum atoms drain charge from palladium atoms, whereas silver has little effect on the distribution. The most striking synergistic effect on alloying is found for Pd_3Pt_1, in which the platinum occupies the atop site. The platinum atom in this case gains a charge of 0.34 electrons, which is the largest single site transfer of all M_4 compositions, and is approximately equivalent to the single platinum atom charge. The palladium atoms effectively play the role of a charge buffer, which presents the platinum atom with a base of high charge density to which it is bound in a μ_3 arrangement. This composition is additionally the most stable according to the mixing energy, and thus presents a cooperativity between electronic and energetic factors, which would be beneficial for cluster design.

3.4 CO adsorption

3.4.1 M_4COA carbon monoxide molecule is bound to the global minimum structure of each of the compositions, allowing for binding at each cluster atom site, aligned either radially or along a metal-metal bond. Spin restricted local minimisation at the spin state of the lowest energy metal cluster and all lower spin states is performed. The structures of the resultant putative GM M_4CO clusters are shown in figure 8.

The preferred binding mode is radially outward from the cluster, in agreement with previous studies of CO upon late transition metal clusters[18,29]. In addition, the molecule binds preferentially to the surface-bound metal atom for tetrahedral clusters, as evidenced most clearly by CO on Pd_4 and CO on Pt_4, which, as monometallic clusters, cannot exhibit mixing effects. This surface/cluster binding site is more sterically hindered than the atop site, and agrees with the result of the previous section. This hindered binding has been found to reduce the overall stability where the metal-CO bond is highly directional, as in the case of Au on MgO[50]. In the case of silver-rich clusters, which do not adopt the tetrahedral geometry, the CO binds to the metal-on-top site. For Ag_3Pd_1, the global minimum of the cluster has the palladium atom at the interface. However, the binding of CO induces a change in global stability, in which the permutational isomer with palladium directly bound to the CO molecule at site 1 (on fig 8) becomes lower in energy by 0.68 eV. The adsorption of a molecule therefore creates a thermodynamic driving force to rearrange the cluster, which has previously been observed both for O_2 on gold clusters[49] and O_2 on Pd clusters[15]. The overall trend is for the CO ligands to bind to platinum in preference to palladium, and to palladium in preference to silver. In the case of Pd_3Pt_1, the strength of the preference for platinum binding is enough to cause CO to bind to the unfavourable apical site.

To investigate the energetics, we consider the adsorption energy of CO to the cluster, as defined by the equation:

$$E_{\text{ad-CO}} = E_{\text{Clust+CO}} - E_{\text{CO}} - E_{\text{Clust}} \qquad (3)$$

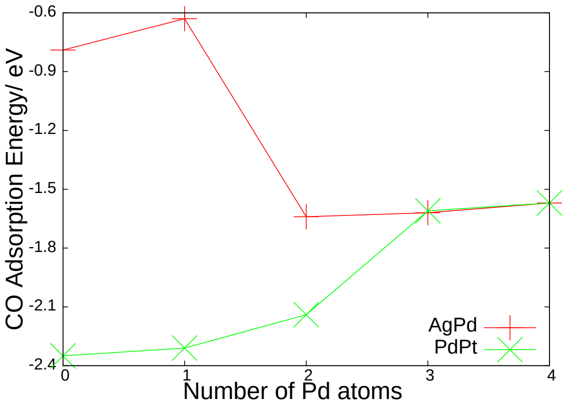

Fig. 7 Adsorption energy of CO binding to the global minima of $Ag_nPd_{(4-n)}$ and $Pd_nPt_{(4-n)}$.

This is an adsorption energy as the system is locally minimised before and after deposition of CO, and therefore accounts for all energetic contributions to the final state including cluster rearrangement. For the PdPt clusters the trend is that the CO adsorption increases in strength the more platinum atoms are present. The binding of the CO molecule is always to a single atomic site, but the decreasing asorption strength on replacing Pd with Pt for the non-bound atoms suggests a non-local, cooperative effect from the cluster. Pd_3Pt_1 exhibits an reduced adsorption energy due to the unfavourable atop site. For AgPd, there is a negligible change between Ag_2Pd_2 and Pd_4, suggesting that the replacement of silver with palladium has little effect on the energetics. For Ag_3Pd_1, as previously noted, the binding to silver is especially unstable, and may drive a rearrangement to the isomer with direct Pd-CO bonding.

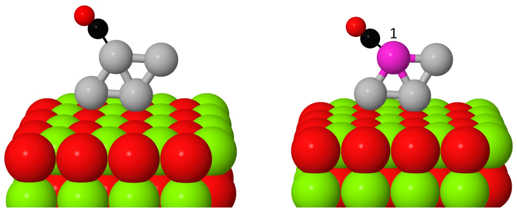

(a) Ag4 **(b)** Ag_3Pd

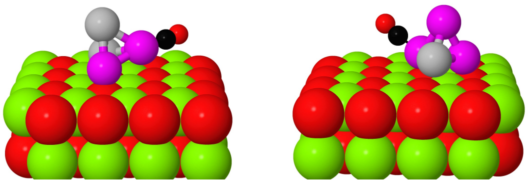

(c) Ag_2Pd_2 **(d)** $AgPd_3$

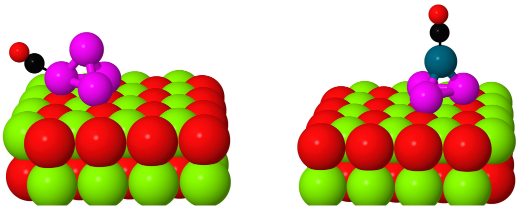

(e) Pd_4 **(f)** Pd_3Pt

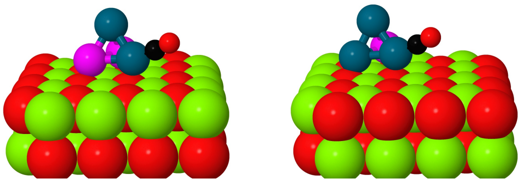

(g) Pd_2Pt_2 **(h)** $PdPt_3$

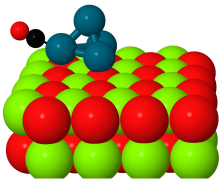

(i) Pt_4

Fig. 8 Putative global minima of $Ag_nPd_{(4-n)}CO$ and $Pd_nPt_{(4-n)}CO$ on MgO(100). Carbon atoms are displayed in black.

3.4.2 Comparison with M_1CO The role of clustering on the binding of CO is determined by comparison of the various bond lengths as a function of cluster size and metal identity. It was observed by Broqvist and Grönbeck that the binding of CO to single atoms of Pt, Pd, Ag and Au shortened, and thus strengthened the metal-oxygen bond[32]. This result was explained by the preorganisation of the metal d orbital involved in surface binding, by the insertion of electron density into the metal d band by the CO 5σ orbital. Equation 4 defines the distance parameter r_N as the difference between the M-O bond length for the bare and CO-bound cluster for cluster size N. Values for Pt, Pd and Ag are given in table 3, showing that this result is reproduced for M_1 for all metal identities.

$$\Delta r_N = r_{M_N CO} - r_{M_N} \tag{4}$$

The trend observed by Broqvist and Grönbeck is not however observed for the M_4 clusters. For each element, the average M-O bond length is virtually unchanged on binding CO, suggesting that there is a size dependent trend on the electronics of surface deposited M-CO systems. By defining the size difference:

$$\Delta r^X_{4\rightarrow 1} = r^X_{M_4 CO} - r^X_{M_1 CO} \tag{5}$$

we can directly compare the effect of size on the bond length variation on CO adsorption for any bond X present in both sizes of cluster. Table 3 contains values for the M-O, M-C and C-O bonds. We observe that there is little size dependence on the metal carbon bond or the carbon-oxygen bond. This implies that the change in bonding between metal atom and surface is due to a difference in the electron distribution in metal orbitals due to CO binding. Furthermore, the difference between metals is striking. $\Delta r^{MO}_{4\rightarrow 1}$ for platinum is considerably greater than for palladium and silver. Pt is therefore more senstive to size changes, and is destabilised upon the surface by CO more than Pd or Ag.

Cluster	Δr_1	Δr_4	$\Delta r^{MO}_{4\rightarrow 1}$	$\Delta r^{MC}_{4\rightarrow 1}$	$\Delta r^{CO}_{4\rightarrow 1}$
Pt_n	-0.19	+0.02	+0.21	+0.01	+0.01
Pd_n	-0.04	-0.02	+0.10	-0.05	-0.01
Ag_n	-0.09	-0.03	+0.11	-0.06	-0.02

Table 3 Bond length variations of M-C, M-O and C-O bonds, for M_1, M_4 on binding CO.

To probe the electronic structure, projected densities of states are calculated for the d electrons of the cluster atoms to which CO is bound. In the M_1-CO system, the metal atom d band is known to be electron-rich due to the CO(5σ)-M(d) interaction. The depletion of the d orbitals involved in the M-O bond due to surface binding is counteracted by the polarisation of the same orbitals on binding CO. This refilling of the d charge is however not observed in the case of M_4CO. The integral of the pDOS shows a further reduction in the total electron density on binding CO, and additionally, that this depletion is localised predominantly into one orbital on one atom. This is the orbital which is involved in backbonding to the vacant CO π^* orbital. Table 4 displays the total d band electron depletion for M_4 and M_4CO for all metal atoms, showing that in all cases the surface binding depletes the d orbitals, and that CO binding depletes them further, in a manner that is localised primarily on a single atom.

Atom	Pt_4	Pt_4CO	Pd_4	Pd_4CO	Ag_4	Ag_4CO
1	0.05	0.05	0.04	0.04	**0.02**	**0.05**
2	0.15	0.15	0.11	0.12	0.01	0.01
3	**0.15**	**0.27**	0.12	0.12	0.04	0.04
4	0.13	0.15	**0.12**	**0.21**	0.03	0.03
Total	0.48	0.62	0.39	0.49	0.10	0.13

Table 4 Metal d-band electron density loss by atom. Totals show loss on binding to the surface, which is exascerbated by CO binding. The atom bound directly to CO is highlighted in bold font.

4 Discussion

The comparison between E_{mix} and E_{b} shows a competition between energetic contributions, in which a binding energy argument suggests both that the pure platinum cluster is most favourable upon deposition, and that in a mixed cluster, the platinum atoms would likely occupy surface binding sites. However, the global optimisation and mixing energies imply that bimetallic compositions are most stable, and that generally, palladium preferentially binds to the surface. The mixing energy result shows that binding energy is insufficient to describe the likely compositions, even on purely thermodynamic grounds, as it only considers the role of the surface in local stability, and cannot predict disproportionation. Additionally, the binding energy as defined in equation 2 only considers the direct role of surface binding. The energetic contribution of including cluster-surface bonds is represented, but the overall effect of deposition, which includes the rearrangement of cluster structure on binding, is not included. The result that Pt has greater binding energies than Pd is a reflection of the greater energetic penalty of distorting platinum bonds. Palladium atoms are more easily redistributed, and Pd bonds more easily polarised, as evidenced by the preference for palladium atoms to occupy the extended "epitaxial" sites when bound to the surface. Therefore, clusters which contain platinum bonds gain more stability on binding to the surface when the gas phase structure is preorganised.

The locality of the bonding is noted in each section of this work, and plays a significant role in the control of composition and homotop preference, charge distributions and adsorption of CO. The clusters are small enough to be considered to be in the molecular size range, before metallic band structure is developed. As a result, the valence electron density is confined predominantly upon atomic sites, and varies significantly from atom to atom. This in turn affects the single atom binding which we observe for all CO adsorbates. Additionally, the effect on the charge distribution is noted from the calculation of per-atom Bader charges. Asymmetries in the surface have a large effect on the degree of charge transfer to atoms, which is retained on individual sites. This localisation both affects the surface, depleting charge from indivdual oxygen atoms, and more importantly, the charge excess built up on the cluster. The calculation of excess charge on a site by site basis is a good descriptor of the likely binding site of the CO. The trend that the most electron-rich cluster atom binds the CO molecule even extends to generally unfavourable sites, such as the apical Pt site in tetrahedral Pd_3Pt_1. This localised bonding has a drastic effect on the electronic structure of the valence orbitals, as observed in two ways. Firstly, through the marked effect on the d orbitals in the metal to which CO is bound, as compared to the case where the CO is unbound. Secondly, on the notable difference in the pDOS of adjacent atoms of the same element in the CO bound cluster. The degree of locality appears to vary between the metals, as noted in the trend of E_{ad-CO}, in which the palladium content of the PdPt cluster affects the adsorption energy of CO, despite the molecule binding to Pt. However, this is likely to be a charge based result, as the doping of Pd into Pt reduces the total charge abstracted from the surface, reducing the binding strength to CO. That this is primarily a charge effect is supported by the invarience of E_{ad-CO} to silver doping in AgPd, as silver has a negligible effect on charge distributions, and draws very little charge from the surface. That the binding to the surface and to asorbates is predominantly a charge controlled occurence, and the electronic effects occur on a single atom, implies an atomistic description of the charge, orbitals and structure is required to understand the preferences in subnanometre noble metal clusters. Furthermore, the necessarily small unit cells required at present for the S-BCGA are justified by this locality, and care is needed to ensure, for scenarios in which the charge distribution controls binding but is more spatially dispersed, that the cell is sufficiently large for future S-BCGA global optimisation strategies.

The binding of small adsorbates determines the applicability of a cluster as a reactive species. We observe that the adsorption of CO is favourable and may be controlled according to the element present, the homotop and the charge transfer, and thus such subnanometre particles may be tuned finely to present specific desired reactivity. The stability is another feature which must be considered, and is a particularly acute issue for very small particles, which will more easily migrate upon a surface and sinter. The binding energies observed between cluster and surface are relatively strong, but the destabilisation effect of the adsorbate will likely reduce the particle stability. It was noted in previous work on subnanometre palladium clusters that the oxidation of tetrameric clusters upon oxide supports induces a change in dimensionality to planar structures, and further, that without Pd-Pd bonds spatially removed from the surface, a catalytic response was not observed[15]. Hence, control of both dimensionality and the location of M-M bonds is sought for rational particle design. It is observed through the localised charging effects on tetramers that small adsorbates may bind more weakly than upon single atoms, however, a thorough screening of potential reactive adsorbates is required to determine for which systems this weaker binding is preferable. Furthermore, the existence of highly charged separate sites upon the cluster which are in close proximity to one another may well promote cooperative reactions between multiple adsorbates, or provide more appropriate binding sites for chelating molecules. As a result, subnanometre particles, which exist in a size range where charge transfer occurs in a discrete, molecular manner, but binding to the surface and adsorbate molecules is similar to the metallic state, may present a unique class for specific heterogenous reactions.

5 Concluding Remarks

The S-BCGA has been successfully employed to the global optimisation of a series of noble metal tetramer clusters upon an oxide support. The structures found show clear doping trends, in which palladium preferenctially binds to the surface of the substrate, and promotes tetrahedral clusters which abstract significant charge from the oxygen atoms of the surface. Direct charge transfer is noted for both Pd and Pt atoms, whereas Ag binds more weakly and draws negligible charge. The localised nature of the excess charge upon the cluster controls the preferred binding sites of CO, which may be predicted by charge analysis of the static cluster structure. CO molecules bind preferentially to Pt, and have a destabilising effect on the cluster-surface interaction, which may enhance the mobility of the cluster, at variance with the known result for single metal atoms on MgO. The 5σ-d donation which preorganises the metal to surface binding is not observed, while electron depletion is noted both from surface-binding and CO-binding d electrons in the cluster atom. Synergistic energetic/electronic effects are observed which may prove useful in the rational design of reactive, surface deposited subnanometre particles. These particles will constitute a new class of reactive species with electronic properties intermediate between metals and atoms, which are tunable for particular reactions and can also represent single site catalysts[72,73].

Work is currently being planned to extend this work to other metals and adsorbates, in order to screen for preferential binding and ultimately to design particles to catalyse specific reactions, in order to support experimental studies on mixed subnanometre particle catalysis. The application of the S-BCGA to irregular surfaces which rearrange upon adsorption, and for

This journal is © The Royal Society of Chemistry [year]

pure surface studies is ongoing, along with the use of dispersion corrections for direct molecule-surface binding.

6 Acknowledgments

The authors acknowledge the following HPC facilities: The MidPlus Regional Centre of Excellence for Computational Science, Engineering and Mathematics, funded under EPSRC Grant No. EP/K000128/1, the University of Birmingham BlueBEAR facility. Use of the Center for Nanoscale Materials was supported by the U.S. Department of Energy, Office of Science, Office of Basic Energy Sciences, under Contract DE-AC02-06CH11357. C.J.H acknowledges the School of Chemistry, University of Birmingham and EPSRC for Ph.D funding. SV acknowledges the support by the U.S. Department of Energy, BES-Materials Sciences, under Contract No. DE-AC-02-06CH11357, with UChicago Argonne, LLC, the operator of Argonne National Laboratory.

References

1 Pacchioni G. and Rösch N., *J. Chem. Phys.*, 1996, **104**, 7329.
2 Inntam C., Moskaleva L.V., Yudanov I.V., Neyman K.M. and Rösch N., *Chem. Phys. Lett.*, 2006, **417**, 515–520.
3 Yudanov I.V., Vent S., Neyman K., Pacchioni G. and Rösch N., *Chem. Phys. Lett.*, 1997, **275**, 245–252.
4 Shayeghi A., Johnston R.L. and Schäfer R., *Phys. Chem. Chem. Phys.*, 2013, **15**, 19715–19723.
5 Weis P., Welz O., Vollmer E. and Kappes M.M., *J. Chem. Phys.*, 2004, **120**, 677.
6 Negishi Y., Nakamura Y., Nakajima A. and Kaya K., *J. Chem. Phys.*, 2001, **115**, 3657.
7 Bonacić-Koutecký V., Burda J., Mitrić R., Ge M. Zampella G. and Fantucci P., *J. Chem. Phys.*, 2002, **117**, 3120.
8 Atanazov I., Barcaro G., Negreiros F., Fortunelli A. and Johnston R.L., *J. Chem. Phys.*, 2013, **138**, 224703.
9 Barcaro G. and Fortunelli A., *J. Chem. Theory. Comput.*, 2005, **1**, 971–985.
10 Oliver-Meseguer J., Cbrero-Antonio J. R., Dominguez I., Leyba-Perez A. and Corma A., *Science*, 2012, **338**, 1452–1455.
11 Lee S., Molina L.M., López M. J., Alonso J. A., Hammer B., Lee B., Seifert S., Winans R. E., Elam J. W., Pellin M. J. and Vajda S., *Angew. Chem. Int. Ed.*, 2009, **48**, 1467–1471.
12 Lee S., Fan C., Wu T. and Anderson S. L., *J. Chem. Phys.*, 2005, **123**, 124710.
13 Lei Y., Mehmood F., Lee S., Greeley B., Lee S., Seifert S., Winans R.E., Elam J.W., Meyer R.J., Redfern P.C., Teschner D., Shlögl R., Pellin M.J., Curtiss L.A. and Vajda S., *Science*, 2010, 224–228.
14 Habibpour V., Yin C.R., Kwon G., Vajda S. and Palmer R.E., *J. Exp. Nanosci.*, 2013, **8**, 993–1003.
15 Kwon G., Ferguson G. A., Heard C. J., Tyo E. C., Yin C., DeBartolo J., Soenke S., Winans R. R. E., Kropf A. J. and Greely J. P. *et al.*, *ACS Nano*, 2013, **7**, 5808–5817.
16 Mehmood F., Greeley J. and Curtiss L.A., *J. Phys. Chem. C.*, 2009, **113**, 21789–21796.
17 Lee S., Lee B., Mehmood F., Seifert S., Libera J.A., Elam J.W., Greeley J., Zapol P, Curtiss L.A., Pellin M.J., Stair P.C., Winans R.E. and Vajda S., *J. Phys. Chem. C.*, 2010, **114**, 10342–10348.
18 Moseler M., Walter M., Yoon B., Landman U., Habibpour V., Harding C., Kunz S. and Heiz U.
19 W. E. Kaden, Kunkel W. A., Roberts F. S., Kane M. and Anderson S. L., *J. Chem. Phys.*, 2012, **136**, 204705.
20 Vajda S., Pellin M. J., Greeley J. P., Marshall C. L., Curtiss L. A., Ballentine G. A., Elam J. W., Catillon-Mucherie S., Redfern P. C., Mehmood F. and Zapol P., *Nature Mat.*, 2009, **8**, 213–216.
21 Heiz U., Sanchez A., Abbet S. and Schneider W.D., *J. Am. Chem. Soc.*, 1999, **121**, 3214–3217.
22 Watanabe Y., Wu X., Hirata H. and Isomura N., *Catal. Sci. Technol.*, 2011, **1**, 1490–1495.
23 Bonanni S., Aït-Mansour K., Harbich W. and Brune H., *J. Am. Chem. Soc.*, 2012, **134**, 3445–3450.
24 Uzio D. and Berhault G., *Cat. Rev. - Sci. Eng.*, 2010, **52**, 106–131.
25 Heard C.J., Vajda S. and Johnston R.L., *J. Phys. Chem. C.*, 2014, **118**, 3581–3589.
26 West P., Johnston R.L., Barcaro G. and Fortunelli A., *J. Phys. Chem. C.*, 2010, **114**, 19678–19686.
27 Paz-Borbón L.O., Johnston R.L., Barcaro G. and Fortunelli A., *Eur. Phys. J. D.*, 2009, **52**, 131–134.
28 Neyman K.M., Rösch N. and Pacchioni G., *Appl. Cat. A.: Gen.*, 2000, **191**, 3–13.
29 Yoon B., Häkkinen H., Landman U., Wörz A.S., Antonietti J-M. Abbet S., Judai K. and Heiz U., *Science*, 2005, **307**, 403–407.
30 Zhang C., Yoon B. and Landman U., *J. Am. Chem. Soc.*, 2007, **129**, 2228–2229.
31 Del Vitto A., Giordano L. and Pacchioni G., *J. Phys. Chem. B.*, 2005, **109**, 3416–3422.
32 Grönbeck H. and Broqvist P., *J. Phys. Chem. B.*, 2003, **107**, 12239–12243.
33 Grönbeck H. and Broqvist P., *J. Chem. Phys.*, 2003, **119**, 3896–3904.
34 Matveev A.V., Neyman K.M., Yudanov I.B. and Rösch N., *Surf. Sci.*, 1999, **426**, 123–139.
35 Yudanov I., Pacchioni G., Neyman K. and Rösch N., *J. Phys. Chem. B.*, 1997, **101**, 2786–2792.
36 Bogicevic A. and Jennison D.R., *Surf. Sci. Lett.*, 1999, **437**, L741–L747.
37 Nasluzov V.A., Rivanenkov V.V., Gordienko A.B., Neyman K.M, Birkenheuer U. and Rösch N., *J. Chem. Phys.*, 2001, **115**, 8157–8171.
38 Giordano L., Di Valentin C., Pacchioni G. and Goniakowski J., *Chem. Phys.*, 2005, **309**, 41–47.
39 Giordano L. and Pacchioni G., *Surf. Sci.*, 2005, **575**, 197–209.
40 Paz-Borbón L.O., Barcaro G., Fortunelli A. and Levchenko S.V., *Phys. Rev. B.*, 2012, **85**, 155409.
41 Musolino V., Dal Corso A. and Selloni A., *Phys. Rev. Lett.*, 1999, **83**, 2761.
42 Ferrando R. and Fortunelli A., *J. Phys.:Condens. Matter*, 2009, **21**, 264001.
43 Xi L., Henkelman G., Campbell C.T. and Jónsson H., *Surf. Sci.*, 2006, **600**, 1351–1362.
44 Barcaro G., Fortunelli A., Nita F. and Ferrando R., *Phys. Rev. Lett.*, 2005, **95**, 246103.
45 Barcaro G. and Fortunelli A., *New. J. Phys.*, 2007, **9**, 1–17.
46 Musolino V., Selloni A. and Car R., *Phys. Rev. Lett.*, 1999, **83**, 3242.
47 Sanchez A., Abbet S., Heiz U., Scheider W.D., Häkkinen H., Barnett R.N. and Landman U., *J. Phys. Chem. A.*, 1999, **103**, 9573–9578.
48 Häkkinen H., Abbet S., Sanchez A., Heiz U. and Landman U., *Angew. Chem. Int. Ed.*, 2003, **42**, 1297–1300.
49 Vilhelmsen L.B. and Hammer B.
50 Molina L.M. and Hammer B., *Appl. Catal. A.*, 2005, **291**, 21–31.
51 Ferrando R., Jellinek J. and Johnston R.L., *Chem. Rev.*, 2008, **108**, 845–.
52 deHeer W., *Rev. Mod. Phys.*, 1993, **65**, 611–.
53 Bouwen W., Thoen P., Vanhoutte F., Bouckaert S., Bespa F., Weidele H., Silverans R. E. and Lievens P., *Rev. Sci. Instrum*, 2000, 54–58.

54 Y. H., *Eur. Phys. J. D.*, 2011, **63**, 195–200.

55 Negreiros F.R., Sementa L., Barcaro G., Vajda S., Aprá E. and Fortunelli A., *ACD Catal.*, 2012, **2**, 1860–1864.

56 Negreiros F.R., Barcaro G., Kuntová Z., Rossi G, Ferrando R. and Fortunelli A., *Surf. Sci.*, 2011, **605**, 483–488.

57 Ferrando R., Rossi G., Levi A.C., Kuntová Z., Nita F., Jelea A., Mottet C., Barcaro G., Fortunelli A. and Goniakowski J., *J. Chem. Phys.*, 2009, **130**, 174702.

58 Goniakowski J., Jelea A., Mottet C., Barcaro G., Fortunelli A., Kuntová Z., Nita F., Levi A.C., Rossi G. and Ferrando R., *J. Chem. Phys.*, 2009, **130**, 174703.

59 Barcaro G. and Fortunelli A., *Faraday Discuss*, 2007, **138**, 37–47.

60 Ismail R., Ferrando R. and Johnston R. L., *J. Phys. Chem. C.*, 2012, **117**, 293–301.

61 Giannozzi P., Baroni S., Bonini N., Calandra M., Car R., Cavazzoni C., Ceresoli D., Chiarotti G. L., Concoccioni M. and Dabo I. *et al.*, *J. Phys.: Condens. Matter*, 2009, **21**, 395502.

62 Rappe A. M., Rabe K. M., Kaxiras E. and Joannopoulos J. D., *Phys. Rev. B.*, 1990, **41**, 1227–1230.

63 Vanderbilt D., *Phys. Rev. B.*, 1985, **32**, 8412–8415.

64 Methfessel M. and Paxton A. T., *Phys. Rev. B.*, 1989, **40**, 3616–3621.

65 Deaven D. M. and Ho K. M., *Phys. Rev. Lett.*, 1995, **75**, 288–291.

66 Johnston R. L., *Dalton Trans.*, 2003, **22**, 4193–4207.

67 Heard C.J. and Johnston R.L., *Eur. Phys. J. D.*, 2013, **65**, 1–6.

68 Heiles S., Logsdail A.J., Schäfer R. and Johnston R.L., *Nanoscale*, 2012, **4**, 1109–1115.

69 Tang W., Sanville E. and Henkelman G., *J. Phys.: Condens. Matter*, 2009, **21**, 084204.

70 Knickelbein M. B., *Phys. Rev. Lett.*, 2001, **86**, 5255–5257.

71 Cox A. J., Louderback J. G. and Bloomfield L. A., *Phys. Rev. Lett.*, 1993, **71**, 923–926.

72 Thomas J. M., *J. Chem. Phys.*, 2008, **128**, 182502.

73 Thomas J. M., Johnson B. F. G., Raja R., Sankar G. and Midgley P. A., *Acc. Chem. Res.*, 2003, **36**, 20–30.

This journal is © The Royal Society of Chemistry [year]

Chapter 10

Dibenzylideneacetone-ligated subnanometre palladium clusters

10.1 Introduction

Palladium clusters are known to make good catalysts for oxidative reactions, such as the oxidation of carbon monoxide [215] and methanol combustion [216], and as such have been researched from the nanoparticle scale down to the subnanometre and atomic size ranges. On the nanoscale, alloying with other metals, such as gold and silver [209, 217, 218, 219], and control of faceting [220] have been applied to enhance and tune the reactivity of particles towards selective, high efficiency reactions. At the subnanometre scale, recent work has been performed with atomic resolution, both experimentally and theoretically to probe the effects of size, oxidation state and mixing with other noble metals on an atom-by-atom basis [221]. The resulting tuned clusters are found to show excellent efficacy for electrocatalysis applications.

Palladium is a well established catalyst for a range of bond activation reactions, and in particular, traditional cross coupling processes, such as Suzuki [87, 222, 223], Hiyama [224, 102, 103] and Negishi [225, 106, 105] reactions. Palladium atoms are often employed in a homogeneous, solvent-phase form, in which Pd(0) is delivered to the reaction scheme via labile organic ligands, such as acetoxy (OAc) or dibenzylideneacetone (dba) precursors, and replaced *in situ* with reactive ligands, such as two electron donor nitrogen or phosphine ligands, which are then involved in the catalytic application. Nanoparticular palladium has been found to catalyse similar reactions to the mononuclear, homogeneous species, and has been utilised extensively for Heck [88, 226] and Suzuki [86, 89] reactions in the colloidal phase. Colloidal Pd nanoparticles have been employed successfully both for electrophilic addition between phenols and alkynes [90], and in chiral catalysis, in the asymmetric hydrosilation of styrene with 2,2'-bis(diphenylphosphino)-1,1'-binaphthyl (BINAP)-bound Pd particles [91]. However, the intermediate size range characterised by subnanometre clusters is poorly understood and underemployed in catalysis. There is evidence both for the growth of clusters, through aggregation of atoms during the course of reactions, and the existence of nanoparticles in the precursors from which palladium is sourced. This issue is exascerbated by the conditions generally required to achieve a catalytic effect, such as the use of high concentrations of the palladium precursor, which promotes aggregation. As a result, clusters from a few atoms to a size of around 100 nm are known to be prevalent in this important class of reactions. Furthermore, the likely new chemical properties of these clusters have not extensively been acknowledged or investigated. It is, given the analogous situation in heterogeneous catalysis upon surfaces, highly likely, that the undercoordination, and unusual structures of clusters will provide new routes to selective reactivity, which will be tunable by size. Given these clusters are certain to contaminate catalytic reactions, it is important to understand what structures, stabilities and reactions these clusters constitute in experiment. In addition to the lack of recognition either for the presence or chemical role of subnanometre palladium clusters, the physical properties, such as growth dynamics, local stability and binding strength to ligands and other metal atoms require analysis.

The common, commercially available palladium(0) precursor $Pd_2(dba)_3$ is considered an archetype of such a complex catalytic reaction, and is known to exist in several forms, either with mononuclear palladium $Pd_1(dba)_3$ [227, 228], $Pd_2(dba)_2.(dba)$ and $Pd_2(dba)_2.x$ [229], where x is a solvent molecule which plays a distinct role in the conformational freedom of the ligand. In the gas phase, experiments are currently ongoing to provide a fundamental understanding of the structural, conformational and binding properties both of the ligands to the clusters, and the clusters themselves, which have been produced for the under-ligated species $\mathrm{Pd}_n(\mathrm{dba})_2$ ($n < 9$). In this work, we support the ongoing experimental studies, modelling the gas phase structures of a range of cluster sizes, conformers of single ligands and ligand dimers (dba_1 and $(\mathrm{dba})_2$), in order to underpin the energetics and preferences of this important class of catalytic Pd precursor complexes.

10.2 Publication draft

Authors Christopher J. Heard, Ian J. S. Fairlamb and Roy L. Johnston

Title Dibenzylideneacetone-ligated subnanometre palladium clusters

Dibenzylideneacetone-ligated subnanometre palladium clusters

Christopher J Heard,*[a] **Ian Fairlamb** [b] **and Roy L. Johnston**[a]

Received Xth XXXXXXXXXX 20XX, Accepted Xth XXXXXXXXX 20XX
First published on the web Xth XXXXXXXXXX 200X
DOI: 10.1039/b000000x

The structures and energetics of subnanometre palladium clusters bound to dibenzylideneactone (dba) ligands are investigated with density functional theory. Clusters Pd_n ($n < 9$) are bound to single dba molecules and a sandwich complex of $(dba)_2$, in order to probe the effect of cluster-induced structure deformation and ligand-induced templating of clusters for an important organometallic catalytic system. The effect of ligand upon the cluster is profound, driving energetic trends in direct opposition to those of gas phase clusters, which in turn will affect catalytic mechanisms. Intercalation of Pd_n is found to be strongly favourable in the subnanometre size range, suggesting no clear limit to cluster growth within the dba complex, which is always preferred to the isolated cluster+dba_2. Protonation is examined as a means to affect stability and geometry, showing little impact, due to the localisation of electron density in Pd-(alkene)C bonds, which is controlled by metal-induced disruption of the dba π system. The energy landscapes of the bare ligand and ligand dimer are mapped, finding a hierarchical structure of deep kinetic traps between energetically low-lying isomers.

1 Introduction

Palladium based catalysis in the homogeneous phase is an important area of research for a wide range of application, in particular, for cross coupling and bond activation reactions[1]. In general, Pd precursors for catalysis involving Pd(0)→(II)→Pd(0) cycles are thought to employ Pd in a homogeneous manner, delivering single Pd(0) atoms bound to labile ligands, such as $Pd(OAc)_2$, to the reaction. However, it is known that with the high Pd loading required for many catalytic reactions, metal aggregation is a common result, either due to the mechanism of the reaction itself, or diffusion through the solvent medium. These nanoparticles are often non-innocent[2], and the utility of Pd nanoparticles in Suzuki[3,4] and Heck[5,6] cross coupling reactions, for example, is well established. This is unsurprising, given the known efficacy of bare and protected Pd nanoparticles in catalysis[7–12], but is often of concern, as uncontrolled side-reactions may also be catalysed. The presence of clustering under the conditions for C-H bond activation reactions is less well understood, but is known to occur in common precursors for such reactions. Zalesskiy and Ananikov[13] recently noted that up to 40% of $Pd_2(dba)_3$, a commercially available source of catalytic Pd(0), was found to contain Pd nanoparticles over an immense size range of 10-100 nm. They note that the true state of the particles during their experimental application will have drastic effects on their catalytic activity, and the mode by which they react. The belief in atomic Pd(0) as the active species in the catalytic activity of this complex is thereby challenged.

Intermediate between nanoparticles and atoms is the subnanometre cluster regime, which represents the bridging size region between homogeneous catalysis at atomic sites and heterogeneous catalysis at surfaces. Such clusters are often found to have chemical and physical properties which are notably different from atoms or surfaces and thus are likely to constitute a new reactive regime. Late group noble metal clusters have displayed prominent catalytic utility in recent studies with gold[14], silver[15], platinum[16] and palladium[9,17] all presenting remarkable turnover frequency and number. The structure and binding energies of metal clusters are most variable in the subnanometre size range, and thus size control may provide a tunable feature for catalyst design. The structures of ligand-bound clusters are expected to play a role in their reactivity, by controlling both the sterics of the reactive site and the binding energies. It has been shown that for C-H bond activation processes, many reactions are controlled most acutely by the strength of the Pd-C bond, which is in turn determined by the structure of the cluster. Despite this, little is yet known about the growth and stability of ligand-bound clusters, nor their ability to provide new selectivity, efficiency or mechanisms for reactions.

Tris(dibenzylideneacetone)dipalladium(0) ($Pd_2(dba)_3$) is a common Pd(0) precursor, used for a wide range of reactions, including Suzuki[18–20], Negishi[21–23] and Hiyama[24–26] cross coupling and C-C transformations in allenes[27–29] and alkynes[30–32]. Its relative ease of production and good stability make it an attractive reactant and as such a great deal of research has been performed to elucidate accurate structures and

---

† Electronic Supplementary Information (ESI) available:

[a] *School of Chemistry, University of Birmingham, Edgbaston, Birmingham, UK E-mail: cjh085@bham.ac.uk*
[b] *Department of Chemistry, University of York, Heslington, York, UK*

tune the stability and properties. Takayashi[33] suggested a dinuclear complex of Pd(dba)$_2$ in 1970, on the basis of IR spectroscopy. Later work[34] showed the actual species to likely be of the form Pd$_2$(dba)$_2$.(dba), which follows the solvent crystallisation results that Pd$_2$(dba)$_2$.x, where x = dichloromethane or chloroform, may be produced. Pd$_1$(dba)$_3$ has also been observed[35,36]. X-ray studies have been performed on solid state Pd$_2$(dba)$_3$, in order to probe the Pd-Pd bonding and the preferred conformations of (dba) molecules[34,35,37,38], which may exist in an s-cis,cis, s-cis,trans or s-trans,trans forms. It was found that different solvents lead to difference preferences for conformers, suggesting a complex interplay in the energetics of metal-bound (dba) complexes. The structural behaviour in the solvent phase, however, is more complex. Studies involving in situ ^{1}H NMR and isotopic labelling[13,39,40] have been employed to resolve the issue. Recently, Kapdi and coworkers used a multiple isotopic labelling, ^{1}H NMR, single crystal X-ray structure and DFT calculation approach to determine the accurate structures of Pd$_2$(dba-Z)$_3$, where Z is a range of electron withdrawing/donating groups (OMe, t-Bu, H, F, CF$_3$) known to affect the reactive properties of the catalyst[41]. Regarding the growth of metal nuclearity in these systems, Mingos and Vilar[42] considered Pd clustering resulting from reaction of Pd$_2$(dba)$_3$ with CFCl$_3$ and PBu$^t_3$, in which dimeric and tetrameric Pd cluster complexes are formed which have impact on the catalysis of the hydrogenation of CFCs to HFCs. Gas phase, partially ligated clusters Pd$_{(3-8)}$(dba)$_2$H$^+$ have been produced and examined with MALDI-TOF analysis[43]. The structural and energetic behaviour of these undercoordinated ultrasmall clusters are currently unknown, and are likely to constitute a novel class of (dba)-based palladium catalysts towards oxidative addition reactions. Overall, these complexes show great complexity in metal-metal binding, cluster growth, ligand conformer, oligomer and substituent, and solvent effects. If these features are understood and rationalised in terms of the environment and energetic propeties, they will allow the design of improved catalysts from a popular class of complexes.

In this paper, we consider the effect of ligand binding on the preferential binding modes, geometries and energetics of ultrasmall palladium clusters, and reciprocally, the effect that cluster binding has upon the ligand. In section 3.1, the energy landscape of the bare ligand and dimer system is explored, in order to generate low lying geometries for electronic structure calculations, and to isolate thermodynamic properties of the dba system, such as activation energies, and kinetic trapping. In section 3.2, palladium clusters Pd$_n$ are bound to the dba monomer, followed by the dimeric system, for $n < 5$. Protonation of the ligand is considered in sections 3.3 and 3.4, and compared to the neutral species. Larger clusters ($5 \leq n \leq 8$) are treated in section 3.4, in order to investigate the energetics of cluster growth. The aim is to provide high accuracy structural data to support gas phase, partially ligated Pd$_n$(dba)$_m$ complexes for catalytic applications in the near future.

2 Computational Details

A variety of computational techniques are employed for both predicting energetically low-lying structures, and mapping the energy landscape for rearrangements between geometric isomers. Density functional theory (DFT) is used, in order to balance accuracy and computational cost, and is employed in sections 3.2-3.4 for all Pd$_n$(dba)$_m$ interactions. For unbiased structure prediction of gas phase initial cluster structures, the Birmingham Cluster Genetic Algorithm (BCGA)[44] is employed, at the DFT level of theory[45]. For considering the thermodynamic basis of kinetic behaviour, such as energetic barriers to cis-trans isomerisation, a less expensive model is adopted. In this case, AMBER09[46] forcefields are employed with the GMIN[47] and OPTIM[48] basin-hopping and transition state sampling codes to treat ligand energetics.

2.1 Forcefield thermodynamics

We employ a standard organic forcefield approach with AMBER09 and perform molecular dynamics simulations coupled with global optimisation and transition state sampling. The dba ligand is generated from the structure of DFT output, and AMBER09 input is then produced using the Generalised Amber Forcefield (GAFF) which creates an appropriate potential energy function. Global optimisation of the dba structure is performed with the GMIN basin hopping code, using short MD simulation steps with an implicit solvent model, allowing unrestricted molecular translation and free rotations about the two C-C alkene bonds in the ligand backbone as moveclasses. Basin hopping efficiently locates low lying and globally optimal structures by taking steps in configurational space with local minimisation after every move. This removes kinetic barriers to rearrangements, and speeds up exploration of the energy landscape. Energy landscape mapping is performed with the OPTIM code, which takes databases of local minima from basin hopping simulations, and attempts double-ended nudged elastic band searches between pairs of minima. By converging to transition states (ts) along the pathway between pairs, min-ts-min triplets are generated. As the database of minima and transition states grows, more efficient pathways are found. This method is useful for not only producing the transition states along reaction coordinates, but determining minimum energy paths between pairs of minima (activation energies).

2.2 DFT

For many-body systems on the nanoscale, DFT can be well parameterised and is extensively utilised for modelling binding events and structural parameters, such as bond lengths, dissociation energies and conformational preferences. For organic systems, additional factors, such as non-bonding, σ-π and π-π interactions, and the wide range of hybridisation states of carbon and heteroatoms must be considered. We therefore screen a number of common basis sets and exchange-correlation (xc) functionals against known bond lengths and previous DFT calculations for the dba monomer. Calculations for ligand and ligand-metal interactions are performed within the NWCHEM v6.1.1 atomic orbital based DFT[49]. Several basis sets are tested initially for the dba monomer: 6-31G+P, LANL2DZ, aug-cc-PTVZ, cc-pVTZ-DK and def2-TZVPP. With these bases, the xc-functionals B3LYP[50], PBE[51] and M06-L[52] are employed. B3LYP is selected due to its popularity for organic systems, while PBE is commonly used for metallic systems. M06-L is a local version of the Minnesota class of meta-GGAs, which is found to treat the non-covalent interactions between transition metals and organic ligands well[53]. Combinations of basis sets and xc-functional are judged by phenyl, alkene and C=O bond lengths, planarity of the ligand and resilience of calculation to initial structure. The best compromise of these factors is found for the LANL2DZ basis with the MO6-L xc-functional. These are used for all successive ligand and ligand-cluster calculations with DFT.

2.3 BCGA

The BCGA is used to calculate the global minima of free Pd$_n$ clusters ($n < 9$) in the gas phase. For this calculation, standard GA operators are used, as found in ref[44]. These parameters include the mutation type (cluster replacement), mutation rate (10%) and crossover type (two-point weighted crossover). Each population contains ten individuals, with an elitist method applied, which retains the best clusters in each successive generation. The GA search is considered to have converged when the lowest energy cluster is unchanged for five consecutive generations. PBE xc-functionals combined with ultrasoft RRKJ[54] pseudopotentials with ten explicit electrons per atom are used to define the plane-wave wavefunctions within the pw-SCF framework of the Quantum Espresso DFT package[55]. Energy calculation and local geometry optimisation is performed within this package, with convergence criteria of 10^{-4} Ry and 10^{-3} Ry/a$_0$ respectively. Electronic convergence is aided by use of the Methfessel-Paxton[56] smearing of electronic states with a smearing width of 0.03 Ry.

3 Results

3.1 Forcefield Energy Landscape

Using an accurate DFT structure for the dba monomer, GAFF parameterisation of the potential is performed, from which basin hopping+MD global optimisation of both the dba monomer and dimer are carried out, in order to determine the library of energetically low-lying local minima, optimal rotation angles and intra-dimer association distances. Metal binding is possible with such forcefields, but does not take into account polarization of charge distributions or bond-induced changes in metallic oxidation state. Therefore, the bare ligand(s) are treated here.

For the dba monomer, sixteen non-equivalent isomers are found to be low in energy (within around 25 kcal mol^{-1} of the global minimum). At higher energies, to which more exotic structures belong, the forcefield is unlikely to remain sufficiently accurate, and thus the results are discarded. Displayed in figure 1 are the lowest nine structures, which clearly show a preference for extended, planar motifs. The global minimum structure, at -16.17 kcal mol^{-1} is the planar s-cis,cis (cc) isomer, followed by the s-cis,trans (ct) isomer at -14.62 kcal mol^{-1}, The third lowest energy structure is the s-trans,trans (tt) isomer at -10.13 kcal/mol. The competition between the lowest two isomers is close, and thus it is likely both will be present in a major isomer/minor isomer mixture, which is observed experimentally. These structures and relative energies are in general agreement with the DFT structures at the LANL2DZ/M06-L level, and the energetic gap between the lowest three, and the next lowest minimum is great enough that we justify using only the three lowest energy structures in the DFT local minimisations in section 33.2. Higher energy geometries include twisted helical subunits (isomers VII and IX), and often contain π-π stacking of the phenyl rings.

In addition to the structures and total energies, we calculate the potential energy barriers to rearrangement between pairs of minima, and build a representation of the connectivity of the energy landscape. The barriers between the low lying structures are calculated and displayed in the disconnectivity graph in figure 2, in which nodes represent the energies of local minima, and branches between nodes represent the lowest energy transition state which connects the pair.

The landscape has a hierarchical structure, in which the minima are grouped into local regions which are interchangeable with relatively low activation barriers, but are separated from other regions by much higher barriers. This result implies a significant degree of kinetic trapping between isomers, such that relaxation to low energy geometries will be difficult from higher-lying structures. In the case of dba$_1$, this frustration proves beneficial, as the isolation of the group containing the lowest three motifs allows for ergodic sampling of the subset of configuration space which minimises the total energy, and will constrain the molecule to such low-lying motifs. For the global minimum group, the three isomers are interconverted by a single transition state, which corresponds to a concerted half-rotation of both alkene bonds, with phenyl rings brought to an angle of 90° with the ketone plane. From this state, half rotations of either bond lead to one of the three minima. That the lowest transition state to interconvert any pair of the three minima is the concerted twist of both alkene bonds, rather than a single rotation for each pair suggests a remarkable cooperativity in the rotational dynamics of dba. The supplemental information contains the pathway of this rearrangement and the ts structure.

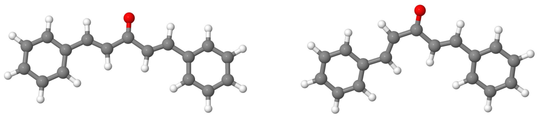

(a) Global minimum I (cc) **(b)** II (ct)

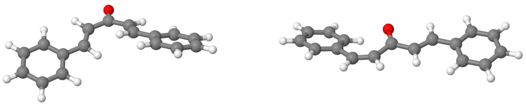

(c) III (tt) **(d)** IV

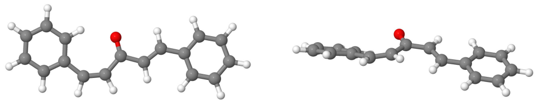

(e) V **(f)** VI

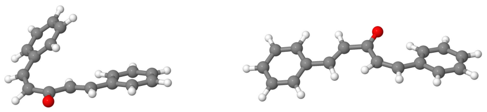

(g) VII **(h)** VIII

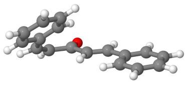

(i) IX

Fig. 1 The lowest lying isomers of the dba monomer from global optimisaiton. The minima are labelled by increasing energy from I to IX.

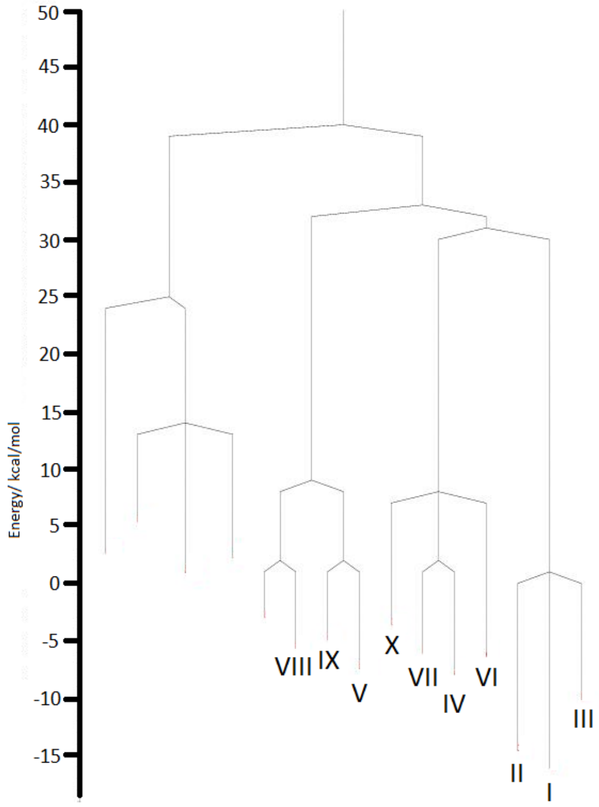

Fig. 2 Disconnectivity graph of the dba monomer, with the minima from figure 1 labelled by increasing energy.

Applying the global optimisation scheme to the dimer shows a greatly increased number of local minima due to the broken symmetry introduced by the presence of a second molecule. In the simulation, dynamical moves allow the monomers to self assemble/disassemble, generating a wide range of low lying structures, which for a given conformer may include parallel and antiparallel motifs, colinearity or assembly at an angle, and slipped or stacked pairs. The lowest nine minima are displayed in figure 3, in which the structures are dominated by planar, colinear sandwich complexes. The molecules retain planarity and lie above one another at a spacing of around 3.5 $\AA$ in each case. The dimers are almost always slipped, which maximises alkene-aryl π stacking. In addition, there is a preference for aligned (parallel) over anti-aligned (anti-parallel) dimers. Considering the conformers, the s-cis,cis-s-cis,cis (cc-cc) pair are the most stable at -40.19 kcal mol^{-1} , with the aligned pair lower than the anti-aligned pair by 0.39 kcal mol^{-1}. The next most favourable motifs are the s-cis,cis-s-cis,trans conformation, (cc-ct) followed by the s-cis,trans-s,cis-trans (ct-ct) conformers. The first dimer containing a tt motif is the s-trans,trans-s-cis,cis (tt-ct) pair at -34.09 kcal/mol. Therefore, the trend of conformer preference

This journal is © The Royal Society of Chemistry [year]

found for the monomer is repeated for the dimer, and is summarized in table 1, which displays the total and relative energy of the lowest found incidence of each confromer pair.

Figure 4 displays a disconnectivity graph of the lowest 100 distinct minima for the dba dimer. By focusing on the low energy minima the landscape is simplified, although the barrier structure between minima is considerably more complex than for the monomer. The rapid growth of landscape complexity with system size suggests many more structures must be considered for a truly exhaustive investigation of possible structures in experiment. However, the high activation barriers between structural motifs suggest frustrated kinetics which will be dominated by low-lying minima, as in the case of the monomer.

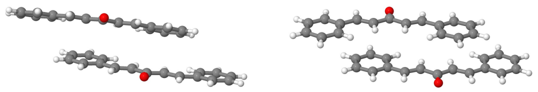

(a) Global minimum I (cc) **(b)** II (ct)

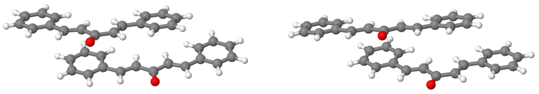

(c) III (tt) **(d)** IV

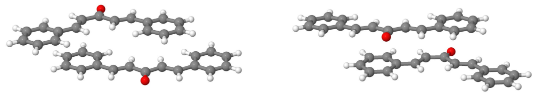

(e) V **(f)** VI

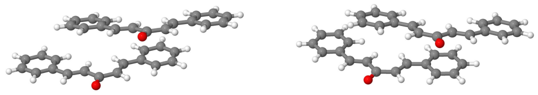

(g) VII **(h)** VIII

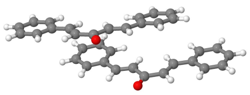

(i) IX

Fig. 3 The lowest lying isomers of the dba dimer from global optimisation. The minima are labelled by increasing energy from I to IX.

Conformer	Energy/kcal mol^{-1}	E_{rel}/kcal mol^{-1}
cc-cc	-40.19	0.00
cc-ct	-38.62	1.57
ct-ct	-37.15	3.04
cc-tt	-34.09	6.10
ct-tt	-32.55	7.64
tt-tt	-28.32	11.87

Table 1 Relative energies of various conformer pairs in $(dba)_2$.

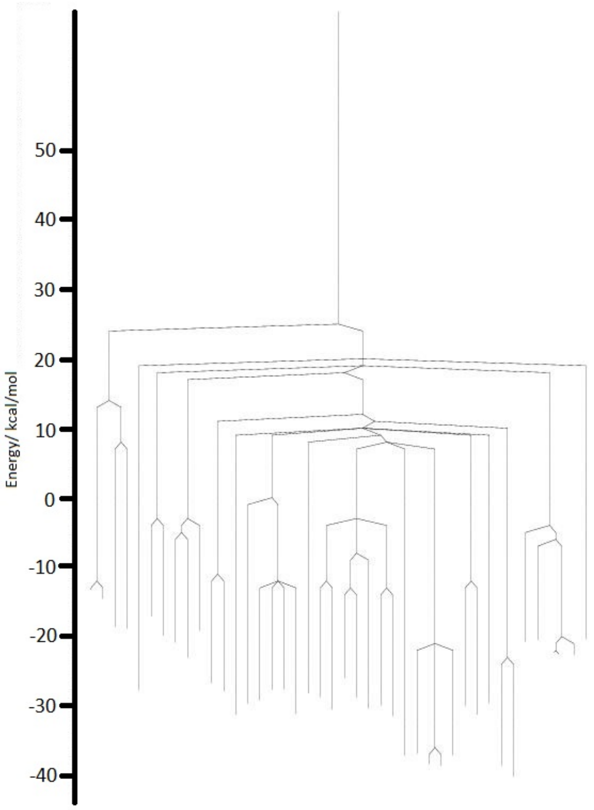

Fig. 4 Disconnectivity graph of the dba dimer.

3.2 $Pd_n(dba)_1$

Local minimisation of ligand structure is performed with LANL2DZ-M06-L-DFT for the monomer, using the low energy structures found at the forcefield level as initial geometries. The cc and ct isomers are found to be almost degenerate in total energy (to within 21 meV, which is within the range of uncertainty in our energetic calculations). The third isomer, tt, is significantly higher in energy, at +250 meV, again suggesting two dominant isomers, in agreement with the results of previous theoretical studies. This result broadly agrees with that of Tanaka (1974), who found total energies within 120 meV for cc and ct, with tt +8 eV from room temperature NMR experiments, which implies the trends remain on inclusion of temperature and solvent. Other structures for the monomer are possible, but are expected to be significantly higher in energy.

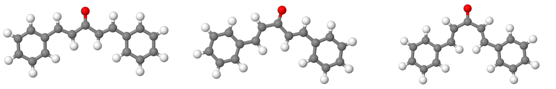

Fig. 5 Conformational isomers cc, ct, tt of dba calculated with DFT.

For the bare metal clusters, the DFT global minima are found with the BCGA. The clusters' structures are well characterised in the literature, and form compact geometries for all sizes. The trimer forms a triangular structure, which is lower in energy than the linear motif. For Pd_4, the local minima are well spaced in energy, with the tetrahedron the global minimum, a rhombic form at +54 meV, the y-shape higher in energy, at +136 meV and a linear geometry at +204 meV. This is in agreement with the expected result that palladium forms 3D structures at the smallest possible size, with an energetic ordering which simply follows the number of Pd-Pd bonds. The energetic trend with dimensionality is therefore 3D $<$ 2D $<$ 1D.

In order to determine the preferential binding modes and positions of palladium clusters to dba, we attach Pd_n, ($n < 5$) to a single neutral ligand over a range of positions, binding distances and cluster structures, followed by local geometry optimisation. The putative global minima are displayed in figure 6.

Pd_1 preferentially binds to the alkene bond in a μ_2 bridging manner. Many of the initial structures migrate on local minimisation to the bridging site by barrierless transitions, showing that there are few local minima for this composition. Minima exist bound into the π system of the alkene ring, and to the C-C bond adjacent to the ketone group. The first suboptimal minimum is 150 meV higher in energy than the alkene-bound geometry, suggesting a strong driving force for Pd-C(alkene) bonding, which is known experimentally for $Pd_2(dba)_3$.

Pd_2 binds as a dimer over the alkene sites. The Pd-Pd bond is strained, extending from the gas phase dimer bond length of 2.59, to 2.81 Å , in order to maximise overlap with both of the alkene sites. The dimer is oriented asymmetrically, binding in a μ_2 and μ_3 fashion at the two sites. The metal-on-top effect, known to play a significant role in the energetics of noble metal surface binding, is not found to compete with the direct alkene-Pd bonding, and thus there are no energetically low lying perpendicular Pd_2 motifs.

Pd_3 exhibits a competition between linear and triangular motifs, and is the first size at which there may be several structures containing Pd-Pd bonds. The global minimum for $Pd_3(dba)$ is the linear structure, which maximises Pd-C bonds, to the detriment of Pd-Pd bonds (with a difference of 109 meV between lowest lying minima). This size provides evidence that the formation energy of Pd-C(alkene) bonds is enough to disrupt the Pd-Pd network.

Pd_4 is the first isomer for which there is a competition between 2D and 3D isomers. The tetrahedron is the preferred geometry over the rhombic, y-shape and linear clusters in the gas phase, and the trend is maintained for the dba-bound cluster. The rhombus is the first sub-optimal cluster at +0.6 eV with the linear form higher still. The preferred arrangement of the Pd_4 tetrahedron contains Pd-C bonds to alkene and phenyl carbons, and a bond to the ketone oxygen. Therefore, in the case of Pd_4, the drive towards Pd-C bonding is not sufficient to reduce the cluster dimensionality, with the GM the same as for the gas phase. This is likely due to frustration. The rhombic cluster provides no additional Pd-C bonds over the tetrahedron, due to the shape of the dba molecule, and the linear cluster contains two palladium atoms bound only to phenyl carbons, rather than alkene carbons, therefore, the tetrahedron with the additional Pd-Pd bonds is preferred. The competition between 3D, 2D and 1D cluster structures is finely balanced. In all cases, the cc isomer is found to bind most strongly to the Pd_n clusters, suggesting that the clusters have some templating effect, raising the energy of the ct conformer relative to cc, breaking the near degeneracy found for the bare ligand.

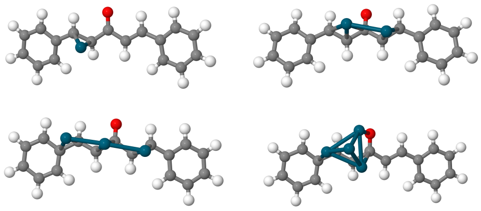

Fig. 6 Putative global minima of $Pd_n(dba)_1$.

3.3 $Pd_{(1-4)}(dba)_2$

To represent the situation in which palladium atoms are bound within sandwich complexes of several ligands, as predicted by experiment, a prototypical dba sandwich complex system is constructed, in which the dba dimer is intercalated by metal atoms. Initial geometries of the ligands are provided by the local minima of the monomer calculations, producing cc-cc, cc-ct and ct-ct pairs. The tt structures, being considerably higher in energy are not considered. Global optimisation of the DFT structures of $(dba)_2$ or $Pd_n(dba)_2$ is unfeasible, so a restricted set of initial structures is used. Ligands are aligned parallel or anti-parallel, with the three available isomer pairings, and for Pd_{1-3}, in which 3D geometries are not available, a spacing of

5 Å is used for initial geometries, while for ($n > 3$) a range of initial ligand separations (6, 7 and 8 Å) are applied, and the effect of spacing on final energies considered. For Pd_{1-4}, a range of palladium cluster structures are used, in order to find the global minimum for the sandwich complex.

For the smallest particles (Pd_1, Pd_2 and Pd_3), the structures of the clusters associated with $(dba)_2$ follow the same trends found for the $Pd_n(dba)$ results, where atoms bind over the electron rich alkene bonds, and form Pd-Pd bonds in a linear fashion. There is no energetic basis for the cleavage of the Pd-Pd bond in Pd_2, so the strained dimer remains the lowest energy motif, and for Pd_3, the linear form becomes increasingly favourable, as the number of Pd-C bonds lost on formation of a triangular structure is increased for dba_2 relative to dba. The aligned cc-cc conformation is always preferred, due to the preferable alignment for palladium atoms above alkene sites. These results agree with those in the literature for the $Pd_2(dba)_3$ system, in which the Pd is considered essentially as separate atoms bound to the alkene. This behaviour appears to hold for the palladium monomer, dimer and trimer. The Pd atoms bound within the ligand complex force a separation of the dba molecules to an average of 5 Å , which is significantly greater than found for the ligand dimer in the absence of palladium. Thus, the dba-dba binding is broken on insertion of Pd, and the gain in binding energy between metal and alkene carbons overcomes this loss of dispersive binding for all cluster sizes. The structure of the dba ligands is not significantly altered by the presence of metal atoms, despite the disruption of the conjugated π system on localising additional bonds at the alkene site.

For Pd_4, all four gas phase local minima are considered, along with two ligand alignments, three dba dimer conformers and several ligand spacings. The structures of the putative global minima are displayed in figure 8 and the relative energetics are given in the supplementary information. The linear structure is preferred over all other geometries, as it is the lowest minimum for all conformers and alignments for which it relaxes succefully to a local minimum, with the single exception of anti-aligned ct-ct. Therefore the linear form bound into the cc-cc conformer with a spacing of around 5 Å is the putative global minimum. The rhombic and y-shape minima are the next lowest energy forms, ranging from +0.51 to +1.28 eV above the GM. It is of note that the tetrahedron is always considerably higher in energy than any of the planar structures, ranging from +1.45 to +2.76 eV. It appears very unlikely the tetrahedron will be found within the dba dimer, due to the requirement to either substantially rearrange the ligand or the cluster to maximise bonding. This energetic penalty causes a reversal of the gas phase cluster structural trend, such that upon binding to dba_2, 1D < 2D < 3D.

There is experimental evidence for a stable monoprotonated state of $Pd_n(dba)_m$. This charging is likely to play a role in the reactive properties of palladium as a catalyst, and potentially the final structures of clusters and the binding energies to the ligands. By repeating the local optimisation and energetic analysis of the previous section for $Pd_4(dba)_2$ with a singly protonated ketone upon one of the ligand molecules, it is observed that the protonation has a remarkably insignificant effect on the ligand structure. Some clusters reminimise to distorted geometries, such that the rhombic motifs often undergo a barrierless rearrangement to more open structures. However, the binary sandwich complexes remain stable, and the energetic ordering of the clusters still show a preference for the linear motif, over the two dimensional structures, with tetrahedral clusters at +2.24 to +2.48 eV. Structures and energetics for each conformer, cluster structure and alignment for $Pd_4(dba)_2$ are provided in the supplementary information.

The charge distribution is probed with Bader analysis for $Pd_4(dba)_2$. For the neutral system, the valence electrons of the aryl carbon and hydrogen atoms are unaffected, as the electron density is shared across the π systems through conjugation. The same is true of the alkene carbon atoms. The

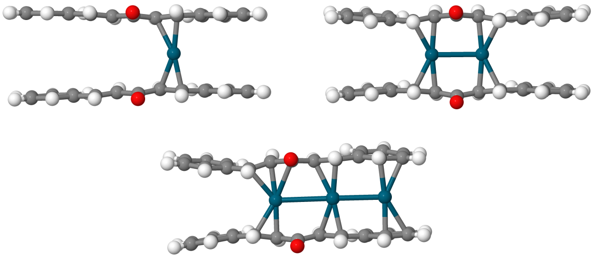

Fig. 7 The lowest lying examples of each Pd_n geometry, n = 1, 2, 3, bound within neutral dba_2.

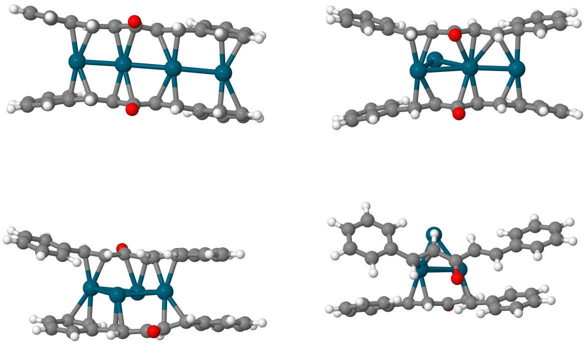

Fig. 8 The lowest lying examples of each Pd_4 geometry, bound within neutral dba_2.

ketone oxygen atom draws approximately 1.0 electrons, predominantly from the adjacent carbon atom. On protonation, the ketone oxygen atom to which the proton is bound gains 0.8 electrons, and the proton abstracts around 0.5 electrons. This suggests a disruption of the π system, in which the OH group attains greater valence electron density than in the neutral case. This charge density is drawn from the aryl carbon and hydrogen atoms, which become depleted to between 0.02 and 0.1 and 0.04 to 0.11 electrons respectively, dependence on location around the ring. The alkene carbons, however, do not exhibit any electron density depletion on protonation. On binding Pd atoms, the metal transfers between 0.2 and 0.25 electrons per atom into the alkene bond, which disrupts the π system, further localising the electron density excess upon the alkene carbon atoms, which supports the description of Pd(0) as a π donor on ligation. Therefore, the insignificant effect of protonation on the binding modes and energetics of Pd to dba is due to the charge locality. The molecule only interacts with Pd at the point of direct bonding to the alkene, and this is the site least affected electronically by protonation.

3.4 $Pd_{(5-8)}(dba)_2$

The gas phase global minima for $Pd_{(5-8)}$ are inserted into the dba_2 complex and locally relaxed. Due to rapidly increasing energy landscape complexity on cluster and ligand size, the full range of potential isomers may not be explored the DFT level, as was performed for $Pd_{(1-4)}$. Therefore, it is not claimed that the resultant relaxed structures represent the global minima of the sandwich complex, but rather locally stable structures which may be kinetically trapped as the gas phase Pd_n clusters associate with the dba ligands. As noted for the Pd_4 clusters in dba_2, these 3D motifs may be significantly higher in energy than planar structures, but serve as examples of larger clusters which will be constrained to adopt 3D geometries. The resultant structures of these local minima are displayed in figure 9 for the lowest energy spacing and ligand alignment found. It is clear that for these clusters, there is little distortion of the cluster structure from that of the gas phase. The ligands flex to accommodate the metal particle, which associates centrally, maximising Pd-C(alkene) bonding. Most palladium atoms bind in a μ_2 bridging mode to alkene carbons, and from Pd_6 to Pd_8, a direct bond is formed to the oxygen. The loss of planarity in the ligands is due to the greatly affected conjugation of electron density, brought on by strong binding to the metal atoms at electron-rich sites. Therefore, for these larger sizes, there is a stronger cluster-induced ligand templating, unlike the dominant ligand-induced cluster templating found for smaller particles which distort significantly on dba binding.

The global minimum structure is usually a cc-cc geometry, though both aligned and anti-aligned arrangements are competitive. By considering the lowest energy spacing for each dimer pair, a 6 Å initial spacing is the most favourable more commonly than greater separations. The distribution of preferred spacing is such that there is little clear trend for increased spacing as clusters grow. The ligands will associate as closely as possible to maximise Pd-C bonds. In addition, a significant proportion of geometries failed to converge to a local minimum in the 100 relaxation steps allowed in the DFT minimisation, suggesting this is a difficult energy landscape to explore. The largest of spacings (8 Å) was the most likely to fail, primarily because the binding of palladium between the two ligands was too weak to act as a template for the bound system, and both ligands were free to dissociate.

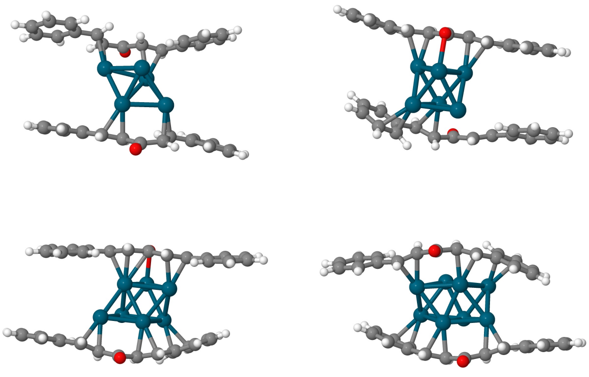

Fig. 9 The putative global minima for larger clusters within neutral dba_2.

The total energetic benefit of associating the ligands, templated by a palladium cluster can be calculated by the association energy E_a, which is defined in equation 1 as the difference between the total energy of the free gas phase minima for both Pd_n and each dba molecule, and the overall global minimum for the complex when bound. The variation of this value with cluster size allows us to infer which cluster is most likely to be found on purely thermodynamic grounds, and predict at what size the intercalated binding of Pd_n becomes unfavourable, relative to the separated system. By considering the bound GM structure, the energetic effect of distorting the structure of the cluster and the ligands is implicit.

$$E_a = E_{TOT} - E_{clust} - E_{dba_1} - E_{dba_2} \qquad (1)$$

where E_{TOT} is the total GM energy of the bound state, E_{clust} is the gas phase GM total energy, and E_{dba_i} is the energy of free dba ligand i .

This method has certain limitations. The association energy does not take into account the entropic loss on binding the individual components together. We may, however, expect the entropic contribution to be fairly similar for each system, giving an approximately constant error factor. Energetic barriers to rearrangement are not considered, which may well be a significant driving force towards association of particular motifs/sizes in experiment. Association energy only models the binding of free dba ligands to pre-formed palladium clusters, and as such is applicable to the question of fluctional behaviour, in which ligands interchange between clusters in the limit that clusters do not change in size. This approximation will be valid in the dilute regime, in which experimental evidence shows ligands are exchanged. Table 2 shows E_a value as a function of size, for which there is a consistent trend that the larger the cluster, the more energy is to be gained for binding within two dba ligands. This result agrees on energetic grounds with the experimental finding that particles grow within dba complexes. These clusters are unlikely to be the global minima and so it is likely that the true association energy for fully relaxed clusters is greater still.

Cluster	E_a/ eV	Relative E_a/ eV
Pd_5	-3.52	+1.58
Pd_6	-4.00	+1.10
Pd_7	-4.75	+0.26
Pd_8	-5.1	0.00

Table 2 Association energies of the larger clusters into neutral $(dba)_2$. There is a trend towards associating larger clusters.

Protonation of the larger clusters is also simulated for each cluster from the pentamer to the octamer, alignment and spacing of 6-8 $\AA$. Similarly to the case of the smaller clusters, the structures are virtually unchanged, either from the gas phase geometries or the neutral $(dba)_2$-bound global minima. The preferred binding motifs are consistently Pd-C(alkene) as for the neutral clusters. cc-cc pairs are the preferred conformers for Pd_5, Pd_7 and Pd_8, with a cc-ct conformer preferred for Pd_6. The overall trend for cc pairs is clear, in agreement with the mono-dba-Pd_n, neutral $Pd_n(dba)_2$ and forcefield results. For Pd_5 and Pd_6, anti-aligned arrangements are preferred, whilst for Pd_7 and Pd_8, aligned arrangements are lower in energy, though in most cases, there is a local minimum with the opposite arrangement within 0.2 eV of the ground state, suggesting a minor trend. The structures of the $Pd_n(dba)_2H^+$ putative global minima are displayed in the supplementary information, with the relative energetics of each arrangement.

4 Discussion

Overall it is found that the binding of small palladium clusters into $(dba)_2$ in an intercalated manner is energetically favourable and that the association of Pd atoms to the ligand is preferentially to alkene C-C bonds: a trend which persists over the the entire subnanometre size range of clusters considered and when bound to one or two dba molecules. The strength of this association is noted in several ways. Firstly, a direct calculation of the preference of intercalation over dissociation is made with the association energy, showing not only that the clusters strongly bind to the ligand, but also that there is no apparent decay of this strength as a function of size. This impressive binding suggests that even for large, 3D clusters which are severely constrained when bound in the complex, and to which only a fraction of the bonds are to the preferred alkene sites, there is a large energetic benefit to association. It may therefore be predicted that the growth of clusters, which is shown to occur kinetically in experiment, is thermodynamically favourable, despite imperfect binding modes to dba. The second measure is the qualitative observation that the association with dba is sufficient to reorder the energetic stability of cluster isomers. For the case of Pd_4, the reordering of minima is severe enough to oppose the gas phase preference entirely. While the dynamics of this ligand-induced rearrangement are not studied, it is clear that thermodynamically, the maximisation of Pd-alkene(C-C) bonds controls the cluster geometry, and is the dominant energetic contribution to the association. When compared to the results for Pd_4 upon a single dba molecule, it becomes clear that the balance between the preference for Pd-Pd and Pd-C bonding has a critical point between the number of Pd-C bonds available to $Pd_4(dba)$ and $Pd_4(dba)_2$. For dba_1, there is one Pd atom in the apical site of the tetrahedron which cannot bind to another electron rich C-C bond. For dba_2, this atom can form additional bonds. However, the steric strain of the tetrahedron is sufficient for the dba_2 complex to overcome this benefit, and drive planarity. Test calculations on tetrahedra implanted into ligand pairs with higher spacing show a greater stability, but no local minimum was found in which the tetrahedron lies lower in energy than the planar clusters with smaller spacings. The combination of sterics and maximisation of Pd-C(alkene) bonding controls the overall structural preference. This ligand-mediated structural effect will play a significant role in the subsequent reactive properties of the palladium cluster. $Pd_n(dba)_m$ is commonly employed as a source of Pd(0) for catalytic purposes, while the ligand is considered labile. The result that clusters will form, and that the ligand can alter their shape will thus impact on the reaction mechanisms, binding energies of adsorbates and electronic properties of the catalyst. The final evidence for the strength of binding is that the minimal dba-dba separation which binds clusters is always preferential. We consider several initial molecular separations in this study, ranging from 5 to 8 Å , allowing for a large degree of freedom for the cluster to rearrange, extend spatially, and attain binding modes which are not obvious by construction. It is determined that approximately 5 Å is the lowest separation for planar clusters. For 3D clusters, the separation is necessarily larger, but still locally minimises to the smallest distance which allows for unstrained Pd-C bonds of around 2.23 Å . The separation between ligands is sufficient to break any dispersive stacking interactions, and so the complex may be regarded as held together solely by the Pd-C bonds.

The effect of the cluster on ligand structure is often considered less important from an experimental perspective, as dba is treated as a precursor molecule which may be easily displaced by others in solution. However, evidence that dba is non-innocent in reactions, and may in fact be tuned to affect the electronic properties of Pd_n, and thus catalysis, suggests any cluster induced-ligand templating will have importance in the reactive behaviour of Pd. Furthermore, an understanding of the role of the metal upon the ligand allows for more accurate catalytic design. Therefore, the effect of cluster structure and size is noted throughout this study, finding that for clusters of < 5 atoms, there is little effect upon the ligand. The disruption of the conjugated π electron system on binding Pd causes moderate deviation at the phenyl ring ends of the molecule, opening the complex, which may have a reactive effect, allowing reactive adsorbates access to the metal more easily, but overall, bond extension and twisting is rarely observed among the low lying local minima. For larger clusters, we do not consider the true global minima of the sandwich complex, and it is conceivable that planar clusters will continue the trend of minimal ligand distortion, but for 3D structures, which may be considered an archetype for larger clusters which eventually must remain three dimensional, there is a much stronger effect upon ligand structure.

The effect of charge upon the overall structures is seen to be minor for $Pd_n dba_m$, due to the synergistic lack of charge depletion of the alkene bonds on protonation, the preference of the cluster to bind to the alkene, and the localisation of charge into the alkene C-C bonds induced by the cluster. The disruption of the π system on cluster binding which leads to the small deviations of ligand structure also accounts for the resilience to charging. This result is surprising, and suggests that in solution, where the complex is known experimentally to exist in the neutral or monoprotonated state, the reactive properties, governed by the structure of the complex are largely independent of charge. There is a small degree of reordering of conformer and alignment, which is explored by comparing the size dependence of preference for alignment/anti-alignment and cc-cc/cc-ct/ct-ct ligand conformers on protonation. For clusters $Pd_{(4-8)}$, there is an overall preference for cc-cc isomers, which is in agreement with the result both of the small clusters $Pd_{(1-3)}$, the $Pd_n(dba)_1$ result and those of the forcefield analysis. In fact, only for one of the five cluster sizes of $Pd_{(4-8)}$ is the overall lowest conformer not cc-cc. On protonation, the results are largely unchanged. The trend for cc-cc conformers remains, with four out of five cluster sizes retaining cc-cc as the global minimum. Additionally, the role of size and charge on the alignment shows very little impact. For the larger clusters, aligned molecules are more stable than anti-aligned for Pd_6 and Pd_8 when neutral, and Pd_7 and Pd_8 when protonated. This result differs from the smaller clusters, which display a clear preference for aligned motifs, both for dba_1 and dba_2. This is likely due to the decrease in importance, on increasing cluster size, of maximised Pd-alkene(C) overlap. Above Pd_3, all palladium atoms cannot be optimally bound over electron-rich sites, and so there is less of a driving force towards arranging the ligands to maximise such arrangements. Overall, the conformation of the ligand plays a larger role than the alignment, which exhibits a cluster-size dependence.

5 Conclusions

We have employed a systematic DFT search of low lying structural motifs for the dba_1, dba_2, Pd_n and $Pd_n(dba)_m$ ($n < 9$, $m < 3$) systems, in order to determine the trends of preferred geometry on cluster size and ligand oligomer for an experimentally important class of catalytic species. We determine that there is a strong ligand-induced reordering of cluster minima, in which the sandwich complex is found to be strongly favourable and causes a flattening of clusters from 3D to 2D geometries on binding. This effect is likely to play a role in the catalytic properties of palladium clusters. Clusters preferentially bind to alkene carbon-carbon bonds, acting as π donors. Additionally, the role of protonation is considered, finding little effect on the structural or energetic properties of the ligand, and only small deviations to cluster structure for the smallest cluster sizes, which is attributed to the localisation of electron density to the alkene bonds. We conclude that the role of the ligand in palladium complexes is great, and assert that a full mechanistic exploration of palladium clusters for catalysis must include the consideration of the cluster structure, which will require a detailed analysis of ligand binding. The oligomer of the ligand and the size of the cluster may be tuned to control reactivity and lead to the rational design of ligand-bound, cluster-based palladium catalysts.

Current investigation is planned to extend the forcefield method to allow for metal binding. Polarizable forcefields which allow for charge redistribution are required to adequately represent the effect of the cluster on the electron density distribution, and would allow for an understanding of the effect of metal clustering upon the energy landscape as a function of size, as well as unbiased predictions of true global minima, which would be of use for screening isomers prior to high level electronic structure calculations. Furthermore, an investigation into the mechanistic role of clustering in catalysis is planned, in which the adsorption of important molecular species is modelled, for C-H/C-x bond activation processes.

This journal is © The Royal Society of Chemistry [year]

6 Acknowledgements

Computing resources were provided via our membership of the UKs HPC Materials Chemistry Consortium, which is funded by EPSRC (EP/L00202), this work made use of the facilities of HECToR, the UKs national highperformance computing service, which is provided by UoE HPCx Ltd at the University of Edinburgh, Cray Inc and NAG Ltd, and funded by the Office of Science and Technology through EPSRCs High End Computing Programme. CJH acknowledges the EPSRC and the School of Chemistry, University of Birmingham for financial support.

References

1 Ananikov V.P. and Beletskaya I.P., *Organometallics*, 2012, **31**, 1595.
2 Roucoux A., Schultz J. and Patin H., *Chem. Rev.*, 2002, **102**, 3757.
3 R. M.T., B. R. and W. K., *Tetrahedron. Lett.*, 1996, **37**, 4499.
4 Mandeli P.K. and Chand D.K., *Catal. Comm.*, 2013, **31**, 16.
5 Beller M., Fischer H., Kühlein K., Reisinger C.-P. and Herrman W.A., *J. Organomet. Chem.*, 1996, **520**, 257.
6 R. C. and G. J.A., *Org. Lett.*, 2002, **4**, 1993.
7 Moshfegh A.Z., *J. Phys. D.: Appl. Phys.*, 2009, **42**, 233001.
8 Tamura M. and Fujihara H., *J. Am. Chem. Soc.*, 2003, **125**, 15742.
9 Kwon G., Ferguson G. A., Heard C. J., Tyo E. C., Yin C., DeBartolo J., Soenke S., Winans R. R. E., Kropf A. J. and Greely J. P. *et al.*, *ACS Nano*, 2013, **7**, 5808–5817.
10 Pakarinen O.H., Barth C., Foster A.S. and Henry C.R., *J. Appl. Phys.*, 2003, **103**, 054313.
11 Goodman D.W., *J. Catal.*, 2003, **216**, 213.
12 Demoulin O., Rupprecheter G. Seunier I., LeClef B., Navez M. and Ruiz P., *J. Phys. Chem. B.*, 2005, **109**, 20454.
13 Zalesskiy S.S. and Ananikov V.P., *Organometallics*, 2012, **31**, 2302.
14 Oliver-Meseguer J., Cbrero-Antonio J. R., Dominguez I., Leyba-Perez A. and Corma A., *Science*, 2012, **338**, 1452–1455.
15 Lei Y., Mehmood F., Lee S., Greeley B., Lee S., Seifert S., Winans R.E., Elam J.W., Meyer R.J., Redfern P.C., Teschner D., Shlögl R., Pellin M.J., Curtiss L.A. and Vajda S., *Science*, 2010, 224–228.
16 Vajda S., Pellin M. J., Greeley J. P. Marshall C. L., Curtiss L. A., Ballentine G. A., Elam J. W., Catillon-Mucherie S., Redfern P. C. and Mehmood F. *et al.*, *Nature Mat.*, 2009, **8**, 213–216.
17 Lee S., Lee B., Mehmood F., Seifert S., Libera J.A., Elam J.W., Greeley J., Zapol P, Curtiss L.A., Pellin M.J., Stair P.C., Winans R.E. and Vajda S., *J. Phys. Chem. C.*, 2010, **114**, 10342–10348.
18 Vargas V.C., Rubio R.J., Hollis T.K. and Salcido M.E., *Org. Lett.*, 2003, **5**, 4847.
19 Grasa G.A., Viciu M.S, Huang J., Zhang C., Trudell M.L. and Nolan S.P., *Organometallics*, 2002, 2866.
20 Weng Z., Teo S., Koh L.L. and Hor T.S.A., *Organometallics*, 2004, **23**, 4342.
21 Zhou J. and Fu G.C., *J. Am. Chem. Soc.*, 2003, **125**, 12527.
22 Andrei D. and Wnuk S.F., *J. Org. Chem.*, 2006, **71**, 405.
23 Ross A.J., Lang H.L. and Jackson R.F.W., *J. Org. Chem.*, 2010, **75**, 245.
24 Itami K., Nokami T., Ishimura Y., Mitsudo K., Kamei T. and Yoshida J.-I., *J. Am. Chem. Soc.*, 2001, **123**, 11577.
25 Murata M., Watanabe S. and Masuda Y., *Tetrahedron Lett.*, 1999, **40**, 9255.
26 Denmark S.E. and Baird J.D., *Org. Lett.*, 2004, **6**, 3649.
27 Yang F.-Y. and Cheng C.-H., *J. Am. Chem. Soc.*, 2001, **123**, 761.
28 Franzén J., Löfstedt J., Dorange L. and Bäckvall J.-E., *J. Am. Chem. Soc.*, 2002, **124**, 11246.
29 Chang K.-J., Rayabarapu D.K., Yang F.-Y. and Cheng C.-H., *J. Am. Chem. Soc.*, 2005, **127**, 126.
30 Alper H. and Saldana-Maldonado. M., *Organometallics*, 1989, **8**, 1124.
31 Zhou L., Ye F., Zhang Y. and Wang J., *J. Am. Chem. Soc.*, 2010, **132**, 13590.
32 Awuah E. and Capretta A., *Org. Lett.*, 2009, **11**, 3210.
33 Takayashi Y., Ito T., Sakai S. and Ishii Y.J., *J. Chem. Soc. D: Chem. Commun.*, 1970, 1065.
34 Ukai T., Kawazura H., Ishii Y., Bonnet J.J. and Ibers J.A., *J. Organomet. Chem.*, 1974, **65**, 253.
35 Mazza M.C. and Pierpont C.G., *J. Chem. Soc., Chem. Commun.*, 1973, 207.
36 Tanaka H. and Kawazura H., *Bull. Chem. Soc. Jpn.*, 1980, **53**, 1743.
37 Harvery P.D., Adar F. and Gray H.B., *J. Am. Chem. Soc.*, 1989, **111**, 1312.
38 Pierpont C.G. and Mazza M.C., *Inorg. Chem.*, 1974, **13**, 1891.
39 Kawazura H., Tanaka H., Yamada K.-I., Takahashi T. and Ishii Y., *Bull. Chem. Soc. Jpn.*, 1978, **51**, 3466.
40 Tanaka H. and Kawazura H., *Bull. Chem. Soc. Jpn.*, 1979, **52**, 2815.
41 Kapdi A.R., Whitwood A.C, Williamson D.C., Lynam J.M., Burns M.J., Williams T.J., Reay A.J., Holmes J. and Fairlamb I.J.S, *J. Am. Chem. Soc.*, 2013, **135**, 8388.
42 Mingos M. and Vilar R., *J. Organomet. Chem.*, 1998, **557**, 131.
43 Fairlamb I.J.S., Unpublished experimental results.
44 Johnston R. L., *Dalton Trans.*, 2003, **22**, 4193–4207.
45 Heiles S., Logsdail A.J., Schäfer R. and Johnston R.L., *Nanoscale*, 2012, **4**, 1109–1115.
46 Cornell W.D., Cieplak P., Bayly C.I., Gould I.R., Merz K.M. Jr., Ferguson D.M., Spellmeyer D.C., Fox T., Caldwell J.W. and Kollman P.A., *J. Am. Chem. Soc.*, 1995, **117**, 5179.
47 Wales D.J.W. and Doye J.P.K, *J. Phys. Chem. A.*, 1997, **101**, 5111.
48 Wales D.J., OPTIM: A program for optimizing geometries and calculating reaction pathways. www-wales.ch.cam.ac.uk/OPTIM.
49 Valiev M., Bylaska E.J., Govind N., Kowalski K., Straatsma T.P., van Dam H.J.J., Wang D., Nieplocha J., Apra E., Windus T.L. and de Jong W.A., *Comput. Phys. Commun.*, 2010, **181**, 1477.
50 Stephens P.J., Devlin F.J., Chabalowski C.F. and Frisch M.J., *J. Phys. Chem.*, 1994, **98**, 11623.
51 Perdew J. P., Burke K. and Ernerhof M., *Phys. Rev. Lett.*, 1996, **77**, 3865–3868.
52 Zhao Y. and T. D.G., *J. Chem. Phys.*, 2006, **125**, 194101.
53 Zhao Y. and Truhlar D.G., *Theor. Chem. Account*, 2008, **120**, 215.
54 Rappe A. M., Rabe K. M., Kaxiras E. and Joannopoulos J. D., *Phys. Rev. B.*, 1990, **41**, 1227–1230.
55 Giannozzi P., Baroni S., Bonini N., Calandra M., Car R., Cavazzoni C., Ceresoli D., Chiarotti G. L., Concoccioni M. and Dabo I. *et al.*, *J. Phys.: Condens. Matter*, 2009, **21**, 395502.
56 Methfessel M. and Paxton A. T., *Phys. Rev. B.*, 1989, **40**, 3616–3621.

Supplementary information for "Dibenzylideneacetone-ligated subnanometre palladium clusters"

Christopher J Heard,*[a] Ian Fairlamb [b] and Roy L. Johnston[a]

July 12, 2014

	aligned				anti-aligned	
Structure	cc-cc	ct-ct	ct-cc	cc-cc	ct-ct	ct-cc
Tetrahedron	-	2.761	2.152	2.097	1.996	1.452
Y-shape	1.072	0.729	1.083	1.276	-	-
Rhombus	0.936	0.650	1.083	-	0.506	-
Linear	**0.000**	-	0.873	0.356	0.568	-

Table S1: Relative total energies (in eV) for tetrameric palladium inside $(dba)_2$. Dashed entries are those which failed to locally minimise.

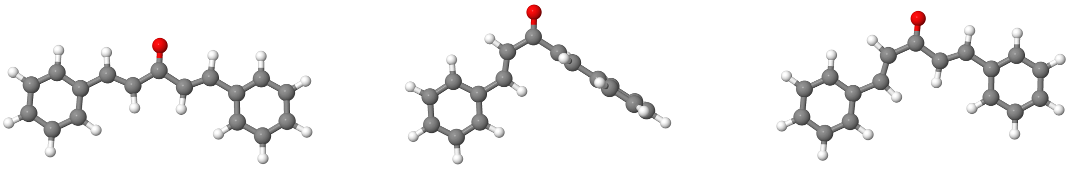

Figure S1: Structures of the two lowest energy minima (I and II) of the dba monomer, with the lowest energy transition state which interconverts them. The transition state consists of a half twist of one phenyl group, and is the same structure as the lowest transition state which interconverts isomers I and III.

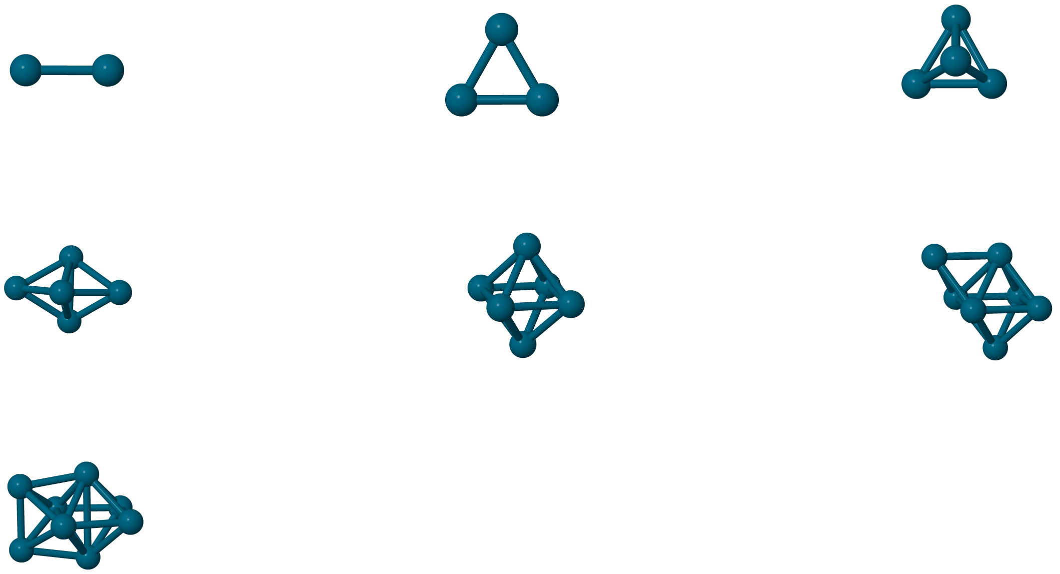

Figure S2: Global minimum structures for the Pd_n (n < 9) clusters, as found by the BCGA with the PBE exchange-correlation functional.

		aligned			anti-aligned		
Cluster	Spacing/ $\mathring{A}$	cc-cc	ct-ct	ct-cc	cc-cc	ct-ct	ct-cc
Pd_5	6	0.427	0.166	0.998	0.136	0.628	-
	7	-	**0.000**	0.895	-	0.090	0.403
	8	-	-	0.781	-	0.378	-
Pd_6	6	**0.000**	0.362	0.778	0.370	-	0.626
	7	0.114	0.432	0.234	-	2.402	0.125
	8	0.375	-	0.193	0.394	-	-
Pd_7	6	0.495	-	1.006	**0.000**	-	0.756
	7	0.552	-	1.452	0.060	-	0.745
	8	-	-	-	0.182	-	-
Pd_8	6	**0.000**	-	1.390	-	0.166	0.242
	7	0.253	-	0.919	0.661	0.261	-
	8	0.536	1.047	0.895	1.858	0.340	0.895

Table S2: Relative total energies (in eV) for larger clusters inside neutral $(\mathrm{dba})_2$. The best spacing and isomer for each cluster size is given in bold. Dashed entries are those which failed to locally minimise.

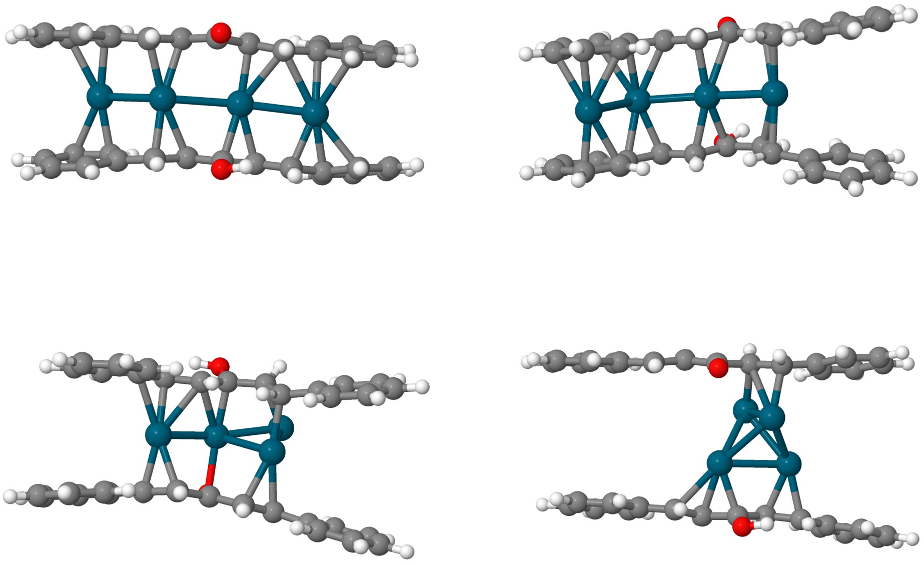

Figure S3: The lowest lying examples of each Pd_4 geometry, bound within dba_2H^+.

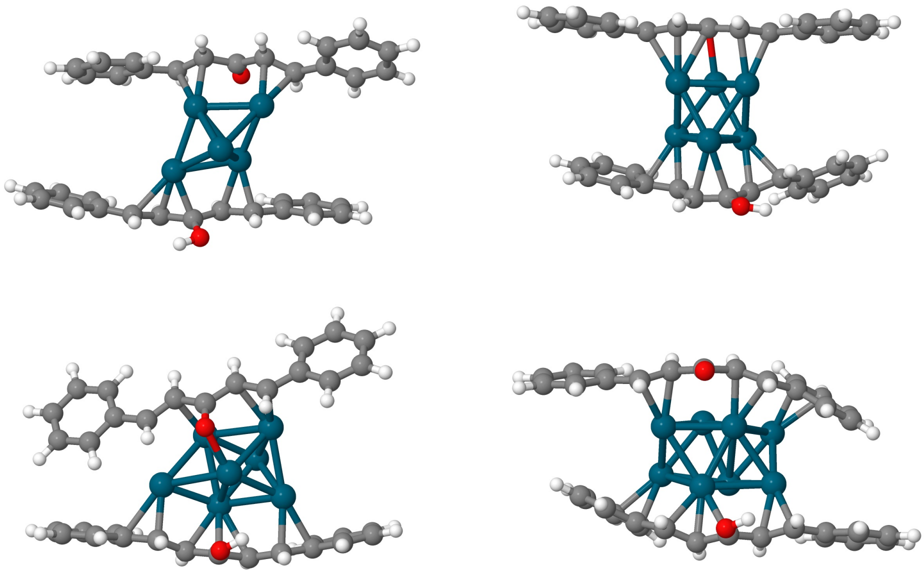

Figure S4: The putative global minima for larger clusters ($4 < n < 9$), within dba_2H^+.

Chapter 11

Discussion

11.1 Group 10 and 11 elements

The two parts of this work are concerned with subnanometre metal clusters of the platinum and coinage metal groups. The coinage metals have been considered primarily from the point of view of novel experiments which produce size selected gas phase clusters of controlled composition and charge state. These experiments require for analysis, the accurate prediction of energetic and electronic properties, and structural trends on doping. These clusters are known to be of interest from a fundamental perspective, in order to describe the physical nature of small systems of simple metals. In addition, the optical properties are of interest, providing a means to rationalise the trends down to the molecular size range, and predict the onset of characteristics such as surface plasmons. In this work, we consider a number of pure and mixed metal clusters of several of sizes and charge states and calculate these properties for energetically low lying structures and chiral motifs. The electronic behaviour of coinage metals, which are commonly assumed to be simple low spin systems with the $d^{10}s^1$ electronic configuration, are found to be complex and depend sensitively on all of the aforementioned parameters. s/d mixing is known for small coinage metal particles, and in the work contained herein we find it to be significant for the types of geometric motif favoured, the position of the 3D/2D transition on doping, and the profile of the optical response spectrum. Isoelectronic doping of coinage metals gives rise to a rich library of competitive structural motifs, with subtle variation in chemical ordering preference. The electronic properties are strongly dependent on the treatment of charge and charge separation, particularly for clusters containing gold, which differs in electronegativity significantly from silver and copper. These considerations have led to the determination of appropriate DFT methods to calculate electronic behaviour, and show that mixed coinage metal systems exhibit notable complexity even at the subnanoscale.

Palladium based clusters are the subject of the second part of this work, and are representative of a late metal group with direct, practical chemical applications. With palladium nanoparticles the subject of numerous recent theoretical and experimental examinations, this work aims to consider various scenarios in which palladium subnanometre clusters may be found in experiment, accidentally or by design, and to calculate properties which connect closely with ongoing practical work. These systems are known to have catalytic utility in homogeneous and heterogeneous catalysis and experimental effort is currently being made to investigate the novel subnanometre size range for applicability in the same fields. It is shown in this work that subnanometre particles of palladium deposited upon oxide supports have a striking activity and stability for electrocatalytic uses, and may potentially be tuned through alloying or size control to have additional heterogenous catalytic uses. Through local and global optimisation we isolate the factors which control palladium cluster structure and binding properties, in order to support at an atomistic level of detail, current and future experiments. Charge distribution, cluster size, oxidation level, support identity, compostion and chemical ordering are all found to play a role in determining structure, which is known in turn to determine function. For palladium clusters, a more sophisticated computational methodology is required than for gas phase coinage metal clusters, as the effect of the medium in which the clusters are found must be considered. Oxide supports are employed, leading to the application of a novel surface-GA to perform unbiased global optimisation directly at the surface/vacuum interface. For organic ligand-bound palladium clusters, the effect of cluster size is taken into account in parallel with ligand geometry and number. This work aims to rationalise experimental results, in order to aid in the design of ligand-cluster systems for catalytic use in the field of C-C and C-H bond activation reactions.

In both the palladium and the coinage metal systems, the methodology requires global and local optimisation at the DFT level of theory, followed by the calculation of energetic and electronic properties. It is observed that supportive theoretical calculations for experiments on late subnanometre metal particles and their alloys is fruitful both for rationalising and predicting important characteristics.

11.2 Global optimisation

The global optimisation of small metal clusters at the DFT level of theory has been employed to determine with high accuracy, the structures of metal clusters at the subnanometre size range. A variety of search methodologies were applied in order to determine low lying motifs, which play a special role in the physical and chemical propeties of nanoparticle systems. For ultra-small cluster systems, an unbiased search of reasonably large regions of the energy landscape is straightforward to achieve, given the limited number of viable structural motifs, and well optimised computational landscape search tools. For the threshold algorithm, simple cartesian moves allow for the exhaustive exploration of structural space. With the BCGA, more sophisticated moves are employed, including the splicing together of configurations. This size range is found to be amenable to relatively high levels of computational theory, and so full DFT exploration with appropriate functionals and large basis sets is directly undertaken.

A global optimisation study, even at a high level of computational sophistication is often insufficient to truly describe the nature of a continuous system in experiment at finite temperature, and so comparison with experimental data is sought where available. The goal of theoretical structure prediction is to make predictions for the future rational design of subnanometre systems with tunable properties, but these results may only be verified by the appropriate comparison to experiment. Throughout this work, we aim to connect with experiment through optical spectra (coinage metals), the results of infrared and mass spectrometric analysis (ligand-bound palladium) and EXAFS data (Pd_xO_y on MgO/Al_2O_3). Given the small size, and thus the close competition between geometric and permutational isomers and compositions, accurate comparison between the energetics of the available isomers, and crucially, the properties which result from them, is key. In addition, properties which may be determined accurately both in experiment and theory are needed, particularly those which may distinguish sensitively between structures. By producing accurate structures, a baseline is therefore generated, from which the required calculation of properties is available. Furthermore, these geometries represent the first approximation to the structures available to experiment. While it is known that rearrangement and fluxionality is important, nevertheless, these low-energy structures are likely to be significantly populated, and are the sensible first attempt for the calculation of physical properties to compare to experiment.

11.3 Energetic properties

Energetic properties may be further divided into external energetics, such as the binding energy (for adsorbates), adsorption energies to a surface or association energies (for intercalation of clusters into ligands), and internal energetics, such as total cohesive energies or mixing energies for multimetallic clusters.

In the case of molecular adsorbates binding to small palladium-based particles, the binding energy of individual binding events allows for the prediction of preferred sites at an atomistic level unavailable to most experimental analyses. This information therefore guides the understanding of potential reaction mechanisms and the propensity for cluster catalysts to become poisoned. Furthermore, for large, ligand-bound cluster systems such as $Pd_n(dba)_m$, binding energies inform the experimentalist of the existence of upper or lower bounds on cluster size if they exist while the association energies determine the variation of cluster binding into the ligand sandwich complex as a function of other controllable parameters, such as charge, binding site or particle size.

For mixed clusters, in which there is a competition between compositions, characterised dynamically by disproportionation rates, the mixing energies provide a route to predicting favourable cluster compositions on purely thermodynamic grounds. We apply this concept to

$\mathrm{Pd}_n\mathrm{Ag}_{(4-n)}$ and $\mathrm{Pd}_n\mathrm{Pt}_{(4-n)}$ clusters, in order to estimate the propensity to form particular compositions, both in the gas phase and upon a surface. Where there is a significant variation in the mixing energies between compositions, we may suggest, in the absence of dynamic or entropic considerations, a skewed distribution of products, and potentially rule out certain compositions. It is observed that mixed clusters are preferred upon the surface for both systems, with a significant energetic gain on mixing, and therefore, we may predict a lack of pure clusters in the products, unless there is only one element available. It is however possible that whilst there is an energetic preference for mixed clusters when deposited, that the barriers to decomposition or disproportionation are high, or the gas phase products may not include mixed clusters.

This analysis may be extended to clusters upon which atoms or molecules are bound and is applied to the case of the palladium cluster-bound oxygen species. The energetic basis for the preferred oxidation state is calculated for the free and surface-bound clusters, in order to compare with atmospheric conditions. The relative energy, defined as the difference between the total energy of the oxygen bound cluster upon local relaxation, and the global minima for the fully reduced cluster plus the appropriate number of oxygen molecules is equivalent to the mixing energy, and for $\mathrm{Pd}_x\mathrm{O}_y$ is found to increase with increasing oxidation state. This suggests that the cluster will strongly bind oxygen at least up to the PdO oxidation state found in the bulk. This result has significant influence over the subsequent theoretical study of $\mathrm{Pd}_x\mathrm{O}_y$ clusters, as it informs the likely compositions, and crucially, the structures which will govern the reactive potential of the particle. For the electrocatalysis of water splitting reactions, the structure of the cluster, in particular the presence of appropriate adsorbate binding sites is suggested to be the dominant factor in controlling activity. For the theoretical study of oxidation and size on surface supported palladium particles, the oxidation effect, especially that of deposited oxygen atoms greatly affects stability and cluster geometry.

Dynamical studies of the rearrangement rates are required in order to determine the extent of kinetic trapping into suboptimal minima which may be found in experiment, and the specific details of the preparation method play a large role in minimising the role of kinetics on the final thermodynamic distributions of minima. Additionally, the temperature-free regime which DFT and empirical potential calculations represent does not include the effects upon the free energy landscape of entropic contributions to the total energy.

Dynamic models exist to allow for approximations to this kinetic activation barrier issue. Molecular dynamics methods attempt the treat the dynamical system, though become prohibitively expensive when considering DFT-MD for a range of compositions, sizes or metal identities as we aim to perform in the studies presented here. For appropriate systems, such as the free dba ligand, unbound by metallic particles, forcefield methods are sufficient to gain a reasonable picture of the landscape, and for these forcefields, dynamical studies may be performed.

Another means by which we may attempt to connect quantitative thermodynamic calculations with kinetic measurements is through a statistical exploration of the landscape. For a prototypical coinage metal cluster, we perform this analysis, calculating the barrier heights, probability flows between basins and their threshold energy dependence, and the configurational density of states within basins. The result that the statistical weight of the basin does not correlate closely with the energy of the minimum, and that the ease of traversing pathways between minima is not simply a function of basin size and thermodynamic barrier height, show that entropic contributions to the landscape play a large role, even for very small clusters for which the configuration space is limited.

11.4 Electronic properties

The electronic structure of clusters are known to control reactive properties, both through binding to adsorbates, ligands and surfaces, and also in their application as electro- and photocatalysts. For subnanometre clusters, this role will be even greater than in conventional nanoparticles, owing to finite size quantum effects, such as orbital filling, Jellium shell closing and hybridisation. Potentials which do not allow for such treatments perform poorly for clusters and necessitate the use of DFT methods to find accurate global minima. Additionally, charge transfer, which may strongly influence the permutational isomer or even overall structure of the cluster is rarely well described without elecronic structure methods. We therefore examine the affect of electronic properties upon the structures, binding and mixing energies, and optical properties of small clusters. Several methods to probe the electronic properties of noble metals are employed, including calculation of the density of states, the charge distributions and the optical excitation spectrum.

The density of states (DOS), and in particular a projection of the DOS onto the spherical harmonic functions allows for the distribution of electron density across the occupied orbitals to be determined. In the case of the coinage metal octamers, this calculation is key to explaining the propensity towards 3D or 2D structural motifs. The onset of the d band below the Fermi energy is much closer in gold than silver or copper, and leads to s/d hybridisation which affects the transition to three dimensionality. By measuring both the onset of the d band, and noting the contribution of d orbitals to the highest lying occupied orbitals, the dimensionality transition is rationalised in chapter 3. This method is further employed in the study of the coinage metal helices in chapter 5, in order to explain the shift in the excitation spectrum. It has been proposed that intraband transitions are the primary cause of the decay of plasmon resonances in gold, as they occur in the same energy range at small sizes. This has been explored by other authors, with nanorods of gold and their silver alloys. We calculate the densities of states in the present work for the various dopant locations and dopant sites of the helices, finding that the copper d band shifts the overall d band for the cluster in the same manner as the major excitation peak shifts in the absorption spectrum. For multiple copper dopants, the effect is systematic and more profound, shifting the d band by 0.2 eV, and driving an offset of the main molecular excitation peak. By decomposing the excitation peak into molecular orbital contributions, the same result is observed, with an increase in Cu 3d influence as doping increases. This analysis has previously been applied to the simulation of the optical responses of tetrameric silver and gold cluster cations.

Charge transfer dictates to a large extent, the occupation of sites in a multimetallic cluster, and the preference for compact or open structures. By mixing elements with significantly different electronegativities, dipoles may be set up which activate atoms for binding, as observed in the case of surface bound palladium clusters. Mixed metal clusters, $\text{Pd}_n\text{Pt}_{(4-n)}$ and $\text{Pd}_n\text{Ag}_{(4-n)}$ show asymmetric charge distributions, which may be exploited to generate active sites for adsorbate binding. For oxidised palladium clusters, the deposition of oxygen upon the cluster generates a vertical dipole, in which charge is drawn from the surface to the cluster, and from the cluster to the oxygen. This transfer is found to be very local in nature, and so is sensitively affected by the cluster geometry and the binding site of the oxygen atom. Accurate calculation of the final charges on such systems is therefore a useful tool to locate potentially catalytically active sites on low symmetry clusters.

GADFT structure prediction followed by calculation of properties has been recently used to support electric field deflection measurements for subnanometre silicon and mixed tin-bismuth clusters, by comparing dipoles of various minima produced in the GO stage. Optical response spectra have been fruitfully simulated for tetrameric pure silver and gold cations produced with the GADFT, in order to identify minima from longitudinal beam deflection measurements. We observe that ion mobility simulations are capable of separating structural isomers, whilst the simulation of optical absorption spectra provide a sensitive means to distinguish both structural and permutational isomers for mixed coinage metal clusters. The combination of the two theoretical methods allows for unambiguous determination of isomer in most cases, and is likely to scale reasonably well with cluster size, as the optical response “fingerprint” becomes more complex.

11.5 Tunability of cluster properties

One of the primary benefits of the use of metallic clusters is that they may be tuned at the atomic scale in a number of ways. The size, structure, chemical ordering and composition are all known to have drastic effects on the final chemical and physical properties. In the work presented here, we control for these effects and attempt to isolate them individually. For gas phase coinage metal particles, the effect of size is well established, and thus we consider archetypal subnanometre clusters of eight atoms, both for a DFT global optimisation, and for a statistical analysis of the energy landscape in the case of CuAg. For palladium and palladium based clusters, we focus primarily on tetramers as the example of a subnanometere cluster, as these are the first sizes at which there is competition between planar and three dimensional motifs. In the size regime in which we are concerned, where finite size effects are dominant, it is not expected that the properties determined from these ultrasmall clusters are representative over a wide range of sizes. This is observed, for example, in the investigation of size effects in surface-bound palladium clusters. For a ten atom cluster, the balance between oxidation, surface binding and the preferred geometry on deposition differs greatly from that of the tetrameric cluster, and leads to significantly different structures. The structure-function relationship for these systems has been established, and is profound, controlled at the level of a single Pd-Pd bond, therefore the size is expected to have a strong effect in the ultrasmall regime.

11.6 Composition control

Composition is the first of the additional tunable factors available in a multimetallic cluster experiment, and one which introduces significant complexity to the energy landscape. From a practical perspective, it is possible in various cluster beam generation schemes to control the composition with mass selection, so that particular clusters may be selected for subsequent deposition and reaction. In these cases, the important question is to what extent the dopant affects the structure of the cluster, and hence the reactivity. This question is approached by investigating the trends in energetics and electronics over multiple compositions. Several of the studies presented here are concerned with the effect of doping, by considering the reordering of low energy strucuctures, and transitions in dimensionality of the global minimum. For $\mathrm{Cu}_n\mathrm{Ag}_{(8-n)}$ and $\mathrm{Cu}_n\mathrm{Au}_{(8-n)}$ clusters, we find the conversion between low lying motifs is subtle and consistent across a doping series. For $\mathrm{Cu}_n\mathrm{Ag}_{(8-n)}$, the transition is always between three dimensional structures, which vary between the global minima of the pure clusters, and contain an additional structure for intermediate compositions $\mathrm{Cu}_7\mathrm{Ag}_1$ and $\mathrm{Cu}_6\mathrm{Ag}_2$. For $\mathrm{Cu}_n\mathrm{Au}_{(8-n)}$, in which the pure clusters differ in dimensionality, there is necessarily a dopant dependent transition, the position of which is interesting when compared to the similar series of $\mathrm{Ag}_n\mathrm{Au}_{(8-n)}$ clusters. Cu causes an earlier transition from 2D to 3D structures than Ag when doped into Au, and the effect is probed with electronic structure. The cause of this structural change and energetic reordering is electronic in basis, and for the coinage metals is controlled by the varying influence of the d band on the electronic states near the Fermi energy. This is relativistic in origin, and as such, the strength of this relativistic effect, which is a function of the mass of the element may be considered a descriptor of the propensity towards planarity.

The theoretical study of helical coinage metals gives another example of composition effects on electronics, controlled through the shift in d band position between elements. The number of copper atoms doped into a thirteen atom Bernal helix cluster of silver atoms has a notable effect on the electronic structure, inducing a shift in the major excitation in the optical response spectrum. Little change is noted in the Fermi energy or the composition of the orbitals which contribute to the major transitions. However, the shift in major peak position is ascribed to the d band below the Fermi energy shifting in position on replacement of silver with copper. More subtle electronic effects on doping coinage metal clusters are found in core shell systems, in which the replacement of the core of a silver cluster with gold induces a less clear change in optical response. The intermediate cluster displays peaks which are not intermediate between the pure clusters, and highlights the requirement for doping to be taken into account for coinage metals, where the hybrid band formation between s and d electrons may dramatically alter the electronic properties.

For AuAg^+ tetramers, the energetics of the various potential isomer products in a beam cluster source are complex, and theoretically difficult to predict. The several xc-functionals applied give differing results, and often show no strong preference for a particular geometry, implying a possible facile interconversion between structures. The electronic reponse, characterised by optical spectroscopy was able to distinguish between isomers, eliminating several which could not be dismissed on purely energetic grounds. This study shows that for the smallest of clusters, electronic properties represent a powerful tool for structure elucidation, and that combined approaches, whilst computationally more demanding, may be necessary for complete mapping of theoretical motifs to experimental results.

With palladium based tetramers, doping provides a means to fine tune the chemical traits of a potentially catalytic species. Composition-dependent trends are observed in the binding energies, which contribute to the stability and longevity of catalysts. Additionally, the surface binding is affected, which is a significant factor in the mobility of particles. Mobility upon the surface is expected to play a great role for subnanometre clusters as potential catalysts, and thus composition control allows for a qualitative rationalisation of cluster migration which would provide a starting point for kinetic studies to fully elucidate. Electronic influence on activity is mediated predominantly through localisation of excess charge. Particularly electron-rich atomic sites are suggested to be preferential for the binding of reactive asorbates, and may be generated both through electron withdrawal from the substrate, and by control of the composition of the cluster. For the $\mathrm{Pd}_n\mathrm{Ag}_{(4-n)}$ and $\mathrm{Pd}_n\mathrm{Pt}_{(4-n)}$ clusters considered, significant charge is indeed drawn from the MgO surface, likely enhancing the reactivity of the cluster. Interestingly, the cluster, whilst drawing more total charge, is less electron rich on a per-atom basis than a single Pd/Pt/Ag atom deposited upon the same surface. Therefore, in order to enhance the charge upon the cluster and improve upon the characteristics of a single deposited atom, composition control is useful. It is found that $\mathrm{Pd}_3\mathrm{Pt}_1$, with the platinum atom atop a Pd_3 base creates a vertical charge dipole, with the platinum atom attaining an excess charge as high as the single atom. This composition is additionally the more energetically favourable, and suggests a synergy between electronic and energetic components which may be useful for cluster design.

11.7 Chemical ordering

Chemical ordering is the second additional variable to consider for multimetallic systems. This property is usually very difficult to control in experiment, as many permutational isomers of a structure are essentially isoenergetic, and may interconvert with small energetic barriers. This is particularly true of metals, where the bond breaking mechanism is less directional and sterically controlled than in molecular systems. For nanoscale systems, the large-scale permutational isomer groups may be classified into core/shell, subsurface layered, onion-like, mixed or Janus type. These groups require clusters of a sufficiently large size, and a large enough number of dopant atoms to be useful as classifications, and involve complex rearrangements to interconvert and significant energy input to create. For this reason, there may be great energetic differences between groups, which are ordered by parameters such as cohesive energy, atom radius and surface energy. For subnanometre particles, it is less clear to distinguish between such classes, because of the small number of available dopant sites and compositions. Thus arguments based on bulk properties such as lattice spacings or surface energy are reduced in predictive power. Nevertheless, chemical ordering does play a role in ultrasmall cluster physics and chemistry.

For the tetrameric AgAu^+ clusters, the chemical ordering is reduced to the choice between a few dopant sites. The competition is due to a complex interplay between first and second order charge properties and is non trivial to predict. Analysis of the pure and mixed clusters shows there is a primary charge effect, due to the location of the dopant relative to the other atoms, in which charge transfer occurs locally and is governed by connectivity. The secondary effect is one of geometric frustration in the pure cluster. Because of the inequivalence of different sites, the base charge, independent of doping, differs from site to site. The first and second order effects may cooperate or compete, and have a strong final result, even for such small clusters. The differences between permutational isomers is on the same energetic scale as the difference between structural isomers for the tetramer, which complicates the unambiguous prediction of preferred isomers and makes a global optimisation scheme more difficult to apply.

In the case of small helical clusters, all inequivalent permutational isomers of monodoped CuAg are considered, giving a subtle energetic and electronic dependence on dopant site location. The energetic preferences conform qualitatively with predictions based on connectivity and atomic radius. Copper atoms are generally more stable in the internal sites, whereas silver occupies the end sites of the helix. This agrees well with the preferred homotops found in the $\mathrm{Cu}_n\mathrm{Ag}_{(8-n)}$ systems investigated with GADFT. In both cases, while the concept of core and surface sites breaks down, the atomic radius of the atom, rather than a charge transfer argument controls the energetic ordering, driving copper into the more constrained locations in order to minimise strain on the cluster. Bader charge analysis for the neutral octamers shows that the transfer is small, unlike in the case of $\mathrm{Cu}_n\mathrm{Au}_{(8-n)}$, in which the electronegativity difference is the key factor in determining the preferred homotop. For the helices, which are more exotic structures, consisting of three inequivalent intertwined strands, with strongly varying connectivity, the charge transfer is more complex and element dependent. Doping silver into copper has little effect on the overall transfer, whereas copper dopants in the silver cluster show a consistent trend of drawing electron density as the dopant moves into central and highly connected sites. This shows that on adoption of unusal geometries, the predictions made for larger clusters based on bulk properties, or global minimum structures for the smaller clusters do not necessarily apply.

Homotop dependence is exhibited more strongly for surface deposited clusters, in which the substrate provides a large energetic perturbation to the individual atomic sites. The additional factor of the individual binding strengths of particular elements to the surface atoms drives the preference for the energetically favoured homotop, which in turn affects the charge transfer and reactive properties of the cluster. This surface homotop effect is well studied for larger nanoparticles, and we determine its strength at the subnanoscale. For the $\mathrm{Pd}_n\mathrm{Ag}_{(4-n)}$ and $\mathrm{Pd}_n\mathrm{Pt}_{(4-n)}$ tetramers, in general, the surface binding varies in strength in the order $Pt > Pd > Ag$. The differences between homotop energies are thus magnified by the presence of the surface, and serve to separate potential isomers more than in the gas phase. When considering the binding of adsorbates, this driving force has a substantial effect, as the binding energies to CO vary in the same order. The CO molecule generally then binds to a surface/cluster site which is sterically more strained than the atop site, and so a mechanistic role of this homotop effect is expected for subsequent reactions. For other adsorbates, with different preferred binding sites, this may allow for selectivity in binding. In summary, it is noted that even down to the smallest of clusters, the difference in binding energies to surface atoms is strong enough, for group 10 and 11 elements, to guide the isomer and charge state, and impinge upon the further chemistry of the cluster. This implies that the doping of ultrasmall clusters may provide a sensitive means to control reactive properties of selected reactions.

11.8 Conclusions

A range of local and global optimisation strategies to determine stable motifs of ultrasmall pure and bimetallic noble metal clusters have been employed, under the principle that structure determines function in the subnanometre size range. Static calculations are performed to rationalise and direct experimental work on this novel class of systems, which show promise for a wide range of optical and catalytic applications. The subnanometre size range is best described as an additional class, distinct both from the atomic and the nanoparticular ranges, with features separate from both, which is successfully probed by the isolation of electronic and structural contributions to the energy. In order to explore energetic, electronic and structural properties, density functional theory is primarily used, showing excellent utility in the determination of trends over dopant series, cluster sizes, oxidation states and substrate identity.

11.9 Current and future work

Ongoing theoretical studies are being performed to support further projects involving longitudinal beam photodepletion and photodetachment experiments. These projects aim to explore the dependence of optical properties of ultrasmall coinage metal clusters on size, doping and charge state.

One such study aims to isolate the effects of charge and doping of an isoelectronic system of coinage metal bimetallic clusters. The octamer is chosen as a well-studied archetype of the subnanometre cluster, from which direct comparisons to recent work may be made. Gold-silver particles are used, as these may be produced in the longitudinal beam photodepletion/mass spectrometry apparatus used for our previous theoretical/experimental studies of the same metal systems. With this theoretical framework, we perform GADFT global optimisation of the monocationic, monoanionic and neutral $\mathrm{Au}_n\mathrm{Ag}_{(8-n)}$ clusters for all n. Reoptimisation with several xc-functionals is performed in order to control for their significant effects, which are discussed in detail in chapter 4. It has been noted, for example that Minnesota type functionals have a stronger tendency to prefer compact, high-coordination structures than standard GGA functionals such as PBE. We have investigated this effect in $\mathrm{Cu}_n\mathrm{Au}_{(8-n)}$/$\mathrm{Cu}_n\mathrm{Ag}_{(8-n)}$ neutral clusters, and previous work with the BCGA using DFT has identified the dimensionality transition transition for $\mathrm{Au}_n\mathrm{Ag}_{(8-n)}$ neutral clusters. However, a systematic study which takes into account the role of absolute charge for a dopant series has not been performed. It is known that for the monometallic clusters, which have been experimentally studied in the gas phase as a function of size for a number of charge states, that the 2D/3D transition may be supressed with the addition of negative charge to the cluster. The correlation between the ability to sustain negative charge through high electronegativity and the propensity towards planarity is noted for CuAg and CuAu clusters in the current work, suggesting that the doping of less electronegative elements (which additionally have reduced relativistic driving forces towards planarity) induces an earlier onset of compact 3D geometries. By characteristing the individual roles of charge and doping level, we intend to identify and understand this transition. Furthermore, by considering the ionisation potentials of individual geometric motifs, we intend to make predictions about the electronic behaviour of these clusters which may be experimentally tested with photoelectron spectroscopy.

Another continuing study is concerned with the effect upon structure and optical absorption spectra of non-isoelectronic doping of palladium atoms into gold clusters. There is experimental interest in determining the role of a palladium dopant in the modification of gold cluster optical spectra. There is some evidence of a size dependent variation in the optical response between mono-doped, size selected clusters, from photodetachment spectroscopy, using noble gas tagging atoms (Ar/Xe). This effect on the response may be due to the potentially significant role of palladium atoms to alter the dimensionality and structure of the clusters. It may be due instead to the electronic effect of doping coinage metal clusters with one of lower valence electron count. Additionally, interaction between these effects may occur, in which the effective electron deficiency of doped clusters induces the 2D/3D transition, as is found for cationic clusters when compared with neutral species. Global optimisation of the small gold and gold-palladium clusters provides information on the energetic competition between planar and compact structures as a function of size, and allows for predictions on the crossover size at which the transition will occur. Additionally, the electronic decomposition of the orbitals involved in determining structure will provide theoretical insight into the mechanism responsible for size dependent trends in structure and optical response. By controlling cluster size, the presence of a dopant and the location of the dopant atom, each potential cause of a change in electronic structure may be isolated. Calculations performed thus far upon a subset of low-lying local minima for the Au_4, Au_3Pd_1, Au_8, and Au_7Pd_1 cationic clusters show a strong propensity for the doping of a single palladium to promote three dimensionality. Local minimisation of various motifs generated for the pure gold cluster is repeated with palladium atoms inserted into all symmetry inequivalent sites. For both the tetramer and the octamer, the inclusion of this dopant causes barrierless rearrangements from structures close to pure gold minima to 3D geometries. This strong doping effect is found additionally to be site-specific. For the rhombic global minimum of Au_4, the two inequivalent dopant sites differ in the resulting minima found on reoptimisation. For the central dopant site there is a barrierless transition to a tetrahedral geometry, whereas the wingtip site retains the rhombic structure. For the octamer, several isomers are considered, including the square planar global minimum, the bicapped octahedron (BcOh) and the dodecahedral-based (dodec) motifs. These structures are known to be low energy motifs for the Au_8 neutral cluster. For the planar motif, the effect of dopant site is again profound. For one of the two inequivalent sites, local minimisation leads to an unchanged structure, whereas the other leads to a barrierless conversion to a three dimensional motif.

A further research direction involves extending the energy landscape analysis to larger mixed metal clusters. By mapping the landscape of coinage metal particles as a function of size and doping, the growth of system complexity may be quantitatively examined. The rearrangement pathways for internalisation and externalisation of dopants are produced, which gives insight into the thermodynamics and dynamics of cluster rearrangement for an important class of systems. Statistical information regarding the activation barriers and connectivity of structural classes will be useful for rational design of coinage metal nanoparticles, and develops the application of the methods described in chapters 6 and 10.

Bibliography

[1] Johnston R.L. *Atomic and molecular clusters*. Taylor and Franicis, 1st edition, 2002.

[2] Wang Y.L., Wang X.B., Xing X.P., Wei F., Li J., and Wang L.S. *J. Phys. Chem. A.*, 114:11244, 2010.

[3] Savoca M., Lagutschenkov A., Langer J., Harding D.J., Fielicke A., and Dopfer O. *J. Phys. Chem. A.*, 117:1158, 2013.

[4] Häkkinen H., Yoon B., Landman U., Li X., Zhai H.-J., and Wang L.S. *J. Phys. Chem. A.*, 107:6168, 2003.

[5] Toebes M.L., van Dillen J.A., and de Jong K.P. *J. Mol. Cat. A.*, 173:75, 2001.

[6] Strobel R., Grunwaldt J.-D., Camenzind A, Pratsinis S.E., and Baiker A. *Catal. Lett.*, 104:9, 2005.

[7] Fukamori Y., Konig M., Yoon B., Wang B., Esch F., Heiz U., and Landman U. *Chem. Cat. Chem.*, 5:3330, 2013.

[8] Mingos M. and Vilar R. *J. Organomet. Chem.*, 557:131, 1998.

[9] Demir M.M, Gulgun M.A., Menceloglu Y.Z., Erman B., Abramchuk S.S, Makhaeva E.E., Khokhlov A.R., Matveeva V.G., and Sulman M.G. *Macromolecules*, 37:1787, 2004.

[10] deHeer W. *Rev. Mod. Phys.*, 65:611–, 1993.

[11] Ferrando R., Jellinek J., and Johnston R.L. *Chem. Rev.*, 108(3):845, 2008.

[12] Brack M. *Rev. Mod. Phys.*, 65(3):677–732, 1993.

[13] Knight W.D., Clemenger K., deHeer W.A., Saunders W.A., Chou M.Y., and Cohen M.L. *Phys. Rev. Lett.*, 52:2141, 1984.

[14] Nealon G.L., Donnio B., Greget R., Kappler J.-P., Terazzi E., and Gallani J.-L. *Nanoscale*, 4:5244, 2012.

[15] Gubin S.P. *Magnetic Nanoparticles*. Wiley-VCH, 2009.

[16] Weissker H-Ch. and Mottet C. *Phys. Rev. B*, 84(16):165443, 2011.

[17] Bonacić-Koutecký V., Boiron M. Pittner J. Fantucci F., and Koutecký J. *Eur. Phys. J. D.*, 9:183, 1999.

[18] Bonacić-Koutecký V., Burda J., Mitrić R., Ge M. Zampella G., and Fantucci P. *J. Chem. Phys.*, 117:3120, 2002.

[19] Bonacić-Koutecký V., Veyret V., and Mitrić R. *J. Chem. Phys.*, 115:10450, 2001.

[20] Heiz U., Sanchez A., Abbet S., and Schneider W.D. *J. Am. Chem. Soc.*, 121(13):3214–3217, 1999.

[21] de Heer W. *Rev. Mod. Phys.*, 65(3):611–676, 1993.

[22] Knight W.D., deHeer W.A., Saunders W.A., Clemenger K., Chou M.Y., and Cohen M.L. *Chem. Phys. Lett.*, 134:1, 1987.

[23] Knight W.D., deHeer W.A., Clemenger K., and Saunders W.A. *Solid State Commun.*, 53:445, 1985.

[24] Weis P., Welz O., Vollmer E., and Kappes M.M. *J. Chem. Phys.*, 120:677, 2004.

[25] Fournier R. *J. Chem. Phys.*, 115(5):2165, 2001.

[26] Moseler M., Walter M., Yoon B., Landman U., Habibpour V., Harding C., Kunz S., and Heiz U. *J. Am. Chem. Soc.*, 134:7690–7699, 2012.

[27] Grönbeck H. and Broqvist P. *J. Phys. Chem. B.*, 107:12239–12243, 2003.

[28] Grönbeck H. and Broqvist P. *J. Chem. Phys.*, 119(7):3896–3904, 2003.

[29] Bowlan J., Harding D.J, Jalink J., Kirilyuk A., Meijer G., and Fielicke A. *J. Chem. Phys.*, 138:031102, 2013.

[30] Yuan X., Liu L., Wang X., Yang M., Jackson K.A, and Jellinek J. *J. Phys. Chem. A.*, 115:8705, 2011.

[31] Yang M., Jackson K.A., and Jellinek J. *J. Chemm. Phys.*, 125:144308, 2006.

[32] Maillet T., Solleau C., Barbier Jr. J., and Duprez D. *Appl. Catal., B*, 14:85–95, 1997.

[33] Babu N. S., Lingaiah N., Gopinath R., Reddy P. S. S., and Prasad P. S. S. *J. Phys. Chem. C.*, 111:6447–6453, 2007.

[34] Tessier D., Rakai A., and Bozon-Verduraz F. *J. Chem. Soc. Faraday. Trans.*, 88(5):741–749, 1992.

[35] Heiles S., Logsdail A.J., Schäfer R., and Johnston R.L. *Nanoscale*, 4(4):1109–1115, 2012.

[36] Häkkinen H., Abbet S., Sanchez A., Heiz U., and Landman U. *Angew. Chem. Int. Ed.*, 42(11):1297–1300, 2003.

[37] Neyman K. M., Vent S., Roesch N., and Pacchioni G. *Top. Catal.*, 9:153–161, 1999.

[38] Neyman K.M., Rösch N., and Pacchioni G. *Appl. Cat. A.: Gen.*, 191:3–13, 2000.

[39] Nasluzov V.A., Rivanenkov V.V., Gordienko A.B., Neyman K.M, Birkenheuer U., and Rösch N. *J. Chem. Phys.*, 115:8157–8171, 2001.

[40] Barcaro G. and Fortunelli A. *J. Chem. Theory. Comput.*, 1(5):971–985, 2005.

[41] Cruz Hernandez N. and Sanz J. F. *J. Chem. Phys. B.*, 105:12111–12117, 2001.

[42] Barcaro G. and Fortunelli A. *Faraday Discuss*, 138:37–47, 2007.

[43] Giordano L., Di Valentin C., Pacchioni G., and Goniakowski J. *Chem. Phys.*, 309:41–47, 2005.

[44] Giordano L. and Pacchioni G. *Surf. Sci.*, 575:197–209, 2005.

[45] Nigam S. and Majumder C. *Langmuir*, 26(24):18776–18787, 2010.

[46] Nigam S. and Majumder C. *J. Phys. Chem. C.*, 116(4):2863–2871, 2012.

[47] Xi L., Henkelman G., Campbell C.T., and Jónsson H. *Surf. Sci.*, 600:1351–1362, 2006.

[48] Barcaro G. and Fortunelli A. *New. J. Phys.*, 9(22):1–17, 2007.

[49] Maiti A. and Ricca A. *Chem. Phys. Lettl*, 395:7, 2004.

[50] Reske R., Duca M., Oezaslan M., Schouten K.J.P., and Koper M.T.M. Strassert P. *J. Phys. Chem. Lett.*, 4:2410, 2013.

[51] Shayeghi A., Johnston R.L., and Schäfer R. *Phys. Chem. Chem. Phys.*, 15(45):19715–19723, 2013.

[52] Yoon B., Landman U., Habibpour V., Harding C., Kunz S., Hei U., Moseler M., and Walter M. *J. Phys. Chem. C.*, 116:9594, 2012.

[53] Fielicke A., Rabin I., and Meijer G. *J. Phys. Chem. A.*, 110:8060, 2006.

[54] Götz, Shayeghi A., Johnston R.L., Schwerdtfeger P., and Schäfer R. *J. Chem. Phys.*, 140:164313, 2014.

[55] Heiles S., Johnston R.L., and Schäfer R. *J. Phys. Chem. A.*, 116:7756, 2012.

[56] Heiles S. and Schäfer R. *Phys. Chem. Chem. Phys.*, 12:247, 2010.

[57] Lee S., Lee B., Mehmood F., Seifert S., Libera J.A., Elam J.W., Greeley J., Zapol P, Curtiss L.A., Pellin M.J., Stair P.C., Winans R.E., and Vajda S. *J. Phys. Chem. C.*, 114(23):10342–10348, 2010.

[58] Vajda S., Pellin M. J., Greeley J. P. Marshall C. L., Curtiss L. A., Ballentine G. A., Elam J. W., Catillon-Mucherie S., Redfern P. C., and Mehmood F. *et al.* *Nature Mat.*, 8:213–216, 2009.

[59] Astruc D. *Transition-metal Nanoparticles in Catalysis: From Historical Background to the State-of-the Art, in Nanoparticles and Catalysis*. Wiley-VCH Verlag GmbH, 2008.

[60] Richards R. and Bönneman H. *Nanofabrication Towards Biomedical Applications*. Wiley-VCH, 2005.

[61] Turkevich J., Stevenson P.C., and Hillier J. *Disc. Faraday. Soc.*, 11:55, 1951.

[62] Esumi K., Tano T., Torigue K., and Meguro K. Chem. Mater.(2):564, 1990.

[63] Wada Y., Kuramoto H., Sakata T., Mori H., Sumida T., Kitamura T., and Yanagida S. *Chem. Lett.*, 7:607, 1999.

[64] Oh J.-G., Oh H.-S., Lee W.H., and Kim H. *J. Mater. Chem.*, 22:15215, 2012.

[65] Matveev A.V., Neyman K.M., Yudanov I.B., and Rösch N. *Surf. Sci.*, 426:123–139, 1999.

[66] Logsdail A.J. and Akola Y. *J. Phys. Chem. C.*, 115:15240, 2011.

[67] Logsdail A.J., Johnston R.L., and Akola Y. *J. Phys. Chem. C.*, 117:22683, 2013.

[68] Ashby M.F., Ferreira P.J.S.G., and Schodek D.L. *Nanomaterials, nanotechnologies and design: an introduction for engineers and architects*. Butterworth-Heinemann, 2009.

[69] Saha K., Agasti S.S., Kim C., Li X., and Rotello V.M. *Chem. Rev.*, 112:2739, 2012.

[70] Lee K-S. and El-Sayed M. A. *J. Phys. Chem. B*, 110:19220–19225, 2006.

[71]

[72] Liao M.-S., Bonifassi P., Leszczynski J., Ray P.C., Huang M.-J., and Watts J.D. *J. Phys. Chem. A.*, 114:12701, 2010.

[73] Johnson H.E. and Aikens C.M. *J. Phys. Chem. A.*, (113):4445, 2009.

[74] Lozano X-L., Barron H., Mottet C., and Weissker H-Ch. *Phys. Chem. Chem. Phys.*, 16(5):1820–1823, 2014.

[75] Aikens C. M., Li S., and Schatz G. C. *J. Phys. Chem. C.*, 112:11272–11279, 2008.

[76] Cazzaniga M., Weissker H-Ch., Huotari S., Pylkkänen T., Salvestrini P., Monaco G., Onida G., and Reining L. *Phys. Rev. B*, 84(7):075109, 2011.

[77] Chan G. C., Zhao J., Hicks E. M., Schatz G. C., and Van Duyne R. P. *Nano Lett.*, 7(7):1947–1952, 2007.

[78] Rabilloud F. *Eur. Phys. J. D.*, 67(18), 2013.

[79] Negreiros F.R., Aprá E., Barcaro G., Sementa L., Vajda S., and Fortunelli A. *Nanoscale*, 4:1208–1219, 2011.

[80] Ferguson G.A., Mehmood F., Rankin R.B., Greeley J.P., Vajda S., and Curtiss L.A. *Top. Catal.*, 55(5-6):353–365, 2012.

[81] Yoon B., Häkkinen H., Landman U., Wörz A.S., Antonietti J-M. Abbet S., Judai K., and Heiz U. *Science*, 307:403–407, 2005.

[82] Zhang C., Yoon B., and Landman U. *J. Am. Chem. Soc.*, 129:2228–2229, 2007.

[83] Negreiros F.R., Sementa L., Barcaro G., Vajda S., Aprá E., and Fortunelli A. *ACS Catal.*, 2(9):1860–1864, 2012.

[84] Parsons R. *Catalysis in Electrochemistry: From Fundamentals to Strategies for Fuel Cell Development*. Wiley, 1st, edition, 2011.

[85] Primo A., Corma A., and Garcia H. *Phys. Chem. Chem. Phys.*, 13:886, 2011.

[86] Reetz M.T., Breinbauer R., and Wanninger K. *Tetrahedron. Lett.*, 37:4499, 1996.

[87] Vargas V.C., Rubio R.J., Hollis T.K., and Salcido M.E. *Org. Lett.*, 5:4847, 2003.

[88] Beller M., Fischer H., Kühlein K., Reisinger C.-P., and Herrman W.A. *J. Organomet. Chem.*, 520:257, 1996.

[89] Mandeli P.K. and Chand D.K. *Catal. Comm.*, 31:16, 2013.

[90] Huang W., Liu J. H.-C., Alayoglu P., Li Y., Witham C.A., Tsung C.-K., Toste F.D., and Somorjai G.A. *J. Am. Chem. Soc.*, 132:16771, 2010.

[91] Tamura M. and Fujihara H. *J. Am. Chem. Soc.*, 125:15742, 2003.

[92] Oliver-Meseguer J., Cbrero-Antonio J. R., Dominguez I., Leyba-Perez A., and Corma A. *Science*, 338:1452–1455, 2012.

[93] Lei Y., Mehmood F., Lee S., Greeley B., Lee S., Seifert S., Winans R.E., Elam J.W., Meyer R.J., Redfern P.C., Teschner D., Shlögl R., Pellin M.J., Curtiss L.A., and Vajda S. *Science*, (9):224–228, 2010.

[94] T. Kobayashi H. Kageyama M. J. Genet B. Delmon M. Haruta, S. Tsubota. *J. Catal.*, 144:175, 1993.

[95] Zhang H., Watanabe T., Okumura M., Haruta M., and Toshima N. *Nature Mater.*, 11:49, 2012.

[96] Hermes A.C., Hamilton S.M., Cooper G.A., Kerpal C., Harding D.J., Meijer G., Fielicke A., and Mackenzie S.R. *Faraday Discuss.*, 157:213, 2012.

[97] H. Sano N. Yamada M. Haruta, T. Kobayashi. *Chem. Lett.*, page 405, 1987.

[98] Stephens I.E.L., Bondarenko A.S., Gronbjerg U., Rossmeisl J., and Chorkendorff I. *Energy Environ. Sci.*, 5:6744, 2012.

[99] Perez-Alonso F.J., McCarthy D.N., Nierhoff A., Hernandez-Fernandez P., Strebel C., Stephens I.E.L., Nielsen J.H., and Chorkendorff I. *Angew. Chem. Int. Ed.*, 51:4641, 212.

[100] Singh J.P., Zhang X.G., Li H.L., Singh A., and Singh R.N. *Int. J. Electrochem.*, 3:416, 2008.

[101] Wang C., Markovic N.M., and Stamenkovic V.R. *ACS Catal.*, 2:891, 2012.

[102] Murata M., Watanabe S., and Masuda Y. *Tetrahedron Lett.*, 40:9255, 1999.

[103] Denmark S.E. and Baird J.D. *Org. Lett.*, 6:3649, 2004.

[104] Zhao Y. and Truhlar D.G. *Theor. Chem. Account*, 120:215, 2008.

[105] Ross A.J., Lang H.L., and Jackson R.F.W. *J. Org. Chem.*, 75:245, 2010.

[106] Andrei D. and Wnuk S.F. *J. Org. Chem.*, 71:405, 2006.

[107] Haruta M. *Chem. Rec.*, 3:75, 2003.

[108] Wei W., Lu Y., Chen W., and Chen S. *J. Am. Chem. Soc.*, 133:2060, 2011.

[109] Grönbeck H. and Andreoni W. *Chem. Phys.*, 262(1):1–14, 2000.

[110] Guvelioglu G.H., Ma P., He X., Forrey R.C., and Cheng H. *Phys. Rev. Lett.*, 94:026103, 2005.

[111] Wales D.J. *Energy Landscapes With Applications To Clusters, Glasses and Biomolecules*. Cambridge University Press, 2003.

[112] Schön J.C., Cancarevic Z.P., Hannemann A., and Jansen M. *J. Chem. Phys.*, 128:194712, 2008.

[113] Wevers M.A.C., Schön J.C., and Jansen M. *J. Phys.: Condens. Mater.*, 11:6487, 1999.

[114] Schön J.C, Wevers M.A.C., and Jansen M. *J. Phys.: Condens. Mater.*, 15:5479, 2003.

[115] Smeeton L.C., Oakley M.T., and Johnston R.L. *J. Comput. Chem.*, accepted, 2014.

[116] Murrell J.N. and Motram R.E. *Mol. Phys.*, 69:571, 1990.

[117] Cleri F. and Rosato V. *Phys. Rev. B.*, 48:22, 1993.

[118] Nunez S. and Johnston R.L. *J. Phys. Chem. C.*, 114(13255), 2010.

[119] Darby S., Mortimer-Jones T.V., Johnston R.L., and Roberts C. *J. Chem. Phys.*, 116:1536, 2002.

[120] Ismail R. and Johnston R.L. *Phys. Chem. Chem. Phys.*, 12:8607, 2010.

[121] Thomas L.H. *Proc. Cambridge Phil. Soc.*, 23:524, 1927.

[122] Fermi E. *Rend. Accad. Naz. Lincei.*, 6:602, 1927.

[123] Hohenberg P. and Kohn W. *Phys. Rev.*, 136:B864, 1964.

[124] Kohn W. and Sham L.J. *Phys. Rev.*, 140:A1133, 1965.

[125] Perdew J.P. and Zunger A. *Phys. Rev. B.*, 23:5048, 1981.

[126] Perdew J. P., Burke K., and Ernzerhof M. *Phys. Rev. Lett.*, 77:3865–3868, 1996.

[127] Zhao Y. and Truhlar D.G. *J. Chem. Phys.*, 125:194101, 2006.

[128] Zhao Y. and Truhlar D.G. *J. Chem. Phys. A.*, 110:13126, 2006.

[129] Rohrdanz M. A., Martins K. M., and Herbert J. M. *J. Chem. Phys.*, 130:054112, 2009.

[130] Refaely-Abramson S., Baer R., and Kronik L. *Phys. Rev. B.*, 84:075144, 2011.

[131] Wong B.M. *Mater. Res. Soc. Symp. Proc.*, 1120, 2009.

[132] Pastore M., Mosconi E., De Angelis F., and Gratzel M. *J. Phys. Chem. C.*, 114:7205, 2010.

[133] Vydrov O. A. and Scuseria G. E. *J. Chem. Phys.*, 125:234109, 2006.

[134] Basis set exchange. *www.bse.pnl.gov/bse/portal.*

[135] Runge E. and Gross E.K.U. *Phys. Rev. Lett.*, 52:997, 1984.

[136] Zwijnenburg M.A., Sokol A.A., Sousa C., and Bromley S.T. 2009. *J. Chem. Phys.*, 131:034705.

[137] Zwijnenburg M., Illas F., and Bromley S.T. *Phys. Chem. Chem. Phys.*, 13:9311, 2011.

[138] Metropolis N., Rosenbluth A.W., Rosenbluth M.N., Teller A.H., and Teller E. *J. Chem. Phys.*, 21:1087, 1953.

[139] Wales D.J. and Doye J.P.K. *J. Phys. Chem. A.*, 101:5110, 1997.

[140] Schön J.C., Putz H., and Jansen M. *J. Phys.: Condens. Mater.*, 8:143, 1996.

[141] Wales D.J. OPTIM: A program for optimizing geometries and calculating reaction pathways. *www-wales.ch.cam.ac.uk/OPTIM*.

[142] Deaven D. M. and Ho K. M. *Phys. Rev. Lett.*, 75:288–291, 1995.

[143] Johnston R. L. *Dalton Trans.*, 22:4193–4207, 2003.

[144] Giannozzi P., Baroni S., Bonini N., Calandra M., Car R., Cavazzoni C., Ceresoli D., Chiarotti G. L., Concoccioni M., and Dabo I. *et al.* *J. Phys.: Condens. Matter*, 21:395502, 2009.

[145] Valiev M., Bylaska E.J., Govind N., Kowalski K., Straatsma T.P., van Dam H.J.J., Wang D., Nieplocha J., Apra E., Windus T.L., and de Jong W.A. *Comput. Phys. Commun.*, 181:1477, 2010.

[146] Jennings P.C. and Johnston R.L. *Comp. Theor. Chem.*, 1021:91, 2013.

[147] Schön J.C. and Jansen M. *Angew. Chem. Int. Ed.*, 35:1286, 1996.

[148] Neelamraju S., Schön J.C., Doll K., and Jansen M. *Phys. Chem. Chem. Phys.*, 14:1223, 2012.

[149] Schön J.C., Wevers M.A.C., and Jansen M. *J. Phys.: Condens. Mater.*, 15:5479, 2003.

[150] Li Z. and Sheraga H. *Proc. Nat. Acad. Sci. USA*, 84:6611, 1987.

[151] Tsai C.J. and Jordan K.D. *J. Chem. Phys.*, 99:6957, 1993.

[152] Doye J.P.K. and Wales D.J. *J. Chem. Phys.*, 116:377, 2002.

[153] Sheppard D., Terrell R., and Henkelman G. *J. Chem. Phys.*, 128:134106, 2008.

[154] Trygubenko S.A. and ales D.J. *J. Chem. Phys.*, 120:2082, 2004.

[155] Munro L.J. and Wales D.J. *Phys. Rev. B.*, 59:3969, 1999.

[156] Becker O.M. and Karplus M. *J. Chem. Phys.*, 106:1495, 1997.

[157] Soto J.R., Molina B., and Castro J.J. *RSC Advances*, 4:8157, 2014.

[158] Remacle F. and Kryachko E.S. *J. Chem. Phys.*, 122:044304, 2005.

[159] Gilb S., Weis P, Furche F., Ahrlich R., and Kappes M.M. *J. Chem. Phys.*, 116:4094, 2002.

[160] Furche F., Ahlrichs R., Weis P., Jacob C., Gilb S., Bierweiler T., and Kappes M.M. *J. Chem. Phys.*, 117:6982, 2002.

[161] Johannson M.P., Lechtken A., Schooss D.F., Kappes M.M., and Furche F. *Phys. Rev. Lett.*, 77:053202, 2008.

[162] Chen M., Dyer J.E., Li K., and Dixon D.A. *J. Phys. Chem. A.*, 117:8298, 2013.

[163] Fernandez E.M., Soler J.M., Garzon I.L., and Balbas L.C. *Phys. Rev. B.*, 70(16):165403, 2004.

[164] Akeby H., Panas I., L.G.M. Pettersson, Siegbahn P., and Wahlgren U. *J. Phys. Chem.*, 94:5471, 1990.

[165] Jug K., Zimmermann B., Calaminici P., and Köster A. *J. Chem. Phys.*, 116:4497, 2002.

[166] Koretsky G.M. and Knickelbein M.B. *J. Chem. Phys.*, 107:10555, 1997.

[167] Molina L.M. and Hammer B. *Appl. Catal. A.*, 291:21–31, 2005.

[168] *J. Phys. Chem. A.*, 103(48):9573–9578, 1999.

[169] Kwon G., Ferguson G. A., Heard C. J., Tyo E. C., Yin C., DeBartolo J., Soenke S., Winans R. R. E., Kropf A. J., and Greely J. P. *et al.* *ACS Nano*, 7:5808–5817, 2013.

[170] Kerpal C., Harding D.J., Rayner D.M., and Fielicke A. *J. Phys. Chem. A.*, 117:8230, 2013.

[171] Heiles S. and Schäfer R. *Dielectric Properties of Isolated Clusters: Beam Deflection Studies*. Springer Netherlands, 1st edition, 2014.

[172] A. Burow, T. Wende, M. Sierka, R. Wlodarczyk, J. Sauer, P. Claes, L. Jiang, G. Meijer, P. Lievens, and K. Asmis. *Phys. Chem. Chem. Phys.*, 13(43):19393, 2011.

[173] Wang Y.L., Zhai H.J., Xu L., Li J., and Wang L.S. *J. Phys. Chem. A.*, 114:1247, 2010.

[174] Mesleh M.F., Hunter J.M., Schvartzburg A.A, Schatz G.C., and Jarrold M.F. *J. Phys. Chem.*, 100:16082, 1996.

[175] Lecoultre S., Rydlo A., Felix C., Buttet J., Gilb S., and Harbich W. *J. Chem. Phys.*, 134(7):074303, 2011.

[176] Tiago M. L., Idrobo J. C, Öğüt S., Jellinek J., and Chelikowsky J. R. *Phys. Rev. B*, 79(15):155419, 2009.

[177] Lecoultre S., Rydlo A., Buttet J., Felix C., Gilb S., and Harbich W. *J. Chem. Phys.*, 134(18):184504, 2011.

[178] Palpant B., Prével B., Lermé J., Cottancin E., Pellarin M., Treilleux M., Perez A., Vialle J. L., and Broyer M. *Phys Rev. B*, 57(3):1963–1970, 1998.

[179] Lecoultre S., Rydlo A., Felix C., , Buttet J., Gilb S., and Harbich W. *J. Chem. Phys.*, 134(7):074302, 2011.

[180] Botti S., Sottile F., Vast N., Olevano V., and Reining L. *Phys. Rev. B*, 69(14):155112, 2004.

[181] Pedersen D. B. and Wang S. *J. Phys. Chem. C*, 111:17493–17499, 2007.

[182] Piccini G., Havenith R.W.A., Broer R., and Stener M. *J. Phys. Chem. C.*, 117:17196, 2013.

[183] López ozano X., Mottet C., and Weissker H.C. *J. Phys. Chem. C.*, 117:3062, 2013.

[184] Velázquez-Salazar J. J., Esparza R., Mejía-Rosales S. J., Estrada-Salas R., Ponce A., Deepak F. L., Castro-Guerrero C., and José-Yacamán M. *ACS Nano*, 5(8):6272–6278, 2011.

[185] Zheng C., Hoffman R., and Nelson D. R. *J. Am. Chem. Soc.*, 112:3784–3791, 1990.

[186] Sciortino F., Tartagli P., and Zaccarelli E. *J. Phys. Chem. B*, 109(46):21942–21953, 2005.

[187] Zwijnenburg M. and Bromley S.T. *Phys. Rev. B.*, 83:024104, 2011.

[188] Pacheco-Contreras R., Dessens-Félix M., Borbón-González D. J., Paz-Borbón L. O., Johnston R. L., Schön J. C., and Posada-Amarillas A. *J. Phys. Chem. A*, 116:5235–5239, 2012.

[189] Henry C. R. *Surf. Sci. Rep.*, 31(7-8):235–325, 1998.

[190] Friebel D., Bajdich M., Yeo B.S., Louie M.W., Miller D.J., Casalongue H.S., Mbuga F., Weng T.-C., Nordlund D., Sokaras D., Alonso-Mori R., Bellac A.T., and Nilsson A. *Phys. Chem. Chem. Phys.*, 15:17460, 2013.

[191] Greeley J., Jaramillo T.F., Bonde J., Chorkendorff I., and Nørskov J.K. *Nat. Mater.*, (5):909, 2006.

[192] Nørskov J.K., Rossmeisl J., Logadottir A., Lindqvist L., Kitchin J.R., Bligaard T., and Jónsson H. *J. Phys. Chem. B*, 108:17886, 2004.

[193] Greeley J., Stephens I.E.L., Bondarenko A.S., Johansson T.P., Hansen H.A., Jaramillo T.F., Rossmeisl J., Chorkendorff I., and Nørskov J.K. *Nat. Chem.*, 1:552, 2009.

[194] Trasatti S. *Electrochim. Acta*, 29:1503, 1984.

[195] Garcá-Mota M., Vojvodic A., Metiu H., Man I.C., Su H.-Y., Rossmeisl J., and Nørskov J.K. *ChemCatChem*, 3:1607, 2011.

[196] Man I.C., Su H.-Y., Calle-Vallejo F., Hansen H.A., Martińez J.I., Inoglu N.G., Kitchin J., Jaramillo T.F., Nørskov J.K., and Rossmeisl J. *ChemCatChem*, page 1159, 2011.

[197] Suntivich J., May K.J., Gasteiger H.A., Goodenough J.B., and Shao-Horn Y. *Science*, 334:1383, 2011.

[198] Vojvodic A. and Nørskov J.K. *Science*, 334:1355, 2011.

[199] Jiao F. and Frei H. *Angew. Chem., Int. Ed.*, 48:1841, 2009.

[200] Yeo B.S. and Bell T. *J. Am. Chem. Soc.*, 133:5587, 2011.

[201] Ferguson G.A., Yin C., Kwon G., Tyo E.C., Lee S., Greeley J.P., Zapol P., Lee B., Seifert S., Winans R.E., Vajda S., and Curtiss L.A. *J. Phys. Chem. C.*, 116:24027–24034, 2012.

[202] Habibpour V., Yin C.R., Kwon G., Vajda S., and Palmer R.E. *J. Exp. Nanosci.*, 8(7-8):993–1003, 2013.

[203] Musolino V., Selloni A., and Car R. *Surf. Sci.*, 402-404:413–417, 1998.

[204] Bogicevic A. and Jennison D.R. *Surf. Sci. Lett.*, 437:L741–L747, 1999.

[205] Campbell C.T. *Surf. Sci. Rep.*, 27:1–111, 1997.

[206] Pacchioni G. and Rösch N. *J. Chem. Phys.*, 104:7329, 1996.

[207] Yudanov I.V., Vent S., Neyman K., Pacchioni G., and Rösch N. *Chem. Phys. Lett.*, 275(3-4):245–252, 1997.

[208] Reveles J.U., Köster A.M., Calaminici P., and Khanna S.N. *J. Chem. Phys.*, 136:114505, 2012.

[209] Ismail R., Ferrando R., and Johnston R. L. *J. Phys. Chem. C.*, 117:293–301, 2012.

[210] Moseler M., Häkinnen H., and Landman U. *Phys. Rev. Lett.*, 89(17):176103, 2002.

[211] Heiles S. and Johnston R.L. *Int. J. Quant. Chem.*, 113(18):2091, 2013.

[212] Boatwright A., Feng C., Spence D., Latimer E., Binns C., Ellis A.M., and Yang S. *Faraday Discuss.*, 162:113, 2013.

[213] Bartelt A., Close J.D., Federmann F., Quaas N., and Toennies J.P. *Phys. Rev. Lett.*, 77(17):3525, 1996.

[214] Vilhelmsen L.B. and Hammer B. *Phys. Rev. Lett.*, 108:126101, 2012.

[215] Goodman D.W. *J. Catal.*, 216:213, 2003.

[216] Demoulin O., Rupprecheter G. Seunier I., LeClef B., Navez M., and Ruiz P. *J. Phys. Chem. B.*, 109:20454, 2005.

[217] Blomberg S., Gustafson J., Martin N.M., Messing M.E., Deppert K., Liu Z., Chang R., Fernandes V., Borg A. Grönbeck H., and Lundgren E. *Surf. Sci.*, 616:186, 2013.

[218] Yin Z., Zhang Y., Chen K., Li J., Li W., Tang P., Zhao H., Zhu Q., Bao X., and Ma D. *Scientific Rep.*, 4:4288, 2014.

[219] Enache D.I., Edwards J.K., Landon P., Solsona-Espriu B., Carley A.F., Herzing A.A., Watanabe M., Kiely C.J., Knight D.W., and Hutchings G.J. *Science*, 311:362, 2006.

[220] Atanazov I., Barcaro G., Negreiros F., Fortunelli A., and Johnston R.L. *J. Chem. Phys.*, 138:224703, 2013.

[221] Heard C.J., Vajda S., and Johnston R.L. *J. Phys. Chem. C.*, 118:3581, 2014.

[222] Grasa G.A., Viciu M.S, Huang J., Zhang C., Trudell M.L., and Nolan S.P. *Organometallics*, (21):2866, 2002.

[223] Weng Z., Teo S., Koh L.L., and Hor T.S.A. *Organometallics*, 23:4342, 2004.

[224] Itami K., Nokami T., Ishimura Y., Mitsudo K., Kamei T., and Yoshida J.-I. *J. Am. Chem. Soc.*, 123:11577, 2001.

[225] Zhou J. and Fu G.C. *J. Am. Chem. Soc.*, 125:12527, 2003.

[226] Rocaboy C. and Gladysz J.A. *Org. Lett.*, 4(12):1993, 2002.

[227] Mazza M.C. and Pierpont C.G. *J. Chem. Soc., Chem. Commun.*, page 207, 1973.

[228] Tanaka H. and Kawazura H. *Bull. Chem. Soc. Jpn.*, 53:1743, 1980.

[229] Ukai T., Kawazura H., Ishii Y., Bonnet J.J., and Ibers J.A. *J. Organomet. Chem.*, 65:253, 1974.